Design and Fabrication of

Diffractive Optical Elements with MATLAB®

Downloaded From: https://www.spiedigitallibrary.org/ebooks/ on 27 Feb 2022
Terms of Use: https://www.spiedigitallibrary.org/terms-of-use

Tutorial Texts Series

- *Practical Electronics for Optical Design and Engineering*, Scott W. Teare, Vol. TT107
- *Automatic Target Recognition*, Bruce J. Schachter, Vol. TT105
- *Design Technology Co-optimization in the Era of Sub-resolution IC Scaling*, Lars W. Liebmann, Kaushik Vaidyanathan, and Lawrence Pileggi, Vol. TT104
- *Special Functions for Optical Science and Engineering*, Vasudevan Lakshminarayanan and L. Srinivasa Varadharajan, Vol. TT103
- *Discrimination of Subsurface Unexploded Ordnance*, Kevin A. O'Neill, Vol. TT102
- *Introduction to Metrology Applications in IC Manufacturing*, Bo Su, Eric Solecky, and Alok Vaid, Vol. TT101
- *Introduction to Liquid Crystals for Optical Design and Engineering*, Sergio Restaino and Scott Teare, Vol. TT100
- *Design and Implementation of Autostereoscopic Displays*, Byoungho Lee, Soon-gi Park, Keehoon Hong, and Jisoo Hong, Vol. TT99
- *Ocean Sensing and Monitoring: Optics and Other Methods*, Weilin Hou, Vol. TT98
- *Digital Converters for Image Sensors*, Kenton T. Veeder, Vol. TT97
- *Laser Beam Quality Metrics*, T. Sean Ross, Vol. TT96
- *Military Displays: Technology and Applications*, Daniel D. Desjardins, Vol. TT95
- *Interferometry for Precision Measurement*, Peter Langenbeck, Vol. TT94
- *Aberration Theory Made Simple, Second Edition*, Virendra N. Mahajan, Vol. TT93
- *Modeling the Imaging Chain of Digital Cameras*, Robert D. Fiete, Vol. TT92
- *Bioluminescence and Fluorescence for* In Vivo *Imaging*, Lubov Brovko, Vol. TT91
- *Polarization of Light with Applications in Optical Fibers*, Arun Kumar and Ajoy Ghatak, Vol. TT90
- *Digital Fourier Optics: A MATLAB Tutorial*, David G. Voeltz, Vol. TT89
- *Optical Design of Microscopes*, George Seward, Vol. TT88
- *Analysis and Evaluation of Sampled Imaging Systems*, Richard H. Vollmerhausen, Donald A. Reago, and Ronald Driggers, Vol. TT87
- *Nanotechnology: A Crash Course*, Raúl J. Martin-Palma and Akhlesh Lakhtakia, Vol. TT86
- *Direct Detection LADAR Systems*, Richard Richmond and Stephen Cain, Vol. TT85
- *Optical Design: Applying the Fundamentals*, Max J. Riedl, Vol. TT84
- *Infrared Optics and Zoom Lenses, Second Edition*, Allen Mann, Vol. TT83
- *Optical Engineering Fundamentals, Second Edition*, Bruce H. Walker, Vol. TT82
- *Fundamentals of Polarimetric Remote Sensing*, John Schott, Vol. TT81
- *The Design of Plastic Optical Systems*, Michael P. Schaub, Vol. TT80
- *Fundamentals of Photonics*, Chandra Roychoudhuri, Vol. TT79
- *Radiation Thermometry: Fundamentals and Applications in the Petrochemical Industry*, Peter Saunders, Vol. TT78
- *Matrix Methods for Optical Layout*, Gerhard Kloos, Vol. TT77
- *Fundamentals of Infrared Detector Materials*, Michael A. Kinch, Vol. TT76
- *Practical Applications of Infrared Thermal Sensing and Imaging Equipment, Third Edition*, Herbert Kaplan, Vol. TT75
- *Bioluminescence for Food and Environmental Microbiological Safety*, Lubov Brovko, Vol. TT74
- *Introduction to Image Stabilization*, Scott W. Teare and Sergio R. Restaino, Vol. TT73
- *Logic-based Nonlinear Image Processing*, Stephen Marshall, Vol. TT72
- *The Physics and Engineering of Solid State Lasers*, Yehoshua Kalisky, Vol. TT71
- *Thermal Infrared Characterization of Ground Targets and Backgrounds, Second Edition*, Pieter A. Jacobs, Vol. TT70
- *Introduction to Confocal Fluorescence Microscopy*, Michiel Müller, Vol. TT69
- *Artificial Neural Networks: An Introduction*, Kevin L. Priddy and Paul E. Keller, Vol. TT68
- *Basics of Code Division Multiple Access (CDMA)*, Raghuveer Rao and Sohail Dianat, Vol. TT67
- *Optical Imaging in Projection Microlithography*, Alfred Kwok-Kit Wong, Vol. TT66
- *Metrics for High-Quality Specular Surfaces*, Lionel R. Baker, Vol. TT65
- *Field Mathematics for Electromagnetics, Photonics, and Materials Science*, Bernard Maxum, Vol. TT64
- *High-Fidelity Medical Imaging Displays*, Aldo Badano, Michael J. Flynn, and Jerzy Kanicki, Vol. TT63

(For a complete list of Tutorial Texts, see http://spie.org/publications/books/tutorial-texts.)

Downloaded From: https://www.spiedigitallibrary.org/ebooks/ on 27 Feb 2022
Terms of Use: https://www.spiedigitallibrary.org/terms-of-use

Design and Fabrication of

Diffractive Optical Elements with MATLAB®

A. Vijayakumar
Shanti Bhattacharya

Tutorial Texts in Optical Engineering
Volume TT109

SPIE PRESS
Bellingham, Washington USA

Downloaded From: https://www.spiedigitallibrary.org/ebooks/ on 27 Feb 2022
Terms of Use: https://www.spiedigitallibrary.org/terms-of-use

Library of Congress Cataloging-in-Publication Data

Names: Bhattacharya, Shanti (Professor in Optics), author. | Vijayakumar, Anand, author.
Title: Design and fabrication of diffractive optical elements with MATLAB / Shanti Bhattacharya and Anand Vijayakumar.
Other titles: Tutorial texts in optical engineering ; v. TT 109.
Description: Bellingham, Washington : SPIE Press, [2017] | Series: Tutorial texts in optical engineering ; volume TT 109 | Includes bibliographical references and index.
Identifiers: LCCN 2016043114 | ISBN 9781510607057 (softcover ; alk. paper) | ISBN 1510607056 (softcover ; alk. paper) | ISBN 9781510607064 (pdf) | ISBN 1510607064 (pdf) | ISBN 9781510607071 (epub) | ISBN 1510607072 (epub) | ISBN 9781510607088 (Kindle/mobi) | ISBN 1510607080 (Kindle/mobi)
Subjects: LCSH: Diffraction–Mathematics. | Optics–Mathematics. | MATLAB.
Classification: LCC QC415 .B48 2017 | DDC 535/.420284–dc23 LC record available at https://lccn.loc.gov/2016043114

Published by

SPIE
P.O. Box 10
Bellingham, Washington 98227-0010 USA
Phone: + 1 360.676.3290
Fax: + 1 360.647.1445
Email: books@spie.org
Web: http://spie.org

Copyright © 2017 Society of Photo-Optical Instrumentation Engineers (SPIE)

All rights reserved. No part of this publication may be reproduced or distributed in any form or by any means without written permission of the publisher.

The content of this book reflects the work and thought of the authors. Every effort has been made to publish reliable and accurate information herein, but the publisher is not responsible for the validity of the information or for any outcomes resulting from reliance thereon.

Printed in the United States of America.
First Printing.
For updates to this book, visit http://spie.org and type “TT109” in the search field.

Downloaded From: https://www.spiedigitallibrary.org/ebooks/ on 27 Feb 2022
Terms of Use: https://www.spiedigitallibrary.org/terms-of-use

To the Lord God Almighty—for being my strength
To my beloved mother Jacintha—for showing me the meaning of love and sacrifice
To my dearest wife and best friend Arthi—for loving me unconditionally
To all of my teachers—for guiding me through various journeys in my life

–Vijay

To my husband, Subbu:
Note: An empty day with clan is better handled with you! (2, 4, 6)

–Shanti

Downloaded From: https://www.spiedigitallibrary.org/ebooks/ on 27 Feb 2022
Terms of Use: https://www.spiedigitallibrary.org/terms-of-use

Downloaded From: https://www.spiedigitallibrary.org/ebooks/ on 27 Feb 2022
Terms of Use: https://www.spiedigitallibrary.org/terms-of-use

Introduction to the Series

Since its inception in 1989, the Tutorial Texts (TT) series has grown to cover many diverse fields of science and engineering. The initial idea for the series was to make material presented in SPIE short courses available to those who could not attend and to provide a reference text for those who could. Thus, many of the texts in this series are generated by augmenting course notes with descriptive text that further illuminates the subject. In this way, the TT becomes an excellent stand-alone reference that finds a much wider audience than only short course attendees.

Tutorial Texts have grown in popularity and in the scope of material covered since 1989. They no longer necessarily stem from short courses; rather, they are often generated independently by experts in the field. They are popular because they provide a ready reference to those wishing to learn about emerging technologies or the latest information within their field. The topics within the series have grown from the initial areas of geometrical optics, optical detectors, and image processing to include the emerging fields of nanotechnology, biomedical optics, fiber optics, and laser technologies. Authors contributing to the TT series are instructed to provide introductory material so that those new to the field may use the book as a starting point to get a basic grasp of the material. It is hoped that some readers may develop sufficient interest to take a short course by the author or pursue further research in more advanced books to delve deeper into the subject.

The books in this series are distinguished from other technical monographs and textbooks in the way in which the material is presented. In keeping with the tutorial nature of the series, there is an emphasis on the use of graphical and illustrative material to better elucidate basic and advanced concepts. There is also heavy use of tabular reference data and numerous examples to further explain the concepts presented. The publishing time for the books is kept to a minimum so that the books will be as timely and up-to-date as possible. Furthermore, these introductory books are competitively priced compared to more traditional books on the same subject.

When a proposal for a text is received, each proposal is evaluated to determine the relevance of the proposed topic. This initial reviewing process has been very helpful to authors in identifying, early in the writing process, the need for additional material or other changes in approach that would serve to strengthen the text. Once a manuscript is completed, it is peer reviewed to ensure that chapters communicate accurately the essential ingredients of the science and technologies under discussion.

It is my goal to maintain the style and quality of books in the series and to further expand the topic areas to include new emerging fields as they become of interest to our reading audience.

James A. Harrington
Rutgers University

Downloaded From: https://www.spiedigitallibrary.org/ebooks/ on 27 Feb 2022
Terms of Use: https://www.spiedigitallibrary.org/terms-of-use

Downloaded From: https://www.spiedigitallibrary.org/ebooks/ on 27 Feb 2022
Terms of Use: https://www.spiedigitallibrary.org/terms-of-use

Contents

Downloaded From: https://www.spiedigitallibrary.org/ebooks/ on 27 Feb 2022
Terms of Use: https://www.spiedigitallibrary.org/terms-of-use

Downloaded From: https://www.spiedigitallibrary.org/ebooks/ on 27 Feb 2022
Terms of Use: https://www.spiedigitallibrary.org/terms-of-use

Downloaded From: https://www.spiedigitallibrary.org/ebooks/ on 27 Feb 2022
Terms of Use: https://www.spiedigitallibrary.org/terms-of-use

Downloaded From: https://www.spiedigitallibrary.org/ebooks/ on 27 Feb 2022
Terms of Use: https://www.spiedigitallibrary.org/terms-of-use

Foreword

Light sustains life. It enthralls, captivates, and provides immense pleasure. It connects cultures and establishes vocal and visual communication among different life forms. We admire the beauty of flowers, of butterflies, and of the feathers of a peacock. There is something mystical about light, with even the ancients speculating on its nature. Although we now accept its dual nature, we continue to explore its other hidden features.

Diffractive optical elements (DOEs) essentially function due to the interplay of the phenomena of diffraction and interference that often display vivid colors. Diffraction of light takes place when a wavefront is limited in space; the limitation may be imposed either by the mountings of the optics or by the apertures. Therefore, diffraction of light always takes place, and its effects become significant when an aperture allows only a tiny portion of the wavefront to pass. Grimaldi (1618–1663) carried out extensive experimental investigations on diffraction, although the term *diffraction* is attributed to Leonardo da Vinci (1452–1519). In 1818 Fresnel (1788–1827) wrote a memoir on diffraction that is fundamental to the theory of diffraction of light. While making a presentation to the French Academy of Sciences, Fresnel showed the appearance of a bright spot in the shadow of a round object. Not believing the theory, Arago rushed to the laboratory and indeed found that it is true, and the spot became known as an Arago spot. Kirchhoff (1824–1887) put the theory of diffraction of light on sound mathematical footing. Thereafter, it became known that light could be bent either by reflection, refraction, or diffraction; hence, devices based on diffraction—like those based on reflection and refraction—could be conceived. Fresnel indeed showed that an interesting planar artifact, when properly fabricated, would act as a positive lens, a negative lens, and a plate; this artifact is known as a Fresnel zone plate.

DOEs can have both scientific and nonscientific applications. Nonscientific applications include security holograms and elements for amusement. These are used on bank notes and on products as a sign of authenticity. This particular application has, in fact, spread to many marketable products.

Scientific applications of DOEs lie in beam manipulation and the miniaturization of instruments for imaging and sensing. Gratings were the earliest DOEs and were painstakingly fabricating by drawing lines with a

Downloaded From: https://www.spiedigitallibrary.org/ebooks/ on 27 Feb 2022
Terms of Use: https://www.spiedigitallibrary.org/terms-of-use

diamond tip on speculum metal. With the invention of holography by Gabor (1900–1979), gratings could be made with considerable ease: the gratings were the record of the interference pattern between two plane waves or between a spherical wave and a plane wave on a light-sensitive material. With an understanding of the holographic principle in place, methods to record amplitude and phase of the light reflected/transmitted by works of art were developed. The phase detour method attributed to Lohmann (1926–2013) was used to record both the amplitude and phase of an object wave in the artwork created by the computer-controlled plotter. These computer-generated holograms (CGHs) were used as filters for optical processing in photoreduction, making it much easier to draw line artwork, i.e., by skeletonizing the interferogram. These same elements were used for testing optical surfaces and systems. Following the work of Wyant, in 1976 I made the CGH for testing a planoconvex lens. One of authors (SB in 1996) of this tutorial made a checker grating on a desktop-controlled plotter for splitting the wavefront into a large number of spots. After photoreduction and on illumination, the checker grating produced spots that were surprisingly of almost equal intensities. Many different types of elements, all of them line elements, were made on this plotter for several other applications. It is worth mentioning that all CGHs are DOEs. On the contrary, all DOEs are not CGHs.

Coming to this book, the authors present the art and technology of making DOEs using MATLAB® and have simulated the results. They successfully explain the transition from 3D optics to 2D optics, taking the example of a Fresnel lens used even today in lighthouses. The transition from 3D to 2D is important in understanding the functioning of DOEs. The authors develop the topic by starting with a 1D binary grating. In order to direct diffracted light into a single order, usually the first order, the grating is blazed. The book moves to a discussion of 2D elements, such as the Fresnel zone plate. Methods to improve efficiency are also discussed. For example, multilevel zone plates provide high diffraction efficiency. An array of such zone plates constitutes the Hartman sensor used in adaptive optics applications. Other 2D diffractive optical elements include circular gratings or axicons, axilenses, spiral phase plates, cross binary gratings, and their combinations. These elements and their combinations having interesting, multifunctional properties are all discussed in the book. The design of DOEs in Fresnel and Fraunhofer regions is explained separately. These designs are based on the scalar theory of diffraction, and a ray-tracing approach is followed. Because the DOEs are written on refracting surfaces in order to compensate for certain aberrations, MATLAB codes for the aberration evaluation are also provided.

CGHs are the interference record between a reference and object wave; a reference wave is usually a plane wave, while the object wave at the plane of recording is obtained by use of a Fresnel propagator. In some cases, Fourier/

Downloaded From: https://www.spiedigitallibrary.org/ebooks/ on 27 Feb 2022
Terms of Use: https://www.spiedigitallibrary.org/terms-of-use

Fraunhofer holograms are also recorded. The transmittance of the hologram is usually linearly related to the intensity distribution in the interference pattern. When illuminated with the reference wave, the CGH generates the desired object wave. A CGH with a mathematically defined wavefront or a picture as input can be designed.

This book provides MATLAB codes for almost all of the examples described, be they DOEs or CGHs. It is therefore a 'must-have' book for a person intent on carrying out DOE design for research or economic reasons. Because detailed theory of the functioning of these elements is not provided, the Ph.D. thesis* by one of the authors (VK) is also a 'must read.' The fabrication procedures of these DOEs/CGHs using electron beam lithography, ion beam lithography, and photolithography are described. The exercises provided at the end of the chapters add value in the way of beneficial practice afforded to the readers.

Needless to say, this tutorial will be useful to students, teachers, and optical designers. Diffraction patterns of complex apertures can be visualized using the knowledge acquired by attempting the codes provided in the book.

R. S. Sirohi
Tezpur, Assam, India

*doi: 10.13140/RG.2.2.25996.51847

Downloaded From: https://www.spiedigitallibrary.org/ebooks/ on 27 Feb 2022
Terms of Use: https://www.spiedigitallibrary.org/terms-of-use

Downloaded From: https://www.spiedigitallibrary.org/ebooks/ on 27 Feb 2022
Terms of Use: https://www.spiedigitallibrary.org/terms-of-use

Preface

Diffractive optics, if not yet a household word, is certainly a household phenomenon. Many systems encountered in our everyday world contain or use diffractive optics. A good example is DVD players or barcode scanners. Elements that work on the principles of diffraction, or diffractive optical elements (DOEs), can successfully replace refractive elements used in different systems. This is because DOEs are capable of manipulating light in ways not possible by conventional refractive optical elements. In addition, DOEs are light in weight and compact compared to their refractive counterparts. The development of this technology will encourage the conversion of bulky refractive optical systems into highly compact, lightweight diffractive optical systems. It is our belief that fabrication of diffractive optics needs to be further developed and simplified so that more diffractive elements replace refractive elements in the future. We hope that this book will ease this transition.

Several excellent books* already exist that explain the basics and important concepts in the field of DOEs. This book does not intend to replace them. Rather, the idea is to supplement the available information with a text that will equip one with the skills required to start designing, simulating, and even fabricating diffractive optics. Given the many different applications and uses of diffractive optics, the importance of this field cannot be underestimated. Surprisingly, there are only a few books that provide a hands-on approach to the field. The lacuna of such information from a single source motivated us to create a resource based on our practical experience. In this book, learning occurs with assistive MATLAB® codes that enable visualization of the ideas presented and a better understanding of the parameters controlling different aspects of light. We believe that this manner of treatment will enable a new graduate student to quickly grasp the fundamentals of diffractive optics, beginning with the design of simple DOEs and moving to more complex ones.

We hope the reader will benefit from this practical approach to designing and fabricating diffractive optical elements. Experimentalists will be able to design appropriate structures that can be used in many different applications such as

*See Chapter 1, Refs. 6, 33, and 57–59.

Downloaded From: https://www.spiedigitallibrary.org/ebooks/ on 27 Feb 2022
Terms of Use: https://www.spiedigitallibrary.org/terms-of-use

spectroscopy, optical trapping, or beam shaping. The design of DOEs is presented with simple equations and step-by-step procedures for simulation—from the simplest 1D grating to the more-complex multifunctional DOEs—along with analysis of their diffraction patterns using MATLAB. The fundamentals of fabrication techniques such as photolithography, electron beam lithography, and focused ion beam lithography with basic instructions for the beginner are presented. Basic error analysis and error-correction techniques for a few cases are also discussed. It must be noted that this book will focus only on passive DOEs; SLMs are not required for demonstration. However, the MATLAB codes provided can be used for displaying DOE designs on SLMs as well. Thus, we hope that this book will help not only new students but also scientists in the industry to quickly learn techniques to help with the design, simulation, and testing of DOEs.

The book consists of eight chapters. A brief summary of the content of each chapter is as follows:

Chapter 1 introduces the fundamentals of diffractive optics and compares diffractive and refractive optics. A quick review of the theoretical formulation of diffraction are presented, along with different theoretical approximations and their validity regimes.

Chapter 2 presents the fundamentals of design and far-field analysis of simple binary DOEs such as 1D and 2D gratings, axicons, and Fresnel zone plates (FZPs). It shows the beginner how to make simple calculations to extract the intensity values and spacing between the different diffraction maxima.

Chapter 3 discusses the design, simulation aspects, and far-field analysis of multilevel and blazed DOEs such as multilevel gratings, diffractive axicons, blazed FZPs, axilenses, spiral phase plates, etc. It also discusses the basic algorithms for designing DOEs to obtain any desired intensity profile.

Chapter 4 describes the design and analysis of DOEs in the Fresnel diffraction regime to simulate diffraction patterns at different planes in the propagation direction. It also discusses some interesting phenomena such as the Talbot effect.

Chapter 5 presents the basic aberration correction techniques used to reduce and avoid errors while designing DOEs.

Chapter 6 introduces the art of creating different advanced multifunctional DOEs, along with their design, simulation, and analysis. The important properties of multifunctional DOEs are also discussed.

Chapter 7 describes the design and analysis of holographic optical elements for different applications. Computer-generated Fourier and Fresnel holography techniques are also discussed.

Chapter 8 presents the fundamentals of designing lithography files and the fabrication of DOEs using photolithography, electron beam lithography, and focused ion beam lithography, with basic fabrication recipes provided.

The content of the chapters is supported throughout by clearly commented MATLAB codes, making this book useful even to a novice programmer.

Happy Diffracting!

A. Vijayakumar and Shanti Bhattacharya
November 2016

Downloaded From: https://www.spiedigitallibrary.org/ebooks/ on 27 Feb 2022
Terms of Use: https://www.spiedigitallibrary.org/terms-of-use

Acknowledgments

As with any project, this book began with one small step or rather one seemingly small suggestion. Vijay (Vijayakumar), who was then my doctoral student in the finishing stages of his work, proposed that we record the basics of what we had done over the last few years in the form of a book. He felt that although a number of books on diffractive optics exist, they did not cover the hands-on knowledge required to actually start designing and fabricating such elements. Over the next few days, we discussed his proposal, and in one of those coincidences that seem to happen uncannily often, an email from SPIE Press popped into both of our email boxes, encouraging researchers to publish. It seemed that the time was right to create this book. The rest, as they say, is history.

The first person to thank, therefore, is my fellow author Vijay, for his enthusiasm and hard work. This book would not exist if it were not for him. Many of the examples and results presented were developed over the course of Vijay's Ph.D. work, and we both thank Prof. Enakshi Bhattacharya, Prof. Harishankar Ramachandran, Dr. Deepa Venkitesh, and Dr. Balaji Srinivasan of the Department of Electrical Engineering, IIT Madras, for their invaluable suggestions during that period and Dr. Bijoy Krishna Das, from the same department, for lending us his fiber-coupled sources with which to test our elements.

All of the electron beam lithography (EBL) work presented in this book was carried out at the Centre for NEMS and Nanophotonics, IIT Madras. We thank the Ministry of Communications and Information Technology for funding this Centre and our research work. The EBL work would not have been possible without help from several staff members associated with the EBL system, and we thank them and the students who have helped with the running of the machine or preparation of the samples. In particular, we are deeply indebted to Dr. Manu Jaiswal, Department of Physics, IIT Madras, for his support and help when the RAITH electron beam lithography system was being set up and to the ever-helpful, ever-present staff of the Centre, namely, Mr. Rajendran, Mr. Prakash, Mr. Joseph, and Mr. Sridhar. We also thank Mr. Karthick Raj, EBL operator (2013–2014), Centre for NEMS and Nanophotonics, IIT Madras, for his help relating to the work described in Section 8.3.4.

Downloaded From: https://www.spiedigitallibrary.org/ebooks/ on 27 Feb 2022
Terms of Use: https://www.spiedigitallibrary.org/terms-of-use

The focused ion beam (FIB) work was carried out at two institutions. At IIT Madras, the Quanta 3D FEG FIB system located in the Nano-Functional Materials Technology Centre (NFMTC), IIT Madras, was used for all of the initial FIB work. We are grateful to the NFMTC faculty in charge for giving us access to the tool. The FIB work on fibers was carried out at the Max Planck Institute (MPI) for Intelligent Systems, Stuttgart, Germany. We thank Dr. Michael Hirscher and Prof. Joachim P. Spatz, MPI, for offering the use of their FIB system to us any time we needed it. We are also grateful for their helpful suggestions and discussions. Several of the results presented in Chapter 8 arose from collaborative work between Dr. Shanti Bhattacharya and Dr. Pramitha Vayalamkuzhi, Inspire Faculty, IIT Madras, and Ms. Ulrike Eigenthaler and Dr. Kahraman Kesinbora, MPI. Figures 8.52, 8.54, 8.56, 8.57, 8.58, and 8.59 were taken with the FIB system made available to us at MPI. We gratefully acknowledge their permission to use these results in this book. We thank Mr. Jayavel, staff member, and Ms. Gayathri, M.S. doctoral student, Department of Electrical Engineering, IIT Madras, for their suggestions and help in handling and preparing fibers for diffractive optic fabrication with the FIB system. Dr. Pramitha is specially thanked for her many contributions to Chapter 8.

We would be remiss if we did not acknowledge Prof. S. S. Bhattacharya and Dr. Deepa Venkitesh for reviewing the initial chapters of this book. Their suggestions greatly enhanced the clarity of those chapters. Vijay also thanks his friend and former colleague, Mr. Vinoth, for his suggestions while writing this book.

Special thanks goes to the SPIE Press editor, Ms. Dara Burrows, for her useful suggestions and constant words of encouragement throughout the book project.

Writing a book requires two kinds of support: that relating to the book itself and that provided by the network of family and friends who surround us. We hope that we have thanked everyone connected with the former and apologize if, by oversight, we have left someone out.

We reserve the final part of this acknowledgment to the people who made the task of writing easy just by being part of our lives. We truly appreciate the constant encouragement and support extended to us by our families during this book project.

Shanti thanks her friend Anu for their weekly runs that helped keep her sane and her daughter Sumi for all the fun they share. As for her husband Subbu, who once commented, "One day, I will get you to put in writing how you cannot manage without me," he may consider that day as having arrived! Shanti would also like to use this opportunity to thank her Ph.D. advisor, Prof. R. S. Sirohi for starting her out on this journey with light.

We hope that readers find this book useful and encourage them to contact the authors with questions, comments, or suggestions at physics.vijay@gmail.com or shantib@iitm.ac.in.

Downloaded From: https://www.spiedigitallibrary.org/ebooks/ on 27 Feb 2022
Terms of Use: https://www.spiedigitallibrary.org/terms-of-use

Symbols and Notation

A	Aperture function
d	Distance
d	Lateral feature
D_m	Fourier coefficients of order m
E	Optical field (complex amplitude)
f	Focal length
f_0	Focal length of axilens
f_x	Spatial frequency along x direction
fx	Focal length along x direction
f_y	Spatial frequency along y direction
fy	Focal length along y direction
g	Number of levels
I_m	Relative intensity for diffraction order m with respect to incident intensity
I_0	On-axis intensity
k	Wave vector ($2\pi/\lambda$)
$k\psi(\bar{u})$	Phase of beam
L	Topological charge
m	Order of diffraction
m_x	Order of diffraction along x direction
m_x	Order of diffraction along y direction
M	Magnification
M_r	Radial magnification
n	Order of zones of FZP/mesh
n	Refractive index
n_1	Number of rings in mesh
n_g	Refractive index of glass medium
n_r	Refractive index of resist
N	Number of sampling points
P_r	Power in a circle of radius r
P_{TOT}	Power over the entire beam
r_n	Radius of n^{th} zone
R	Radius of diffractive optical element

Downloaded From: https://www.spiedigitallibrary.org/ebooks/ on 27 Feb 2022
Terms of Use: https://www.spiedigitallibrary.org/terms-of-use

t	Thickness/height of resist/substrate
T	Transmittance value
u	Object distance
v	Image distance
w_0	Waist of the Gaussian beam
z_T	Talbot distance
α	Base angle of prism
β	Deviation/diffraction angle
Δ	Sampling period
Δf	Focal depth
λ	Wavelength
Λ	Period of the grating
Λ_x	Period of the grating along x direction
Λ_y	Period of the grating along y direction
Φ	Phase
Φ_{1D}	Phase of 1D binary phase grating
Φ_{2D}	Phase of 2D binary phase grating
Φ_A	Phase aberration
$\Phi_{Axilens}$	Phase of axilens
Φ_{FZP}	Phase of Fresnel zone plate
Φ_G	Phase of grating
Φ_{in}	Phase of input wave
Φ_m	Phase of multifunctional diffractive optical element
Φ_{out}	Phase of output wave
Φ_R	Phase of reference wave
$\Phi_{Ring\ lens}$	Phase of ring lens
Φ_{SPP}	Phase of spiral phase plate
ψ	Complex amplitude of a wave
$\nabla\psi$	Gradient of a wavefront

Downloaded From: https://www.spiedigitallibrary.org/ebooks/ on 27 Feb 2022
Terms of Use: https://www.spiedigitallibrary.org/terms-of-use

Acronyms and Abbreviations

1D	One-dimensional
2D	Two-dimensional
3D	Three-dimensional
BPSE	Beam path steering element
CAD	Computer-aided design
CCD	Charge-coupled device
CGH	Computer-generated hologram
CIF	Caltech Intermediate Format
DFT	Discretized Fourier transform
DI	De-ionized
DOE	Diffractive optical element
DXF™	Drawing Exchange Format
EBL	Electron beam lithography
FBMS	Fixed-beam moving stage
FF	Fill factor
FFT	Fast Fourier transform
FIB	Focused ion beam
FT	Fourier transform
FZA	Fresnel zone axilens
FZP	Fresnel zone plate
GDS	Graphic Data System
HF	Hydrofluoric acid
HMDS	Hexamethyldisilizane
HOBB	Higher-order Bessel beam
HOE	Holographic optical element
ICP	Inductively coupled plasma
IFTA	Iterative Fourier transform algorithm
IPA	Isopropyl alcohol
ITO	Indium tin oxide
KOH	Potassium hydroxide
MEMS	Micro-electromechanical system
MIBK	Methyl isobutyl ketone
NDF	Neutral density filter

Downloaded From: https://www.spiedigitallibrary.org/ebooks/ on 27 Feb 2022
Terms of Use: https://www.spiedigitallibrary.org/terms-of-use

PMMA	Poly methyl methacrylate
RCWA	Rigorous coupled-wave analysis
ROE	Refractive optical element
SEM	Scanning electron microscope
SLM	Spatial light modulator
SMF	Single-mode fiber
SPP	Spiral phase plate
STL	STereoLithography
UV	Ultraviolet
X-OR	Exclusive OR

Downloaded From: https://www.spiedigitallibrary.org/ebooks/ on 27 Feb 2022
Terms of Use: https://www.spiedigitallibrary.org/terms-of-use

Chapter 1
Introduction

This chapter introduces the fundamentals of diffractive optics, the similarities and differences between diffractive and refractive optics, the advantages of diffractive optics, and current challenges in this field. A quick review of the theoretical formulation of diffraction is presented, along with different theoretical approximations and their validity regimes.

1.1 Fundamentals of Diffractive Optics

1.1.1 Introduction

Diffraction was first observed by Francesco Maria Grimaldi in the year 1665. It was Grimaldi who first coined the term diffraction.[1] The study of diffraction was continued by Sir Isaac Newton,[2] James Gregory,[3] Thomas Young, etc.[4] Later, Augustin-Jean Fresnel used Huygens' wave principle to explain the diffraction phenomenon. Much later, scientists such as Poincaré, Sommerfeld, Kirchhoff, and Kottler, to name a few, added to the knowledge of the field.[5] Sommerfeld himself defined diffraction by what it was not, stating that diffraction could be considered to be any bending of rays not caused by refraction or reflection. Optical elements, surfaces, or interfaces change the behavior of light, or, in other words, change the basic properties of light, such as its amplitude, phase, direction, and polarization. These changes are brought about through the optical processes of refraction, reflection, interference, and diffraction. However, the amount of control and the ease of fabricating an element that exploits one or more of these processes vary. This book is about how to design diffractive elements that will modify some or all of these properties to create a desired behavior. The elements can be either reflective or transmissive in nature.

Diffraction, or, more correctly, diffractive optics, are now commonly used in many experimental and commercial systems.[6] The reasons for this are several: our use of light has gone far beyond illumination and communication. These, as well as the many other applications, such as imaging and sensing,

Downloaded From: https://www.spiedigitallibrary.org/ebooks/ on 27 Feb 2022
Terms of Use: https://www.spiedigitallibrary.org/terms-of-use

require light to be manipulated in complicated ways, yet in compact systems. Diffractive optical elements (DOEs) are able to address both of these requirements simultaneously. With diffractive optics, as the name suggests, the main phenomenon used is diffraction rather than refraction. In this first chapter, we look at the transition between these effects. We examine the specific circumstances in which optics can be considered refractive or diffractive. This is important because the manner of describing them will be quite different. Most optical elements will exhibit a combination of refractive and diffractive properties. However, the dimensions of the element will determine the dominating phenomenon. By dimensions, we mean both the overall dimensions as well as the feature sizes. When feature sizes approach several wavelengths, an extended scalar theory is required, while for subwavelength features, a rigorous vector theory will be required to describe the element and its effect on light.[7]

In this book, we focus on elements that can be described by geometric optics and the scalar theory. No special software is required, and because feature sizes are relatively large, fabrication, too, is often simple. However, more importantly, scalar theory suffices in many situations and allows one to achieve fairly complex operations. The user will be introduced to different techniques that can be used to design and fabricate diffractive elements for specific applications. Special attention has been taken to present practical guidelines for fabrication. Since fabrication often requires the use of sophisticated, expensive equipment and consumables, it is prudent to carry out detailed simulations before actually fabricating. We also present well-commented programs in MATLAB® for direct use.

1.1.2 Refractive and diffractive optics

Diffraction is present in almost all phenomena involving light, although it may not always be dominant. Consider the case of focusing light with the aid of a refractive lens. Assuming the lens to be aberration-free, the smallest spot size obtained at the focal plane is called a diffraction-limited spot. This is because using conventional means it is impossible to focus light to a spot smaller than the diffraction-limited spot due to diffraction at the edges of the lens. With a refractive lens, image parameters are calculated based on geometric laws instead of diffractive principles as most of the incident light undergoes refraction, while only a small fraction of the input light undergoes diffraction. This is true with slits of dimensions much larger than the incident wavelength, as well. When the slit opening is large, it is a refraction-dominated system, and when it is smaller (with respect to the wavelength), it is a diffraction-dominated system, as shown in Fig. 1.1.

Diffraction can be qualitatively explained using Huygens' wave principle. Let us consider a plane wave. By Huygens' principle, every point on a wavefront acts as a source of secondary wavelets generating another plane

Downloaded From: https://www.spiedigitallibrary.org/ebooks/ on 27 Feb 2022
Terms of Use: https://www.spiedigitallibrary.org/terms-of-use

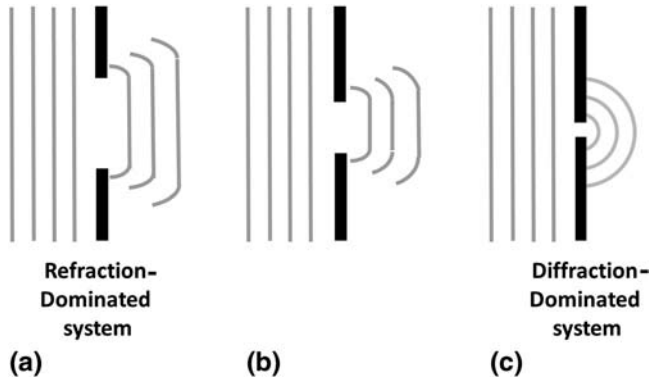

Figure 1.1 Diffraction of light in slits with different widths: (a)–(c) decreasing slit widths show increasing domination of diffraction.

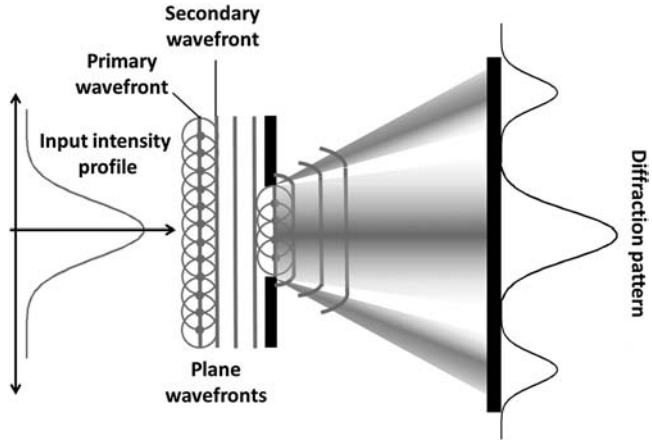

Figure 1.2 Diffraction of a plane wavefront with a Gaussian intensity profile at a single-slit aperture.

wavefront. However, when part of the wavefront is blocked by a slit, the wavefront bends at the edges, as shown in Fig. 1.2.

In refraction, light can be thought of as traveling in straight lines in a medium of constant refractive index. Snell's law applies at interfaces (surfaces where the refractive index changes) and can be used to determine the new direction. Refractive elements, in general, consist of a single bulk unit, whose shape and refractive index determine its imaging properties. Diffractive elements, unlike their refractive counterparts, are made of many different zones. The final image is a coherent superposition of light diffracted from the various zones. Every point on the aperture contributes to the intensity at one location of the output. Of course, refraction will also take place. The resulting behavior will, therefore, be a combination of both effects. For example, the 0^{th} diffraction order of a reflection grating is nothing but the light that obeys

Downloaded From: https://www.spiedigitallibrary.org/ebooks/ on 27 Feb 2022
Terms of Use: https://www.spiedigitallibrary.org/terms-of-use

geometric optics laws. It should be clear that although diffraction is an interference effect, these two effects are distinguished from each other by the number of interacting beams. Most interferometers, for example, will create two beams that interfere later in the optical path. In diffraction, an infinite number of beams play a role.

The well-known Fresnel lens was invented by Augustin-Jean Fresnel in 1822 to replace the heavy, conventional spherical lenses used in lighthouses.[7] Fresnel converted the bulk conventional spherical lens shown in Fig. 1.3(a) into a thin Fresnel lens by arranging different sections of the conventional lens in a plane, as shown in Fig. 1.3(b). The curvature of the material at the glass–air interface and the refractive index of the glass material govern the light-bending profile; hence, the inactive glass material present in the conventional lens can be removed without altering the function of the device. In this example, the Fresnel lens has been made by sectioning the original lens into three horizontal parts. It behaves almost like the conventional lens except for extra diffraction effects occurring at the boundaries between its different sections. What is important is that the Fresnel lens is still a refractive optical element with dimensions of t and d much greater than λ, the wavelength of the incident light. However, if the same element were to be designed with feature sizes closer to the wavelength of light, then the resulting element would be predominantly diffractive.[8] In the latter case, even though the function of the lens remains the same, wavefront control is achieved by diffraction rather than refraction.

From the above discussion, it seems that it is relatively easy to design a diffractive element from the shape information of an equivalent refractive optical element (ROE), assuming that such an element exists. Let us study this concept in some more detail.

In refractive optics, the bending of light occurs due to the geometry of the structure and the index of refraction, while in diffractive optics, bending of light occurs due to the features and the aperture edges. Given a particular intensity distribution across an aperture, it is possible to design the features

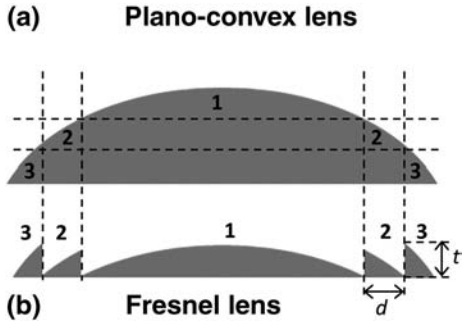

Figure 1.3 Scheme showing the generation of a Fresnel lens from a conventional plano-convex lens: (a) conventional lens and (b) Fresnel lens. If t and $d \gg \lambda$, the lens is refractive. If t and d are on the order of, or less than, the wavelength, the element is diffractive.

Downloaded From: https://www.spiedigitallibrary.org/ebooks/ on 27 Feb 2022
Terms of Use: https://www.spiedigitallibrary.org/terms-of-use

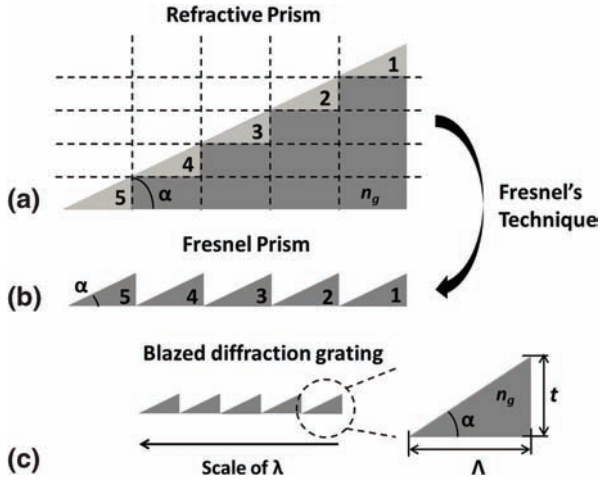

Figure 1.4 (a) Refractive prism and (b) generation of a Fresnel prism from it. (c) Blazed diffraction grating with dimensions on the order of the wavelength.

that will fill the aperture to obtain a desired intensity distribution at an output plane. The first DOEs were modified versions of refractive elements with feature sizes on the order of the incident wavelength. To understand the above statement, let us consider the conversion of a prism into a diffraction grating. In the refractive regime, a prism can be used to disperse light or change the direction of an incident monochromatic light. A similar element in the diffractive regime is a grating.

The construction of a diffraction grating from a prism is shown in Fig. 1.4. The base angle of the prism and its refractive index are given by α and n_g, respectively. The refractive bulk prism is converted into a thin element using Fresnel's technique, as shown in Figs. 1.4(a) and (b). Figure 1.4(c) shows a diffraction grating, which is similar to Fig. 1.4(b), except that the feature sizes are closer to the wavelength of light with a period Λ and thickness t. A Fresnel prism is a refraction-dominated system, while a diffraction grating is a diffraction-dominated one. A major difference arising because of this is the fact that the former will bend the incident beam into one direction, while the latter will generate multiple orders. The shape of the diffraction grating will determine the number of orders and will be discussed in more detail in later chapters. In order to force most of the diffracted light into a single diffraction order, the diffraction grating must be blazed (i.e., have a triangular shape) with a height or thickness t given by

$$t = \frac{\lambda}{(n_g - 1)}, \tag{1.1}$$

which corresponds to a phase difference of 2π.[9] Hence, the relationship between α of the prism and Λ of the grating for normal incidence of light is given by

Downloaded From: https://www.spiedigitallibrary.org/ebooks/ on 27 Feb 2022
Terms of Use: https://www.spiedigitallibrary.org/terms-of-use

$$\alpha = \tan^{-1}\left[\frac{\lambda}{\Lambda(n_g - 1)}\right]. \tag{1.2}$$

Equation (1.2) shows that the geometrical profile of the prism is related to the period of the diffraction grating.

The deviation angle β of the prism with a base angle of α and refractive index n_g can be calculated using trigonometry as

$$\beta = \sin^{-1}(n_g \sin\alpha) - \alpha. \tag{1.3}$$

In order to become familiar with the terms and the language of diffractive optics, we briefly introduce the amplitude grating here. Many of the concepts will directly hold true for a phase grating as well. The second chapter provides a much more detailed look at gratings and methods by which to design and simulate their behavior.

Imagine a structure comprising a number of reflective slits surrounded by opaque regions, as shown in Fig. 1.5. The slits are periodically spaced with a distance Λ. This structure defines a basic diffraction grating. Light is incident at an angle of β_i with respect to the grating normal, which is indicated as vertical dashed lines in the figure. The question is what determines the angle(s) β_r of the beam after incidence on this surface? Since we have chosen reflective slits, the light will travel back into the region of incidence, but we will not call this reflection as the resulting intensity is due to the superposition of many beams. For a more detailed description, we refer readers to a number of books that discuss Huygens' principle (every point in the slit acts a secondary source) and scalar diffraction.[1–5] Suffice to say that the multitudes of beams from each slit interact with each other and result in an intensity pattern in the far field. This pattern is not uniform, and the goal is to determine the locations of the intensity peaks.

To arrive at the pattern, we look at two rays AB and $A'B'$ that both originated from the wavefront AA'. In other words, at the plane AA', both rays started with the same phase. For the diffracted wave shown in the figure, to represent an actual wave, BB' should be a wavefront. That is, the path

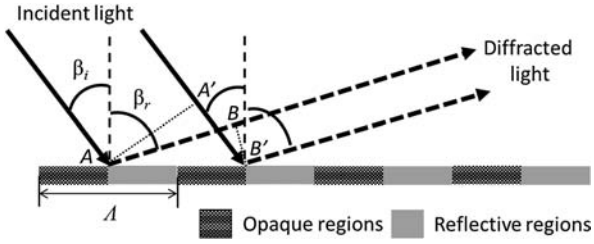

Figure 1.5 Schematic of light diffraction in a reflective amplitude grating.

Downloaded From: https://www.spiedigitallibrary.org/ebooks/ on 27 Feb 2022
Terms of Use: https://www.spiedigitallibrary.org/terms-of-use

length difference between AB and $A'B'$ must be equal to a multiple of the wavelength λ, as described in

$$n_1 A'B' - n_2 AB = m\lambda_0, \tag{1.4}$$

where, n_1 and n_2 are the refractive indices seen by the incident and reflected rays, respectively. Since both are in the same medium, $n_1 = n_2$. With this information, and comparing the triangles $AA'B'$ and $BB'A$, the equation can be rewritten as

$$\Lambda(\sin\beta_i - \sin\beta_r) = m\lambda_0, \tag{1.5}$$

where, $\lambda = \lambda_0/n_1$, and m is the order number. The implication of the order parameter m is that Eq. (1.5) is satisfied for different values of β_r. Therefore, the equation could be more accurately be written as

$$\Lambda(\sin\beta_i - \sin\beta_{mr}) = m\lambda, \tag{1.6}$$

where, β_{mr} represents the m^{th} diffraction order. Thus, a picture of what is happening after diffraction from the grating slowly emerges. Unlike specular reflection, where the reflected light travels in one direction only, or scattered light disperses into a solid angle from a surface, several 'diffraction' orders exist. One could think of this as reflection occurring in a finite number of preferred directions. If the grating had been a transmissive one, then refraction would occur in more than one direction. The condition $m = 0$ represents the classical optics case. For example, in the above grating, the condition $m = 0$ results in $\beta_i = \beta_r$, which is the law of reflection. For a transmission grating, $m = 0$ would reduce the equation to Snell's law. While the equation allows us to predict the possible directions of travel, it gives us no information about how much light travels in each order. This means that we cannot predict the efficiency of the diffractive structure. Obviously, efficiency is important, and later chapters will include further equations that can be used during the design stage to maximize it. The convention used to name the various orders of a grating is indicated in Fig. 1.6. The figure can be used for either a transmission or reflection grating. Angles are always measured from the grating normal. The sign of the angle depends on the direction of rotation of the ray from the normal (indicated by $\pm$ signs in the figure). On the other hand, the sign of the order parameter m depends on the direction from the 0^{th} order. For example, for the reflected $m = +1$ order in the figure, angle β_1 is positive but would have been negative if the ray happened to lie on the other side of the normal.

For simplicity, normal incidence is considered, and for the 1^{st} diffraction order, Eq. (1.6) can be simplified. The diffraction angle β_1 of the 1^{st} diffraction order of the diffraction grating with a period of Λ is given by

Downloaded From: https://www.spiedigitallibrary.org/ebooks/ on 27 Feb 2022
Terms of Use: https://www.spiedigitallibrary.org/terms-of-use

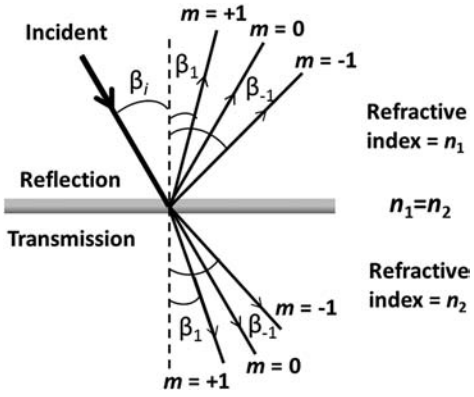

Figure 1.6 Orders of a grating.

$$\beta_1 = \sin^{-1}\left(\frac{\lambda}{\Lambda}\right). \tag{1.7}$$

By substituting Eqs. (1.1) and (1.2) in (1.7), β_1 can be expressed as

$$\beta_1 = \sin^{-1}[(n_g - 1)\tan\alpha]. \tag{1.8}$$

From Eqs. (1.3) and (1.8), for cases where the base angle of prism α and the refractive index n_g are small, or where the period of the diffraction grating Λ is large, Eqs. (1.3) and (1.8) reduce to a simpler equation:

$$\beta_1 = \beta = (n_g - 1)\alpha. \tag{1.9}$$

This is an interesting result. When the period of the diffraction grating is large, it behaves more like a refractive element; however, its behavior is different when Λ approaches λ. To quantitatively understand this, a few typical cases are considered with $n_g = 1.1$, 1.5, and 1.9. The deviation angles β of a prism and diffraction angles β_1 of a grating were calculated using Eqs. (1.3) and (1.4), respectively, and plotted against base angles α of a prism, as shown in Fig. 1.7.

For smaller values of α, there is good overlap between β and β_1. Therefore, for DOEs with small diffraction angles, it is possible to derive the profile blueprint from a ROE with an equivalent function. Examples of some other elements that can be achieved in a similar way are the axicon,[9] circular grating,[10] ring lens,[11] and diffractive ring lens.[12] We must however, always keep in mind that in any optical element, both refraction and diffraction coexist. The dominating effect, dictated by the feature sizes, decides whether the element is diffractive or refractive.

Several researchers have studied the transition between refractive and diffractive elements quite extensively.[13,14] As discussed, this can be done by

Downloaded From: https://www.spiedigitallibrary.org/ebooks/ on 27 Feb 2022
Terms of Use: https://www.spiedigitallibrary.org/terms-of-use

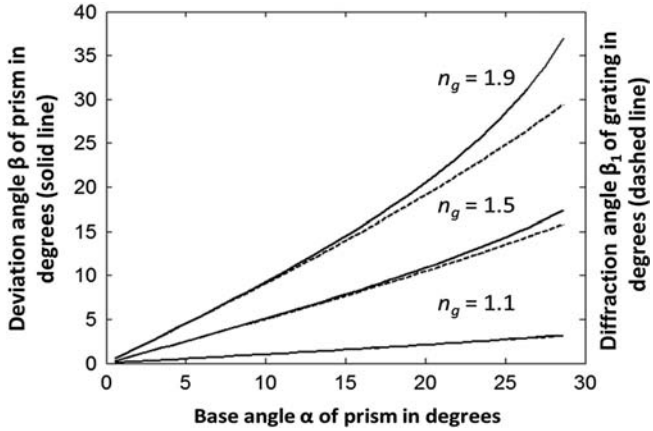

Figure 1.7 Plot of deviation angle β of a prism (solid line) and diffraction angle β_1 of a grating (dashed line) versus variations in the base angle α of the prism for $n_g = 1.1$, 1.5, and 1.9.

changing the feature sizes of an element and studying its behavior as the size changes. In particular, the dispersive nature will vary depending on the feature size. Again, let us take the examples of a lens and a prism. In the latter case, we will compare a 1D (diffractive) grating and a (refractive) prism, as both result in an off-axis deflection of the incident beam.[14] In both cases, the refractive index and, hence, the wavelength plays a role in the amount of deflection. It is shown in Ref. 14 that the nature of dispersion is quite different for the refractive and diffractive cases, with the latter experiencing much greater dispersion for the same angle of deflection. Even more interesting is the negative sign of the grating dispersion compared to that of the prism. In other words, when light bends, different wavelengths bend by different amounts, and the direction of bending is determined by the base optical behavior of the element. The opposite signs of the dispersion of refraction and diffraction have been used from very early on to provide some amount of achromatization.[15] Recent publications show that this concept is still being manipulated for achromatization.[16,17] In the refractive case, dispersion caused by the material dominates, whereas, the structure of the element controls the diffractive dispersion. Given these two very different causes, diffraction and refraction cannot be balanced in a single element. Researchers are now studying harmonic DOEs that lie somewhere between these two distinct effects.[18] In conclusion, it is clear that the structure of a DOE can be deduced from the structure of a ROE that performs a similar optical operation.

1.1.3 Scalar diffraction formulation

Diffraction is a phenomenon that is observable due to the wave nature of light. The effects of diffraction are more noticeable when light interacts with an

Downloaded From: https://www.spiedigitallibrary.org/ebooks/ on 27 Feb 2022
Terms of Use: https://www.spiedigitallibrary.org/terms-of-use

interface or an optical element whose dimensions are close to that of the incident wavelength. Diffraction theory allows one to calculate how wavefronts change and how they travel after interaction with such an element. A complete analysis of a diffractive system can be carried out using the vector diffraction equations.[19,20] Vector diffraction formulation can be used to understand the behavior of DOEs with features both superwavelength as well as subwavelength. This formulation can determine not only the intensity and phase profiles at different planes, but also the state of polarization at these planes. However, the formulation is quite difficult to implement and also to simulate. For most of the analysis, which does not involve DOEs with features smaller than or equal to the wavelength of light, and does not need to explain the polarization state of the diffracted field, the simpler scalar diffraction formulation is sufficient. The focus of this text book is only on superwavelength DOEs; therefore, the discussion is limited only to the scalar diffraction formulation. Few models have been developed that can explain the polarization state of a diffracted field using only scalar diffraction formulation.[21] The scalar diffraction formulation is described in numerous text books.[4,5] With the assumption that the features of the DOE are larger than the wavelength of the source, and for spherical wavefronts, the scalar diffraction formula based on Huygens–Fresnel theory is given by

$$E(u,v) = \frac{z}{\lambda j}\iint_{\sum} A(x,y)\frac{\exp(jkr)}{r^2}\,dxdy, \tag{1.10}$$

where (x, y) is the diffraction plane, and (u, v) is the observation plane. The radius r can be given by

$$r = \sqrt{z^2 + (u-x)^2 + (v-y)^2}. \tag{1.11}$$

For smaller angles, spherical wavefronts can be approximated as parabolic wavefronts, which results in the Fresnel approximation formula. Now the radius can be approximated as

$$r \approx z\left[1 + \frac{1}{2}\left(\frac{u-x}{z}\right)^2 + \frac{1}{2}\left(\frac{v-y}{z}\right)^2\right]. \tag{1.12}$$

The Fresnel diffraction formula is given by

$$\begin{aligned} E(u,v) = \frac{e^{jkz}e^{j\frac{k}{2z}(x^2+y^2)}}{j\lambda z}\int_{-\infty}^{+\infty}\int_{-\infty}^{+\infty}\left\{A(x,y)\exp\left[j\frac{k}{2z}(x^2+y^2)\right]\right\} \\ \times \exp\left[-j\frac{2\pi}{\lambda z}(xu+yv)\right]dxdy. \end{aligned} \tag{1.13}$$

It can be seen that the Fresnel diffraction formula is relatively simpler to solve (as is simulating the diffraction field) compared to the prior

Downloaded From: https://www.spiedigitallibrary.org/ebooks/ on 27 Feb 2022
Terms of Use: https://www.spiedigitallibrary.org/terms-of-use

Huygens–Fresnel approximation. However, this approximation will fail in the region closer to the diffraction plane and for large diffraction angles. Equation (1.13) is valid only when

$$z^3 \gg \frac{\pi}{4\lambda}\left[(x-u)^2+(y-v)^2\right]^2_{\max}. \tag{1.14}$$

Equation (1.13) for large values of z reduces to just a Fourier transform operation, which is called the far-field approximation. This approximation, also known as the Fraunhofer approximation, is valid only for very large distances given by

$$z \gg \frac{k(u^2+v^2)}{2}. \tag{1.15}$$

At these distances, the radius of the spherical wavefront is large, so a section of the spherical wavefront can be approximated to be a plane wavefront. A summary of the approximations of the scalar diffraction formulation is shown in Fig. 1.8. In this book, only the Fresnel and Fraunhofer approximations are used for analysis of DOEs. The scalar diffraction integrals can be thought of as

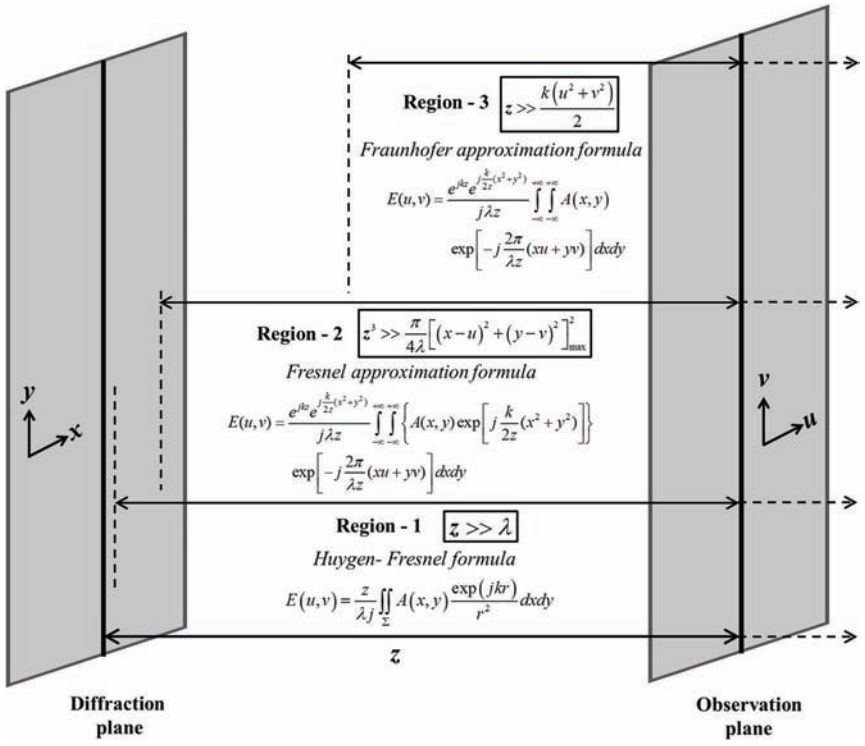

Figure 1.8 Depiction of the validity of different approximations of the scalar diffraction formula.

Downloaded From: https://www.spiedigitallibrary.org/ebooks/ on 27 Feb 2022
Terms of Use: https://www.spiedigitallibrary.org/terms-of-use

scalar diffraction propagators. In other words, they are a means to find the diffraction amplitude and phase at any plane, given these values at an earlier plane. These integral equations are used in their analog continuous form only when analytic solutions for the diffraction problem being studied exist. For all other cases, different techniques can be used to solve them to determine the diffraction field at some plane. While the similarity to a Fourier transform (FT) is clear when studying Fraunhofer diffraction, even diffraction at closer planes can use the FT concept, as is obvious from Eq. (1.13). (Further details are provided in Chapter 4.) Therefore, one common method to solve scalar diffraction integral equations uses discretized Fourier transforms (DFTs). One particularly efficient and fast algorithm that implements a DFT is known as the fast Fourier transform (FFT). This algorithm carries out the FT operation for N discrete samples in $O(N \log N)$ steps, rather than the $O(N^2)$ steps of a standard FT operation. Algorithms that carry out a DFT with $O(N^2)$ steps can also be used. These algorithms have other benefits; for example: the size of the matrices (arrays) used does not need to be powers of 2; there is more freedom in choosing matrix sizes (hence, more freedom in fixing resolution at the diffraction plane); they can tackle problems that cannot be handled by the FFT algorithm, etc. While these benefits may seem attractive, they come at the price of longer computation times. In addition to techniques that use the FT as a basis for a diffraction solution, other beam propagation techniques such as wavelets,[22] finite element methods,[23] etc.,[24–26] can be used.

1.2 Software for Designing Diffractive Optics

In the preface, the importance of diffractive optics was discussed. Given its many uses, clearly, the ability to design and simulate DOEs is critical. Most researchers use their own programming scripts to do this. And, of course, the goal of this book is to help such a researcher. For the sake of completeness, however, we mention other resources[57–59] that are available.

The company Wyrowski Photonics UG[27] markets a software package called VirtualLab Fusion.[28] Its diffractive optics toolbox can be used for the generation of micro- and diffractive optical elements. With this software, a variety of DOEs such as beam shapers, splitters, and diffusers can be designed. It also has a grating toolbox with which rigorous analysis of grating can be carried out. VirtualLab Fusion can then be used to analyze imaging in systems containing gratings and diffractive or hybrid lenses.

GSolver,[29] on the other hand, is a software that allows rigorous analysis of all types of diffractive gratings. It provides a vector solution for complex periodic grating structures.

DiffractMOD™[30] is used to model a wide range of devices including diffractive optics, such as diffractive optical elements, subwavelength periodic

Downloaded From: https://www.spiedigitallibrary.org/ebooks/ on 27 Feb 2022
Terms of Use: https://www.spiedigitallibrary.org/terms-of-use

structures, and photonic bandgap crystals. It is based on rigorous coupled-wave analysis (RCWA) and can handle both metallic and dielectric materials, allowing for the inclusion of plasmonic effects as well.

Even software like OSLO[31] and Zemax[32] that typically are used for modeling and designing refractive optics allow some amount of diffractive modeling. They do so without using any of the diffraction equations and, therefore, can most easily deal with relatively simple periodic diffractive elements. Diffraction is included, taking into account the fact that a diffractive surface introduces additional ray bending over what a refractive element would achieve.

While a variety of software tools exist, the authors believe that much of the required modeling can be done by the users themselves, with software such as MATLAB, Scilab, Python, or C. This is especially true for scalar diffractive optics. The advantage, apart from cost, is that design and simulation programs can be tuned exactly to the users' requirements.

1.3 Concluding Remarks

A brief history of diffraction and the similarities and differences between DOEs and ROEs are presented in the previous sections with a glimpse of the fundamental scalar diffraction formula. In this concluding section, the scope of research and development in diffractive optics is summarized followed by the contents of the following chapters.

DOEs in general are smaller and thinner compared to their refractive equivalents.[33] Additionally, DOEs can be engineered to nanometer accuracy due to the remarkable growth in the field of micro/nanolithography and fabrication techniques.[34] DOEs can be fabricated with feature sizes from few hundreds of nanometers to few millimeters. Extremely fine features smaller than the diffraction limit of light can be achieved using extreme ultraviolet lithography,[35] electron beam lithography,[36,37] and focused ion beam lithography.[38,39] The transfer of smaller features to glass and hard substrates can be carried out using sophisticated etching processes;[40,41] therefore, elements that can withstand higher optical powers can be fabricated. DOEs can also be designed and implemented for other parts of the electromagnetic spectrum, such as x rays, etc.[42,43] Hence, DOEs can replace refractive optics in various applications.[44]

In many optical setups with refractive optical elements,[45] some elements are paired without any relative motion between them. In such cases, it is often convenient to replace these elements with one DOE with equivalent functionality (of the replaced elements).[46] Multiple functions such as beam re-orientation, focusing, and splitting have been reported.[47,48] Hence, it is possible to convert bulky optical systems into lightweight, compact systems with high-quality beam profiles in less space. In the case of DOEs, the

Downloaded From: https://www.spiedigitallibrary.org/ebooks/ on 27 Feb 2022
Terms of Use: https://www.spiedigitallibrary.org/terms-of-use

resolution of the element can be less than 10 nm, which is at least three orders of magnitude higher than that of conventional spatial light modulators; in addition, DOEs are lighter. Clearly, one can obtain a resolution better than that of refractive elements while maintaining a compact optics configuration. Besides the above advantages, some beam profiles, such as vortex beams, chiral beams, etc.,[49–52] cannot be generated using ROEs. Therefore, it is possible to revolutionize the field of optical instrumentation by replacing ROEs with equivalent lightweight DOEs and DOE- based optical instruments. Recent research reports the fabrication of DOEs on the tip of optical fiber, where the patterned fiber can be attached directly to a fiber laser to achieve high-power beam shaping.[53] These results could be useful for a wide variety of biomedical applications such as laser-based surgery,[54] endoscopy,[55] laparoscopy,[56] etc.

References

1. A. Authier, *Early Days of X-Ray Crystallography*," Oxford University Press, Oxford (2013).
2. J. Z. Buchwald and I. B. Cohen, Eds., *Isaac Newton's Natural Philosophy*, MIT Press, Cambridge, Massachusetts (2001).
3. S. Singh, *Fundamentals of Optical Engineering*, Discovery Publishing House Pvt. Ltd, New Delhi (2009).
4. E. Hecht, *Optics*, Fourth Edition, Addison Wesley, San Francisco (2002).
5. J. W. Goodman, *Introduction to Fourier Optics*, Second Edition, McGraw-Hill Companies Inc., New York (1996).
6. H. P. Herzig, *Micro-optics: Elements, Systems and Applications*, Taylor and Francis Ltd., London (1997).
7. Y. G. Soskind, *Field Guide to Diffractive Optics*," SPIE Press, Bellingham, Washington (2011) [doi: 10.1117/3.895041].
8. K. Miyamoto, "The phase Fresnel lens," *J. Opt. Soc. Am.* **51**, 17–20 (1961).
9. J. H. McLeod, "The axicon: a new type of optical element," *J. Opt. Soc. Am.* **44**, 592–592 (1954).
10. J. Dyson, "Circular and spiral diffraction gratings," *Proc. R. Soc. London Ser. A* **248**, 93–106 (1958).
11. J. B. Goodell, "Eccentric lenses for producing ring images," *Appl. Opt.* **8**, 2566–2566 (1969).
12. M. R. Descour, D. I. Simon, and W.-H. Yei, "Ring-toric lens for focus-error sensing in optical data storage," *Appl. Opt.* **38**, 1388–1392 (1999).
13. I. Snigireva, A. Snigirev, C. Rau, T. Weitkamp, V. Aristov, M. Grigoriev, S. Kuznetsov, L. Shabelnikov, V. Yunkin, M. Hoffmann, and E. Voges, "Holographic x-ray optical elements: Transition between refraction and diffraction," *Nucl. Instrum. Methods Phys. Res. Sect. A* **467-468**, 982–985 (2001).

Downloaded From: https://www.spiedigitallibrary.org/ebooks/ on 27 Feb 2022
Terms of Use: https://www.spiedigitallibrary.org/terms-of-use

14. S. Sinzinger and M. Testorf, "Transition between diffractive and refractive micro-optical components," *Appl. Opt.* **34**, 5970–5976 (1995).
15. T. Stone and N. George, "Hybrid diffractive-refractive lenses and achromats," *Appl. Opt.* **27**, 2960–2971 (1988).
16. Y. Yoon, "Design and tolerancing of achromatic and anastigmatic diffractive–refractive lens systems compared with equivalent conventional lens systems," *Appl. Opt.* **39**, 2551–2558 (2000).
17. P. Valley, N. Savidis, J. Schwiegerling, M. R. Dodge, G. Peyman, and N. Peyghambarian, "Adjustable hybrid diffractive/refractive achromatic lens," *Opt. Express* **19**, 7468–7479 (2011).
18. D. W. Sweeney and G. E. Sommargren, "Harmonic diffractive lenses," *Appl. Opt.* **34**, 2469–2475 (1995).
19. A. S. Marathay and J. F. McCalmont, "Vector diffraction theory for electromagnetic waves," *J. Opt. Soc. Am. A* **18**, 2585–2593 (2001).
20. A. Wang and A. Prata, "Lenslet analysis by rigorous vector diffraction theory," *J. Opt. Soc. Am. A* **12**, 1161–1169 (1995).
21. M. Mansuripur, "Distribution of light at and near the focus of high-numerical-aperture objectives," *J. Opt. Soc. Am. A* **3**, 2086–2093 (1986).
22. F. T. S. Yu, S. Jutamulia, and S. Yin, Eds., *Introduction to Information Optics*, Academic Press, San Diego (2001).
23. D. W. Prather and S. Shi, "Formulation and application of the finite-difference time-domain method for the analysis of axially symmetric diffractive optical elements," *J. Opt. Soc. Am. A* **16**, 1131–1142 (1999).
24. G. N. Nguyen, "Modeling, Design and Fabrication of Diffractive Optical Elements Based on Nanostructures Operating Beyond the Scalar Paraxial Domain," Doctoral Dissertation, Télécom Bretagne; Université de Bretagne Occidentale, France (2014).
25. Q. Cao and J. Jahns, "Comprehensive focusing analysis of various Fresnel zone plates," *J. Opt. Soc. Am. A* **21**, 561–571 (2004).
26. V. A. Soifer, *Diffractive Nanophotonics*, CRC Press, Boca Raton, Florida (2014).
27. J. Turunen and F. Wyrowski, *Diffractive Optics for Industrial and Commercial Applications*, John Wiley & Sons, Hoboken, New Jersey (1997).
28. http://www.wyrowski-photonics.com/virtuallab/toolboxes.html
29. http://www.gsolver.com/
30. https://optics.synopsys.com/rsoft/rsoft-passive-device-diffractMOD.html
31. http://www.lambdares.com/oslo
32. https://www.zemax.com/os/resources/learn/knowledgebase/how-to-design-diffractive-optics-using-the-binary
33. B. C. Kress and P. Meyrueis, *Applied Digital Optics*, John Wiley & Sons, Chichester, UK (2009).

Downloaded From: https://www.spiedigitallibrary.org/ebooks/ on 27 Feb 2022
Terms of Use: https://www.spiedigitallibrary.org/terms-of-use

34. M. T. Gale, "Replication techniques for diffractive optical elements," *Microelectron. Eng.* **34**, 321–339 (1997).
35. B. Wu and A. Kumar, "Extreme ultraviolet lithography: A review, *J. Vac. Sci. Technol. B* **25**, 1743–1761 (2007).
36. A. N. Broers, A. C. F. Hoole, and I. M. Ryan, "Electron beam lithography: Resolution limits," *Microelectron. Eng.* **32**, 131–142 (1996).
37. V. R. Manfrinato, L. Zhang, D. Su, H. Duan, R. G. Hobbs, E. A. Stach, and K. K. Berggren, "Resolution limits of electron-beam lithography toward the atomic scale, *Nano Lett.* **13**, 1555–1558 (2013).
38. J. Melngailis, "Focused ion beam technology and applications, *J. Vac. Sci. Technol. B* **5**, 469–495 (1987).
39. F. Watt, A. A. Bettiol, J. A. V. Kan, E. J. Teo, and M. B. H. Breese, "Ion beam lithography and nanofabrication: A Review," *Int. J. Nanosci.* **4**, 269–286 (2005).
40. S. Ronggui and G. C. Righini, "Characterization of reactive ion etching of glass and its applications in integrated optics," *J. Vac. Sci. Technol. A* **9**, 2709–2712 (1991).
41. L. Li, T. Abe, and M. Esashi, "Smooth surface glass etching by deep reactive ion etching with SF6 and Xe gases," *J. Vac. Sci. Technol. B* **21**, 2545–2549 (2003).
42. W. Chao, J. Kim, S. Rekawa, P. Fischer, and E. H. Anderson, "Demonstration of 12 nm resolution Fresnel zone plate lens based soft x-ray microscopy," *Opt. Express* **17**, 17669–17677 (2009).
43. A. Takeuchi, K. Uesugi, H. Takano, and Y. Suzuki, "Submicrometer-resolution three-dimensional imaging with hard x-ray imaging micro-tomography," *Rev. Sci. Instrum.* **73**, 4246–4249 (2002).
44. S. Sinzinger and M. Testorf, "Transition between diffractive and refractive micro-optical components," *Appl. Opt.* **34**, 5970–5976 (1995).
45. P. A. Belanger and M. Rioux, "Ring pattern of a ring-axicon doublet illuminated by a Gaussian beam," *Appl. Opt.* **37**, 7049–7054 (1978).
46. A. Vijayakumar, "Design, Fabrication, and Evaluation of Diffractive Optical Elements for the Generation of Focused Ring Patterns," Doctoral Thesis, Indian Institute of Technology Madras, Chennai, India (2015) [doi: 10.13140/RG.2.2.25996.51847].
47. Y. Backlund, J. Bengtsson, and A. Larsson, "Waveguide hologram for outcoupling and simultaneous focusing into multiple arbitrary positions," *IEEE Photonics Technol. Lett.* **10**, 1286–1288 (1998).
48. Y. Backlund, J. Bengtsson, C.-F. Carlstrom, and A. Larsson, "Multi-functional grating couplers for bidirectional incoupling into planar waveguides," *IEEE Photonics Technol.* **12**, 314–316 (2000).
49. G. Indebetouw, "Optical vortices and their propagation," *J. Mod. Opt.* **40**, 73–87 (1993).

Downloaded From: https://www.spiedigitallibrary.org/ebooks/ on 27 Feb 2022
Terms of Use: https://www.spiedigitallibrary.org/terms-of-use

50. I. V. Basistiy, M. S. Soskin, and M. V. Vasnetsov, "Optical wavefront dislocations and their properties," *Opt. Commun.* **119**, 604–612 (1995).
51. M. S. Soskin and M. V. Vasnetsov, "Singular optics," *Prog. Opt.* **42**, 219–276 (2001).
52. M. R. Dennis, R. P. King, B. Jack, K. O. Holleran, and M. J. Padgett, "Isolated optical vortex knots," *Nat. Phys.* **6**, 118–121 (2010).
53. V. Pramitha, S. Bhattacharya, U. Eigenthaler, K. Keskinbora, C. T. Samlan, M. Hirscher, J. P. Spatz, and N. K. Viswanathan, "Direct patterning of vortex generators on a fiber tip using a focused ion beam," *Opt. Lett*. **41**, 2133–2136 (2016).
54. J. R. Leger, D. Chen, and Z. Wang, "Diffractive optical element for mode shaping of a Nd:YAG laser," *Opt. Lett.* **19**, 108–110 (1994).
55. B. A. Flusberg, E. D. Cocker, W. Piyawattanametha, J. C. Jung, E. L. M. Cheung, and M. J. Schnitzer, "Fiber-optic fluorescence imaging," *Nature Methods* **2**, 941–950 (2005).
56. Y. Qin, H. Hua, and M. Nguyen, "Multiresolution foveated laparoscope with high resolvability," *Opt. Lett.* **38**, 2191–2193 (2013).
57. S. Sinzinger and J. Jahns, *Microoptics*, Second Edition, Wiley-VCH, Weinheim (2003).
58. J. Jahns and S. Helfert, *Introduction to Micro- and Nanooptics*, Wiley-VCH, Weinheim (2012).
59. H. Zappe, *Fundamentals of Micro-Optics*, Cambridge University Press, Cambridge (2010).

Downloaded From: https://www.spiedigitallibrary.org/ebooks/ on 27 Feb 2022
Terms of Use: https://www.spiedigitallibrary.org/terms-of-use

Chapter 2
Design of Diffractive Optical Elements

Diffractive optical elements tailor optical fields via diffraction.[1] The diffraction patterns of standard apertures such as single slit, double slit, circular aperture, and square slit are well known.[2] However, for applications, apertures with higher levels of complexity may be required. A DOE can be thought of as a special aperture and can be engineered to obtain a desired intensity and phase profile at the plane of interest. Therefore, it is necessary to be familiar with such aperture functions and their respective diffracted fields, and to reconstruct the aperture function from the intensity and phase profile required at the plane of interest. DOEs can be of different versions,[3] such as amplitude-only and phase-only, as well as hybrid types[4] containing both amplitude and phase components in the same DOE. Phase DOEs possess higher efficiency than their amplitude counterparts. Hence, for most applications, phase-only DOEs are preferred, while in a few cases hybrid DOEs with both phase and amplitude profiles are used. This chapter presents step-by-step procedures for designing amplitude-only, phase-only, and hybrid DOEs with MATLAB® codes.

2.1 Design of Simple Diffractive Optical Elements

This section presents the design of three basic diffractive optical elements, namely, a grating, a Fresnel zone plate (FZP), and an axicon.

2.1.1 Design and analysis of 1D gratings

The fundamental theory of gratings is presented in numerous research papers and text books.[2,3,5–9] A 1D binary phase grating has phase variations in only one direction, as shown in Fig. 2.1. Three design parameters are used in the design of a binary phase grating: the period of the grating Λ; the phase difference Φ between the ridge (of width d) and the groove regions of the grating; and the fill factor (FF) d/Λ. The phase difference itself is controlled by

Downloaded From: https://www.spiedigitallibrary.org/ebooks/ on 27 Feb 2022
Terms of Use: https://www.spiedigitallibrary.org/terms-of-use

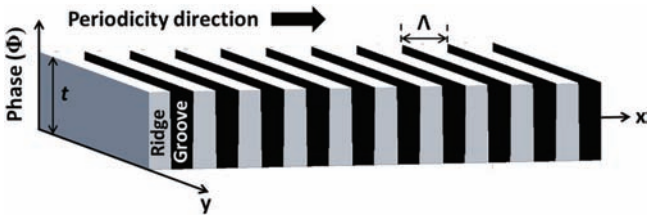

Figure 2.1 Phase profile of a 1D binary diffraction grating with period Λ and FF = 0.5.

two parameters: the physical height or thickness t of the ridge and the refractive index of the material of which the grating is made. In general, the material is either glass or resist, which means that the refractive index is fixed, and the design parameter used is only the thickness. To start, we look only at gratings with a FF of 0.5, as this value provides the maximum efficiency. (It is left to the readers to prove this using the MATLAB codes given in this chapter.) The phase profile of the 1D binary phase grating with a FF of 0.5 is given by

$$\Phi_{1D}(x) = \begin{cases} \Phi & 0 \le x \le \frac{\Lambda}{2} \\ 0 & \frac{\Lambda}{2} \le x \le \Lambda \end{cases} \qquad \Phi_{1D}(x) = \Phi_{1D}(x + \Lambda). \tag{2.1}$$

The period of the grating controls the diffraction angle and, hence, the spacing between the diffraction spots at the plane of interest. On the other hand, the FF and the phase height Φ control the distribution of intensities in different orders. The basic grating equation relating the wavelength of light λ, the period of the grating Λ, and the diffraction angle can be derived from Fig. 2.2.

Using Fourier analysis,[2] a binary phase 1D grating of period Λ can be considered as a sum of many sinusoidal gratings of different amplitudes, phases, and periods, namely, Λ, $\Lambda/2$, $\Lambda/3$, and so on. However, for a binary phase grating with a FF of 0.5, the even diffraction orders vanish,[10] and only

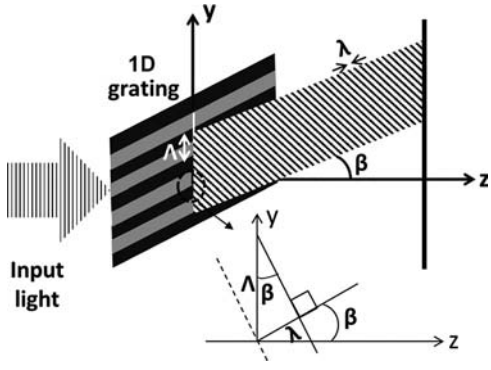

Figure 2.2 Schematic of diffraction of light by a 1D diffraction grating.

Downloaded From: https://www.spiedigitallibrary.org/ebooks/ on 27 Feb 2022
Terms of Use: https://www.spiedigitallibrary.org/terms-of-use

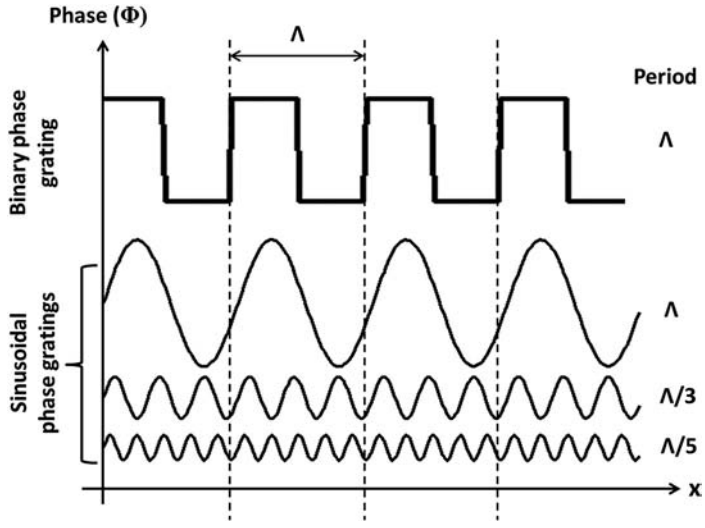

Figure 2.3 Sinusoidal grating components with periods (Λ, $\Lambda/3$, $\Lambda/5$, ...) of the binary 1D grating with period Λ.

odd diffraction orders $m = 1, 3, 5, \ldots$ appear, as shown in Fig. 2.3. As with any infinite series, an accurate profile of the binary phase grating can be generated by adding more terms. From Fig. 2.3, it can also be noted that the contributions of the sinusoidal gratings in the formation of the binary phase grating are not equal.

The amplitude values of the different-order sinusoidal gratings are given by Fourier coefficients, which are also the measure of relative intensity in various diffraction orders. The Fourier coefficients for the 0^{th} and m^{th} diffraction orders are shown in Eqs. (2.2) and (2.3), respectively:[11]

$$D_0 = e^{j\frac{\Phi}{2}} \cos\left(\frac{\Phi}{2}\right), \tag{2.2}$$

$$D_m = \frac{2}{jm\pi} e^{j\left(\frac{\Phi + m\pi}{2}\right)} \sin\left(\frac{\Phi}{2}\right) \sin\left(\frac{m\pi}{2}\right). \tag{2.3}$$

From Eq. (2.3) it can be noted that $D_m = 0$ for all even values of m. The diffracted beams' intensity values I_m relative to the incident beam can be obtained from the square of the absolute values of the Fourier coefficients. The relative intensity for diffraction orders $m = 0$, ± 1, and ± 3 are given by Eqs. (2.4), (2.5), and (2.6), respectively:

$$I_0 = |D_0|^2 = \left[\cos\left(\frac{\Phi}{2}\right)\right]^2. \tag{2.4}$$

Downloaded From: https://www.spiedigitallibrary.org/ebooks/ on 27 Feb 2022
Terms of Use: https://www.spiedigitallibrary.org/terms-of-use

$$I_{\pm 1} = |D_{\pm 1}|^2 = \left[\frac{2}{\pi}\sin\left(\frac{\Phi}{2}\right)\right]^2, \tag{2.5}$$

$$I_{\pm 3} = |D_{\pm 3}|^2 = \left[\frac{2}{3\pi}\sin\left(\frac{\Phi}{2}\right)\right]^2. \tag{2.6}$$

Diffraction can be thought of as controlling the direction and amount of light in higher orders. Any light that does not get diffracted ends up in the 0^{th} order, which can be considered to be the direction taken by light traveling in ways expected by refraction and classical optics alone. The Fourier transform of the grating gives rise to a number of orders and a Dirac delta function in the Fourier plane, which represents the 0^{th} order of the grating. The ± 1 diffraction orders arise due to diffraction by a sinusoidal grating with period Λ. The ± 3 diffraction orders arise due to diffraction by a sinusoidal grating with period $\Lambda/3$, and so on. The values of Fourier coefficients of different diffraction orders can be used to control the intensity distribution in different orders. Let us consider two design examples for generation of intensity profiles for specific applications.

Case 1: To generate maximum intensity in the 1^{st} order.

From Eq. (2.5) the maximum intensity in the 1^{st} order arises when $\Phi = \pi$ with a value of 40.5% of the input intensity. The thickness of the resist for the case of binary grating is given by $\lambda/[2(n_r - 1)]$. The thickness of the resist for a wavelength of $\lambda = 633$ nm and refractive index of resist $n_r = 1.5$ is $t = 633$ nm. Substituting the corresponding phase value in Eq. (2.4) shows that the intensity in the 0^{th} order is zero when the 1^{st} orders have maximum intensity. In other words, only when there is destructive interference in the 0^{th} diffraction order is there maximum intensity in the 1^{st} order. It should also be noted that the intensity in the ± 1 orders are equal due to the symmetric phase profile of the binary grating. Hence, the total intensity in both of the 1^{st} orders is 81%.

Case 2: To generate $\pm 1^{st}$ and 0^{th} order diffraction with equal intensity values.

This can be done by equating Eqs. (2.4) and (2.5). The phase value is $\Phi = 2.01$, and the corresponding resist thickness value is $t = 405$ nm. A plot of the intensity values of the 0^{th}, $\pm 1^{st}$, and $\pm 3^{rd}$ diffraction orders with respect to the resist thickness for a binary grating is shown in Fig. 2.4. The study of variation in efficiency for variation in phase or resist thickness is equivalent to the study of the variation in the wavelength of light. At a resist thickness of 633 nm for wavelength $\lambda = 633$ nm, the curve for the 0^{th} diffraction order becomes 0, confirming Case 1. The points of intersection of the curves for the 0^{th} and the $\pm 1^{st}$ diffraction orders confirm the results of Case 2. The points of intersection of the curves for the 0^{th} and the $\pm 3^{rd}$ diffraction order show the

Downloaded From: https://www.spiedigitallibrary.org/ebooks/ on 27 Feb 2022
Terms of Use: https://www.spiedigitallibrary.org/terms-of-use

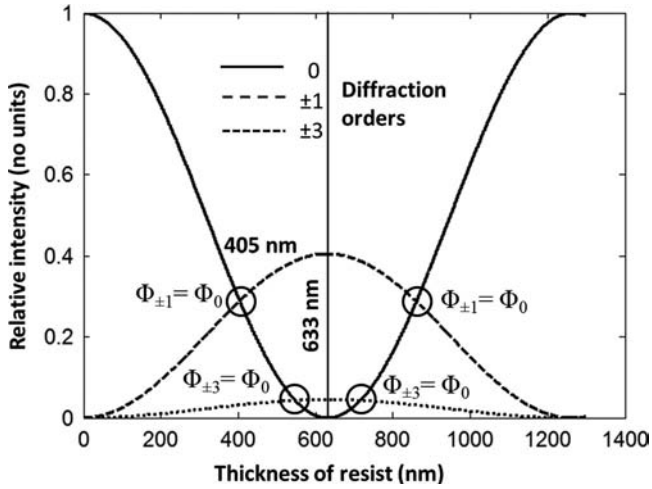

Figure 2.4 Plot of the normalized relative intensity values for 0^{th}, $\pm1^{st}$ and $\pm3^{rd}$ diffraction orders with a variation in wavelength (or phase) for a binary grating with a resist thickness of 633 nm.

wavelength for which the intensity of the 0^{th} diffraction order is same as that of the $\pm3^{rd}$ diffraction order. The maximum efficiency for the $\pm3^{rd}$ diffraction order is 4.5%.

This technique can be used to engineer 1D gratings to obtain the essential intensity profiles at the application plane. In many cases, the grating is used in conjunction with a focusing lens having a focal length f as shown in Fig. 2.5. The spacing between the 0^{th} diffraction order and the m^{th} diffraction order can be estimated using trigonometry as $f \tan \beta$.

In general, the diffraction pattern in the far field is estimated by calculation of the Fourier transform of the aperture function.[2,3] If $A(x, y)$ is the aperture function, then the amplitude profile of the diffraction pattern in the Fourier domain (spatial frequency domain) $E(u, v)$ is given by

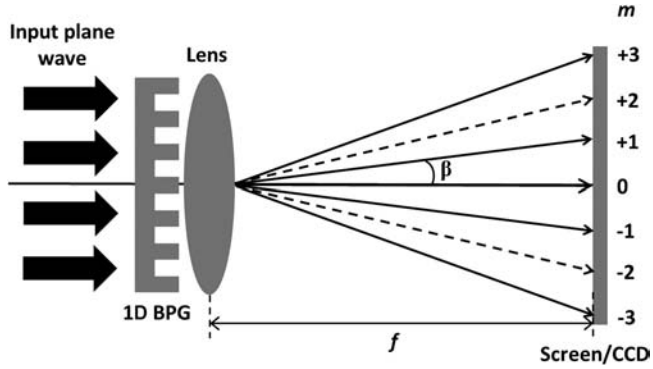

Figure 2.5 Optics configuration for focusing the diffraction orders generated by a binary phase grating (BPG) with a convex lens.

Downloaded From: https://www.spiedigitallibrary.org/ebooks/ on 27 Feb 2022
Terms of Use: https://www.spiedigitallibrary.org/terms-of-use

$$E(u,v) = \frac{e^{jkf}\, e^{j\frac{k}{2f}(u^2+v^2)}}{j\lambda f} \int_{-\infty}^{+\infty}\int_{-\infty}^{+\infty} A(x,y) \exp\left[-j\frac{2\pi}{\lambda f}(xu+yv)\right] dxdy, \qquad (2.7)$$

where f is the focal length of the lens used to cancel the quadratic phase factor of the Fresnel diffraction integral.[2,3] The spatial frequencies along the x and y directions are $f_x = x/\lambda f$ and $f_y = y/\lambda f$, respectively.

2.1.2 Design of 1D gratings with MATLAB®

The basic algorithm for design and far-field analysis of simple DOEs with known amplitude and phase profiles of the aperture is shown in Fig. 2.6.

In general, there are four basic steps. In the first step, the constant terms are defined; these include matrix size (size of the DOE) in pixels × pixels, period of the grating, wavelength, fill factor, etc. The design of the DOE is carried out in the second step, which is the most crucial part of the algorithm. This is done by assigning values of complex amplitude ($Ae^{i\Phi}$) to each pixel of the matrix, where A is the amplitude transmittance, and Φ is the phase value. In the case of amplitude-only and phase-only DOEs, $\Phi = 0$ or a constant, and $A = 1$, respectively. In the case of hybrid DOEs, it is necessary to assign both transmittance as well as phase values to each pixel of the matrix. The third step is the analysis step, in which the diffraction pattern of the DOE is calculated using scalar diffraction formulae. The final step is the display step, in which the DOE amplitude or phase profile and its diffraction patterns are displayed to verify the accuracy of the code is. It is always a good habit to evaluate the code at each step to make sure that it is proceeding in the correct

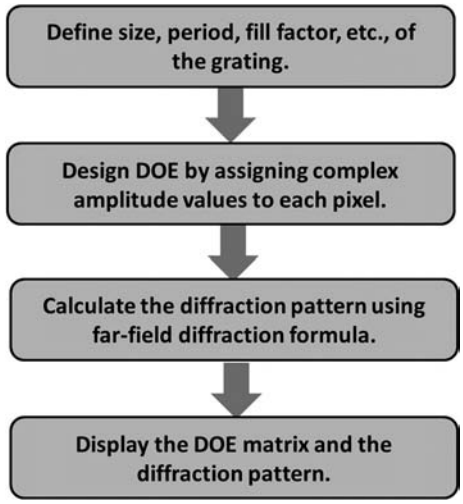

Figure 2.6 Algorithm for design and analysis of a DOE. The algorithm uses analytic expressions and is applicable to any software.

Downloaded From: https://www.spiedigitallibrary.org/ebooks/ on 27 Feb 2022
Terms of Use: https://www.spiedigitallibrary.org/terms-of-use

direction, instead of writing the full code and verifying later. In this book, the design and analysis is performed using MATLAB. For SCILAB users, the MATLAB code can be easily converted into SCILAB code.[12] Schemes for converting MATLAB code to C, C++, Mathcad, and Python codes are available in numerous websites.

1D gratings are designed as matrices of size $N \times M$, where N and M are the number of pixels along x and y axes, respectively. In most of the examples in this book, $N = M$. For simulation of diffraction patterns, the matrix size has been chosen as 500×500 to minimize the computation time. However, the choice of the value of N and M depends on various factors, such as the overall size of the element, the resolution with which it needs to be described, and even the resolution of the tool that will be used to actually fabricate the element. The fundamentals of sampling are discussed in various text books[13] and research papers.[14,15] The values stored in each pixel represent a sampled version of the structure to be designed. The amplitude and phase values are assigned assuming the size of each pixel to be 1 μm. The far-field diffraction pattern can be calculated by performing a Fourier transform of the aperture profile generated in MATLAB.[15,16] In particular, the Fourier transform for a 2D matrix is calculated using the '`fft2`' function in MATLAB.

2.1.2.1 Design of 1D amplitude gratings with MATLAB

In the case of amplitude gratings, the transmittance values $T = 0$ and $T = 1$ are assigned to the two binary levels of the grating. The phase value Φ is assumed to constant throughout and is normally set to zero. Hence, the time-frozen wave equation reduces from $T \exp(i\Phi)$ to just T. The MATLAB code for simulation and analysis of a 1D amplitude grating is given Table 2.1.

It should be noted that the module titled 'Constructing the grating' in Table 2.1 has been written using *for* and *if* loops. In terms of programming, this is not the best way to create the desired matrix, especially for large matrix sizes, as such loops are computationally intensive. MATLAB has inbuilt functions that will perform these operations in more efficient ways. However, the *for* and *if* functions have been used here because they are easy to understand, and some similar form of these functions exists in all programming languages. Examples of programs with more efficient codes are included throughout the book.

One other method of making codes more efficient is to create functions out of segments of code that repeat either within a program or across programs. For example, in Table 2.1, the last part of the code with the heading 'Observing the grating output in the far field' appears in almost all programs, as it generates the observable output of the program. We recommend creating a function with this code and then calling the function every time this output is to be generated. User-defined functions can be saved by going to the File tab and then pressing the 'setpath' button. Click on 'add

Downloaded From: https://www.spiedigitallibrary.org/ebooks/ on 27 Feb 2022
Terms of Use: https://www.spiedigitallibrary.org/terms-of-use

Table 2.1 MATLAB code for design and analysis of 1D binary amplitude grating.

```
%%1D Amplitude grating%%
clear %Clear all memory
% Defining Grating Parameters
    N=500; %Define Matrix size
    A=zeros(1,N); %Define a row Matrix by assigning 0 to all pixels
    P=100; %Define the period of the grating
    FF=0.5; %Define fill factor
% Constructing the Grating
for q=1:N;
  if rem(q,P)<P*FF; %Use remainder function 'rem' to construct
  %the grating
    A(1,q)=1;
  end
end
A=repmat(A,N,1); %replicate the row to create a 2D grating
% Alternative code for constructing the grating
    O=ones(N,FF*P);
    Z=zeros(N, P-FF*P);
    unit=[O Z];
    A=repmat(unit,1,N/P); %replicate to create a 1D grating
%Observing the grating output in the far field
    E=fftshift(fft2(A)); %fftshift is used to re-order the terms
    %in their natural order
    IN=(abs(E)/(N*N)).*(abs(E)/(N*N)); % Calculating intensity
    figure (1)
    colormap(gray); %colormap(gray) is used to display grayscale
    %image
    imagesc(A);% imagesc is used to display a high constrast image
    figure (2)
    colormap(gray);
    imagesc(IN);
```

folder' and then choose the folder that contains the functions that need to be permanently available, similar to inbuilt MATLAB commands. Each function must be saved as an individual file with the name that will be used to call it. We have created a set of functions that use either normalized intensity or the intensity values as directly calculated. These functions are provided in the Appendix.

After executing the program, the grating profile is visible in the first figure window [Fig. 2.7(a)], while the diffraction spots will be seen in the second one [Fig. 2.7(b)]. In the latter case, one should "zoom in" until the spots are clear. Now, by selecting the 'data cursor' icon in the figure and clicking on the diffraction spots, the relative intensity directed in that particular order will be displayed. It can be noted that the efficiency of the $\pm 1^{st}$ order is only 10.14%, which is only 1/4 of the maximum intensity in the case of 1D grating profile arising due to blocking of 50% of the light input at the grating plane. The MATLAB code of Table 2.1 can be implemented for different FFs by assigning different values to the parameter FF. Figure 2.1 can be generated using the command '`meshz(A)`'.

Downloaded From: https://www.spiedigitallibrary.org/ebooks/ on 27 Feb 2022
Terms of Use: https://www.spiedigitallibrary.org/terms-of-use

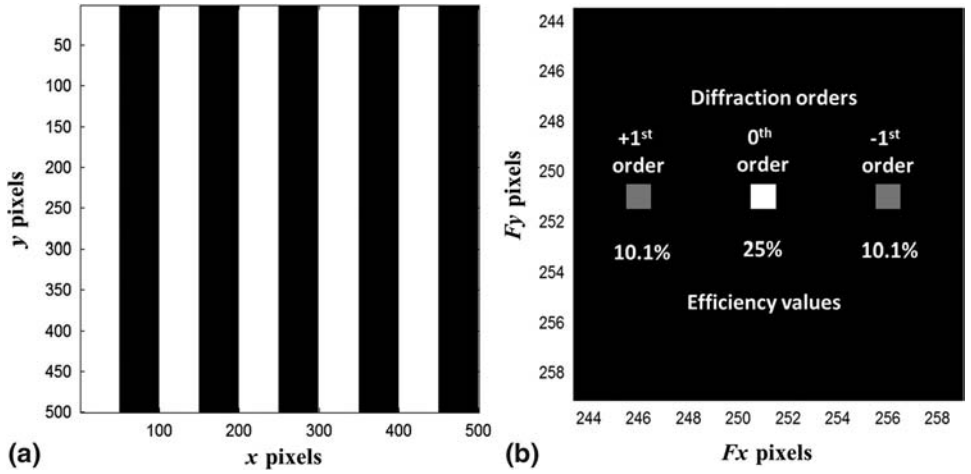

Figure 2.7 Output of the code shown in Table 2.1 (a) Profile of the 1D amplitude grating and (b) diffraction patterns at the Fourier plane. The latter image was obtained by zooming in on the generated output figure.

In order to compare simulation results with experimental results, it is important to relate pixel information to the physical dimensions. This can be done using the grating diffraction equation and trigonometry. First, let us assume the pixel size in the DOE matrix to be a square of side Δ_{DOE}. Hence, in the DOE plane, $x = (x \text{ pixels}) \times \Delta_{\mathrm{DOE}}$ [μm], and $y = (y \text{ pixels}) \times \Delta_{\mathrm{DOE}}$ [μm]. Considering the relationship between continuous and discrete Fourier transforms, at a distance z and sampling size $N \times N$ in the DOE plane, the pixel size in the observation window during simulation is given by $\Delta_I = (\lambda z / N \Delta_{\mathrm{DOE}})$.

The spacing between the 0^{th} and 1^{st} order diffraction spots seen in Fig. 2.7(b) is $F_x = 5$ pixels, which corresponds to a physical spacing of 6.33 mm (recalling that $\Delta_I = \lambda z / N \Delta_{\mathrm{DOE}}$) for $N = 500$, $z = 1$ m, $\lambda = 633$ nm, and $\Delta_{\mathrm{DOE}} = 1$ μm. From the sampling relation, it is possible to connect the pixel information in the output figure [e.g., Fig. 2.7(b)] to actual dimensions. The above result can be verified using the grating diffraction equation and trigonometric relations.

Numerous sampling criteria can be used to obtain simulation results that will accurately predict the experimental results.[17–19] Some of the most important requirements are presented in the following paragraph. The first and foremost requirement for sampling is that it must satisfy the Nyquist criterion; i.e., the sampling frequency must be at least twice that of the maximum frequency of the signal.[20] This criterion can be verified by choosing a period that is twice the sampling period in Table 2.1. In this case, sampling is at its limit when the 0^{th} diffraction order is at the center of the observation window and the 1^{st} diffraction order is at the edge of the observation window,

Downloaded From: https://www.spiedigitallibrary.org/ebooks/ on 27 Feb 2022
Terms of Use: https://www.spiedigitallibrary.org/terms-of-use

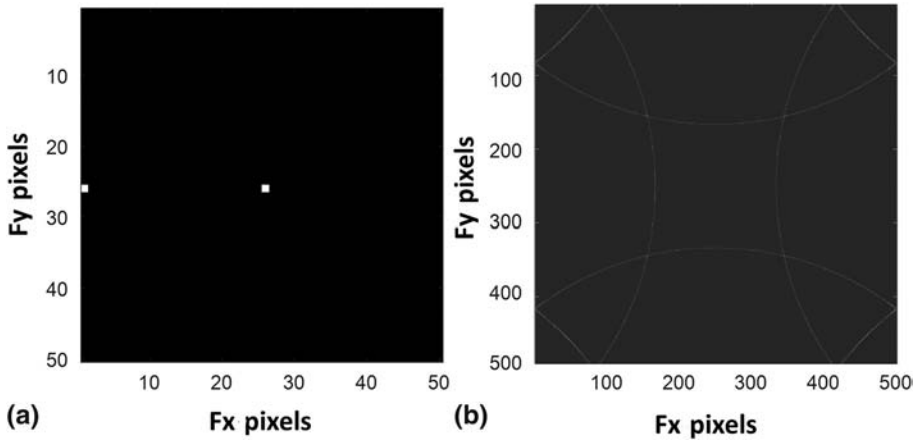

Figure 2.8 (a) Output figure for diffraction by an amplitude grating with a period twice that of the sampling period and (b) output figure for diffraction by a circular grating (Table 2.8) when the period is 12 μm sampled at a rate of 10 μm/pixel.

as shown in Fig. 2.8(a). Since the central peak is located at pixel number 251, only one of the orders is visible on one side, while the other order is out of range (by one pixel). The aliasing effects are clearly visible when the DOE period is smaller than the sampling period.[21,22] For instance, let us consider the case where the sampling period is 10 μm but the period is 12 μm for a circular grating (generating by running the code of Table 2.8). Instead of a circle, the pattern in Fig. 2.8(b) is obtained.

The second requirement is zero padding of the diffraction plane. Zero padding is the process of adding zeros around a matrix such that the information-carrying part actually occupies a smaller (central) area of the matrix. The use of this technique always involves some trade-offs, as must be obvious from the fact that useful resolution in the DOE plane is being sacrificed. For instance, in the case of Fresnel diffraction, which we will introduce in Chapter 4, zero padding is used to provide more information at the observation plane.[23] While this can be thought of as an improvement in resolution in the far-field pattern, one has to be careful with that statement, as zero padding cannot improve resolution beyond what is provided at the DOE plane.[24,25] The only way to do that would be to increase the spatial size rather than decrease it. The higher level of detail at the observation plane with zero padding is therefore obtained at the cost of resolution at the DOE plane itself.

Let us once again consider the simulation of a 1D amplitude grating. This time, let us zero pad the grating structure and repeat the calculation. Images of the diffraction patterns when the diffraction grating is zero padded by 125 pixels and 200 pixels are shown in Figs. 2.9(a) and (b), respectively. This means that for a 500×500 pixel matrix, the grating occupies an area corresponding to 250×250 pixels and 100×100 pixels, respectively, for these

Downloaded From: https://www.spiedigitallibrary.org/ebooks/ on 27 Feb 2022
Terms of Use: https://www.spiedigitallibrary.org/terms-of-use

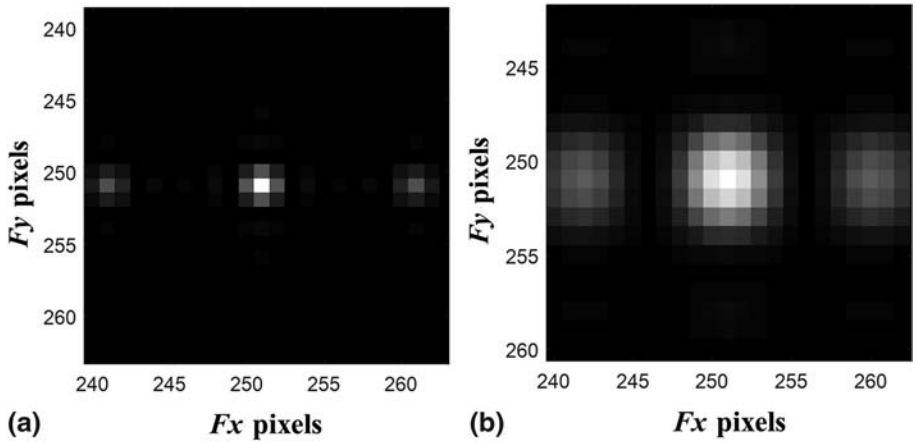

Figure 2.9 Images of the diffraction patterns when the diffraction grating is zero padded by (a) 125 pixels and (b) 200 pixels.

two cases. The result is that at the observation plane, an increase in resolution of the diffraction patterns is observed, resulting in a better match between simulation and experimental results. However, for analysis of efficiency, the case without zero padding is convenient, as it is easy to extract the information about the efficiency by just clicking on the spot. In Section 2.1.4 a similar analysis is shown for a circular grating.

2.1.2.2 Design of 1D phase gratings with MATLAB

A constant transmittance value ($T = 1$) is assigned to all the pixels, while the phase values $\Phi = 0$ and $\Phi = \pi$ are assigned to the two binary levels of the grating, respectively. The MATLAB code for simulation and analysis of a 1D phase grating is similar to that of the previous MATLAB code given for 1D amplitude grating, except for a few changes, as shown in Table 2.2.

In earlier versions of MATLAB, one may have to use '`exp (i*pi)`'. If the MATLAB code line was '`imagesc(A)`', then a gray image with a size 500×500 will be displayed as $T = 1$. The 'angle' function is used to display the phase values. The image of the phase grating and the zoomed-in image of the diffraction pattern are shown in Figs. 2.10(a) and (b), respectively.

A 'data cursor' click on the black regions of Fig. 2.10(a) displays a value of 0, while a click on the white regions displays a value of 3.142. In Fig. 2.10(b), the normalized values displayed for the diffraction orders $\pm 1^{st}$, $\pm 3^{rd}$, and $\pm 5^{th}$ were 0.405, 0.045, and 0.016, respectively. It can also be noted that the 0^{th} diffraction order is completely cancelled, as it should be, according to the explanation given in Case 1 of Section 2.1.1. A follow-up exercise would be to simulate the phase grating and its diffraction pattern for a phase value of $\Phi = 2.01$ and verify the results shown in Fig. 2.4. In this case, the 0^{th} and $\pm 1^{st}$

Downloaded From: https://www.spiedigitallibrary.org/ebooks/ on 27 Feb 2022
Terms of Use: https://www.spiedigitallibrary.org/terms-of-use

Table 2.2 MATLAB code for design and analysis of a 1D binary phase grating.

```
%%1D Phase grating%%
clear; %Clear all memory
% Defining Grating Parameters
    N=500; %Define Matrix size
    A=ones(1,N); %Define a Matrix by assigning 1 to all pixels
    P=100; %Define the period of the grating
    FF=0.5; %Define fill factor
% Constructing the Grating
for q=1:N; %Scan pixel by pixel
  if rem(q,P)<P*FF; %Use remainder function 'rem' to construct
  %the grating
     A(1,q)=exp(1i*pi);
  end
end
    A=repmat(A,N,1); %replicate the row to create a 2D grating
%Observing the grating output in the far-field
    E=fftshift(fft2(A)); %fftshift is used to re-order the terms
    in their natural order
    IN=(abs(E)/(N*N)).*(abs(E)/(N*N)); % Calculating intensity
    figure(1)
    colormap(gray);
    imagesc(angle(A))
    figure(2)
    colormap(gray);
    imagesc(IN);
```

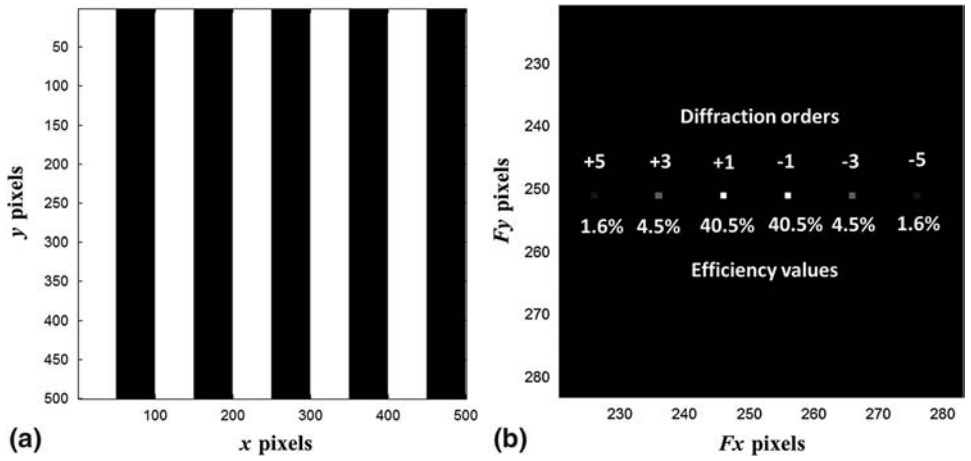

Figure 2.10 Output of the code shown in Table 2.2. (a) Profile of the 1D phase grating and (b) diffraction patterns at the Fourier plane. The latter image was obtained by zooming in on the generated output figure.

diffraction orders will display the same value: 0.29. One can repeat the exercise for the case to equalize the intensity of the 0^{th} diffraction order with that of $\pm 3^{rd}$ diffraction orders. Once again, the exercise may be repeated by varying the FF of the grating.

Downloaded From: https://www.spiedigitallibrary.org/ebooks/ on 27 Feb 2022
Terms of Use: https://www.spiedigitallibrary.org/terms-of-use

2.1.2.3 Design of 1D amplitude and phase sinusoidal gratings with MATLAB

The above procedure and MATLAB simulation can be extended to other interesting 1D gratings such as sinusoidal amplitude and phase gratings.[26] The maximum efficiency in the $\pm 1^{st}$ order is only 6.25% for the amplitude sinusoidal grating and 33.8% for the phase sinusoidal grating with a phase of 0.59π.[2,26] For amplitude sinusoidal gratings, the module 'Constructing the grating' in Table 2.1 is replaced by the code shown in the upper part of Table 2.3. The image of the grating profile and the zoomed-in diffraction screen are shown in Figs. 2.11(a) and (b), respectively. A simpler version of the code is shown in the lower part of Table 2.3. Here, the *for* loop is not used. In the second line, 'A' will be calculated for every value in the matrix 'q'.

For phase sinusoidal gratings, the MATLAB code in Table 2.4 is modified by replacing code lines as follows in Table 2.4. The other code modifications in Table 2.2 for phase type must also be included.

The output generated when running the full code will be as shown in Figs. 2.11(a) and (b), with the latter showing diffraction spots corresponding

Table 2.3 MATLAB code for design of 1D sinusoidal amplitude grating.

```
%%1D sinusoidal amplitude grating%%
for q=1:N;
    A(1,q)=(1+sin(rem(q,P)*(2*pi)/P))/2;
end
A=repmat(A,N,1);
%% Simpler code
q=1:N;
A=(1+sin(rem(q,P)*(2*pi)/P))/2;
A=repmat(A,N,1);
```

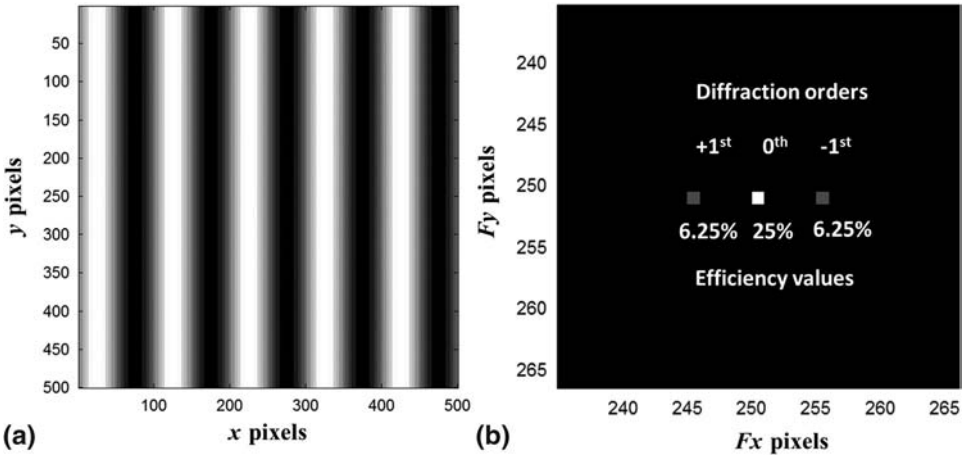

Figure 2.11 Output of the code shown in Table 2.3 (a) Profile of the 1D sinusoidal amplitude grating and (b) diffraction patterns at the Fourier plane. The latter image was obtained by zooming in on the generated output figure.

Downloaded From: https://www.spiedigitallibrary.org/ebooks/ on 27 Feb 2022
Terms of Use: https://www.spiedigitallibrary.org/terms-of-use

Table 2.4 MATLAB code for design of a 1D sinusoidal phase grating.

```
%%1D sinusoidal phase grating%%
for q=1:N;
    A(1,q)= exp(1i*0.59*pi*(sin(rem(q,P)*(2*pi)/P)));
end
A=repmat(A,N,1);
```

to 0^{th}, $\pm1^{st}$, $\pm2^{nd}$, and $\pm3^{rd}$ diffraction orders with efficiency values of 1%, 33.9%, 10%, and 1%, respectively.

2.1.3 Design of 2D gratings

A 2D binary phase grating has phase variations in both x and y directions. The phase profile of a 2D grating with periods of Λ_x and Λ_y along the x and y directions, respectively, is given by

$$\Phi_{2D}(x,y) = \begin{cases} \Phi, & 0 \le x \le \frac{\Lambda_x}{2}, \quad 0 \le y \le \frac{\Lambda_y}{2}, \Phi_{2D}(x) = \Phi_{2D}(x+\Lambda_x), \\ 0, & \frac{\Lambda_x}{2} \le x \le \Lambda_x, \frac{\Lambda_y}{2} \le y \le \Lambda_y, \Phi_{2D}(y) = \Phi_{2D}(y+\Lambda_y). \end{cases} \quad (2.8)$$

The periodicity along the x and y directions gives rise to diffraction spots along those directions. The relative intensity in various diffraction orders can be calculated using Eqs. (2.4)–(2.6). The $\pm m_x$ diffraction orders generated by x periodicity of the 2D binary phase grating is divided further into $\pm m_y$ diffraction orders due to periodicity along the y direction. The relative intensity in (m_x, m_y) diffraction orders can be calculated by multiplication of the respective relative intensities in different orders along the x and y directions. For instance, the relative intensity in ($m_x = \pm1$, $m_y = \pm1$) and ($m_x = \pm1$, $m_y = \pm3$) can be calculated using Eqs. (2.9) and (2.10), respectively:

$$I_{\pm1,\pm1} = |D_{\pm1}|^2 |D_{\pm1}|^2 = \left[\frac{2}{\pi}\sin\left(\frac{\Phi}{2}\right)\right]^2 \left[\frac{2}{\pi}\sin\left(\frac{\Phi}{2}\right)\right]^2, \quad (2.9)$$

$$I_{\pm1,\pm3} = |D_{\pm1}|^2 |D_{\pm3}|^2 = \left[\frac{2}{\pi}\sin\left(\frac{\Phi}{2}\right)\right]^2 \left[\frac{2}{3\pi}\sin\left(\frac{\Phi}{2}\right)\right]^2. \quad (2.10)$$

Hence, the maximum possible efficiency in the ($m_x = \pm1$, $m_y = \pm1$) and ($m_x = \pm1$, $m_y = \pm3$) diffraction orders are only 16% and 1.8%, respectively. The image of a 2D grating seen in many text books[13] and literature[27–32] is shown in Fig. 2.12. The grating has periodicity in both the x and y directions.

In the former case (amplitude elements), the white and black portions represent areas with transmittance '1' and '0', respectively. For the latter case (phase elements), the entire area has transmittance '1', but the white regions all have a constant phase difference with respect to the black regions, which can be considered to have phase '0'.

Downloaded From: https://www.spiedigitallibrary.org/ebooks/ on 27 Feb 2022
Terms of Use: https://www.spiedigitallibrary.org/terms-of-use

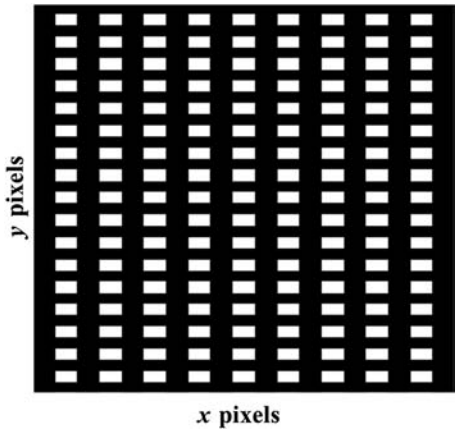

Figure 2.12 Amplitude or phase profile of a 2D grating.

Table 2.5 MATLAB code for design of a 2D binary amplitude grating.

```
%%2D Amplitude grating%%
clear; %Clear all memory
% Defining Grating Parameters
    N=500; %Define Matrix size
    A=zeros(N,N); %Define a Matrix by assigning 0 to all pixels
    Px=100; Py=100; %Define the period of the grating
    FFx=0.5; FFy=0.5; %Define fill factor
% Constructing the Grating
for p=1:N; %Scan pixel by pixel using for loops and construct
%grating using 'rem'
  for q=1:N;
    if rem(q,Px)<Px*FFx && rem(p,Py)<Py*FFy;
      A(p,q)=1;
    end
  end
end
```

The MATLAB code for generation of a 2D amplitude grating is given in Table 2.5.

Once again, a 2D phase grating can be designed with slight modifications of the above MATLAB code, as described in Table 2.2. The orders of a 2D phase grating are shown in Fig. 2.13. A closer evaluation shows that the efficiency values obtained from the figure do not match the values estimated using Eqs. (2.9) and (2.10). The 0^{th} diffraction order is expected to completely vanish when $\Phi = \pi$. Instead, the 0^{th} diffraction order is stronger with 23% of the input light. Why is this? It may seem that there is some problem with the MATLAB code. A deeper look reveals the problem associated with 2D gratings available in many text books. Yes, the image seen in Fig. 2.12 has periodicity along both the x and y directions. But a closer look reveals that the

Downloaded From: https://www.spiedigitallibrary.org/ebooks/ on 27 Feb 2022
Terms of Use: https://www.spiedigitallibrary.org/terms-of-use

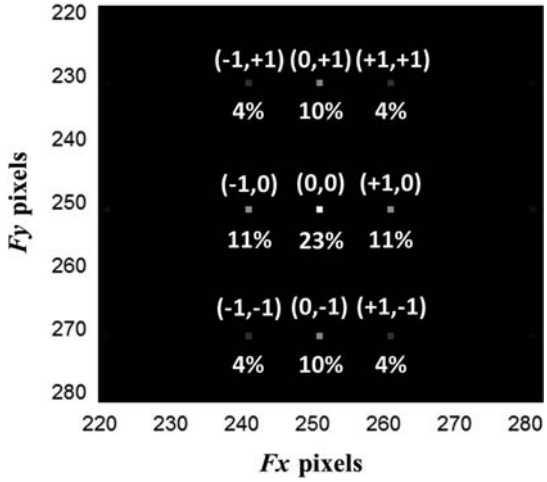

Figure 2.13 Diffraction pattern of the 2D phase grating with $\Phi = \pi$.

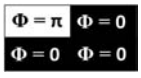

Figure 2.14 Fundamental building block of the 2D grating shown in Fig. 2.12.

grating to be evaluated with Eqs. (2.9) and (2.10) is not the grating shown in Fig. 2.12.

Let us consider the fundamental building unit (Fig. 2.14) of the 2D grating shown in Fig. 2.12. It can be noted that 75% of the unit has a phase value of 0, while only 25% of the unit has a phase value of π. In that sense, the actual FF of this grating is 0.25. The Fourier coefficients for $\Phi = \pi$ yield the values corresponding to Eqs. (2.4)–(2.6) only when the FF is 0.5. This can easily be tested by designing a 1D phase grating such that the FF is not 0.5. The FF can be modified in the MATLAB code shown in Table 2.2. Another way to understand this effect by recalling the fact that the 1^{st} diffraction order has maximum efficiency only when the 0^{th} diffraction order is completely cancelled. This can only happen when the light emanating from the 0 phase regions and the π phase regions are equal. Hence, the areas of the two binary phase regions must be always equal to each other in order to extract the maximum efficiency values. Therefore, the grating that more accurately describes the 2D version of the 1D grating with a FF of 0.5 is known as a checkerboard grating and is shown in Fig. 2.15.

The checkerboard grating[27,28] can be generated by many methods; MATLAB even has a function named '`checkerboard`'. MATLAB codes for designing a checkerboard phase grating are presented Tables 2.6 and 2.7. Once again, we present two versions. One using *for* and *if* loops, which is easy to understand, and a second version, which is much more compact and

Downloaded From: https://www.spiedigitallibrary.org/ebooks/ on 27 Feb 2022
Terms of Use: https://www.spiedigitallibrary.org/terms-of-use

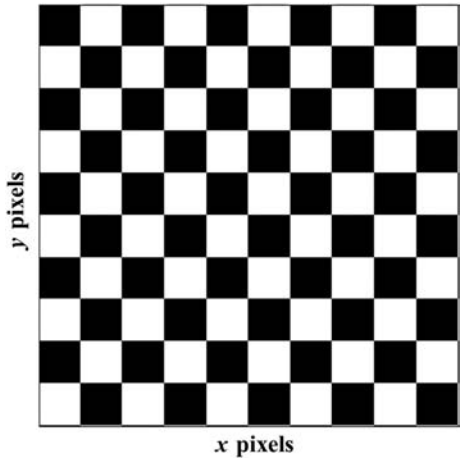

Figure 2.15 Profile of a checkerboard grating.

Table 2.6 MATLAB code for design of a checkerboard grating (version 1).

```
% Version 1
%%Checkerboard phase grating%%
clear; %Clear all memory
% Defining Grating Parameters
    N=500; %Define Matrix size
    A1=zeros(N,N); %Define Matrices by assigning 0 to all pixels
    A2= zeros (N,N);
    A= zeros (N,N);
    Px=100; %Define the periods of the gratings
    Py=100;
    FFx=0.5; %Define fill factors
    FFy=0.5;
% Constructing the grating
tic
for p=1:N;
  for q=1:N;
    if rem(q,Px)<Px*FFx;
      A1(p,q)=1;
    end
    if rem(p,Py)<Py*FFy;
      A2(p,q)=1;
    end
  end
end
A=exp(1i*pi*xor(A1,A2));%% XOR operation between A1 and A2
toc
```

elegant. Using the command 'tic-toc', one can determine how long the 'Constructing the grating' module runs in both cases. The version without the *for* and *if* loops is already an order of magnitude faster for this file size. The module 'Observing the grating output in the far field' is not shown, as it is identical to the corresponding module in Table 2.2.

Downloaded From: https://www.spiedigitallibrary.org/ebooks/ on 27 Feb 2022
Terms of Use: https://www.spiedigitallibrary.org/terms-of-use

Table 2.7 MATLAB code for design of a checkerboard grating (version 2).

```
% Version 2: Checker pattern created without loops
%%Checkerboard phase grating%%
    clear; %Clear all memory
    % Defining Grating Parameters
    N=500; %Define Matrix size
    Px=100; %Define the periods of the gratings
    Py=100;
    FFx=0.5; %Define fill factors
    FFy=0.5;
%Define one unit of the grating
    tic
    O=ones(FFy*Py, FFx*Px)*exp(1i*pi);
    Z=ones(FFy*Py, Px-FFx*Px);
    O1=ones(FFy*Py, Px-FFx*Px)*exp(1i*pi);
    Z1=ones(FFy*Py, FFx*Px);
    unit=[Z O; O1 Z1];
    s=size(unit)
%Constructing the entire grating
    A=repmat(unit,N/s(1),N/s(2)); %replicate to create a 2D
    grating
    toc
```

When either version of the codes from Table 2.6 and Table 2.7 is run, along with the part that generates the output, the diffraction orders will appear as seen in Fig. 2.16. The efficiency values displayed in the figure window are in complete agreement with the values calculated using Eqs. (2.9) and (2.10).

Hence, from the above discussions, care must be taken when designing elements in MATLAB in order to obtain the correct simulation results.

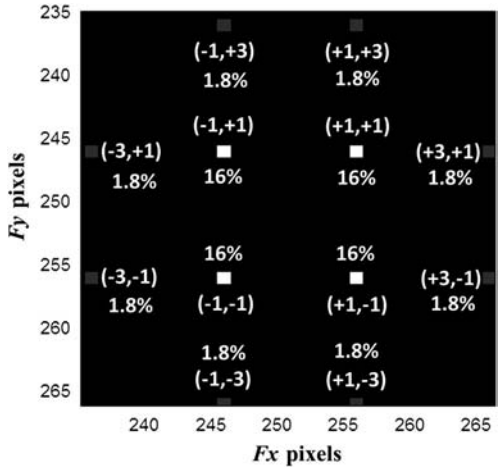

Figure 2.16 Diffraction pattern of the checkerboard grating with $\Phi = \pi$.

Downloaded From: https://www.spiedigitallibrary.org/ebooks/ on 27 Feb 2022
Terms of Use: https://www.spiedigitallibrary.org/terms-of-use

2.1.4 Binary circular gratings

Circular gratings, also called diffractive axicons, have periodicity along the radial direction.[33,34] The far-field diffraction pattern of a circular grating is a ring and is utilized in various applications such micro-drilling.[35] Unlike the 1D phase gratings discussed earlier, which have an efficiency of 40.5% in each of the $+1^{st}$ and -1^{st} orders, circular gratings have an efficiency of approximately 50%.

From Fig. 2.17 it is clear that the $+1^{st}$ and -1^{st} diffraction orders are combined in the ring diffraction pattern. However, a redistribution along the radial direction yields an efficiency of approximately 50% instead of 81%. The MATLAB code for design and analysis of binary phase circular gratings is shown in Table 2.8.

The output of the code, i.e., the grating profile and diffraction orders, are shown in Figs 2.18(a) and (b), respectively. The design of the binary axicon is zero padded in order to improve the resolution of the diffraction pattern.[23] The design in Table 2.8, without zero padding, is also shown in Fig. 2.18(b).

2.1.5 Fresnel zone plates

The amplitude version of the FZP was invented as early as 1871 by Lord Rayleigh.[36] The phase version of the FZP is one of the most useful inventions and is present in many different current applications.[37–39] The basic design of the FZP has been discussed in numerous books.[2,40] The optics configuration for focusing a parallel beam of light using a 1D FZP is shown in Fig. 2.19.

Light diffracted from consecutive zones of the FZP are out of phase by π, which corresponds to a path difference of $\lambda/2$. Hence, in the amplitude FZP, the zones with odd zone numbers are blocked to remove the light that is out of

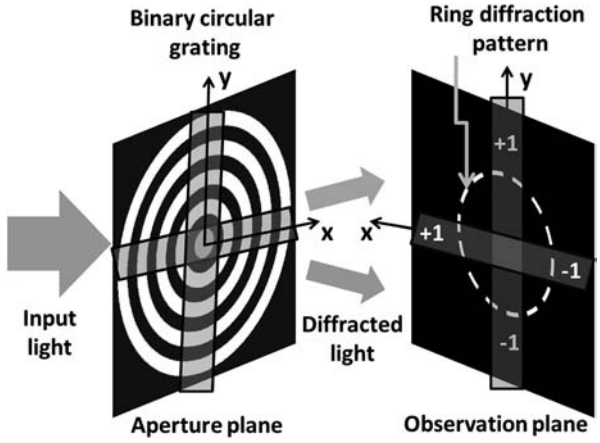

Figure 2.17 Diffraction of light from a binary circular grating.

Downloaded From: https://www.spiedigitallibrary.org/ebooks/ on 27 Feb 2022
Terms of Use: https://www.spiedigitallibrary.org/terms-of-use

Table 2.8 MATLAB code for design of a diffractive axicon.

```
%%Diffractive axicon%%
clear; %Clear all memory
% Defining Grating Parameters
    N=500; %Define Matrix sizes
    A=ones(N,N); %Define Matrices by assigning 1 to all pixels
    r=ones(N,N);
    P=50;%Define the period of the grating
    FFr=0.5;%Define fill factor for radial periodicity
% Constructing the grating
    x=1:N;
    y=1:N;
    del=5;
    [X,Y]=meshgrid(x*del,y*del);
    r=sqrt((X-N/2*del).*(X-N/2*del)+(Y-N/2*del).*(Y-N/
    2*del));
    A(rem(r,P)<P/2)=exp(1i*pi);
    A(r>N/2-2)=0;
%Observing the grating output in the far-field
%See appendix for function definition
    Norm_outputP(A,N)
```

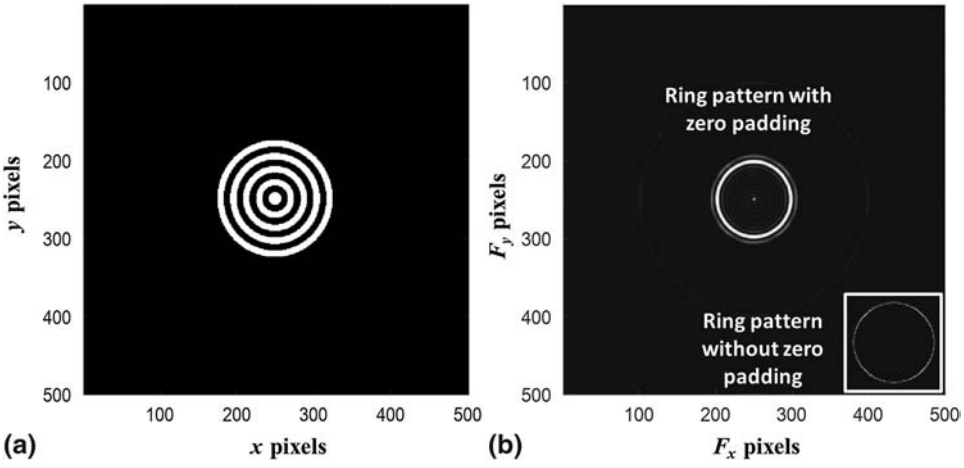

Figure 2.18 (a) Image of the circular grating and (b) the ring diffraction patterns with and without zero padding.

phase with respect to the light diffracted by the zones with even zone numbers. Such an FZP has only 10% efficiency. This disadvantage can be overcome by making a phase element, with the addition of phase π to either the even or odd zones using a refractive material of calculated thickness and refractive index (such as photo resist or electron beam resist). Such binary phase FZPs have a relatively higher efficiency of 40%.

The path difference equation for the design of a 1D FZP is given in by

Downloaded From: https://www.spiedigitallibrary.org/ebooks/ on 27 Feb 2022
Terms of Use: https://www.spiedigitallibrary.org/terms-of-use

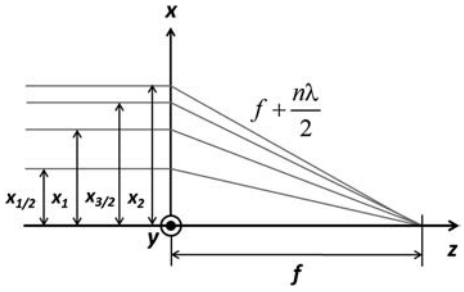

Figure 2.19 Optics configuration for focusing light using a 1D FZP.

$$\sqrt{f^2 + x_n^2} - f = n\lambda. \tag{2.11}$$

Solving Eq. (2.11) and rearranging the terms, we obtain the width of the grating lines x_n as

$$x_n = \sqrt{\frac{n^2\lambda^2}{4} + nf\lambda}. \tag{2.12}$$

The first term inside the square root is negligible compared to the second term. Hence, the approximate value of the widths of the grating lines is given by

$$x_n \cong \sqrt{nf\lambda}. \tag{2.13}$$

The 1D FZP has a line focus similar to that of a cylindrical lens.[29] The MATLAB code for simulation and analysis of a 1D phase FZP is shown in Table 2.9. The image of the 1D FZP and its diffraction pattern are shown in Figs. 2.20(a) and (b), respectively. The same MATLAB code with some modifications described in the previous cases can be used for the design of the amplitude version of the grating. A 2D FZP can be constructed by designing two FZPs orthogonal to each other and combining them using the XOR operation discussed in Section 2.1.3.

A circular FZP can be designed using a similar procedure. In that case, the radius r_n of each zone will be defined instead of the distance away from the axis in one direction:

$$r_n \cong \sqrt{nf\lambda}. \tag{2.14}$$

The MATLAB code for a circular FZP can be designed by replacing the x or y coordinate in the nested-for-loop section using radial coordinates. The circular FZP design part using nested-for-loops is shown in Table 2.10. The M value is modified from 50 to 32 in order to fit the circular FZP to the matrix size.

Downloaded From: https://www.spiedigitallibrary.org/ebooks/ on 27 Feb 2022
Terms of Use: https://www.spiedigitallibrary.org/terms-of-use

Table 2.9 MATLAB code for design of a 1D binary phase FZP.

```
%%1-d FZP%%
clear; %Clear all memory
%Defining FZP parameters
    N=500; %Define Matrix sizes
    M=50;%Define the number of grating lines
    A=ones(N,N); %Define Matrices by assigning 1 to all pixels
    x=zeros(M,M);
    f=3000;%Define the focal length of FZP in micrometers
    lambda=0.633;%Define wavelength in micrometers
% Constructing the FZP
for n=1:M;
  x(n)=sqrt(n*f*lambda);
end
for n=1:2:M;
  for q=1:N;
    if abs(q-N/2)>x(n) && abs(q-N/2)<x(n+1);
    A(:,q)=exp(1i*pi);
    end
  end
end
```

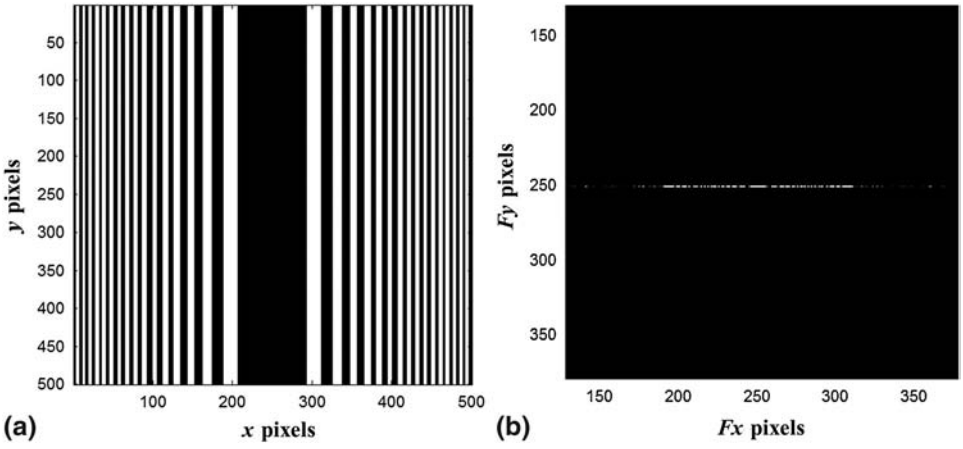

Figure 2.20 (a) Image of the 1D FZP and (b) its diffraction pattern.

The image of the generated circular FZP is shown in Fig. 2.21. In the case of a circular FZP, the first diffraction order (either $+1^{st}$ or -1^{st}) is the center spot, while the other diffraction orders ($\pm 3^{rd}$, $\pm 5^{th}$) with larger diffraction angles appear as circles around the central diffraction order.

The MATLAB code can be modified to design FZPs with other geometries such as elliptical FZPs, 2D FZPs, etc., or even elements with sinusoidal phase variations.

Downloaded From: https://www.spiedigitallibrary.org/ebooks/ on 27 Feb 2022
Terms of Use: https://www.spiedigitallibrary.org/terms-of-use

Table 2.10 MATLAB code for design of a circular binary phase FZP.

```
%%Circular FZP%%
% Constructing the FZP
for n=1:M; %Calculate the width of the grating lines
  r1(n)=sqrt(n*f*lambda);
end
for n=1:2:M;
  for p=1:N;
    for q=1:N;
      r(p,q)=sqrt((p-N/2)*(p-N/2)+(q-N/2)*(q-N/2));
      if r(p,q) > r1(n) && r(p,q) < r1(n+1);
        A(p,q)=exp(1i*pi);
      end
    end
  end
end
```

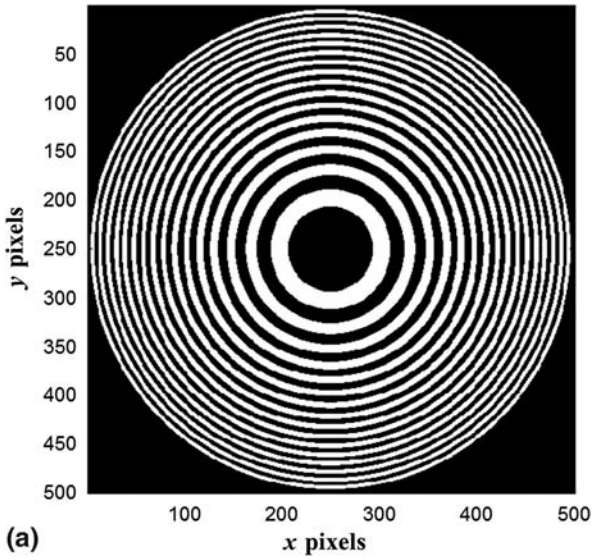

Figure 2.21 Image of the circular FZP with a focal length of 3 mm generated using the MATLAB code in Table 2.10.

2.2 Conclusions

In this chapter, the designs of basic DOEs such as different types of gratings and FZPs have been presented. In each case, the fundamental concepts are introduced in such a way that a novice programmer can begin making his or her own DOE designs almost immediately. The MATLAB codes are discussed in detail so that each line of code makes sense. After completing the chapter, the reader is encouraged to design other complex periodic structures as well.

Downloaded From: https://www.spiedigitallibrary.org/ebooks/ on 27 Feb 2022
Terms of Use: https://www.spiedigitallibrary.org/terms-of-use

2.3 Exercises

E.2.1 Design a 1D phase grating to generate diffraction spots such that the relative intensity of 1st diffraction order is only 50% that of the 0th diffraction order. Verify the result by estimating the efficiency values.

E.2.2 Design a 2D grating to generate 3×3 diffraction spots of equal intensity. Verify the result with MATLAB.

E.2.3 Design a triangular grating array with a period of 100 μm along both the x and y directions and calculate its far-field diffraction pattern using MATLAB.

E.2.4 Design a 2D phase FZP with a focal length of 3000 μm along the x direction and 6000 μm along the y direction.

E.2.5 Design an elliptical FZP with a 1.5 ratio of maximum to minimum focal length values.[41,42]

E.2.6 Design an amplitude axicon array in which the diameter of each element is 100 μm and the period is 10 μm.[43,44]

References

1. G. G. Lendaris and G. L. Stanley, "Diffraction-pattern sampling for automatic pattern recognition," *Proc. IEEE* **58**, 198–216 (1970).
2. J. W. Goodman, *Introduction to Fourier Optics*, Second Edition, McGraw-Hill Companies Inc., New York (1996).
3. B. C. Kress and P. Meyrueis, *Applied Digital Optics*, John Wiley & Sons, Chichester, UK (2009).
4. B. Zhang and D. Zhao, "Focusing properties of Fresnel zone plates with spiral phase," *Opt. Express* **18**, 12818–12823 (2010).
5. L. Rayleigh, "XII. On the manufacture and theory of diffraction-gratings," *Philos. Mag.* **47**, 81–93 (1874).
6. J. B. Keller, "Geometrical theory of diffraction," *J. Opt. Soc. Am.* **52**, 116–130 (1962).
7. H. Kogelnik, "Coupled wave theory for thick hologram gratings," *Bell Systems Technical Journal* **48**, 2909–2947 (1969).
8. J. M. Cowley and A. F. Moodie, "Fourier images IV: The phase grating," *Proc. Phys. Soc*. **76**, 378–384 (1960).
9. T. A. Shankoff, "Phase holograms in dichromated gelatin," *Appl. Opt.* **7**, 2101–2105 (1968).
10. K. Knop, "Rigorous diffraction theory for transmission phase gratings with deep rectangular grooves," *J. Opt. Soc. Am.* **68**, 1206–1210 (1978).

Downloaded From: https://www.spiedigitallibrary.org/ebooks/ on 27 Feb 2022
Terms of Use: https://www.spiedigitallibrary.org/terms-of-use

11. A. Martínez, M. Sánchez-López, and I. Moreno, "Phasor analysis of binary diffraction gratings with different fill factors," *Eur. J. Phys.* **28**(5), 805–816 (2007).
12. V. Couvert and S. Steer, "Matlab M-file to Scilab conversion function," 5th October 2011 [https://help.scilab.org/doc/5.3.3/en_US/mfile2sci.html].
13. D. C. O'Shea, T. J. Suleski, A. D. Kathman, and D. W. Prather, *Diffractive Optics: Design, Fabrication and Test*, SPIE Press, Bellingham, Washington (2003) [doi: 10.1117/3.527861].
14. D. G. Voelz, *Computational Fourier Optics: A MATLAB® Tutorial*, SPIE Press, Bellingham, Washington (2011) [doi: 10.1117/3/858456].
15. F. Gascon and F. Salazar, "A simple method to simulate diffraction and speckle patterns with a PC," *Optik* **117**, 49–57 (2007).
16. D. Mas, J. Garcia, C. Ferreira, and F. Marinho, "Fast algorithms for free-space diffraction patterns calculation," *Opt. Commun.* **164**, 233–245 (1999).
17. P. Ferraro, S. De Nicola, A. Finizio, G. Pierattini, and G. Coppola, "Recovering image resolution in reconstructing digital off-axis holograms by Fresnel-transform method," *Appl. Phy. Lett.* **85**, 2709–2711 (2004).
18. Y. Soskind, *Field Guide to Diffractive Optics*, SPIE Press, Bellingham, Washington (2011) [doi: 10.1117/3.895041].
19. K. Khare and N. George, "Direct coarse sampling of electronic holograms," *Opt. Lett.* **28**, 1004–1006 (2003).
20. A. V. Oppenheim and R. W. Schafer, *Discrete-Time Signal Processing*, Third Edition, Pearson Education Limited, Essex (2014).
21. S. Neeman, "Using MATLAB to illustrate the phenomenon of aliasing," *ASEE Annual Conference Proceedings*, paper 8, Engineering Studies Faculty Publications and Creative Works, (http://scholarsarchive.jwu.edu/engineering_fac/8/?utm_source=scholarsarchive.jwu.edu%2Fengineering_fac%2F8&utm_medium=PDF&utm_campaign=PDFCoverPages) (1995).
22. L. Onural, "Exact analysis of the effects of sampling of the scalar diffraction field," *J. Opt. Soc. Am. A* **24**, 359–367 (2007).
23. S. Trester, "Computer-simulated Fresnel holography," *Eur. J. Phys.* **21**, 317–331 (2000).
24. http://www.ni.com/tutorial/4880/en/
25. J.-P. Liu, "Controlling the aliasing by zero-padding in the digital calculation of the scalar diffraction," *J. Opt. Soc. Am. A* **29**, 1956–1964 (2012).
26. E. Hecht, *Optics*, Fourth Edition, Addison Wesley, San Francisco (2002).
27. R. J. Collier, C. B. Burkhardt, and L. H. Lin, *Optical Holography*, Academic Press, San Diego (1971).
28. S. Bhattacharya and R. S. Sirohi, "Amplitude checker grating from one-dimensional Ronchi grating and its application to array generation," *Appl. Opt.* **36**, 3745–3752 (1997).
29. O. Marchenko and S. Kazantsev, *Demonstrational Optics: Part 2: Coherent and Statistical Optics*, Springer, New York (2007).

Downloaded From: https://www.spiedigitallibrary.org/ebooks/ on 27 Feb 2022
Terms of Use: https://www.spiedigitallibrary.org/terms-of-use

30. J. Sun, A. K. Srivastava, L. Wang, V. G. Chigrinov, and H. S. Kwok, "Optically tunable and rewritable diffraction grating with photoaligned liquid crystals," *Opt. Lett.* **38**, 2342–2344 (2013).
31. T. K. Chong, J. Wilson, S. Mokkapati, and K. R. Catchpole, "Optimal wavelength scale diffraction gratings for light trapping in solar cells," *J. Opt.* **14**(2), 024012 (2012).
32. J. Gjessing, E. S. Marstein, and A. Sudbø, "2D back-side diffraction grating for improved light trapping in thin silicon solar cells," *Opt. Express* **18**, 5481–5495 (2010).
33. A. Fedotowsky and K. Lehovec, "Far field diffraction patterns of circular gratings," *Appl. Opt.* **13**, 2638–2642 (1974).
34. L. L. Doskolovich, S. N. Khonina, V. V. Kotlyar, I. V. Nikolsky, V. A. Soifer, and G. V. Uspleniev, "Focusators into a ring," *Opt. Quant. Electron.* **25**, 801–814 (1993).
35. Z. Kuang, W. Perrie, S. P. Edwardson, E. Fearon, and G. Dearden, "Ultrafast laser parallel microdrilling using multiple annular beams generated by a spatial light modulator," *J. Phys. D: Appl. Phys.* **47**, 115501 (2014).
36. L. Rayleigh, "Wave Theory," *Encylopaedia Brittanica* **24**, Ninth Edition (1889).
37. H. H. Barrett, D. T. Wilson, G. D. DeMeester, and H. Scharfman, "Fresnel zone plate imaging in radiology and nuclear medicine," *Opt. Eng.* **12**(1), 120108 (1973) [doi: 10.1117/12.7971622].
38. J. Kirz, "Phase zone plates for x rays and the extreme UV," *J. Opt. Soc. Am.* **64**, 301–309 (1974).
39. W. Chao, J. Kim, S. Rekawa, P. Fischer, and E. H. Anderson, "Demonstration of 12 nm resolution Fresnel zone plate lens based soft x-ray microscopy," *Opt. Express* **17**, 17669–17677 (2009).
40. K. Iizuka, *Springer Series in Optical Sciences: Engineering Optics*, Third Edition, Springer, New York (2008).
41. J. J. Snyder, P. Reichert, and T. M. Baer, "Fast diffraction-limited cylindrical microlenses," *Appl. Opt.* **30**, 2743–2747 (1991).
42. Q. Gao and X. Zeng, "Beam collimation of the laser diode with a heteroaxial double half-elliptical cylinder lens," *Optoelectron. Lett.* **6**, 435–438 (2010).
43. R. Grunwald, U. Griebner, F. Tschirschwitz, E. T. J. Nibbering, T. Elsaesser, V. Kebbel, H.-J. Hartmann, and W. Jüptner, "Generation of femtosecond Bessel beams with microaxicon arrays," *Opt. Lett.* **25**, 981–983 (2000).
44. R. Grunwald, U. Griebner, E. T. J. Nibbering, A. Kummrow, M. Rini, T. Elsaesser, V. Kebbel, H.-J. Hartmann, and W. Jüptner, "Spatially resolved small-angle noncollinear interferometric autocorrelation of ultrashort pulses with microaxicon arrays," *J. Opt. Soc. Am. A* **18**, 2923–2931 (2001).

Downloaded From: https://www.spiedigitallibrary.org/ebooks/ on 27 Feb 2022
Terms of Use: https://www.spiedigitallibrary.org/terms-of-use

Chapter 3
Design and Analysis of Advanced Diffractive Optical Elements

In Chapter 2, we discussed how to design some basic DOEs, such as binary phase gratings, amplitude gratings, and FZPs, as well as how to simulate their far-field diffraction patterns. In this chapter, the discussion has been extended to multilevel and grayscale DOEs. In the previous chapter, designing DOEs for generation of a few interesting phase profiles such as 2×2, 3×3 spots with desired intensity ratios were presented. In this chapter, we present the procedure for designing DOEs that generate any desired intensity profile using the well-known iterative Fourier transform algorithm (IFTA).

3.1 Design of Multilevel and Grayscale DOEs

In Chapter 2, the design and analysis of both binary amplitude and phase DOEs were presented. Due to the poor efficiency of amplitude DOEs, they are not used in commercial systems. DOEs are, however, very useful in educational applications to demonstrate the effects of diffraction. They can easily be fabricated on transparency sheets using inkjet printers, and their diffraction patterns can be studied using low-cost diode lasers. Although binary phase elements have higher efficiency than amplitude ones, the efficiency is still not adequate. Except for the binary axicon, binary phase elements can have a maximum efficiency of only 40%. In order to achieve high efficiencies (>90%) on par with ROEs, multilevel or grayscale versions of DOEs are necessary. Unfortunately, such elements are rather difficult to fabricate.

3.1.1 Design procedure for multilevel and grayscale gratings

In Chapter 1, the resemblances between the behavior of a ROE and DOE were presented. Grayscale DOEs are nothing but miniature versions of

Downloaded From: https://www.spiedigitallibrary.org/ebooks/ on 27 Feb 2022
Terms of Use: https://www.spiedigitallibrary.org/terms-of-use

equivalent ROEs as presented in Chapter 1. Multilevel DOEs are designed to generate a shape as close as possible to that of an equivalent ROE to achieve high efficiency. Binary phase gratings are symmetric, resulting in equal intensity values for both $\pm m$ orders. In the case of multilevel and blazed gratings, the grating's phase profile is asymmetric, directing most of the light to either the +1 or the –1 diffraction order.[1–3] The efficiency of light in the first diffraction order depends on the number of steps used to construct the phase profile. The efficiency of the m^{th} diffraction order from a grating with g levels is given by[3]

$$\eta_m^g = \left| \frac{\sin\left(\frac{m\pi}{g}\right)}{\frac{m\pi}{g}} \right|^2. \tag{3.1}$$

Hence, from Eq. (3.1), the efficiency of phase gratings with $g = 2$, 4, 8, 16, 32, etc., levels are 41%, 81%, 95%, 99%, and >99%, respectively.

However, the height of each phase level is crucial in achieving the calculated efficiency values. As was done in the binary case, designing the multilevel structure for maximum efficiency will be done by cancelling the 0^{th} diffraction order. Hence, it is necessary to carefully choose the parameters relating to the areas of different phase values in the element.

3.1.1.1 Design of a 4-level 1D phase grating with MATLAB

In the case of a 4-level 1D phase grating, if the phase levels are selected correctly, the maximum efficiency is 81%. The phase levels are selected as shown in Fig. 3.1(a), and the corresponding resist thickness values for $\lambda =$ 633 nm ($n_r = 1.5$) are shown in Fig. 3.1(b). These phase levels were selected with the assumptions that the areas of each phase level are equal, and there is uniform illumination such that they follow $(2\pi/g)q$, where q is the phase level number.[4,5]

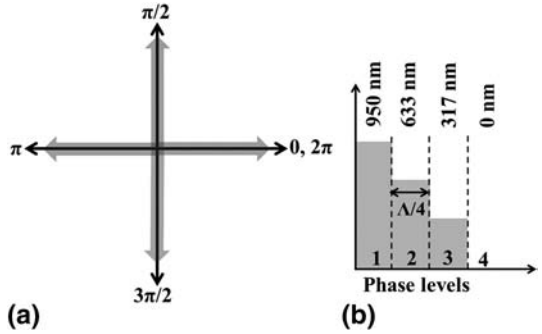

Figure 3.1 (a) Phase values of the 4-level 1D phase grating and (b) their corresponding resist thickness values for $\lambda = 633$ nm.

Downloaded From: https://www.spiedigitallibrary.org/ebooks/ on 27 Feb 2022
Terms of Use: https://www.spiedigitallibrary.org/terms-of-use

Table 3.1 MATLAB code for design and analysis of a 4-level phase grating.

```
%% 4-level 1D grating
clear %Clear all memory
%% Defining grating parameters
    N=500; % Matrix size
    P=100; % Grating period
    A1=ones(P,N); % Size of fundamental building block of grating
    g=4; % Number of phase levels
    delphase= 2*pi/g; %Phase step size
% Constructing one n-level section of the phase grating
sub =round(P/g)-1;
for count = 1:g;
  A1((count -1)*sub+1:count*sub,:)=exp(1i*(count-1)*delphase);
end
%Constructing the full grating
    A2=repmat(A1,N/P,1);
%Observation of the diffraction pattern
%See appendix for function definition
    Norm_outputP(A2, N)
```

The phase values 2π (or 0) and $\pi/2$ have opposite orientations with respect to the phase values π and $3\pi/2$, respectively. Hence, light emanating at these phase levels cancel each other at the 0^{th} diffraction order. Let us verify the efficiency values obtained from Eq. (3.1) with MATLAB simulation. The MATLAB code for design of a 4-level phase grating is shown in Table 3.1.

The profile of the 1D 4-level phase grating and the diffraction spots can be displayed using the standard MATLAB codes presented in Chapter 2. The image of the phase variation of the 1D 4-level phase grating and the zoomed-in figure of the diffraction spots are shown in Figs. 3.2(a) and (b), respectively. By clicking on the diffraction spot using the data cursor of the MATLAB window, the efficiency value can be read as 81%, matching the value calculated using Eq. (3.1). Varying the period of the grating such that the areas of the four levels are not equal will give a lower efficiency value depending upon the discrepancy. In multilevel structures it might be useful to

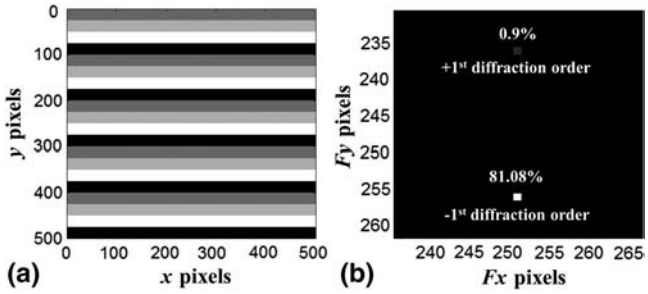

Figure 3.2 (a) Phase profile of a 4-level 1D phase grating generated by the output function. (b) Diffraction spots in the zoomed image.

Downloaded From: https://www.spiedigitallibrary.org/ebooks/ on 27 Feb 2022
Terms of Use: https://www.spiedigitallibrary.org/terms-of-use

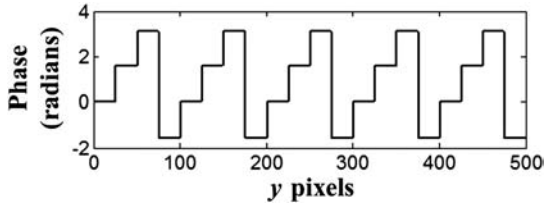

Figure 3.3 Phase profile of a 4-level phase grating plotted across the *y* direction.

plot the phase variation using '`plot(angle(A(:,M/2)))`'. The plot of the phase profile along the *y* direction is shown in Fig. 3.3. The phase value above π radians will be converted into the equivalent negative phase in MATLAB. The selected phase value is 1.5π, but the value displayed in MATLAB is $-\pi/2$, which is equivalent to 1.5π.

3.1.1.2 Design of an 8-level 1D phase grating with MATLAB

The maximum efficiency possible with an 8-level 1D phase grating is 95%. The phase levels were selected with the basic assumption that the areas of the phase levels are equal. The phase levels are selected in steps of $2\pi/g$, where $g = 8$, as shown in Fig. 3.4 and the corresponding resist thickness values for $\lambda = 633$ nm ($n_r = 1.5$) are given in boxes. The MATLAB code for the design of an 8-level 1D phase grating will be identical to that given in Table 3.1, except that the value of g will now be 8 instead of 4.

The code can be easily adapted to any 1D phase grating with a higher number of phase levels. The phase profile of the 8-level 1D phase grating and the zoomed-in figure of the diffraction spots are shown in Figs. 3.5(a) and (b), respectively. The diffraction spot shows an efficiency of 95%, matching the calculated value. The MATLAB code and analysis in Table 3.1 can be extended for simulation and analysis of 1D gratings with higher numbers of phase levels, such as $g = 16$, 32, 64, etc.

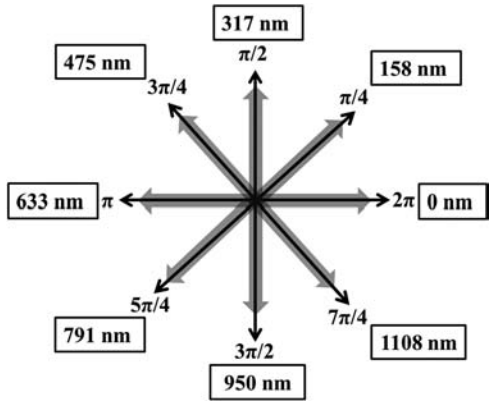

Figure 3.4 Phase values and resist thickness values of an 8-level 1D phase grating.

Downloaded From: https://www.spiedigitallibrary.org/ebooks/ on 27 Feb 2022
Terms of Use: https://www.spiedigitallibrary.org/terms-of-use

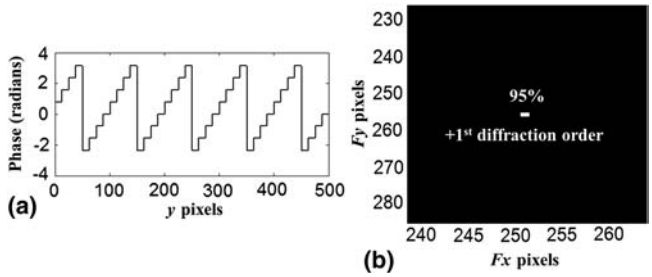

Figure 3.5 (a) Plot of an 8-level 1D phase grating and (b) the zoomed-in diffraction pattern.

3.1.1.3 Design of a blazed 1D phase grating with MATLAB

Blazed 1D phase gratings have a high efficiency of 100%. Such gratings have a linear phase variation from 0 to 2π across the period of the grating. A blazed grating can be considered to be a multilevel grating with large number of phase steps. For example, a grating with a period of 100 μm and a pixel size of 1 μm would have 100 phase levels. The MATLAB code for design of a blazed grating is shown in Table 3.2. The profile of the grating is plotted in Fig. 3.6. The blazed grating is equivalent to a Fresnel prism and, hence, has a high efficiency, which can be verified when running the code and checking the efficiency.

Table 3.2 MATLAB code for design of a blazed phase grating.

```
%%Blazed 1D grating
clear; %Clear all memory
% Defining grating parameters
    N=500; % Matrix size
    P=100; % Grating period
    A1=ones(P,N); % Size of fundamental building block of grating
% Constructing the fundamental block of the blazed grating
for p=1:P;
    A1(p,:)=exp(1i*(p/P)*2*pi);
end
%Constructing the full grating
    A2=repmat(A1,N/P,1);
```

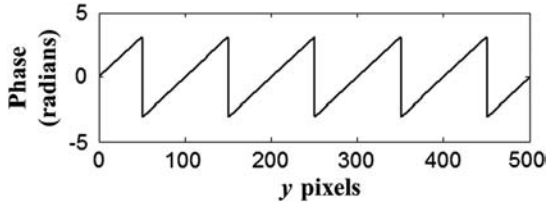

Figure 3.6 Plot of phase profile of a blazed grating.

Downloaded From: https://www.spiedigitallibrary.org/ebooks/ on 27 Feb 2022
Terms of Use: https://www.spiedigitallibrary.org/terms-of-use

Table 3.3 MATLAB code for design of a 8-level diffractive axicon.

```
%% 8-level axicon
clear; %Clear all memory
%Defining axicon parameters
    N=480; % Matrix size
    A=zeros(N,N);
    P=40; % Grating period
    g=8; %Define the number of phase levels in each period
    w=P/g; %Define the width of each phase levels
    delphase=2*pi/g;
%Constructing the 8-level axicon
    x=1:N;
    y=1:N;
    [X,Y]=meshgrid(x,y);
    r=sqrt((X-N/2).*(X-N/2)+(Y-N/2).*(Y-N/2));
for n=1:g;
  A(rem(r+(n-2)*w,P)<P/g)=exp(1i*(w-(n))*delphase);
end
  A(r>N/2)=0;
```

3.1.1.4 Design of an 8-level axicon with MATLAB

In the discussion in Chapter 2 on binary axicons,[6,7] it was observed that the efficiency of a binary axicon is approximately 50%, which is relatively high to start with. In order to improve the efficiency, we therefore begin with an 8-level axicon. The expected efficiency of the 8-level axicon is 95%. The MATLAB code for the design of an 8-level axicon is shown in Table 3.3. The codes were designed to be easily extendable to other higher numbers of phase levels. The phase profile of the 8-level axicon and the zoomed-in diffraction pattern are shown in Figs. 3.7(a) and (b), respectively. It can be noted that the 0^{th} diffraction order is not cancelled completely due to the unequal areas of different phase levels. Summation of the pixels around the ring pattern shows an efficiency of 93%, which is close to the calculated value of 95%.

3.1.1.5 Design of a blazed axicon with MATLAB

Blazed axicons are designed with phase values varying between 0 and 2π. The expected efficiency is 100%. The MATLAB code for design of a blazed axicon

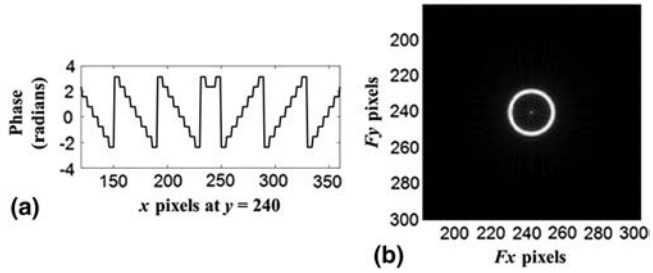

Figure 3.7 (a) Phase profile of the 8-level axicon and (b) its diffraction pattern.

Downloaded From: https://www.spiedigitallibrary.org/ebooks/ on 27 Feb 2022
Terms of Use: https://www.spiedigitallibrary.org/terms-of-use

Table 3.4 MATLAB code for design of a blazed axicon.

```
%%Blazed axicon
clear;%Clear all memory
%Define axicon parameters
    N=500; % Matrix size
    P=100; % Grating period
    A=ones(N,N); % Set up matrix, assigning 1's to all pixels
%Constructing the blazed axicon
    x=1:N;
    y=1:N;
    [X,Y]=meshgrid(x,y);
    r=sqrt((X-N/2).*(X-N/2)+(Y-N/2).*(Y-N/2));
    A=exp(1i*(rem(r,P))*(2*pi)/P);
    A(r>N/2)=0;
```

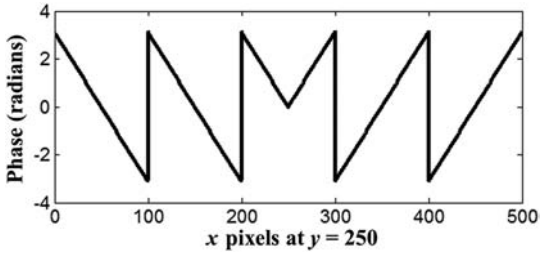

Figure 3.8 Plot of phase profile of a blazed axicon.

is given in Table 3.4. The phase profile of the blazed grating is shown in Fig. 3.8. The diffraction pattern is a ring pattern, and the efficiency was measured to be 98%, which is close to the expected 100%. The phase profile in the figure may seem incorrect, but, as discussed earlier, in MATLAB, phase values above π will be converted to a negative phase, resulting in a phase profile range $[-\pi, \pi]$.

3.1.2 Design procedure for multilevel and grayscale FZPs

Fresnel zone plates are used for focusing light at a point. In Chapter 2, the design and analysis of a binary FZP was presented. The efficiency of a binary FZP is limited to only 40%; hence, for any real application, multilevel or grayscale versions of the FZP are preferred. The design of a grayscale FZP[8–10] is relatively simple, as the phase profile can be directly generated using the following equation [which is similar to Eq. (2.11)]:

$$\sqrt{f^2 + r^2} - f = n\lambda, \tag{3.2}$$

where f is the focal length of the FZP, and λ is the wavelength. The phase profile is given by

Downloaded From: https://www.spiedigitallibrary.org/ebooks/ on 27 Feb 2022
Terms of Use: https://www.spiedigitallibrary.org/terms-of-use

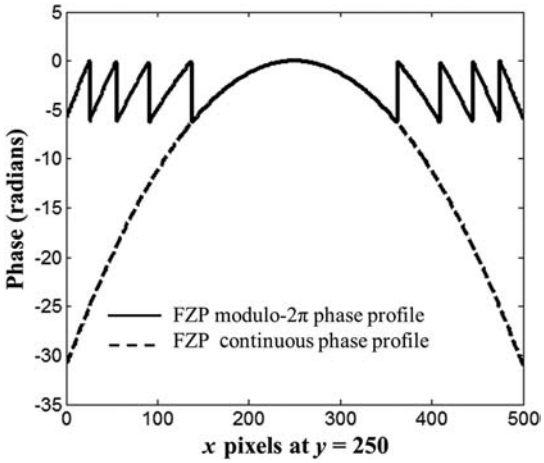

Figure 3.9 Phase profile of a FZP (a) before (dashed line) and (b) after discretizing into modulo-2π zones (solid line).

$$\Phi_{\mathrm{FZP}}(r) = \left[\frac{2\pi}{\lambda}\left(\sqrt{f^2 + r^2} - f\right)\right]_{2\pi}. \tag{3.3}$$

The modulo-2π operation converts the continuous phase profile of FZP into discrete zones whose phase variation lies between [0, 2π]. The plot of the continuous phase profile and the FZP phase profile are shown in Fig. 3.9.

The design and fabrication of a multilevel FZP[11,12] is challenging compared to the gratings described earlier because the periods of the FZP gradually decrease as one moves away from the center. This results in more closely spaced phase levels at the outermost parts of the FZP. Even within a zone of a FZP, the widths of the phase levels decrease away from the center.

3.1.2.1 MATLAB simulation of a blazed FZP

The MATLAB code for the simulation of a blazed FZP is shown in Table 3.5. The modulo-2π phase profile of the FZP is designed using Eq. (3.3).

Table 3.5 MATLAB code for design of a blazed FZP.

```
%% Blazed FZP
clear; %Clear all memory
% Defining FZP parameters
    N=500; % Matrix size
    f=10000; % focal length in microns
    lambda=0.632; % Wavelength in microns
% Constructing the blazed FZP
    x=1:N;
    y=1:N;
    [X,Y]=meshgrid(x,y);
    r=sqrt((X-N/2).*(X-N/2)+(Y-N/2).*(Y-N/2));
    A=exp(1i*(f-sqrt(f*f+r.*r))*(2*pi)/(0.632));
    A(r>N/2)=0;
```

Downloaded From: https://www.spiedigitallibrary.org/ebooks/ on 27 Feb 2022
Terms of Use: https://www.spiedigitallibrary.org/terms-of-use

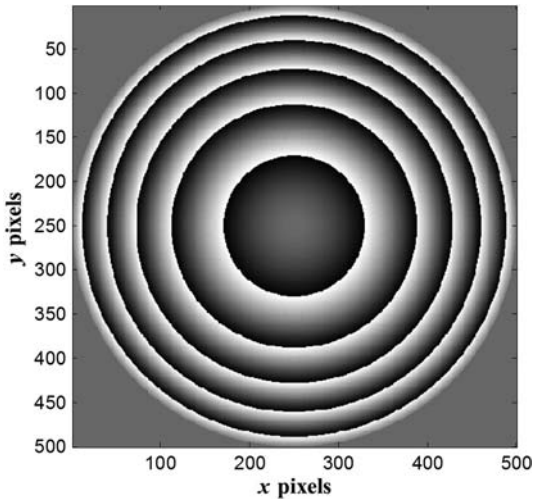

Figure 3.10 Image of the phase profile of a blazed FZP generated using MATLAB.

The image of the phase profile of the FZP is shown in Fig. 3.10. The code can be modified for an elliptical FZP, as presented in Chapter 2, by stretching either the x or the y coordinate with respect to the other.

3.1.2.2 MATLAB simulation of a four-level FZP

A 4-level FZP can be designed for the phase values 0, $\pi/2$, π, and $3\pi/2$, as was done for the 1D phase grating. But due to the circular nature of this element, the area of each segment varies. However, the phase profile of the FZP is not linear like a grating's phase profile, resulting in unequal widths of the different phase levels. The MATLAB code for design of a 4-level FZP is given in Table 3.6. The phase profiles of a 4-level FZP and a blazed FZP are shown in Fig. 3.11. Once again, the profiles seem different because the range of phase values in MATLAB are brought within $[-\pi, \pi]$. This procedure may be extended to the design and simulation of 8- and 16-level FZPs.

3.1.3 Design procedure for multilevel and grayscale spiral phase plates

Spiral phase plates (SPPs) are used for the generation of beams with helical wavefronts.[13,14] The phase profile of a SPP varies along the azimuthal direction. When a plane wavefront is incident on a SPP, it delivers a spiral phase lag to the wavefront, resulting in a helical wavefront and a donut intensity profile.[15] Helical wavefronts can be generated using different types of DOEs.[16–19]

Due to their azimuthal variation, SPPs are relatively difficult to fabricate but can provide a high efficiency close to 100%. SPPs are characterized by a term called the topological charge of the element, which is usually denoted by

Downloaded From: https://www.spiedigitallibrary.org/ebooks/ on 27 Feb 2022
Terms of Use: https://www.spiedigitallibrary.org/terms-of-use

Table 3.6 MATLAB code for design of a 4-level FZP.

```
%% 4-level FZP
clear;%Clear all memory
%Define FZP parameters
    N=500; % Matrix size
    f=10000; % Focal length in microns
    lambda=0.632;% Wavelength in microns
    g=4; % Number of phase levels
    step=(2*pi)/g;
% Set up matrices, assigning 0's or 1's to all pixels
C=ones(N,N);
% Constructing the FZP
    x=1:N;
    y=1:N;
    [X,Y]=meshgrid(x,y);
    r=sqrt((X-N/2).*(X-N/2)+(Y-N/2).*(Y-N/2));
    A=(f-sqrt(f*f+r.*r))*(2*pi)/(0.632);
    B=rem(A,2*pi);
    B(r>N/2)=0;
for p=1:N;%Construct the n-level FZP
  for q=1:N;
    for n1=1:g;
      if B(p,q)> (-2*pi+(n1-1)*step) && B(p,q) <= (-3*pi/2+
      (n1-1)*step);
        C(p,q)=exp(1i*(-2*pi+(n1-1)*pi/2));
      end
    end
  end
end
```

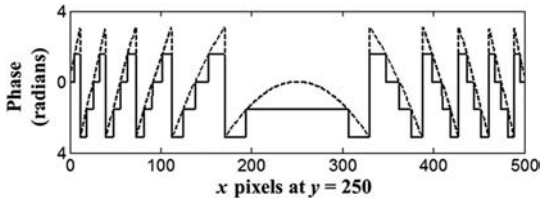

Figure 3.11 Phase profile of (a) a blazed FZP (dashed line) and its (b) 4-level approximation (solid line).

L and represents the number of spiral cycles the beam makes within a distance of the wavelength of light λ. The charge L equals 1, 2, 3, … p, depending on whether the beam's phase varies by 2π, 4π, 6π, … $2p\pi$ along the distance λ. The diameter of the donut beam increases with increasing topological charge value.[20,21] Recently, SPPs with fractional topological charges have attracted attention due to their generated asymmetric donut patterns, which are useful for optical trapping applications.[22–24]

When a plane wave is incident on the SPP, it generates a helical beam with a number of azimuthal rotations matching L. The fabrication of a grayscale

Downloaded From: https://www.spiedigitallibrary.org/ebooks/ on 27 Feb 2022
Terms of Use: https://www.spiedigitallibrary.org/terms-of-use

SPP is a challenge; hence, in most cases, only multilevel SPPs have been designed and fabricated.[20,21] The design of such elements is similar to that of gratings except that the multiple levels are made along the azimuthal direction. The phase profile of a SPP with topological charge L is given by

$$\Phi_{\mathrm{SPP}}(\theta) = [L\theta]_{2\pi}. \tag{3.4}$$

The phase step size of a multilevel SPP with g phase levels is given by

$$\Delta\Phi_{\mathrm{SPP}}(\theta) = \left(\frac{2\pi}{g}\right)L. \tag{3.5}$$

The phase profile of a multilevel SPP can be expressed as

$$\Phi_{\mathrm{SPP}}(\theta) = \Delta\Phi \ \mathrm{floor}\left[\frac{g}{2\pi}\theta\right]. \tag{3.6}$$

3.1.3.1 MATLAB simulation of a grayscale SPP

The MATLAB code for the design of a grayscale SPP is shown in Table 3.7. The SPP is designed with a radius of 30 pixels in this case to magnify the diffraction pattern. The images of the phase profile of SPPs with $L = 1$ are shown in Fig. 3.12.

The SPP has been designed for $L = 1$, 2, 3, and 4. The donut patterns generated by a SPP with $L = 1$, 2, 3, and 4 are shown in Figs. 3.13(a)–(d), respectively. It can clearly be seen that the diameter of the donut beam increases with the increasing L value.

The MATLAB code can be easily extended to other higher phase levels as well as for fractional topological charges[23,24] by modifying the value of L.

Table 3.7 MATLAB code for the design of a grayscale SPP.

```
%Grayscale SPP
clear; %Clear all memory
%Defining SPP parameters
    N=500; % Matrix size
    L=1;% Topological charge number
%Constructing the SPP
    x=1:N;
    y=1:N;
    [X,Y]=meshgrid(x,y);
    theta=atan2((X-N/2),(Y-N/2));
    r=sqrt((X-N/2).*(X-N/2)+(Y-N/2).*(Y-N/2));
    A1=exp(1i*L*(theta));
    A1(r>30)=0;
%Observation of the far-field pattern
    E=fftshift(fft2(A1)); %Calculate the Fourier transform and
    rearrange terms
    I=abs(E).*abs(E);
```

Downloaded From: https://www.spiedigitallibrary.org/ebooks/ on 27 Feb 2022
Terms of Use: https://www.spiedigitallibrary.org/terms-of-use

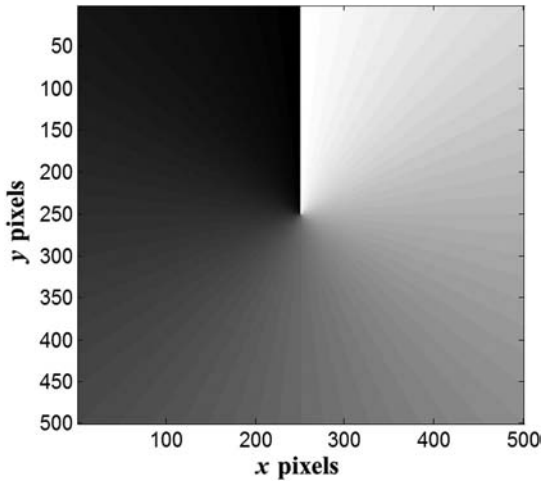

Figure 3.12 Image of the phase profile of a grayscale SPP with $L = 1$.

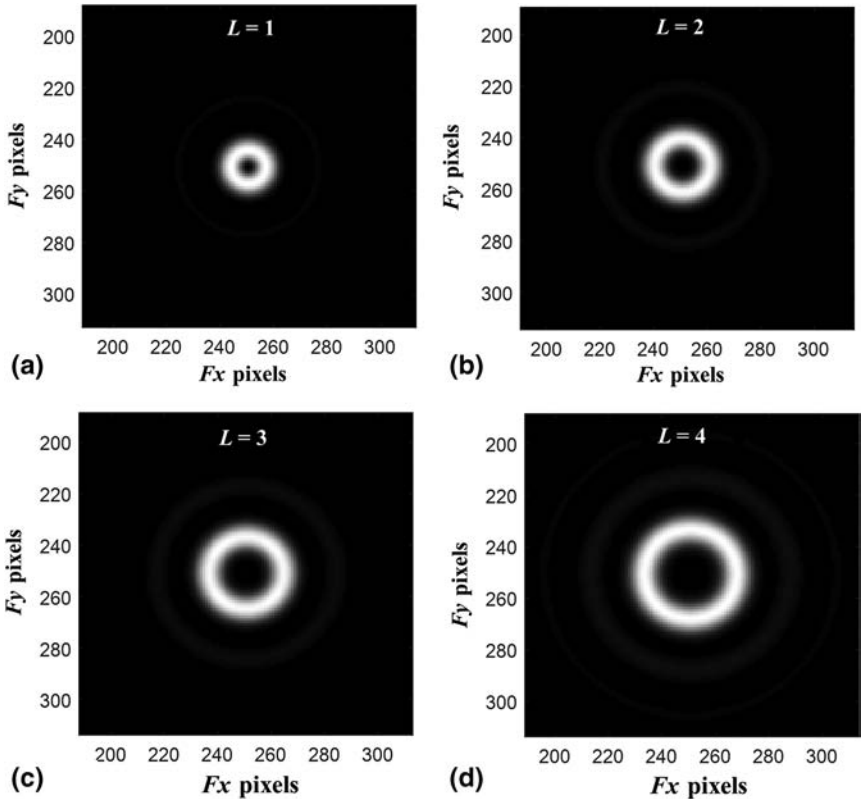

Figure 3.13 Image of the donut patterns generated for (a) $L = 1$, (b) $L = 2$, (c) $L = 3$, and (d) $L = 4$.

Downloaded From: https://www.spiedigitallibrary.org/ebooks/ on 27 Feb 2022
Terms of Use: https://www.spiedigitallibrary.org/terms-of-use

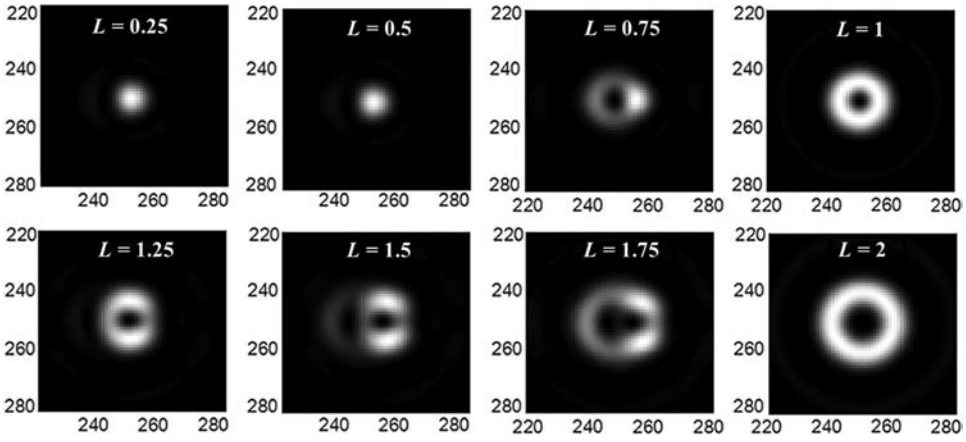

Figure 3.14 Diffraction patterns of spiral phase plates with topological charges $L = 0.25$ to 2 in steps of 0.25.

The images of the asymmetric donut beams generated for $L = 0.25$, 0.5, 0.75, 1, 1.25, 1.5, 1.75 and 2 are shown in Fig. 3.14.

3.1.3.2 MATLAB simulation of a multilevel SPP

The phase profile of a multilevel SPP can be described by Eq. (3.6). The MATLAB code for design of a 4-level SPP is given in Table 3.8. The images

Table 3.8 MATLAB code for design of a multilevel SPP.

```
%Multilevel SPP
clear;%Clear all memory
%Define SPP parameters
    N=500; % Matrix size
    L=1; % Topological charge number
    g=5; % Number of phase levels
    delphase=(L*2*pi)/g; % Phase increment
% Constructing the SPP
    x=1:N;
    y=1:N;
    [X,Y]=meshgrid(x,y);
    theta=atan2((X-N/2),(Y-N/2));
    r=sqrt((X-N/2).*(X-N/2)+(Y-N/2).*(Y-N/2));
    A1=L*(theta)+L*pi;
    A1(r>30)=0;
for n=1:g;
  for p=1:N;
    for q=1:N;
      if A1(p,q) > (delphase*(n-1)) && A1(p,q) <= (delphase*n)
        A1(p,q) = exp(1i*delphase*(n-1));
      end
    end
  end
end
```

Downloaded From: https://www.spiedigitallibrary.org/ebooks/ on 27 Feb 2022
Terms of Use: https://www.spiedigitallibrary.org/terms-of-use

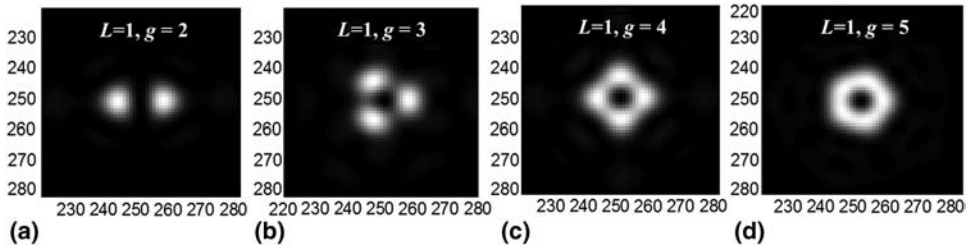

Figure 3.15 Diffraction patterns of spiral phase plates with topological charge $L = 1$ and phase levels (a) $g = 2$, (b) $g = 3$, (c) $g = 4$, and (d) $g = 5$.

of the diffraction patterns corresponding to charge $L = 1$ and phase levels $g = 2$, 3, 4, and 5 are shown in Figs. 3.15(a)–(d), respectively.[25] The number of phase levels can be varied by changing the variable g in the code.

3.1.4 Design procedure for a gradient axilens

An axilens, as the name suggests, is a DOE that is intermediate between a lens and an axicon. The design of a holographic axilens was first reported in 1991 by Davidson et al.[26] The axilens was found to possess interesting focusing properties[27] that are useful for different applications.[28,29] In the case of an axicon, the focal depth extends from the location of the axicon to a particular distance. It is difficult to make use of the section of the focal region in the vicinity of the axicon in many applications, including imaging. In the case of a lens, the focal depth is short. In the case of an axilens, the focal depth and its location can be precisely engineered, making it superior to both a lens and an axicon in many applications.

The optics configuration for focusing light using an axilens in the finite conjugate mode is shown in Fig. 3.16. Unlike a FZP, which has a single focal length associated with it, an axilens has a radially dependent focal length, given by

$$f(r) = f_0 + \left(\frac{\Delta f}{R}\right) r, \tag{3.7}$$

where f_0 is the focal length, Δf is the focal depth, and R is the radius of the element. The phase profile of an axilens can be then given by

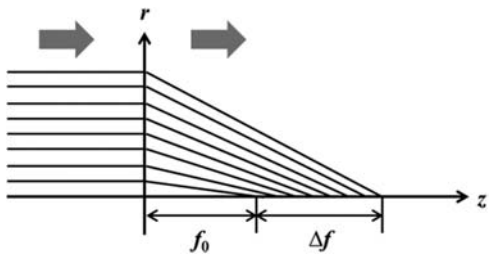

Figure 3.16 Optics configuration for focusing a plane wavefront using an axilens.

Downloaded From: https://www.spiedigitallibrary.org/ebooks/ on 27 Feb 2022
Terms of Use: https://www.spiedigitallibrary.org/terms-of-use

Table 3.9 MATLAB code for design of a blazed axilens.

```
%% Blazed axilens
clear; % Clear all memory
% Define axilens parameters
% All lengths in microns
    N=500; % Matrix size
    f0=5000;% focal length
    delf=1000;% focal depth
    R=1000;% radius of the element
    lambda=0.632;% wavelength
%Constructing the axilens
    x=1:N;
    y=1:N;
    [X,Y]=meshgrid(x,y);
    r=sqrt((X-N/2).*(X-N/2)+(Y-N/2).*(Y-N/2));
    f=f0+(delf/R)*r; % Focal length equation
    A=(f-sqrt(f.*f+r.*r))*(2*pi)/(0.632);
    B=exp(1i*rem(A,2*pi));
    B(r>N/2)=0;
```

$$\Phi_{Axilens}(r) = \left\{ \frac{2\pi}{\lambda} \left[\sqrt{f(r)^2 + r^2} - f(r) \right] \right\}_{2\pi}. \tag{3.8}$$

The MATLAB code for design of a blazed axilens is given in Table 3.9. The element was designed with $f_0 = 5$ mm, $\Delta f = 1$ mm, and radius $R = 1$ mm. The image and phase profile of an axilens are shown in Figs. 3.17(a) and (b), respectively.

3.2 Design of DOEs using Algorithms

Chapter 2 and the first section of Chapter 3 introduced methods and codes that can be used to design DOEs that generate some specific intensity patterns and required efficiency values. However, these methods cannot be applied to the design of DOEs that generate any arbitrary intensity profile at the Fourier

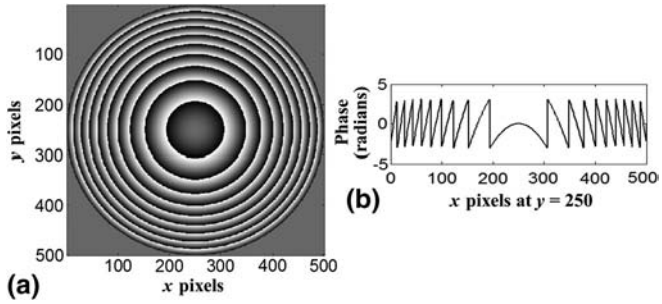

Figure 3.17 (a) Image and (b) plot of the phase profile of an axilens.

Downloaded From: https://www.spiedigitallibrary.org/ebooks/ on 27 Feb 2022
Terms of Use: https://www.spiedigitallibrary.org/terms-of-use

plane. In order to do so, algorithms such as the Gerchberg–Saxton algorithm, also known as the inverse Fourier transform algorithm,[30] are used. In this section, the IFTA is presented with MATLAB codes. Other algorithms such as the optimal rotation angle method,[31] the adaptive weight iterative algorithm,[32] etc., can also be used for the design of arbitrary-intensity DOEs.

3.2.1 Design procedure of DOEs using the IFTA

The idea of the IFTA and similar algorithms is to use known input information at the source plane and calculate the (grayscale) phase of a DOE that will generate a desired intensity pattern at the target plane. The algorithm alternates between the source and target planes using the Fourier and inverse Fourier transform operations. This process is iteratively repeated until the target image is met, as quantified by some predefined metric. The inverse Fourier transform of the required intensity profile will result in amplitude and phase profiles that do not match the actual input at the source plane. Therefore, as the algorithm progresses, the amplitude profile generated by the Fourier and inverse Fourier transform operations will be replaced by the input source and desired target amplitudes at the respective planes.

A flow chart of the algorithm is given in Fig. 3.18. A random phase profile is generated at the source plane, while the amplitude at the same plane is considered to be either Gaussian or uniform. This phase–amplitude profile is Fourier transformed, and the corresponding phase values are extracted. The extracted phase values are assigned to the corresponding pixel locations of the necessary target intensity profile, and its inverse Fourier transform is calculated. The resulting phase profile replaces the phase profile at the source plane. This is one cycle or iteration. The accuracy of the phase profile

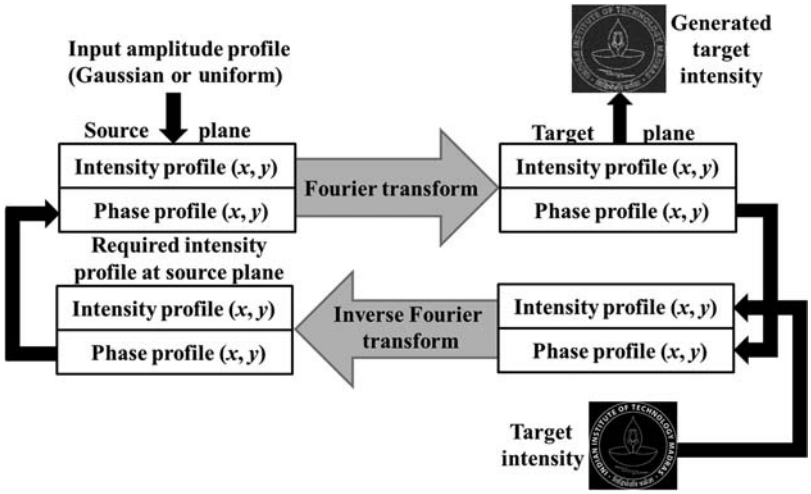

Figure 3.18 Flow chart of the IFTA.

Downloaded From: https://www.spiedigitallibrary.org/ebooks/ on 27 Feb 2022
Terms of Use: https://www.spiedigitallibrary.org/terms-of-use

calculation increases with the number of iterations until it reaches a constant value. The number of iterations may be reduced by proper choice of the initial phase profile. However, an initial constant phase profile will fail the algorithm because the intensity patterns at the source and target planes are centrosymmetric.

For demonstration purposes, the image of the logo of our institution, Indian Institute of Technology Madras, is selected and inverted to have a black background. The image is then resized to fit into the defined matrix. This is followed by a normalization step that sets the amplitude values between 0 and 1. Then the procedure described above is followed in steps. The metric chosen is the difference between the normalized intensity profile generated by the calculated phase profile and the desired intensity profile required at the target plane. The MATLAB code for the IFTA is shown in Table 3.10. The images of the logo generated using the IFTA after 10

Table 3.10 MATLAB code for implementing the IFTA.

```
%% Iterative Fourier Transform Algorithm%
clear; % Clear all memory
% Loading the target image
    N=500;% Matrix size
    target=imread('File location'); % Read image from file
    m=size(target,1); % Size of the image
    scale=N/m; % Estimate the necessary scaling factor
    target=imresize(target,scale); % Resize image to the matrix
    %size
    target=double(target); % Convert symbolic object to a numeric
    %object
    target=target/(max(max(target))); % Normalize matrix
% Defining DOE phase
    DOE=2*pi*rand(N,N); % Generate a N x N matrix of random phase
    %between 0 and 2π
    s=5;
% IFTA algorithm
for t=1:s; %Iterate to calculate the phase value
  DOEphase=exp(1i*DOE);
% Forward iteration
  iterf=fft2(DOEphase);
  intf=abs(iterf);
  angf=angle(iterf);
  A=target.*exp(1i*angf);
% Backward iteration
  iterb=ifft2(A);
  angb=angle(iterb);
  DOE=angb;
  error=target-intf/max(max(intf)); %Calculate error
  E=sum(sum(abs(error)))/(N*N);
  if E<0.05;
    iteration=t;
    break
  end
end
```

Downloaded From: https://www.spiedigitallibrary.org/ebooks/ on 27 Feb 2022
Terms of Use: https://www.spiedigitallibrary.org/terms-of-use

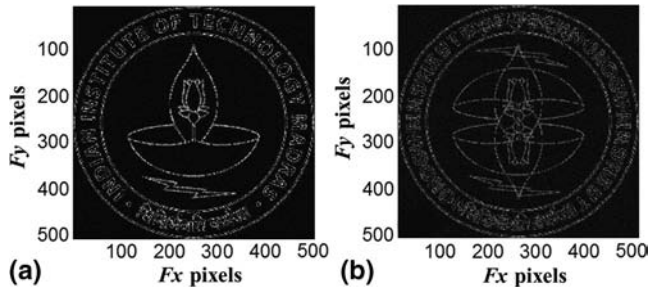

Figure 3.19 Images of the logo generated from (a) a grayscale DOE and (b) a binary DOE.

iterations before and after binarization of the phase profile are shown in Figs. 3.19(a) and (b), respectively. The loop termination can be specified by the number of iterations or by the average error between the ideal and iterated images.

In Fig. 3.19(b), twin images of the logo are formed as the DOE has centrosymmetric support.[33] The twin image is flipped along both the horizontal and vertical direction, as expected. The lateral shift is not seen because the object is aligned with the optical axis. If an object that is not collinear with the optical axis is used, the twin image will occur laterally shifted along the horizontal and vertical directions. The twin image can be removed by approximating the grayscale DOE with a 4-level DOE or with a higher number of phase levels. The problem of twin images arises in many different fields. Research is still ongoing in this area, and several ways of removing one of the twin images have been reported.[34–37] Higher diffraction orders can be seen by zero padding the image and calculating the phase using the algorithm. However, the efficiency of these higher orders is poor (only 4.5% distributed over the entire image).[38]

Although the IFTA and similar algorithms are very powerful (they can be used to create DOES that generate almost any intensity pattern), their main problem is that there is no specific phase relationship from one pixel to another. This leads to scattering and, hence, an overall decrease in efficiency and contrast of the final image.

Alternate techniques that avoid these problems can be used at least for generation of specific intensity profiles. One such technique is described in the next section.

3.3 Design Procedure of Beam-Shaping DOEs using a Simplified Mesh Technique

In order to avoid the scattering caused by the random phase variation across the element, the calculated phase distribution should be continuous.[39] Such a distribution can be achieved by the finite element method. Eikonal equations

Downloaded From: https://www.spiedigitallibrary.org/ebooks/ on 27 Feb 2022
Terms of Use: https://www.spiedigitallibrary.org/terms-of-use

are used to connect the input beam with the desired output beam. The fundamental postulate of geometric optics is the Eikonal equation:[40]

$$(\nabla S)^2 = n^2, \tag{3.9}$$

where n is the refractive index. The surfaces $S(\mathbf{r}) = \text{constant}$ are called the geometrical wavefronts. Geometrical light rays are perpendicular to the wavefronts and indicate the direction of flow of energy. Initially, the areas over the incident and output beams are divided into a mesh, i.e., a number of zones of equal power. The input and output mesh nodes are connected using Eikonal equations. The phase distribution required to produce the desired output is obtained by solving these equations.[41]

The basic idea of this technique is that the energy in each zone in the input plane is redirected to a similarly located zone in the output plane. Since the equations are solved simultaneously for the entire DOE, the obtained phase is continuous.

3.3.1 Mesh generation method

The complexity of the mesh generation technique depends greatly on the intensity distribution over which the mesh is being created. In the case of a circular symmetric Gaussian beam, mesh generation is fairly simple, as the inherent symmetry of the beam is used to generate it. Initially, the power over the entire beam is calculated as

$$P_{TOT} = \pi \frac{w_0^2}{2} I_0, \tag{3.10}$$

where w_0 is the beam waist of the Gaussian beam, and I_0 is the on-axis intensity. Therefore, the power in a circle of radius r is

$$P_r = \left[1 - \exp\left(-2\frac{r^2}{w_0^2}\right)\right] P_{TOT}. \tag{3.11}$$

The beam is then split into a number of rings of equal power. If there are n_1 (= I/2) rings, the power in each ring will be P_r/n_1. Normalizing the power such that $P_{TOT} = 1$, the radius of the n^{th} ring is given by

$$r_n = w_0 \sqrt{\frac{1}{2} \ln\left(\frac{1}{1 - nP_r/n_1}\right)}, \tag{3.12}$$

where, n varies from 1 to n_1. Figure 3.20 shows a Gaussian beam with annular rings of equal power. [This is the output curve obtained as '`figure(2)`' in the MATLAB code given in Table 3.11.] These rings will eventually form part of the mesh and, hence, are plotted only from the starting node to the final node, which is the reason for the apparent gap near 0 on the y axis.

Downloaded From: https://www.spiedigitallibrary.org/ebooks/ on 27 Feb 2022
Terms of Use: https://www.spiedigitallibrary.org/terms-of-use

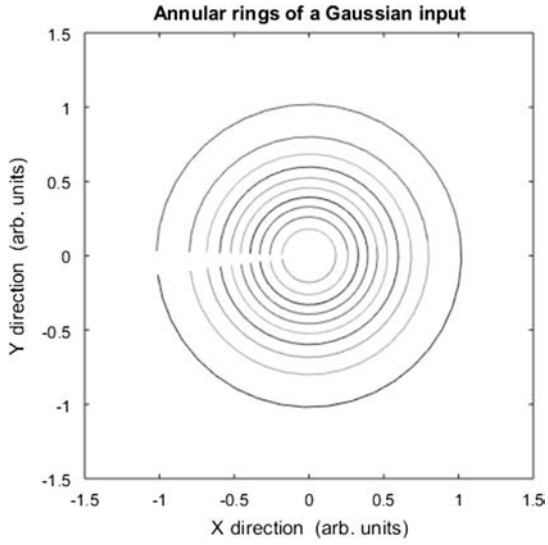

Figure 3.20 Creating the input mesh. Step One: annular rings (reprinted from Ref. 41).

Table 3.11 Creating the input mesh for the Eikonal technique when the incident light is Gaussian.

```
%program creates a mesh of zones of equal energy for a Gaussian
%beam
%mesh is rotated away from axes to avoid zeros
    clear all
    close all
    % all units in mm
    global I J R xh yh sigma
    sigma=0.8; % Gaussian spot size
    R=1; % radius of beam
    %mesh co-ordinates
    I=20; %related to rows and therefore also to y coords
    J=20; %related to columns and therefore also to x coords
    N=(I*J); %total number of zones
    TP=pi*sigma*sigma/2; %total power
    P=(1-exp(-2*R*R/(sigma*sigma)))*TP; %total power in radius R
    rings=I/2; %no of rings
    Pring=P/rings; %Power per ring
%calculating radii of rings
    n=1:rings;
    r=sigma*sqrt(0.5*log(1./(1-n.*Pring)));
%%add very small value for first ring (close to zero)
rad(1)=1e-10;
    i=1:n(end);
    rad(i+1)=r(i);
    r=rad;
% number of zones in a ring-decided by angles chosen
angle_step=pi/I;
angle_shift=pi/100;
```

(*Continued*)

Downloaded From: https://www.spiedigitallibrary.org/ebooks/ on 27 Feb 2022
Terms of Use: https://www.spiedigitallibrary.org/terms-of-use

Table 3.11. Continued

```
  count1=0;
for theta=pi-angle_shift:-angle_step:-angle_shift,
  count1=count1+1;
  if theta==(pi-angle_shift)
    xh=[r.*cos(theta)];
    yh=[r.*sin(theta)];
  else
  xh=[xh;r.*cos(theta)];
  yh=[yh;r.*sin(theta)];
  end
end
xh=flipud(xh');
yh=flipud(yh');
theta=(pi-angle_shift)+angle_step;
for count2=1:count1,
  if theta==((pi-angle_shift)+angle_step)
    xh1=[r.*cos(theta)];
    yh1=[r.*sin(theta)];
  else
  xh1=[xh1;r.*cos(theta)];
  yh1=[yh1;r.*sin(theta)];end
  theta=theta+angle_step;
end
    xh1=(xh1');
    yh1=(yh1');
    xh=[xh(1:end-1,:);xh1];
    yh=[yh(1:end-1,:);yh1];
    figure(1)
    plot(xh,yh,'k.')
    title('Locations of nodes of a Gaussian input')
    xlabel('X-direction (arb. units)')
    ylabel('Y-direction (arb. units)')
    figure(2)
    plot(xh',yh')
    title('Annular rings of a Gaussian input')
    xlabel('X-direction (arb. units)')
    ylabel('Y-direction (arb. units)')
    % Saves mesh details and variables in a file called
    %GaussianMesh
    % for use by further programs
    save GaussianMesh I J R sigma xh yh
```

In order to obtain areas of equal power, the annular rings are further divided into zones. These zones can easily be made to have equal power by drawing radial lines from the origin. In these few steps, the Gaussian circle has now been divided into a number of zones of unequal area but equal power. Table 3.11 gives the code that carries out this operation for a Gaussian beam. Figure 3.21 shows a Gaussian beam that has been divided using this technique.

The black points in Fig. 3.21 indicate the corners or nodes of each zone. In order to program the Eikonal technique correctly, certain factors must be taken into account. Firstly, no zeros should occur in the x and y coordinates,

Downloaded From: https://www.spiedigitallibrary.org/ebooks/ on 27 Feb 2022
Terms of Use: https://www.spiedigitallibrary.org/terms-of-use

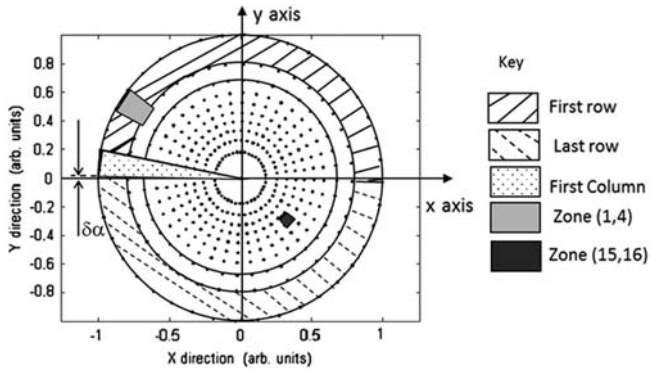

Figure 3.21 A Gaussian beam divided into 20 × 20 nodes (reprinted from Ref. 41).

as they appear in the denominator of the expression for calculating the phase. Therefore, the annular zones are formed by rotating the first zone position by a small angle $\delta\alpha$ as shown on the left side of the figure. Secondly, each zone should have four corner points. This is satisfied by all of the zones except those in the ring closest to the origin, which appear to have triangular zones with one node at the origin. This problem can be overcome by replacing the origin with a ring of very small radius. Doing so ensures that every zone in that ring has four corners. In order for the Eikonal method to work, the location of the zones on the input plane should match as closely as possible the location on the output plane. Therefore, the method by which the area is divided into zones and numbered is crucial for obtaining a continuous phase function that can carry out the conversion. The numbering is done so that the upper half of the outermost ring is taken to be the first row, and the lower half is the last row. Each set of points from the outer ring to the center specifies a column. As an example, two zones are drawn as shaded: one lies in the fourth column, first row; the second lies in the sixteenth column, fifteenth row.

In the case of a flat-top intensity output, the mesh is generated by dividing the desired shape into zones of equal area. This is relatively easy to do. For example, a circle could be divided in exactly the manner described above. However, initially, the circle would be divided into annular rings of equal area instead of equal power. It is important that the number of rows and columns in the output mesh—and hence, the number of nodes in the output mesh—match that of the input mesh. Table 3.12 provides the MATLAB code that creates a flat-top intensity in the shape of a square. The output mesh is shown in Fig. 3.22.

3.3.2 Determination of the phase element

The phase can now be determined using the Eikonal method and the two meshes that have been obtained.[42] The phase of the beam behind the beam-shaping element is

Downloaded From: https://www.spiedigitallibrary.org/ebooks/ on 27 Feb 2022
Terms of Use: https://www.spiedigitallibrary.org/terms-of-use

Table 3.12 Creating a square output mesh with a flat-top intensity.

```
% I, J will be available since defined as global variables
% if memory was cleared, their values must be entered
% creation of image plane co-ordinates for a square
    S=2; %size of square at image plane is 2S
    stepx=2*S/J;
    stepy=2*S/I;
    X=-S:stepx:S;
    Y=-S:stepy:S;
    [xsq,ysq]=meshgrid(X,Y);
    xsq=flipud(xsq);
    ysq=flipud(ysq);
    figure(2)
    plot(xsq,ysq,'b.')
    xlabel('X-direction (arb. units)')
    ylabel('Y-direction (arb. units)')
    clear X Y stepx stepy
    bits=512;
    stepx=2*S/bits;
    indexx=-S:stepx:S; %regular spaced points
    indexx=indexx(1:end-1); %even number of points
    indexy=-Sy:stepy:Sy;; %regular spaced points
    indexy=indexy(1:end-1); %even number of points
    [XS,YS] = meshgrid(indexx,indexx); %creates grid of points
    with limits given by index
% Saves mesh details and variables in a file called square
% for use by further programs
    save square xsq ysq XS YS
```

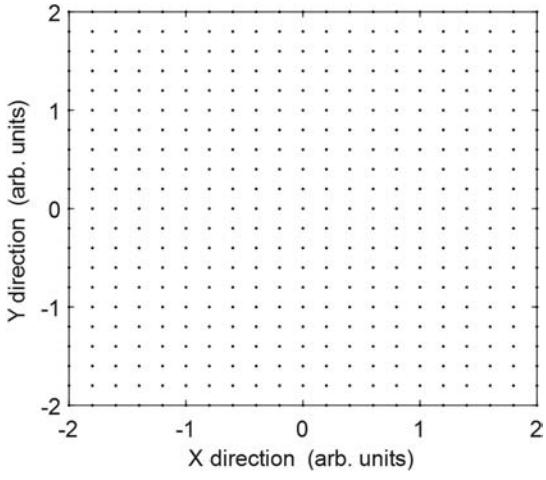

Figure 3.22 Output mesh consisting of 20×20 nodes. All zones have equal area (reprinted from Ref. 41).

$$k\psi(\overline{u}) = k\psi_0(\overline{u}) + \Phi(u), \tag{3.13}$$

where $k = 2\pi/\lambda$, $\Phi(u)$ is the phase of the DOE, and $k\psi_0(u)$ is the phase of the incident beam. The node position is given by $\overline{u} = (u,v)$ and refers to the

Downloaded From: https://www.spiedigitallibrary.org/ebooks/ on 27 Feb 2022
Terms of Use: https://www.spiedigitallibrary.org/terms-of-use

coordinates over the DOE. The corresponding coordinates at the image plane are a function of $\bar{u}$ and are given by $x(\bar{u})$. If the distance between the DOE and image plane is d, then the gradient of the wavefront will be given by

$$\nabla\psi = \frac{\overline{u} - x(\overline{u})}{d}. \tag{3.14}$$

The function ψ is fitted with a polynomial. A function can be defined in terms of the gradient of ψ_{poly} and the coordinates u and $x(\overline{u})$ given by Eq. (3.14). The total number of mesh nodes and the degree of the polynomial can be varied in order to get better results. The code for extracting the phase is shown in Table 3.13.

Table 3.13 Using the Eikonal method to generate the DOE phase.

```
%This program reads mesh data from the files GaussianMesh and
%square
%Phase over the hologram is calculated using the Eikonal technique
%Phase is calculated at a limited number of irregularly spaced
%data points
    close all
    clear all
    load GaussianMesh
    load square
    bits=512;
    x=xsq;
    y=ysq;
%inputs
f=300; %distance between input and output planes in mm
lambda=0.000633; %wavelength in mm
figure(1)
plot(xh,yh,'r.')
title('Mesh over hologram plane')
%Eikonal retrieval
%delta psi
  del_psix=(x-xh)./f;
  del_psiy=(y-yh)./f;
%polynomial calculation to obtain phase of hologram
D=5; %polynomial of degree D
M=(D+2)*(D+1)/2;
%calculates k and l values for each m value
count=0;
for k=0:D
  for l=0:D-k
    count=count+1;
    m=k*((2*D-k+3)/2)+l+1;
    indices(count,1)=m;
    indices(count,2)=k;
    indices(count,3)=l;
  end
end
```

(*Continued*)

Downloaded From: https://www.spiedigitallibrary.org/ebooks/ on 27 Feb 2022
Terms of Use: https://www.spiedigitallibrary.org/terms-of-use

Table 3.13. Continued

```
for n=2:M
  for m=2:M
    m1=m-1;
    n1=n-1;
    c(n1,m1)=0;
    b(n1,1)=0;
    for j1=1:J+1
      for i1=1:I+1
          k=indices(m,2);
          k1=indices(n,2);
          l=indices(m,3);
          l1=indices(n,3);
          c(n1,m1)=c(n1,m1)+(k*k1*(xh(j1,i1)^(k+k1-2))*(yh(j1,
          i1)^(l+l1)))+(l*l1*(xh(j1,i1)^(k+k1))*(yh(j1,i1)^
          (l+l1-2)));
          b(n1,1)=b(n1,1)+del_psix(j1,i1)*k1*(xh(j1,i1)^(k1-
          1))*(yh(j1,i1)^l1)+del_psiy(j1,i1)*l1*(xh(j1,i1)^k1)
          *(yh(j1,i1)^(l1-1));
      end
    end
  end
end
%coefficients
a=c\b;
clear del_psix del_psiy x y
% eikonal -psi
for j1=1:J+1
  for i1=1:I+1
    psi(j1,i1)=0;
    for m=2:M
      psi(j1,i1)=psi(j1,i1)+a(m-1)*(xh(j1,i1)^indices(m,2))*
      (yh(j1,i1)^indices(m,3));
    end
  end
end
clear a b c
    k=2*pi/lambda;
    psi=k*psi%phase of hologram
    colormap(gray)
    figure(3)
    surf(xh,yh,psi)
    title('Phase of hologram')
    xlabel('X-cordinate in units of length')
    ylabel('Y-cordinate in units of length')
    zlabel('Phase (radians)')
    %save phase psi xh yh
    step=R*2/bits;
_____________________________________
%converting arrays to vectors - required for fit process
    [m,n]=size(xh);
    xh1=xh(:,1);
    yh1=yh(:,1);
    psi1=psi(:,1);
for i=2:n
```

(*Continued*)

Downloaded From: https://www.spiedigitallibrary.org/ebooks/ on 27 Feb 2022
Terms of Use: https://www.spiedigitallibrary.org/terms-of-use

Table 3.13. Continued

```
    xh1=[xh1;xh(:,i)];
    yh1=[yh1;yh(:,i)];
    psi1=[psi1;psi(:,i)];
end
%saves data in files that can be retrieved by software that will
%carry out regression
% and generate coefficients to help generate phase at equidistant
%points
output=[xh1 yh1 psi1];
save save('testdata.txt', 'output', '-ascii')
%————————————————————————————
index=-R:step:R; %regular spaced points
index=index(1:end-1); %even number of points
[XH1,YH1]=meshgrid(index,index); %creates grid of points with
limits given by index
%store regularly spaced points and phase for later use
save phase_circle XH1 YH1 sigma k f lambda xh1 yh1 psi1
```

The output of the code given in Table 3.13 is the phase of the hologram that will carry out the conversion from a Gaussian beam to a square-shaped beam with constant intensity. The final figure of this code is shown in Fig. 3.23.

The phase retrieved using the polynomial method only gives discrete values at the specified mesh nodes. For the circular Gaussian input, the nodes are not equidistant and the number of nodes is also quite small. The phase will not provide enough data with which to write the DOE. Also, to simulate the output, we will be using a Fourier transform technique and, hence, need evenly spaced points. Therefore, phase values at many more equidistant points are required. There are several ways this can be achieved. MATLAB

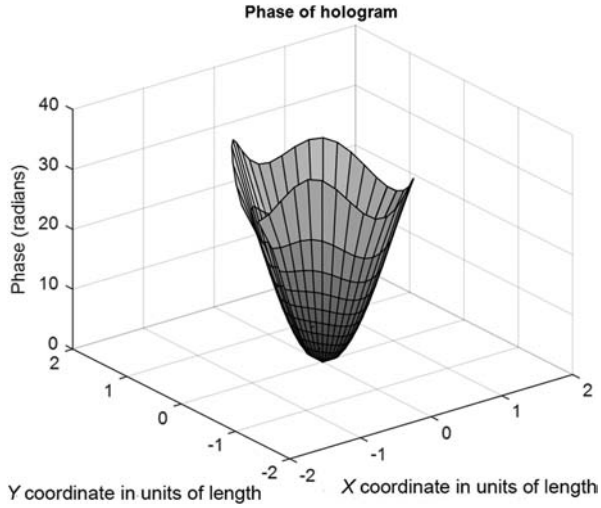

Figure 3.23 Phase that converts a circular Gaussian beam into a flat-top intensity beam with a square shape (reprinted from Ref. 21).

Downloaded From: https://www.spiedigitallibrary.org/ebooks/ on 27 Feb 2022
Terms of Use: https://www.spiedigitallibrary.org/terms-of-use

surface-fitting commands can be used to generate a fit to the existing data. The fit coefficients can then be used to generate phase at evenly spaced points. Alternatively, the nodal phase information can be used with a regressive calculation to evaluate the coefficients of the polynomial that will generate the continuous phase.

If the latter method is chosen, 'testdata.txt' should be opened with software (such as Excel) and regression used to generate coefficients. The coefficients, irrespective of how they were generated, are used to calculate phase information at the evenly spaced X and Y coordinates (i.e., $XH1$ and $YH1$ coordinates saved in the file 'phase_circle'). The MATLAB code with both of these options is given in Table 3.14. This program also simulates the output. The simulated output intensity is shown in Fig. 3.24.

Table 3.14 Creating phase information at equally spaced points and simulating the output intensity.

```
% This program calculates the phase over a grid
%loads uniformly spaced x and y coordinates
%calculates coefficients using Matlab fit
clear all
close all
load phase_circle %contains regularly spaced grid points
choice = input('Enter 1 to generate fit coefficients in matlab and
2 to upload coefficients from other programme: ');
if choice == 1
  ft = fittype('poly55');
  dataFit = fit([xh1,yh1],psi1, ft);
  coeff1=coeffvalues(dataFit);
  coeffN=coeffnames(ft);
  R=confint(dataFit);
  c=size(coeff1);
  psi1=0;
  for count=1:c(2)
    coeffI=coeffN(count);
    coeffI=coeffI{:};
    m=str2double(coeffI(2));
    n=str2double(coeffI(3));
    psi1=psi1+coeff1(count).*(XH1.^m).*(YH1.^n);
  end
elseif choice ==2
%coefficients obtained with R=1, sigma=0.8 and I=J=20, S=2 from
%a data handling software such as excel
%SQUARE
  a0 = 0.106394007
  a1 = -0.836150168
  a2 = 0.020604165
  a3 = 17.61722947
  a4 = 15.83427723
  a5 = -7.266911537
  a6 = -4.752015829
```

(*Continued*)

Downloaded From: https://www.spiedigitallibrary.org/ebooks/ on 27 Feb 2022
Terms of Use: https://www.spiedigitallibrary.org/terms-of-use

Table 3.14. Continued

```
% Calculating phase at regularly spaced points
psi1=a0+a1*XH1+a2*YH1+a3*XH1.^2+a4*YH1.^2+a5*XH1.^4+a6*YH1.
^4;
end
% Output
figure(1)
surf(XH1,YH1,psi1)
title('Phase over DOE')
% to simulate output intensity
i=sqrt(-1);
g=exp(-((XH1).^2+(YH1).^2)/(sigma^2)); %Gaussian beam
amp1=exp(i*psi1).*g; %Amplitude just after hologram
sing=find(isnan(amp1)); %locates singularities
amp1(sing)=zeros(size(sing)); %replaces singularities with
zeros
amp1=amp1.*exp(i*(k/(2*f))*(XH1.^2+YH1.^2));
figure(2)
colormap(gray)
imagesc(amp1.*conj(amp1))
contour(XH1,YH1,amp1.*conj(amp1))
title('Intensity just after DOE')
xlabel('X-direction')
ylabel('Y-direction')
amp2=fft2((amp1));
amp2=fftshift(amp2);
figure(3)
colormap(gray)
contour(abs(amp2)/max(max(abs(amp2))))
title('Output intensity - Gaussian to square')
xlabel('X-direction')
ylabel('Y-direction')
```

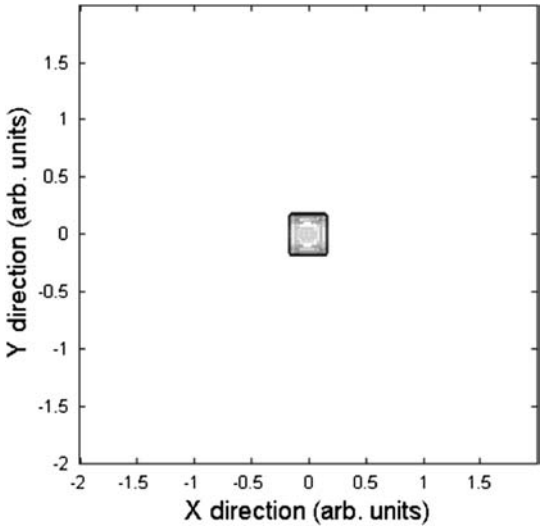

Figure 3.24 Simulated intensity at output plane. The phase used to create this was generated using choice 2 in the code of Table 3.14 (reprinted from Ref. 41).

Downloaded From: https://www.spiedigitallibrary.org/ebooks/ on 27 Feb 2022
Terms of Use: https://www.spiedigitallibrary.org/terms-of-use

3.4 Conclusions

In this chapter, the design, simulation, and analysis of simple multilevel and grayscale elements are discussed with MATLAB codes. We have introduced some methods to design diffractive optics for the generation of any arbitrary intensity profile at a plane of interest. We have also discussed the creation of special beams, such as donut beams, and beam-shaping fundamentals.[43] In addition to designing the diffractive element, in every case the output is also simulated.

The types of diffractive optics presented in this chapter are by no means comprehensive. There are many other interesting and useful DOEs such as Dammann gratings, harmonic gratings, and spot array generators, to name a few. However, the techniques introduced here can be adapted to any type of binary or multilevel DOE.

3.5 Exercises

E.3.1 Design a 16-level 1D phase grating using MATLAB and estimate the efficiency in the 1st diffraction order.

E.3.2 Design a negative 4-level FZP and simulate its far-field diffraction pattern.

E.3.3 Design a binary spiral phase plate with $L = 5$ and simulate its diffraction pattern.

E.3.4 Design a 3-level DOE from an object of your choice and simulate its diffraction pattern.

E.3.5 Design a gradient ring lens with a focal length $f = 2$ mm and a ring diameter $r_0 = 0.1$ mm.

References

1. M. Breidne, S. Johansson, L.-E. Nilsson, and H. Åhlèn, "Blazed holographic gratings," *Opt. Acta* **26**, 1427–1441 (1979).
2. J. W. Goodman, *Introduction to Fourier Optics*, Second Edition, McGraw-Hill Companies Inc., New York (1996).
3. B. C. Kress and P. Meyrueis, *Applied Digital Optics*, John Wiley & Sons, Chichester, UK (2009).
4. J. Jahns and S. J. Walker, "Two-dimensional array of diffractive microlenses fabricated by thin film deposition," *Appl. Opt.* **29**, 931–936 (1990).
5. S. Beretta and M. Cairoli, "Design of multilevel thin-film phase gratings with optimized diffraction efficiency," *Opt. Lett.* **16**, 684–686 (1991).

Downloaded From: https://www.spiedigitallibrary.org/ebooks/ on 27 Feb 2022
Terms of Use: https://www.spiedigitallibrary.org/terms-of-use

6. J. Pu, H. Zhang, S. Nemoto, W. Zhang, and W. Zhang, "Annular-aperture diffractive axicons illuminated by Gaussian beams," *J. Opt. A* **1**, 730–734 (1999).
7. D. M. Brown, D. R. Brown, and J. D. Brown, "High-performance analog profile diffractive systems," *Proc. SPIE* **3633**, 46 (1999) [doi: 10.1117/12/349340].
8. J. A. Jordan, P. M. Hirsch, L. B. Lesem, and D. L. Van Rooy, "Kinoform lenses," *Appl. Opt.* **9**, 1883–1887 (1970).
9. T. R. M. Sales and G. M. Morris, "Diffractive–refractive behavior of kinoform lenses," *Appl. Opt.* **36**, 253–257 (1997).
10. J. J. Clair, "New methods to synthesise kinoforms," *Opt. Commun.* **6**, 135–137 (1972).
11. G. J. Swanson, "Binary optics technology: The theory and design of multi-level diffractive optical elements," MIT Lincoln Lab. Tech. Rep. 854, Lexington, Massachusetts (1989).
12. G. J. Swanson, "Binary optics technology: Theoretical limits on the diffraction efficiency of multilevel diffractive optical elements," MIT Lincoln Lab. Tech. Rep. 914, Lexington, Massachusetts (1991).
13. R. L. Phillips and L. C. Andrews, "Spot size and divergence for Laguerre Gaussian beams of any order," *Appl. Opt.* **22**, 643–644 (1983).
14. T. Watanabe, M. Fujii, Y. Watanabe, N. Toyama, and Y. Iketaki, "Generation of a doughnut-shaped beam using a spiral phase plate," *Rev. Sci. Instrum.* **75**, 5131–5135 (2004).
15. M. W. Beijersbergen, R. P. C. Coerwinkel, M. Kristensen, and J. P. Woerdman, "Helical-wavefront laser beams produced with a spiral phase plate," *Opt. Commun.* **112**, 321–327 (1994).
16. G. H. Kim, J. H. Jeon, K. H. Ko, H. J. Moon, J. H. Lee, and J. S. Chang, "Optical vortices produced with a nonspiral phase plate," *Appl. Opt.* **36**, 8614–8621 (1997).
17. N. R. Heckenberg, R. McDuff, C. P. Smith, and A. G. White, "Generation of optical phase singularities by computer-generated holograms," *Opt. Lett.* **17**, 221–223 (1992).
18. G. F. Brand, "Phase singularities in beams," *Am. J. Phys.* **67**, 55–60 (1999).
19. J. Arlt, K. Dholakia, L. Allen, and M. J. Padgett, "The production of multiringed Laguerre–Gaussian modes by computer-generated holograms," *J. Mod. Opt.* **45**, 1231–1237 (1997).
20. Q. Wang, X. W. Sun, and P. Shum, "Generating doughnut-shaped beams with large charge numbers by use of liquid-crystal spiral phase plates," *Appl. Opt.* **43**, 2292–2297 (2004).
21. C. S. Guo, D. M. Xue, Y. J. Han, and J. Ding, "Optimal phase steps of multi-level spiral phase plates," *Opt. Commun.* **268**, 235–239 (2006).

Downloaded From: https://www.spiedigitallibrary.org/ebooks/ on 27 Feb 2022
Terms of Use: https://www.spiedigitallibrary.org/terms-of-use

22. V. Basistiy, V. A. Pas'ko, V. V. Slyusar, M. S. Soskin, and M. V. Vasnetsov, "Synthesis and analysis of optical vortices with fractional topological charges," *J. Opt. A: Pure Appl. Opt.* **6**, S166–S169 (2004).
23. B. Zhang and D. Zhao, "Focusing properties of Fresnel zone plates with spiral phase," *Opt. Express* **18**, 12818–12823 (2010).
24. A. Vijayakumar and S. Bhattacharya, "Design, fabrication, and evaluation of a multilevel spiral-phase Fresnel zone plate for optical trapping," *Appl. Opt.* **51**, 6038–6044 (2012).
25. N. Zhang, J. A. Davis, I. Moreno, D. M. Cottrell, and X.-C. Yuan, "Analysis of multilevel spiral phase plates using a Dammann vortex sensing grating," *Opt. Express* **18**, 25987–25992 (2010).
26. N. Davidson, A. A. Friesem, and E. Hasman, "Holographic axilens: high resolution and long focal depth," *Opt. Lett.* **16**, 523–525 (1991).
27. J. Sochacki, Z. Jaroszewicz, A. Kołodziejczyk, and S. Bará, "Phase retardation of the uniform-intensity axilens," *Opt. Lett.* **17**, 7–9 (1992).
28. K. B. Rajesh, N. V. Suresh, P. M. Anbarasan, K. Gokulakrishnan, and G. Mahadevan, "Tight focusing of double ring shaped radially polarized beam with high NA lens axicon," *Opt. Laser. Technol.* **43**, 1037–1040 (2011).
29. H.-H. Lin and M.-H. Lu, "Dual-wavelength membrane-based diffractive optical element with extended depth-of-focus for optical pickup head," *Jpn. J. Appl. Phys.* **46**, 5485–5493 (2007).
30. R. W. Gerchberg and W. O. Saxton, "A practical algorithm for the determination of phase from image and diffraction plane pictures," *Optik* **35**, 227–246 (1972).
31. J. Bengtsson, "Kinoform design with an optimal-rotation-angle method," *Appl. Opt.* **33**, 6879–6884 (1994).
32. D. Wang, J. Zhang, and H. Zhang, "Adaptive-weight iterative algorithm for flat-top laser beam shaping," *Opt. Eng.* **51**(7), 074301 (2012) [doi: 10.1117/1.OE.51.7.074301].
33. M. Guizar-Sicairos and J. R. Fienup, "Understanding the twin-image problem in phase retrieval," *J. Opt. Soc. Am.* **29**, 2367–2375 (2012).
34. W. McBride, N. L. O'Leary, and L. J. Allen, "Retrieval of a complex valued object from its diffraction pattern," *Phys. Rev. Lett.* **93**, 233902 (2004).
35. V. Elser, "Random projections and optimization of an algorithm for phase retrieval," *J. Phys. A* **36**, 2995–3007 (2003).
36. H. M. L. Faulkner and J. M. Rodenburg, "Movable aperture lensless transmission microscopy: a novel phase retrieval algorithm," *Phys. Rev. Lett.* **93**, 023903 (2004).
37. C. Gaur, B. Mohan, and K. Khare, "Sparsity-assisted solution to the twin image problem in phase retrieval," *J. Opt. Soc. Am. A* **32**, 1922–1927 (2015).

Downloaded From: https://www.spiedigitallibrary.org/ebooks/ on 27 Feb 2022
Terms of Use: https://www.spiedigitallibrary.org/terms-of-use

38. E. Buckley, A. Cable, and T. Wilkinson, "Precision measurement system using binary phase computer-generated holograms," *Opt. Eng.* **50**(9), 091308 (2011) [doi: 10.1117/1.3596201].
39. M. A. Golub, I. N. Sisakyan, and V. A. Soifer, "Infra-red radiation focusators," *Optics and Lasers in Engineering* **15**(5), 297–309, (1991).
40. M. Born and E. Wolf, "Foundations of Geometrical Optics," in *Principles of Optics*, Seventh Edition, Cambridge University Press, Cambridge, Chapter 3 (1999).
41. S. Bhattacharya, "Simplified mesh techniques for design of beam shaping diffractive optical elements," *Optik* **119**, 321–328, (2008).
42. A. Hermerschmidt, H. J. Eichler, S. Teiwes, and J. Schwartz, "Design of diffractive beam-shaping elements for non-uniform illumination waves," *Proc. SPIE* **3291**, 40–48 (1998) [doi: 10.1117/12.310592].
43. A. Vijayakumar, "Design, Fabrication, and Evaluation of Diffractive Optical Elements for the Generation of Focused Ring Patterns," Doctoral Thesis, Indian Institute of Technology Madras, Chennai, India (2015) [doi: 10.13140/RG.2.2.25996.51847].

Downloaded From: https://www.spiedigitallibrary.org/ebooks/ on 27 Feb 2022
Terms of Use: https://www.spiedigitallibrary.org/terms-of-use

Chapter 4
Analysis of DOEs in the Fresnel Diffraction Regimes

In earlier chapters, the design of DOEs and the simulation of their far-field diffraction patterns using Fraunhofer diffraction formula were presented. However, to characterize a DOE, it is necessary to analyze phase and intensity profiles at different propagation distances. For instance, the binary axicon or circular grating generates a ring-like pattern in its far field, and it generates a Bessel-like beam closer to the element.[1] With its large focal length, the Bessel-like beam, is used for many applications. Hence, it is necessary to simulate and understand the field variations at several planes of interest. In this chapter, a MATLAB® simulation of diffraction patterns in the Fresnel regime is presented. The analysis and simulation presented here are not suitable for planes very close to the DOE.

4.1 Analysis of DOEs with the Fresnel Diffraction Formula

For small angles, a spherical wavefront can be approximated by a parabolic wavefront. This is called the Fresnel or paraxial approximation.[2] Fresnel diffraction has been extensively discussed in literature.[2–4] The description of Fresnel diffraction formulae and their applicability are discussed in Chapter 1. Various computer simulation techniques for calculation of Fresnel diffraction patterns can be used.[5–10] In this section, one of the simplest techniques for implementation of the Fresnel diffraction integral is discussed.

Once again, the Fresnel diffraction formula is given by

$$E(u,v) = \frac{e^{jkz} e^{j\frac{k}{2z}(x^2+y^2)}}{j\lambda z} \int_{-\infty}^{+\infty}\int_{-\infty}^{+\infty} \left\{ A(x,y) \exp\left[j \frac{k}{2z}(x^2+y^2) \right] \right\} \times \exp\left[-j \frac{2\pi}{\lambda z}(xu+yv) \right] dxdy. \tag{4.1}$$

Downloaded From: https://www.spiedigitallibrary.org/ebooks/ on 27 Feb 2022
Terms of Use: https://www.spiedigitallibrary.org/terms-of-use

From this equation it can be noted that the parabolic phase factor $(k/2z)(x^2 + y^2)$ is multiplied with every pixel of the DOE function $A(x, y)$ and Fourier transformed. The equation is different from a pure Fourier transform because of the parabolic phase factor $e^{j\frac{k}{2z}(x^2+y^2)}$ and constant phase e^{jkz} outside of the integral. If we consider a point object in $A(x, y)$, the resulting phase in the plane (u, v) from Eq. (4.1) is nothing but a FZP.[2] Hence, it can be understood that, for any arbitrary object, the field in the observation plane is nothing but a collection of FZPs. Since the parabolic phase factor for large values of z reduces to 1, the equation reduces to a Fourier transform operation, which is the far-field approximation (large z) of the scalar diffraction formula.

As explained in Chapter 1, the Fresnel approximation is valid only when

$$z^3 \gg \frac{\pi}{4\lambda}\left[(x-u)^2 + (y-v)^2\right]^2_{\max}. \tag{4.2}$$

Hence, this approximation is not suitable for studying the field extremely close to the diffraction element. A deeper look at the approximation reveals that it is valid only over a smaller area (in the transverse plane) for shorter distances, while it is valid over a larger area at longer distances. In other words, the Fresnel approximation can be valid for distances very close to the diffraction plane, but this validity is limited to a transverse area proportional to the distance. The far-field approximation, also known as the Fraunhofer approximation, is valid only for very large distances given by

$$z \gg \frac{k\left(u^2 + v^2\right)}{2}, \tag{4.3}$$

where $k = 2\pi/\lambda$. For analysis of diffraction patterns extremely close to the diffraction plane, vector diffraction formula must be used.[11]

For simple designs such as circular and rectangular apertures, it is easier to calculate the Fresnel diffraction pattern analytically. For complex designs, however, simulation is the easiest way to study the diffraction patterns. In the latter case, two important steps are involved: sampling and scaling. The sampling presented in Chapter 2 is the way the diffraction plane is sampled with respect to the wavelength of light. The sizes of the matrices used for the design of the DOE in the diffraction plane and the observation plane are same in most of the cases. Hence, it is necessary to relate the sampling periods of the diffraction plane and the observation plane. Considering the relationship between continuous and discrete Fourier transforms, for a distance z and sampling size $N \times N$ in the DOE plane, the pixel size in the observation plane is given by $\Delta_I = (\lambda z/N\Delta_{\mathrm{DOE}})$, where Δ_{DOE} is the sampling period at the diffraction plane, and z is the propagation distance.[10]

Downloaded From: https://www.spiedigitallibrary.org/ebooks/ on 27 Feb 2022
Terms of Use: https://www.spiedigitallibrary.org/terms-of-use

An alternative way of scaling is uses zero padding of the diffraction plane, as discussed in various literature.[12,13] An interesting relationship, $\lambda z = N$, arises when the analog Fourier transform is converted into the discrete Fourier transform. This equation tells us that by varying the size of the matrix using zero padding, the propagation distance can be varied. A detailed analysis of different techniques such as the angular spectrum method, the convolution method, and the fractional Fourier transform, along with their their validity in space are given in Ref 10. In this chapter, only the basic method using FFT propagators for simulation of Fresnel diffraction patterns is presented.

4.1.1 Fresnel diffraction pattern of a circular aperture

The MATLAB code for design and analysis of a circular aperture can be constructed using the procedure discussed earlier. The parabolic phase factor $(k/2z)(x^2 + y^2)$ is rewritten as $(\pi/\lambda z)(x^2 + y^2)$. The distances are specified in meters. The same code can easily be modified to simulate the diffraction patterns of other DOEs. In this case, a circular aperture with a radius of 1 mm is designed. The Fresnel diffraction patterns are simulated at four distances, namely, 20 mm, 50 mm, 100 mm and 50 m. The pixel size (sampling period) is selected as 10λ. This value is suitable for planes close to the DOE, such as the first three distances. However, for larger distances such as 50 m, the simulated pattern will not be visible in the diffraction window. To shrink the far-field diffraction pattern, it is necessary to increase the sampling period. Hence, the sampling period is selected to be 100λ for simulation at 50 m. In the codes given in the previous chapters, the pixel size was set as 1 μm. The code for simulation of Fresnel diffraction patterns is given in Table 4.1. The diffraction images at distances 20 mm, 50 mm, 100 mm with sampling period of 10λ; and 50 m with a sampling period of 100λ are shown in Figs. 4.1(a)–(d), respectively.

4.1.2 MATLAB simulations of the Fresnel diffraction pattern of a binary phase axicon

A binary axicon is designed as shown in Chapter 2. Fresnel diffraction of a binary axicon yields a Bessel-like intensity profile, which is maintained over its large focal depth.[1] The MATLAB code for analysis of the axicon is presented in Table 4.2. The images of the diffraction pattern simulated at $z = 25$ mm and $z = 50$ m are shown in Figs. 4.2(a) and (c), respectively.[14] A line scan through the center of the intensity pattern given in Fig. 4.2(a) has an approximate Bessel-like intensity profile as shown in Fig. 4.2(b). The far-field diffraction pattern is a ring pattern, which matches the far-field patterns simulated in Chapter 2. The first and higher (3^{rd} order) diffraction order ring patterns are visible in Fig. 4.2(c). It should be noted that in this case, the sampling period is

Downloaded From: https://www.spiedigitallibrary.org/ebooks/ on 27 Feb 2022
Terms of Use: https://www.spiedigitallibrary.org/terms-of-use

Table 4.1 MATLAB code for simulation of Fresnel diffraction of a circular aperture.

```
%Fresnel diffraction of a circular aperture%
clear; %Clear all memory
%Defining the parameters
    N=500;% Define the matrix size
    lambda=0.633*10^-6;%Define wavelength in meters
    z=0.02;%Propagation distance = 20 mm
    r=10^-3;%Radius of aperture = 1 mm
    wsamp=10*lambda;%sampling period or width
%Creating sampled space
    x=1:N;
    y=1:N;
    [X,Y]=meshgrid(x,y);%Sampling
    Rsamp=sqrt((X-N/2).^2+(Y-N/2).^2).*wsamp;%Define sampled
    %radius
%Constructing the aperture
    A=ones(N,N);%Define matrix by assigning zeros to all pixels
    A(Rsamp>=r)=0;
% Calculating the Fresnel diffraction pattern
    PPF=exp(1i*pi/(lambda*z).*Rsamp.*Rsamp); %Calculate the
    %parabolic phase factor
    A1=A.*PPF;%Multiply the circular aperture function with the
    parabolic phase factor
    E=abs(fftshift(fft2(fftshift(A1)))); %Calculate Fourier
    %Transform
%Observation of the diffraction pattern
    colormap(gray)%Display greyscale image
    imagesc(E)%Display scaled image
```

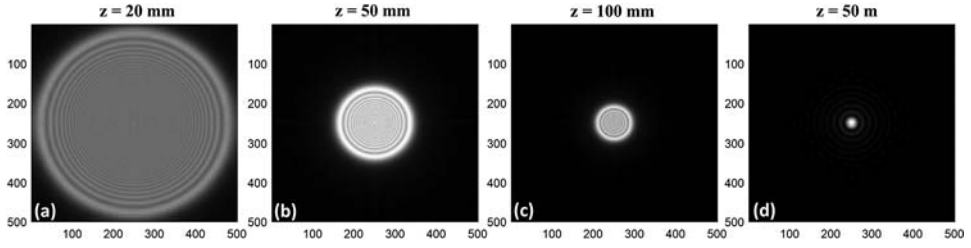

Figure 4.1 Fresnel diffraction patterns for circular aperture at distances (a) $z = 20$ mm, (b) $z = 50$ mm (c), $z = 100$ mm, and (d) $z = 50$ m.

not increased at large distances, as the period of the binary axicon itself was selected to obtain larger ring patterns. However, if the period of the binary axicon were larger, i.e., generating a smaller ring pattern, then the sampling period would need to be increased in order to see the diffraction pattern.

The codes given in Tables 4.1 and 4.2 can be modified to simulate the Fresnel diffraction patterns of any type of amplitude or phase DOE. For example, the DOE design scripts presented in Chapter 2 and in the first section of Chapter 3 can be easily integrated into these codes and the Fresnel diffraction patterns simulated at different planes.

Downloaded From: https://www.spiedigitallibrary.org/ebooks/ on 27 Feb 2022
Terms of Use: https://www.spiedigitallibrary.org/terms-of-use

Table 4.2 MATLAB code for simulation of Fresnel diffraction of a binary phase axicon.

```
%Fresnel diffraction of binary axicon%
clear; %Clear all memory
% Defining the parameters
    N=500;% Define the matrix size
    lambda=0.633*10^-6;%Define wavelength in meters
    z=0.025;%Propagation distance = 25mm and 50 m
    P=10^-4;%Radius of aperture = 0.1 mm
    wsamp=10*lambda;%sampling period or width
%Creating sampled space
    x=1:N;
    y=1:N;
    [X,Y]=meshgrid(x,y);%Sampling
    Rsamp=sqrt((X-N/2).^2+(Y-N/2).^2).*wsamp;%Define sampled
    %radius
%Constructing the DOE
    A=ones(N,N);%Define matrix by assigning ones to all pixels
    A(rem(Rsamp,P) < P/2)=exp(1i*pi);
%Calculating the Fresnel diffraction pattern
    PPF=exp(1i*pi/(lambda*z).*Rsamp.*Rsamp); %Calculate the
    parabolic phase factor
    A1=A.*PPF; %Multiply the circular aperture function with the
    %parabolic phase factor
    E=abs(fftshift(fft2(fftshift(A1)))); %Calculate Fourier
    %Transform
```

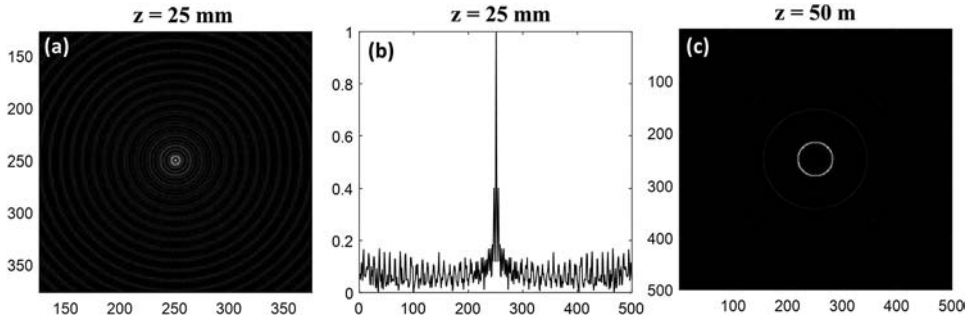

Figure 4.2 (a) Fresnel diffraction pattern of a binary phase axicon at $z = 25$ mm, (b) its intensity profile, and (c) the Fresnel diffraction pattern at $z = 50$ m.

4.1.3 MATLAB simulations of the Fresnel diffraction pattern of an axilens

An axilens[15,16] is a hybrid DOE made up of an FZP and an axicon. By varying the design parameters of an axilens, its optical behavior can be tuned to vary between that of an FZP and that of an axicon. The theory and design of an axilens are presented in detail in Chapter 3. Let us consider the following design parameters to study the Fresnel diffraction pattern of an axilens: focal length $f = 5$ mm, focal depth $\Delta f = 0$ mm to 2 mm, radius of DOE $R = 1$ mm, and $\lambda = 0.633$ μm. When $\Delta f = 0$, the axilens acts as a FZL, and when $f = 0$, it acts as an axicon.

Downloaded From: https://www.spiedigitallibrary.org/ebooks/ on 27 Feb 2022
Terms of Use: https://www.spiedigitallibrary.org/terms-of-use

Table 4.3 MATLAB code for design of a blazed axilens.

```
% Fresnel diffraction of an axilens
clear; %Clear all memory
%Defining all parameters and sampling
    N=500; %Matrix size
    lambda=0.633e-6; %Wavelength
    wsamp=1e-6;%sampling period
    x=-N/2:N/2-1;
    y=-N/2:N/2-1;
    [X,Y]=meshgrid(x*wsamp,y*wsamp);
    Rsamp=sqrt(X.^2+Y.^2);
    f0=0.005;%Focal length
    delf=0.001;%Focal depth
    R=10^-3;%Radius of the axilens
%Design of axilens
    f=(f0+(delf/R)*sqrt(X.^2+Y.^2));%Focal length calculation
    FZA=exp(-1i*(pi/(lambda))*((X.^2+Y.^2)./f));%Phase
    profile of Axilens
%Calculation of Fresnel diffraction pattern
    m=100;
    n=1:m;
    zs2=0.003+(0.005/m).*n; % Propagation distance
    PPF=zeros(N,N,m);
    A1=zeros(N,N,m);
    E=zeros(N,N,m);
    Field1=zeros(100,m);
for counter1=1:1:m;
    PPF(:,:,counter1)=exp(1i*pi/(lambda*zs2(counter1)).
    *Rsamp.*Rsamp); % Parabolic phase factor
    A1(:,:,counter1)=FZA.*PPF(:,:,counter1); %Multiply the
    axilens function with parabolic phase factor
    E(:,:,counter1)=abs(fftshift(fft2(fftshift(A1(:,:,
    counter1)))));
    %Calculate Fourier Transform
    % imagesc(E(201:300,201:300,counter1));
    % pause(1.0)
    Field1(:,counter1)=E(N/2+1,201:300,counter1); %Accumulate
    the intensity profile
end
```

The axial Fresnel diffraction pattern for the above design values and focal depth values of 0 mm, 1 mm, 2 mm, and 3 mm are shown in Figs. 4.3 (a)–(d), respectively. They were simulated using the code in Table 4.3. The design concept of the axilens has been utilized to design DOEs with interesting characteristics.[17–19]

4.1.4 MATLAB simulations of the Fresnel diffraction pattern of nonperiodic DOEs

Nonperiodic DOEs arise when algorithms such as the Gerchberg–Saxton algorithm[20] are used to generate them. This particular algorithm has been discussed in Chapter 3. Let us assume that the goal of the DOE is to generate

Downloaded From: https://www.spiedigitallibrary.org/ebooks/ on 27 Feb 2022
Terms of Use: https://www.spiedigitallibrary.org/terms-of-use

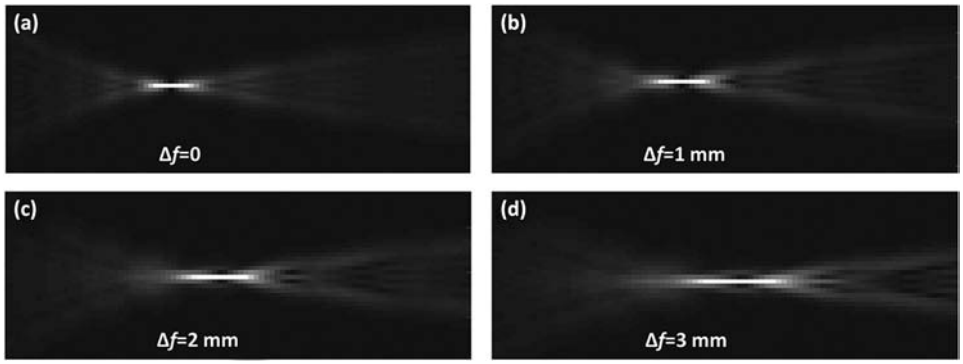

Figure 4.3 Images of Fresnel diffraction along the axial direction for an axilens of $f = 5$ mm and (a) $\Delta f = 0$ mm, (b) $\Delta f = 1$ mm, (c) $\Delta f = 2$ mm, and (d) $\Delta f = 3$ mm.

a certain intensity pattern. For example, we can consider an object such as the logo of Indian Institute of Technology Madras. The phase of the object is calculated using the MATLAB code given in Table 3.10, assuming input light with uniform illumination. The object and the phase of the DOE designed using the algorithm are shown in Figs. 4.4(a) and (b), respectively.

Now, let us study the Fresnel diffraction pattern of the phase-only DOE, assuming uniform illumination. Due to the very different nature of the DOE, the Fresnel diffraction pattern is quite different from any of the patterns seen in earlier sections. Another difference is the manner in which the Fresnel images need to be obtained, which is akin to imaging an object and studying the image at different planes. In order to carry out this experiment, it is necessary to multiply the phase function generated by the algorithm by a lens function. The resulting DOE when subjected to Fresnel diffraction analysis will yield the correct image at a plane corresponding to the focal plane of the lens, while the image will be blurred elsewhere. Hence, in the first step, the phase function shown in Fig. 4.5(b) is multiplied by a lens function of focal

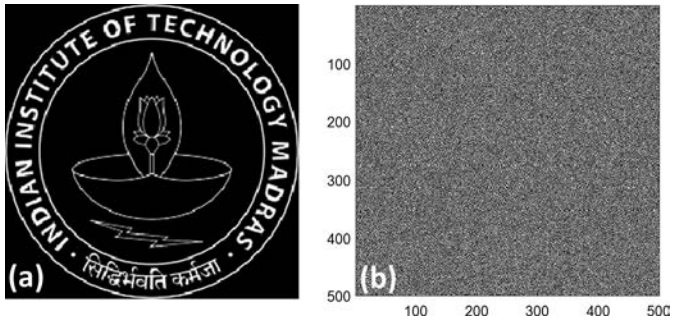

Figure 4.4 Images of the (a) object and (b) phase matrix generated using the Gerchberg–Saxton algorithm.

Downloaded From: https://www.spiedigitallibrary.org/ebooks/ on 27 Feb 2022
Terms of Use: https://www.spiedigitallibrary.org/terms-of-use

Table 4.4 MATLAB code for analyzing a DOE generated by Gerchberg–Saxton algorithm.

```
%% Fresnel diffraction of a DOE designed by Gerchberg-Saxton
%algorithm
%% Use table 3.10 to obtain the "DOE phase"
% Multiply the "DOE phase" with a lens function
    d=0.2;
    Q=exp(-1i*(pi/(lambda*d))*(X.^2+Y.^2));
    DOEphase=DOEphase.*Q;
%Defining all parameters and sampling
    lambda=0.633e-6; %Wavelength
    wsamp=1e-6;%sampling period
    x=-N/2:N/2-1;
    y=-N/2:N/2-1;
    [X,Y]=meshgrid(x*wsamp,y*wsamp);
    Rsamp=sqrt(X.^2+Y.^2);
%Calculation of Fresnel diffraction pattern
    m=100;
    n=1:m;
    zs2=0.1+(0.2/m).*n; % Propagation distance
    PPF=zeros(N,N,m);
    A1=zeros(N,N,m);
    E=zeros(N,N,m);
    Field1=zeros(100,m);
    for counter1=1:10:m;
    PPF(:,:,counter1)=exp(1i*pi/(lambda*zs2(counter1)).
    *Rsamp.*Rsamp); % Parabolic phase factor
    A1(:,:,counter1)=DOEphase.*PPF(:,:,counter1); %Multiply
    %the axilens function with the parabolic phase factor
    E(:,:,counter1)=abs((fft2((A1(:,:,counter1)))));
    %Calculate Fourier Transform
    imagesc(E(:,:,counter1)); title (zs2)
    pause(1.0)
end
```

length (20 cm in this case) followed by application of the Fresnel diffraction formula. The MATLAB code is given in Table 4.4.

The lens function that is multiplied by the phase function actually cancels the quadratic phase function of Eq. (4.1) at the plane corresponding to the focal plane. Hence, the Fresnel diffraction, in this case, reduces to a Fourier transform operation. In this example, the cancellation occurs at $z = 0.2$, which is the focal length of the lens. Therefore, in the other planes (where $z \neq 0.2$), the phase due to the difference between z and the focal length of the lens function introduces defocusing in the image. In this way, a simple imaging experiment can be carried out using the Fresnel diffraction formula. Images of the object at $z = 0.02$ m, 0.05 m, 0.15 m, and 0.2 m are shown in Figs. 4.5(a)–(d), respectively.

4.2 Talbot Imaging

The Talbot effect is an interesting phenomenon that occurs in the Fresnel diffraction region for periodic structures with large periods.[21–25] When a plane

Downloaded From: https://www.spiedigitallibrary.org/ebooks/ on 27 Feb 2022
Terms of Use: https://www.spiedigitallibrary.org/terms-of-use

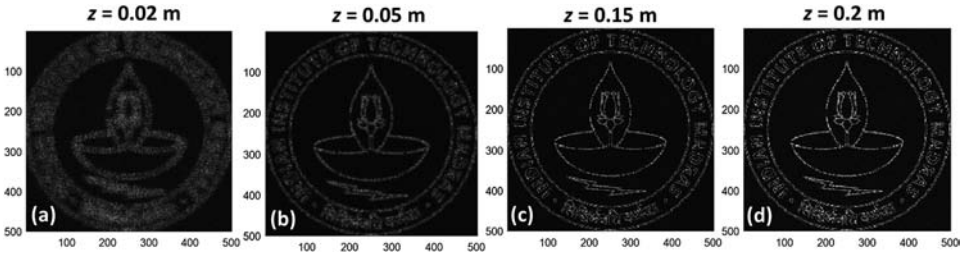

Figure 4.5 Images of the Fresnel diffraction pattern of a DOE generated using Gerchberg-Saxton algorithm with a lensing function of focal length 0.2 m recorded at (a) $z = 0.02$ m, (b) $z = 0.05$ m (c) $z = 0.15$ m and (d) $z = 0.2$ m.

wave illuminates a diffraction grating, an image of the grating occurs at periodic distances along the optical axis. The effect is visible for both amplitude and phase diffraction gratings. Since the image is a copy of the original grating, it is also called a self-image. The distance at which the image repeats is known as the Talbot distance and is given by

$$z_T = \frac{2\Lambda^2}{\lambda}, \tag{4.4}$$

where, Λ is the period of the grating. The pattern also repeats at the distance $z_T/2$ but is shifted laterally by a distance equal to half the period of the grating. The MATLAB code for simulation of the Talbot effect, as seen with an amplitude grating, is shown in Table 4.5.

An image of the simulated grating is shown in Fig. 4.6(a). The intensity at the quarter, half and full Talbot planes can be seen in Figs. 4.6(b), (c,) and (d), respectively.

At fractional Talbot distances, the grating pattern repeats, albeit with different frequencies. This gives rise to a very beautiful phenomenon called the Talbot carpet.[26,27] The program in Table 4.4 can be modified to calculate and create a Talbot carpet. The authors leave this to the readers as an exercise. It is interesting to play with some of the parameters in the program to see how this Fresnel diffraction changes. For example, decreasing the period makes the Talbot effect difficult to observe, as the overlap of orders happens only very close to the grating. This is schematically shown in Fig. 4.7.

The shaded triangles in Fig. 4.7 indicate the regions of overlap between the first orders. It is clear that there is a larger overlap in the case of the second grating, as Λ_2 is larger; therefore, the diffraction angles are smaller. The decreasing area of overlap at distances farther from the grating can be seen in Figs. 4.6(b), (c), and (d).

Clearly, the Talbot effect will be easier to observe for gratings with large periods. However, when simulating a grating with a large period, the matrix has to be large enough that an adequate number of periods occurs in the

Downloaded From: https://www.spiedigitallibrary.org/ebooks/ on 27 Feb 2022
Terms of Use: https://www.spiedigitallibrary.org/terms-of-use

Table 4.5 MATLAB code for studying the Talbot effect.

```
%program to generate Talbot images of amplitude grating
%Output of this file is very dependent on values of r0, P, N, w
clear all
%constants
    lambda=600e-9; %in m
    k=2*pi/lambda;
% Defining Grating Parameters
    N=2000; %Define Matrix size
    P=75; %Define the period of the grating in pixels
    FF=0.25; %Define fill factor
    period=P*1e-6; %period in distance units
    A=ones(1,N); %Define a Matrix by assigning 1 to all pixels
% Constructing the Grating
    q=1:N;
    A(rem(q,P)<P*FF)=0;
    A=repmat(A,N,1); %replicate the row to create a 2-d grating
% Create a window around the grating of pixel width w
    w=500;
    A(1:w,:)=0;
    A(N-w:N,:)=0;
    A(:,1:w)=0;
    A(:,N-w:N)=0;
% Talbot Distance
    zT=(2*period^2)/lambda;%Talbot distance
%Creating sampled space
    r0=(N/P)*period/2; %radius of input beam
    step=2*r0/(N-1);
    index=-r0:step:r0; %regular spaced points
    [XH,YH]=meshgrid(index,index); %creates grid of points with
    %limits given by index
%run this program at various distances
    dist=[zT/ 4 zT/ 2 zT];
    [m,n]=size(dist);
for count=1:n
  z=dist(count);
  z0=z/zT; %distance in terms of Talbot distance
  a=num2str(z0); %used to label figures
%Observing the grating output in the near-field
  E=(A.*exp((1i*k/(2*z))*(XH.^2+YH.^2)))/(lambda*z);
  E=fftshift(fft2(E));
  I=(abs(E)/(N*N)).*(abs(E)/(N*N)); % Calculating intensity
  figure(count)
  colormap(gray)
  imagesc(I);
end
```

grating, yet the window around the grating has to be large enough to simulate the diffraction at different distances along the optical axis. Readers are encouraged to vary the parameters P, N, and w in the code of Table 4.4, and to observe the resulting changes to the Talbot pattern. The same code can also be modified to simulate the Talbot effect with a phase grating.[28]

Downloaded From: https://www.spiedigitallibrary.org/ebooks/ on 27 Feb 2022
Terms of Use: https://www.spiedigitallibrary.org/terms-of-use

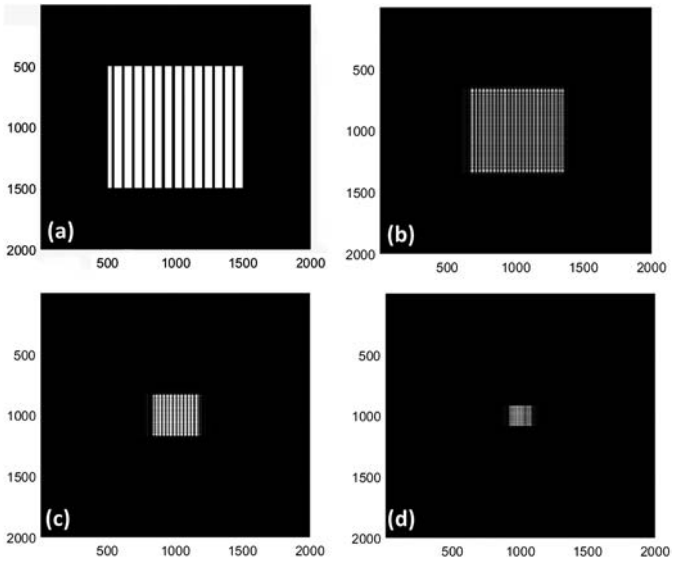

Figure 4.6 (a) Image of the amplitude diffraction grating and its diffraction pattern simulated at (b) $z = 0.25\ z_T$ (c) $z = 0.5\ z_T$, and (d) $z = z_T$.

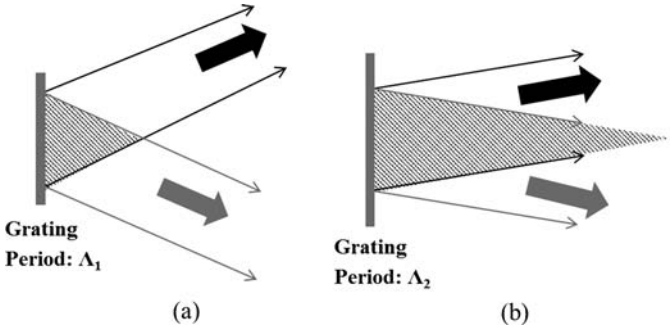

Figure 4.7 Schematic depiction of first orders from gratings with period (a) Λ_1 and (b) Λ_2. The periods are sized such that $\Lambda_1 < \Lambda_2$.

4.3 Conclusions

This chapter describes how to model diffraction in regions other than the far field. Although the programs presented cannot be used to study the region immediately following the DOEs, they can be used to model the diffraction field in an intermediate region (see Chapter 1 for validity of approximations at different axial positions). Two other useful ideas are also discussed, namely, the concept of simulating the axial intensity profiles and the analysis of nonperiodic structures. The technique and procedure presented here can be used for the analysis of the axial intensity profiles for any DOE in the region of the validity of the approximation.

Downloaded From: https://www.spiedigitallibrary.org/ebooks/ on 27 Feb 2022
Terms of Use: https://www.spiedigitallibrary.org/terms-of-use

4.4 Exercises

E.4.1 Calculate the Fresnel diffraction pattern of a blazed axicon at $z = 50$ m with a sampling period of 10λ.

E.4.2 Construct a DOE whose phase profile is given by

$$\Phi = \exp\left[j\left(x + \frac{N}{2}\right)^3 \times 2\pi K\right],$$

where N is the size of the matrix used for simulation, and $K = 5 \times 10^{11}$. Plot the cross section of the intensity at $z = 5$ mm, 10 mm, and 50 mm in the same figure.

E.4.3 Construct a DOE with the linear phase profile of

$$\Phi = \exp\left[j\left(x + \frac{N}{2}\right) \times 2\pi\right],$$

where N is the size of the matrix used for simulation, and plot the cross section of the intensity at $z = 5$ mm, 10 mm, and 50 mm in the same figure. What do you observe?

References

1. J. Dyson, "Circular and spiral diffraction gratings," *Proc. R. Soc. London Ser. A* **248**, 93–106 (1958).
2. J. W. Goodman, *Introduction to Fourier Optics*, Second Edition, McGraw-Hill Companies Inc., New York (1996).
3. B. C. Kress and P. Meyrueis, *Applied Digital Optics*, John Wiley & Sons, Chichester, UK (2009).
4. E. Hecht, *Optics*, Fourth Edition, Addison Wesley, San Francisco (2002).
5. S. Trester, "Computer-simulated Fresnel diffraction using the Fourier transform," *Comput. Sci. Eng.* **1**, 77–83, (1999).
6. J. P. Guigay, "On Fresnel diffraction by one-dimensional periodic objects, with application to structure determination of phase objects," *Opt. Acta* **18**, 677–682 (1971).
7. R. P. Muffoletto, J. M. Tyler, and J. E. Tohline, "Shifted Fresnel diffraction for computational holography," *Opt. Express* **15**, 5631–5640 (2007).
8. R. F. Edgar, "The Fresnel diffraction images of periodic structures," *Opt. Acta* **16**, 281–287 (1969).
9. D. Mendlovic, Z. Zalevsky, and N. Konforti, "Computation considerations and fast algorithms for calculating the diffraction integral," *J. Mod. Opt.* **44**, 407–414 (1997).

Downloaded From: https://www.spiedigitallibrary.org/ebooks/ on 27 Feb 2022
Terms of Use: https://www.spiedigitallibrary.org/terms-of-use

10. D. Mas, J. Garcia, C. Ferreira, L. M. Bernardo, and F. Marinho, "Fast algorithms for free-space diffraction patterns calculation," *Opt. Commun.* **164**, 233–245 (1999).
11. J. A. Stratton and L. J. Chu, "Diffraction theory of electromagnetic waves," *Phys. Rev.* **56**, 99–106 (1939).
12. S. Trester, "Computer simulated holography and computer generated holograms," *Am. J. Phys.* **64**, 474–478 (1996).
13. S. Trester, "Computer-simulated Fresnel holography," *Eur. J. Phys.* **21**, 317–331 (2000).
14. A. Vijayakumar, "Design, Fabrication, and Evaluation of Diffractive Optical Elements for the Generation of Focused Ring Patterns," Doctoral Thesis, Indian Institute of Technology Madras, Chennai, India (2015) [doi: 10.13140/RG.2.2.25996.51847].
15. N. Davidson, A. A. Friesem, and E. Hasman, "Holographic axilens: high resolution and long focal depth," *Opt. Lett.* **16**, 523–525 (1991).
16. J. Sochacki, Z. Jaroszewicz, A. Kołodziejczyk, and S. Bará, "Phase retardation of the uniform-intensity axilens," *Opt. Lett.* **17**, 7–9 (1992).
17. K. B. Rajesh, N. V. Suresh, P. M. Anbarasan, K. Gokulakrishnan, and G. Mahadevan, "Tight focusing of double ring shaped radially polarized beam with high NA lens axicon," *Opt. Laser. Technol.* **43**, 1037–1040 (2011).
18. H.-H. Lin and M.-H. Lu, "Dual-wavelength membrane-based diffractive optical element with extended depth-of-focus for optical pickup head," *Jpn. J. Appl. Phys.* **46**, 5485–5493 (2007).
19. R. Dharmavarapu, A. Vijayakumar, R. Brunner, and S. Bhattacharya, "Composite axilens-axicon diffractive optical elements for generation of ring patterns with high focal depth," *Proc. SPIE* 9753, 97531D (2016) [doi: 10.1117/12.2213037].
20. R. W. Gerchberg and W. O. Saxton, "A practical algorithm for the determination of phase from image and diffraction plane pictures," *Optik* **35**, 227–246 (1972).
21. F. Talbot, "Facts relating to optical science No. IV," *Philos. Mag.* **9**, 401–407 (1836).
22. L. Rayleigh, "On copying diffraction-gratings, and on some phenomenon connected therewith," *Philos. Mag.* **11**, 196–205 (1881).
23. E. A. Hiedemann and M. A. Breazeale, "Secondary interference in the Fresnel zone of gratings," *J. Opt. Soc. Am.* **49**, 372–375 (1959).
24. G. L. Rogers, "Calculations of intermediate Fourier images of a finite line grating on a digital computer, with an application to an unusual case," *Brit. J. Appl. Phys.* **14**, 657–661 (1963).
25. P. Latimer and R. F. Crouse, "Talbot effect reinterpreted," *Appl. Opt.* **31**, 80–89 (1992).

Downloaded From: https://www.spiedigitallibrary.org/ebooks/ on 27 Feb 2022
Terms of Use: https://www.spiedigitallibrary.org/terms-of-use

26. W. B. Case, M. Tomandl, S. Deachapunya, and M. Arndt, "Realization of optical carpets in the Talbot and Talbot–Lau configurations," *Opt. Express* **17**, 20966–20974 (2009).
27. J. Maass, O. Sandfuchs, D. Thomae, A. Gatto, and R. Brunner, "Effective and flexible modeling approach to investigate various 3D Talbot carpets from a spatial finite mask," *J. Eur. Opt. Soc.* **8**, 13004 (2013).
28. A. W. Lohmann and J. A. Thomas, "Making an array illuminator based on the Talbot effect," *Appl. Opt.* **29**, 4337–4340 (1990).

Downloaded From: https://www.spiedigitallibrary.org/ebooks/ on 27 Feb 2022
Terms of Use: https://www.spiedigitallibrary.org/terms-of-use

Chapter 5
Substrate Aberration Correction Techniques and Error Analysis

Aberrations such as spherical aberration, coma, astigmatism, etc., are inevitable in optical systems.[1–3] Hence, numerous aberration correction schemes have been developed to cancel or minimize them.[4–9] Diffractive optical systems are also susceptible to aberrations arising due to inaccurate design and fabrication errors.[10–13] In this chapter, we present a ray tracing procedure that can be used to characterize and correct aberrations. This is followed by two basic aberration correction techniques to cancel the aberration introduced by the thickness of the substrate.

5.1 FZP in Finite Conjugate Mode

The design of a FZP for focusing a plane wavefront to a point, discussed in Chapter 2, is an approximate one based on many assumptions. The accurate expression for the radii of the FZP zones can be obtained from Eq. (3.2) of Chapter 3. By re-arranging the terms in the equation, the radii for an element with a focal length of f is given by

$$r_n = \sqrt{n^2\lambda^2 + 2nf\lambda}, \tag{5.1}$$

where n is the order of each zone, and λ is the wavelength. In the case of a binary FZP, the zones are full period zones; hence, n has to be incremented from 0 in steps of ½.

In many ray optics experiments, it is very common to use the lens equation given by

$$\frac{1}{f} = \frac{1}{u} + \frac{1}{v}, \tag{5.2}$$

where f is the focal length of the lens, and u and v are the object and image distances, respectively. However, this equation was arrived at assuming that

Downloaded From: https://www.spiedigitallibrary.org/ebooks/ on 27 Feb 2022
Terms of Use: https://www.spiedigitallibrary.org/terms-of-use

the angles involved are small, which makes it applicable only in the paraxial case. Therefore, this equation is not valid for larger angles, which arise when the radius of the beam equals the radius of the lens, or for optical systems with small object and image distances.

In other words, a FZP designed for focusing a plane wavefront (infinite conjugate mode) cannot be used for focusing a diverging wavefront (finite conjugate mode) without aberration. In such cases where the paraxial case is violated, it is necessary to design a FZP for the finite conjugate mode.

Finite conjugate mode elements have additional advantages when compared to infinite conjugate mode ones. Most light sources emit diverging wavefronts and will need additional lenses for collimation. By designing the FZP for finite conjugate mode, it is possible to avoid using these additional lenses.

5.1.1 Design of FZPs in finite conjugate mode

The optics configuration for focusing a diverging wavefront is shown in Fig. 5.1. The optical path length equation is given by

$$(u_n + v_n) - (u + v) = n\lambda, \tag{5.3}$$

where

$$u_n = \sqrt{u^2 + r_n^2}, \tag{5.4}$$

$$v_n = \sqrt{v^2 + r_n^2}. \tag{5.5}$$

From Eqs. (5.3)–(5.5), the radii of zones of the FZP designed in finite conjugate mode are given by

$$r_n = \sqrt{\frac{C_1^2 - 4u^2v^2}{4(u^2 + v^2 + C_1)}}, \tag{5.6}$$

where $C_1 = n^2\lambda^2 + 2n\lambda(u + v) + 2uv$. Now let us try to verify the above description of the problems associated with employing a FZP designed for infinite conjugate mode in a finite conjugate system. Two cases are considered with focal distances $u = 1$ mm, $v = 5$ mm and $f = 0.83$ mm; and

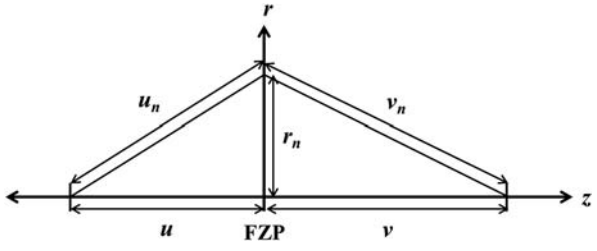

Figure 5.1 Optics configuration for focusing a diverging wavefront using a FZP (reprinted from Ref. 26).

Downloaded From: https://www.spiedigitallibrary.org/ebooks/ on 27 Feb 2022
Terms of Use: https://www.spiedigitallibrary.org/terms-of-use

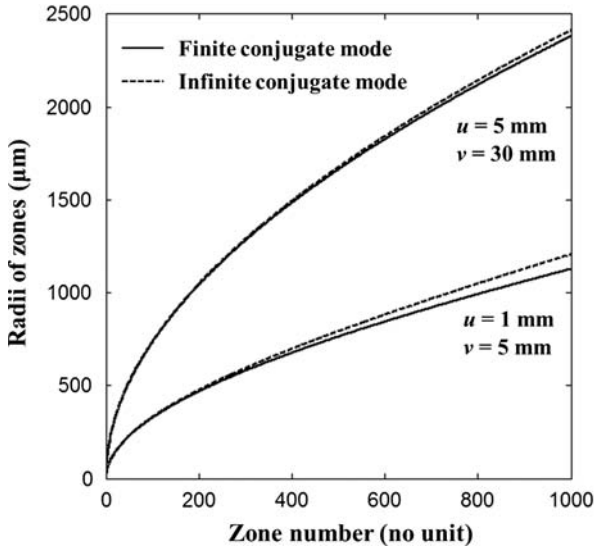

Figure 5.2 Plot of the radii of zones of a FZP as a function of its zone number for finite conjugate mode (solid line) and infinite conjugate mode (dashed line) for $u = 1$ mm, $v = 5$ mm, and $f = 0.83$ mm (bottom lines); and $u = 5$ mm, $v = 30$ mm, and $f = 4.3$ mm (top lines) (reprinted from Ref. 26).

$u = 5$ mm, $v = 30$ mm and $f = 4.3$ mm, respectively. The focal length value is estimated using Eq. (5.2). The radii of zones are plotted for the two cases for n varying from 0 to 1000, as shown in Fig. 5.2.

From Fig. 5.2, it can be noted that there is good overlap between the radii of zones of the FZPs designed for both finite and infinite conjugate modes in the paraxial region, i.e., for small values of the radial coordinate. However, in the nonparaxial case, the two curves separate, showing the possible aberration that could occur if the FZP is designed using Eq. (5.1). In the image plane, the above discrepancy will be reflected as a spot blur and shift of focal plane.

Let us verify this by tracing the rays of light in the image plane for the two cases. The procedure is as follows. Equation (5.1) is substituted in Eq. (5.2) to obtain

$$r_n = \sqrt{n^2\lambda^2 + 2n\left(\frac{uv}{u+v}\right)\lambda}. \tag{5.7}$$

Equations (5.6) and (5.7) are rearranged to calculate the image distance v as a function of the other parameters, as shown in Eqs. (5.8) and (5.9), respectively. In other words, given a FZP with zones located at specific radii and an object distance, the image is located using

$$v_1 = \frac{-B \pm \sqrt{B^2 - 4AC}}{2A}, \tag{5.8}$$

Downloaded From: https://www.spiedigitallibrary.org/ebooks/ on 27 Feb 2022
Terms of Use: https://www.spiedigitallibrary.org/terms-of-use

$$A = 4n^2\lambda^2 + 8un\lambda - 4r_n^2,$$
$$B = 12un^2\lambda^2 + 4n^3\lambda^3 + 8u^2n\lambda - 8r_n^2u - 8r_n^2\lambda n,$$
$$C = n^4\lambda^4 + 4u^2n^2\lambda^2 + 4un^3\lambda^3 - 4r_n^2n^2\lambda^2 - 8r_n^2un\lambda - 4r_n^2u^2;$$

$$v_2 = \frac{u(r_n^2 - n^2\lambda^2)}{\left(n^2\lambda^2 + 2n\lambda u - r_n^2\right)}. \tag{5.9}$$

The MATLAB® code for performing the ray tracing is given in Table 5.1.

The ray tracing images for the above two cases (i.e., with and without paraxial approximation) are shown in Figs. 5.3 and 5.4, respectively.

Table 5.1 MATLAB code for comparing focusing properties of FZP designed with and without paraxial approximation.

```
%%program to compare the FZPs designed with and without paraxial
%%approximation
% Input parameters
    u=5000; % Object distance
    v=30000; % Image distance
    l=0.632; % Lambda-wavelength
% Designing FZPs with n zones
    n=1:200;
    a=n.*n.*l*l+2.*n.*l*(u+v)+2*u*v;
    r=sqrt(((a(n).*a(n))-4*u*u*v*v)./(4.*(a(n)+u*u+v*v)));
    %Radius of zones
    A=(4.*n.*n.*l*l+8.*n*l*u-4.*r(n).*r(n));
    B=(4.*n.^3*l^3+12.*n.*n.*l*l*u+8.*n.*l*u*u-8.*r(n).*r
    (n).*n.*l-8.*r(n).*r(n).*u);
    C=(n.^4.*l.^4+4.*n.*n.*l*l*u*u+4.*n.^3*l^3*u-4.*r(n).*r
    (n)*u*u-4.*r(n).*r(n).*n.*n*l*l-8.*r(n).*r(n).*n*l*u);
    v1=(-B(n)+sqrt(B(n).*B(n)-4.*A(n).*C(n))./(2.*A(n));%
    %Image distance
    the1=atan(r(n)./v1(n));%Angle theta
    v2=u.*(r(n).*r(n)-n.*n.*l*l)./(2.*n.*l*u+n.*n.*l*l-r(n).
    *r(n));
    the2=atan(r(n)./v2(n));%Angle theta
% Ray tracing
for m=1:100; %Ray tracing with 100 points on each ray
  n=m*2;
  for p=1:11;
    v3(p)=(p-1)*3000;
    rr1(p,n)=(v1(n)-v3(p))*tan(the1(n));
    rr2(p,n)=(v2(n)-v3(p))*tan(the2(n));
  end
end
% Display results
n=10:10:200; % Ray tracing display
plot(v3,rr1(:,n),'k','LineWidth',1)
hold on
plot(v3,rr2(:,n),'b','LineWidth',1)
```

Downloaded From: https://www.spiedigitallibrary.org/ebooks/ on 27 Feb 2022
Terms of Use: https://www.spiedigitallibrary.org/terms-of-use

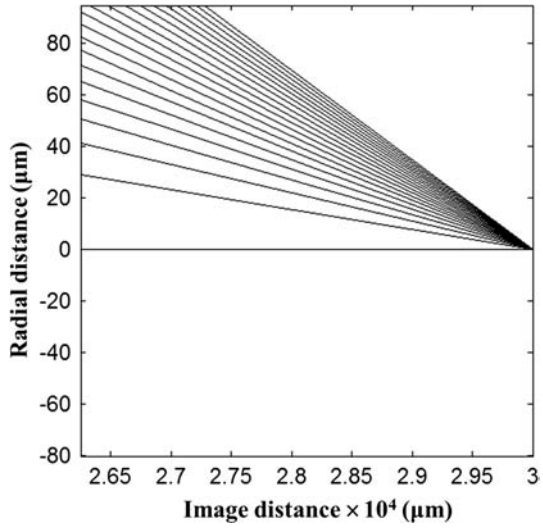

Figure 5.3 Image of the ray tracing at the image plane for a FZP designed using Eq. (5.6).

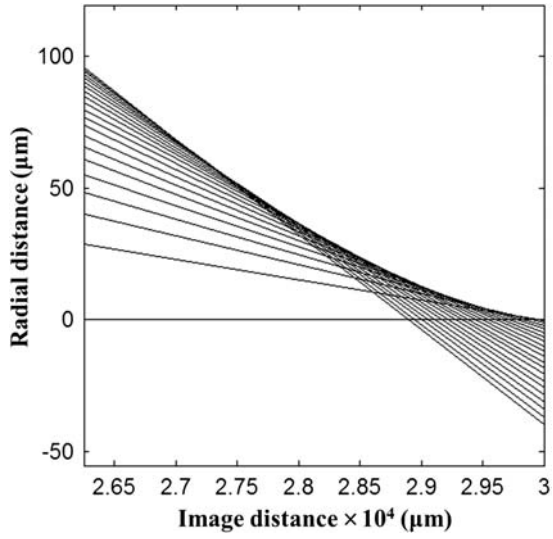

Figure 5.4 Image of the ray tracing at the image plane for a FZP designed using Eq. (5.7).

The magnified images of the focal regions are shown indicating the aberration in the image plane. It can clearly be seen that the FZP designed using Eq. (5.7) has aberrations in the focal plane, resulting in a shift in its image distance and blurring of the spot. If neglected, this one common aberration will result in substantial aberration in the focal plane for a FZP, resulting in focal spot blur and shift in focal plane.

Downloaded From: https://www.spiedigitallibrary.org/ebooks/ on 27 Feb 2022
Terms of Use: https://www.spiedigitallibrary.org/terms-of-use

5.2 Characterization of Substrate Aberrations

The glass substrates on which the DOEs are fabricated can normally be ignored during design. In many cases, the FZPs have been designed for focusing a plane wavefront to a point (infinite conjugate mode).[14–18] In those cases, the aberration introduced by the glass substrate can be easily avoided by making the incident parallel rays of light traverse through the glass substrate first and having the DOE on the other side of the substrate. As the parallel rays are incident normally on the glass substrate, the effect of the substrate can be neglected. However, if the incident parallel rays encounter the DOE (for instance, a FZP) first, followed by the glass substrate, the rays are incident on the glass substrate at different angles and, hence, traverse different optical paths within it. This results in spherical aberration causing a shift of the image plane and blurring of the image. Even then, the aberration is negligible if the thickness of the glass substrate is very small compared to the focal length of the FZP.

As described in the previous section, a FZP designed for infinite conjugate mode requires an additional lens to collimate the light from the source. Hence, the infinite conjugate mode is not suitable for highly compact systems.[19,20] In this case, the above idea of reversing the FZP such that the light rays see the glass substrate first will not help to solve the aberration problem, as the light rays traveling with different angles travel different optical paths within the glass substrate. The propagation of parallel rays and diverging rays through a parallel glass plate is shown in Figs. 5.5(a) and (b), respectively. One technique to solve the aberration problem is to use an ultrathin glass substrate. But, such substrates are extremely difficult to handle during the various fabrication processes such as spin coating, metallization and even optical testing. Therefore, the use of thin substrates is not a very practical solution.

Before solving the aberration problem, it is necessary to understand the effects of the glass substrate. Hence, in this section, the aberration introduced by the glass substrate is characterized first. The effect of the glass substrate is analyzed by designing a FZP for a focal distance without taking into account the thickness of the substrate and then studying its focal properties. Two different design cases of focal distances are considered to understand the magnitude of the aberrations in each case. In case 1, the object distance is larger than the image distance, while in case 2, the image distance is larger than the object distance.

A FZP with a thick glass substrate and illuminated in the finite conjugate mode is shown in Fig. 5.6. Diverging rays of light emanating from the source are incident on the front surface of the glass substrate with refractive index n_g (air–glass interface) at different angles and locations. The angles of refraction inside the glass substrate can be calculated using Snell's law. The angles of refraction are different at different locations, resulting in the rays traversing

Downloaded From: https://www.spiedigitallibrary.org/ebooks/ on 27 Feb 2022
Terms of Use: https://www.spiedigitallibrary.org/terms-of-use

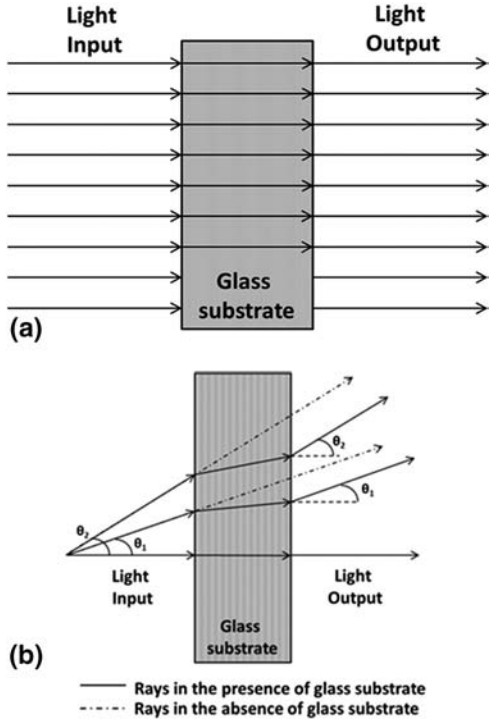

Figure 5.5 (a) Parallel rays and (b) diverging rays propagating through a glass substrate.

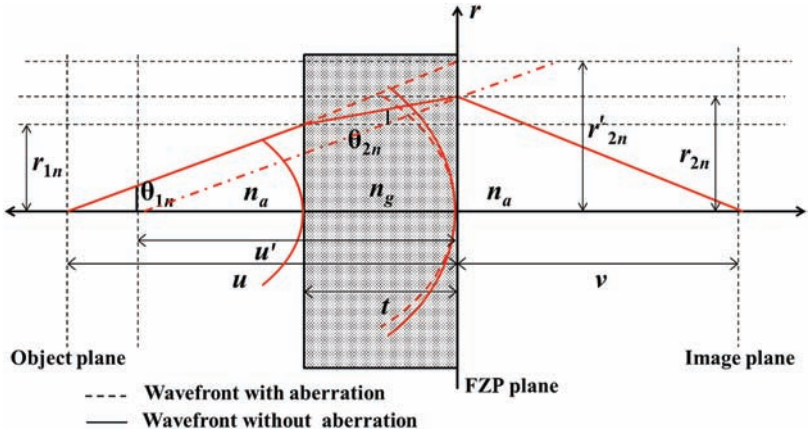

Figure 5.6 Optics configuration for focusing a diverging wavefront using a FZP fabricated on a thick glass substrate (reprinted from Ref. 26).

different optical paths within the glass substrate. The light rays exit the glass–air interface with angles equal to the angles of incidence at the air–glass interface. Hence, the presence of the glass plate only shifts the location of the incident rays depending on their angles of incidence.

Downloaded From: https://www.spiedigitallibrary.org/ebooks/ on 27 Feb 2022
Terms of Use: https://www.spiedigitallibrary.org/terms-of-use

The variable r_{1n} is the distance from the optical axis to the position where the ray emanating from the source with an angle θ_{1n} meets the front surface of the glass substrate. The variable r_{2n} is the distance from the optical axis to the point where the ray emanating from the source with an angle θ_{1n} meets the back surface of the glass substrate. The variable r'_{2n} is the distance from the optical axis to the point where the ray emanating from the source with an angle θ_{1n} would meet the back surface of the glass substrate if it were not present.

From trigonometry we know that

$$\tan\theta_{1n} = \frac{r_{1n}}{u-t} = \frac{r'_{2n}}{u}. \tag{5.10}$$

Applying Snell's law of refraction at the air–glass interface, we obtain

$$n_a \sin\theta_{1n} = n_g \sin\theta_{2n}. \tag{5.11}$$

From Fig. 5.6, we can write

$$r_{2n} = r_{1n} + t\tan\theta_{2n}. \tag{5.12}$$

From Eqs. (5.10), (5.11), and (5.12),

$$r_{2n} = r'_{2n}\left[\frac{u-t}{u}\right] + t\tan\left\{\sin^{-1}\left[\frac{n_a}{n_g(1+u^2/r'^2_{2n})^{1/2}}\right]\right\}. \tag{5.13}$$

As discussed earlier, the presence of the glass substrate does not alter the direction of propagation but shifts the point at which the ray is incident on the FZP. The shift in radial direction at the FZP plane is given by

$$\Delta r = r'_{2n} - r_{2n}. \tag{5.14}$$

Preserving the angle θ_{1n}, the distance between the FZP plane and the source has to be different from u. As a consequence, the presence of the glass substrate generates a virtual source that is shifted from the real source and has a finite spread. The position of the different virtual sources depends on the direction of the rays. The position of the virtual source is given by

$$u'(r'_{2n}) = \frac{r_{2n}}{r'_{2n}}u. \tag{5.15}$$

This is an interesting result. From Eq. (5.15), it can be noted that the presence of the glass substrate generates a virtual source that is shifted away from the source and has a finite blur.

Substituting Eq. (5.13) in Eq. (5.15), the limiting value of u' for $\theta_{1n}\rightarrow 0$ is given by

Downloaded From: https://www.spiedigitallibrary.org/ebooks/ on 27 Feb 2022
Terms of Use: https://www.spiedigitallibrary.org/terms-of-use

$$\lim_{\theta_1 \to 0} u'(r'_{2n}) = u - t + t\frac{n_a}{n_g}. \tag{5.16}$$

When $n_a = n_g$, $u' = u$. From Eqs. (5.15) and (5.16), it is found that:

(a) The presence of the glass substrate generates a virtual source that is spatially away from the real source and has a finite spread. However, for the ray collinear with the optical axis, $\theta_{1n} = 0$, we have a discontinuity where $u' = u$.
(b) The virtual source's spatial shift $(u - u')$ depends only on the thickness and refractive index of the glass substrate.

The aberration in the wavefront at the FZP plane can be quantized as

$$U(r'_{2n}) = \left| u - u'(r'_{2n}) + (u'^2 + r_{2n}^2)^{1/2} - (u^2 + r'^2_{2n})^{1/2} \right|. \tag{5.17}$$

Typical cases were considered as discussed earlier. The element was designed for a wavelength $\lambda = 633$ nm, a substrate thickness $t = 1050$ μm, and refractive index $n_g = 1.5$. In case 1, $u = 5$ mm and $v = 30$ mm, while in case 2, $u = 30$ mm and $v = 5$ mm. A plot of the wavefront shape just before entering the glass substrate, the wavefront shape at the FZL plane in the presence and absence of glass substrate, and the aberration function U as a function of its radial coordinate are shown in Figs. 5.7(a) and (b) for cases 1 and 2, respectively. From Fig. 5.7, it is found that the wavefront with aberration diverges more than the wavefront without aberration.

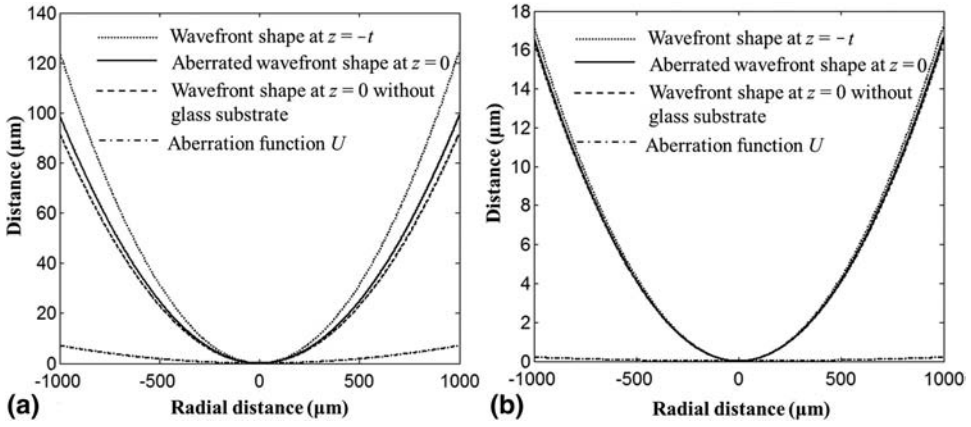

Figure 5.7 Plot of wavefront shapes at $z = -t$ (solid line), z = 0 without glass substrate (dashed line), z = 0 with glass substrate (dotted line), and aberration function U (dashed and dotted line) for (a) $u = 5$ mm and $v = 30$ mm and (b) $u = 30$ mm and $v = 5$ mm [part (a) reprinted from Ref. 26].

Downloaded From: https://www.spiedigitallibrary.org/ebooks/ on 27 Feb 2022
Terms of Use: https://www.spiedigitallibrary.org/terms-of-use

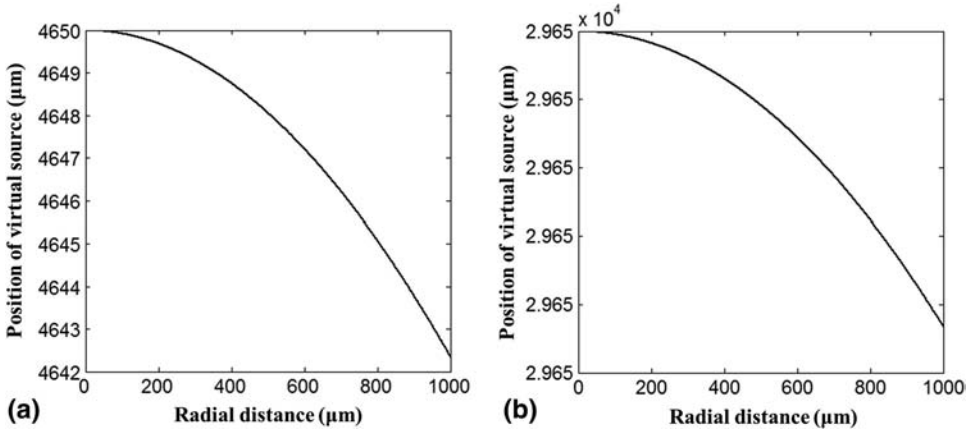

Figure 5.8 Plot of the locations of virtual sources as a function of radial distance for (a) case 1 and (b) case 2 [part (a) reprinted from Ref. 26].

From Figs. 5.7(a) and (b) it can be noted that the wavefront aberration is severe in the case where the object distance is closer to the thickness value of glass substrate, and vice versa. Hence, the wavefront aberration will be much higher when the optics configuration is more compact with $u = 1$ mm and $v = 5$ mm.[19,20] The plots of the locations of the virtual sources as a function of the radial distances for case 1 and case 2 are shown in Figs. 5.8(a) and (b), respectively. The virtual source is not only shifted from the real source, but it also has a finite spread. The limiting value of the shift occurs at $r = 0$, which can be obtained from Eq. (5.16). The limiting values for case 1 and case 2 are 4.650 mm and 29.650 mm, respectively. The spatial spread of the virtual sources for case 1 and case 2 are 7.65 μm and 0.22 μm, respectively. Once again, it is shown that when the focal distances are much larger than the thickness of glass plate, the introduced error is less.

Ray tracing was carried out for these two cases. The MATLAB code for performing the ray tracing is given in Table 5.2. The ray tracing figures are shown in Figs. 5.9 and 5.10 for case 1 and case 2, respectively. The magnified images of the focusing regions are shown and indicate the spread of the virtual sources.

By comparing Fig. 5.9 with Fig. 5.10, it is clear that the effect of aberration is less when the object distance is much larger than the thickness of glass plate, and vice versa. By using Eq. (5.8), it is possible to locate the position of the images for the cases with and without the glass substrate. To estimate the location of the image in the presence of the glass substrate, the variable u can be replaced by the location of the virtual source u'. Plots of the variation in the image distance as a function of the radial distance are shown in Fig. 5.11 and Fig. 5.12 for case 1 and case 2, respectively.

The aberration measured as the shift in the image plane is around 14 mm in case 1, amounting to an error of 46% in the location of the image, while it is

Downloaded From: https://www.spiedigitallibrary.org/ebooks/ on 27 Feb 2022
Terms of Use: https://www.spiedigitallibrary.org/terms-of-use

Table 5.2 MATLAB code for ray tracing from the real and virtual source to the FZP plane.

```
%%program to perform ray tracing from the real and virtual source
%to the FZP plane
% Input Parameters
    u=5000;%Object distance
    t=1050;%Thickness of glass plate
    ng=1.5;%Refractive index of glass plate
    na=1;%Refractive index of air
    N=na/ng;%Refractive index ratio
    U=u*u;
% Calculating the angles of rays and location of real/virtual
%source
for r=1:1000;
  RR(r)=r*r;
  D(r)=(sqrt(1+(U/RR(r))));
  A(r)=(((u-t)/u)*r);
  B(r)=asin(N/D(r));
  r1(r)=A(r)+t*tan(B(r));
  u1(r)=u*(r1(r)/r);
  R1(r)=sqrt(u*u+r*r)-u;
  R3(r)=sqrt((u-t)*(u-t)+r*r)-(u-t);
  R2(r)=sqrt(u1(r)*u1(r)+r1(r)*r1(r))-u1(r);
  delR(r)=R1(r)-R2(r);
  delu(r)=(u-u1(r));
  ratio(r)=r1(r)/r;
  theta(r)=r1(r)/u1(r);
  theta1(r)=r/u;
end
% Ray Tracing and plotting of results
for r=1:100:1000;
for x=1:u1(r)+1;
  y(x)=x-1;
  r11(x)=(x-1)*tan(theta(r));
end
plot(y+(u-u1(r)),r11,'k','LineWidth',1)
hold on
end
for r=1:100:1000;
for x=1:u+1;
  y(x)=x-1;
  r12(x)=(x-1)*tan(theta1(r));
end
    plot(y,r12,'-k')
    hold on
    end
```

only 10 μm with negligible error in case 2. The spreads of the image points in case 1 and case 2 are 350 μm and 0.3 μm, respectively. The analysis can be repeated by performing ray tracing for both cases. Ray tracing is repeated using the procedures shown in Tables 5.1 and 5.2. Results with and without the glass substrate for case 1 and case 2 are shown in Figs. 5.13 and 5.14, respectively. It can be seen that the second case the shift in the image plane is very small (10 μm). The spread is also relatively smaller.

Downloaded From: https://www.spiedigitallibrary.org/ebooks/ on 27 Feb 2022
Terms of Use: https://www.spiedigitallibrary.org/terms-of-use

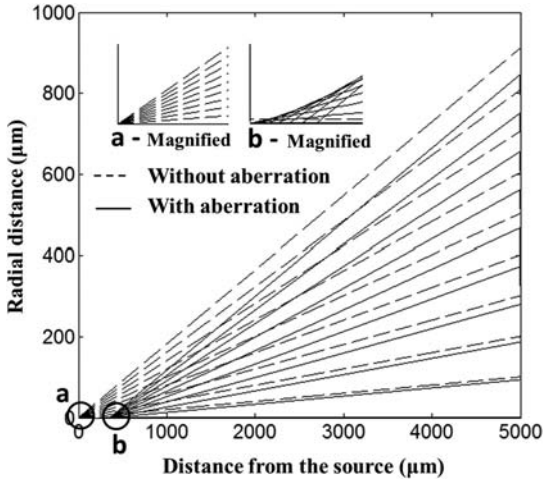

Figure 5.9 Ray tracing of the rays emanating from the real source (dashed line) and virtual source (solid line) generated due to the glass substrate for case 1 (reprinted from Ref. 26).

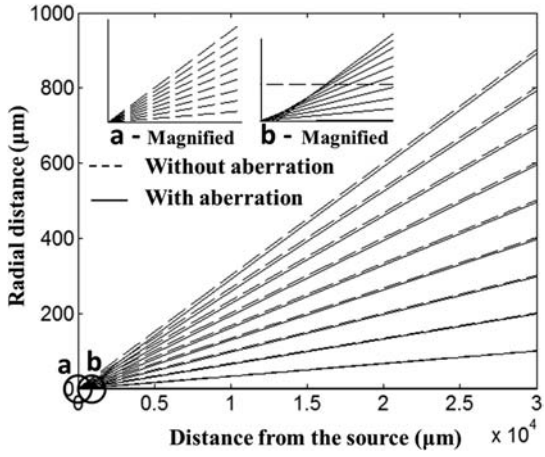

Figure 5.10 Ray tracing of the rays emanating from the real source (dashed line) and virtual source (solid line) generated due to the glass substrate for case 2.

From the above observations it can be noted that for larger optics configurations with object and image distances much larger than the thickness of glass substrate, aberrations are less pronounced, while aberrations are quite severe in compact optics configurations. Aberrations can also be studied in an alternative way by fixing the object and image distances and varying the refractive index or the thickness of the glass plate. Using this method will result in the same conclusion. However, in real applications, it is necessary to design FZPs with compact optics configurations. In such cases, if the glass substrate is not taken into account, the DOE may introduce severe

Downloaded From: https://www.spiedigitallibrary.org/ebooks/ on 27 Feb 2022
Terms of Use: https://www.spiedigitallibrary.org/terms-of-use

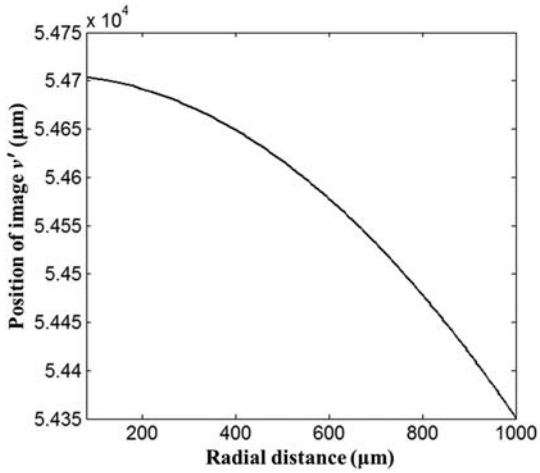

Figure 5.11 Plot of the position of the image for different radial distances in case 1 (reprinted from Ref. 26).

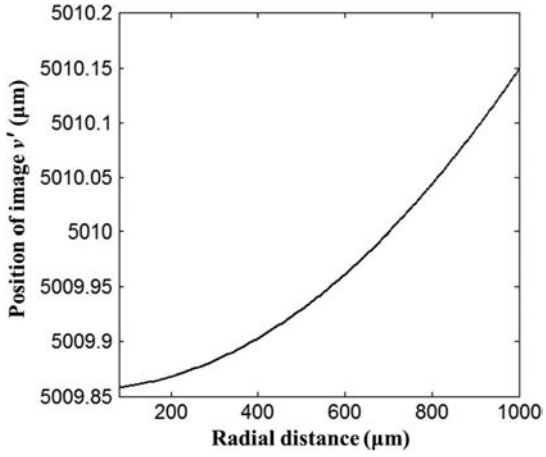

Figure 5.12 Plot of the position of the image for different radial distances in case 2.

aberrations in the system, severely affecting performance. In such cases, it is necessary to cancel the aberrations introduced by the glass substrate.

5.3 Aberration Correction Schemes

Numerous correction schemes are available to overcome the aberrations due to a glass substrate. A pre-distortion pattern can be used to compensate for this type of aberration.[21,22] Alternatively, the pupil size of the objective lens can be varied.[23] In Refs. 21 and 22, the aberration correction was carried out using low-resolution spatial light modulators (SLMs), while in Ref. 23, the corrections was carried out using objective lenses and a variable pupil.

Downloaded From: https://www.spiedigitallibrary.org/ebooks/ on 27 Feb 2022
Terms of Use: https://www.spiedigitallibrary.org/terms-of-use

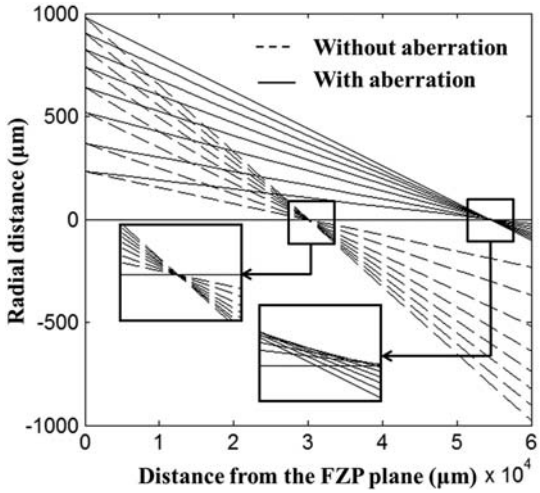

Figure 5.13 Ray tracing of the rays from the FZP plane without the glass plate (dashed line) and with the glass plate (solid line) for case 1 (reprinted from Ref. 26).

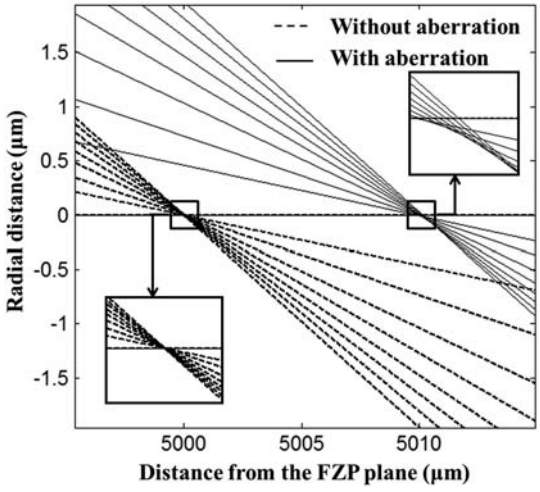

Figure 5.14 Ray tracing of the rays from the FZP plane without the glass plate (dashed line) and with the glass plate (solid line) for case 2.

In some cases, a deformable mirror membrane may be used to correct the aberration.[24] In Ref. 24, the type of aberrations introduced are not anticipated and, therefore, require real-time correction techniques using SLMs or other active devices. In the case of a glass substrate, the aberration is quantifiable *a priori* and can be dealt with in a passive manner. Several simple techniques to compensate such aberrations exist.[25–27]

In this section, two schemes for cancellation of aberrations introduced due to the finite thickness of the glass substrate are presented. In the first scheme,

Downloaded From: https://www.spiedigitallibrary.org/ebooks/ on 27 Feb 2022
Terms of Use: https://www.spiedigitallibrary.org/terms-of-use

the thickness and refractive index of the glass substrate are included in the design of FZP. In the second scheme, a pre-calculated magnification error is deliberately added during fabrication to compensate for the effect of the substrate.

5.3.1 Aberration correction by inclusion of a glass substrate

The presence of a glass substrate generates a virtual source that is spatially shifted from the real source and also has a finite spread, whose position is related to the radial distance in the FZP. A closer look at Figs. 5.6, 5.9, and 5.10 shows that in the finite conjugate mode, the presence of the substrate imitates the action of an axilens (described in Chapter 3 and further discussed in Chapter 7). In the case of an axilens, a plane wave is brought to focus at different focal planes, whose positions depend on the radial distances of the incident beam. Hence, if an axilens is designed for the finite conjugate mode, its behavior will imitate the above case of a FZP with a glass substrate.

In the first scheme, the aberration correction will be carried out by designing an axilens whose object planes are given by u' [Eq. (5.16)]. Therefore, the equation of radii of the zones of the aberration-corrected FZP can be given by Eq. (5.6) by replacing the location of the real source u with the virtual source u'. The modified equation of radii of zones is given by

$$r'_n = \left\{ \frac{C_1'^{\,2} - 4u'(r_n)^2 v^2}{4[u'(r_n)^2 + v^2 + C'_1]} \right\}^{1/2}, \tag{5.18}$$

where $C'_1 = n^2\lambda^2 + 2n\lambda u'(r_n) + 2n\lambda v + 2u'(r_n)v$.

The radii of zones of the FZP are calculated for the design values u, v, and λ. The location of the virtual source u' is calculated from Eq. (5.16), which is substituted in Eq. (5.18). The radii of the FZP are calculated for the above two sets of design values. The plots of the radii of a FZP with and without aberration correction are shown in Figs. 5.15 and 5.16 for case 1 and case 2, respectively.

The radii of zones of the FZP whose design includes the thickness and refractive index of the glass substrate are smaller than those of the zones of the FZP designed without inclusion of glass substrate. In a FZP, the widths of the zones radially decrease away from the center. So rays of light incident away from the axis (i.e., with larger angles) require smaller widths of zones to diffract and bring them to focus at one location. An essential point to be noted is that it appears that the rays passing through the glass substrate have smaller angles compared to the rays passing through air if the glass plate is not present. Therefore, it is expected that the FZP will have larger widths of zones compared to the FZP designed without inclusion of glass substrate. On the contrary, the glass substrate shifts the rays toward the center; as a result,

Downloaded From: https://www.spiedigitallibrary.org/ebooks/ on 27 Feb 2022
Terms of Use: https://www.spiedigitallibrary.org/terms-of-use

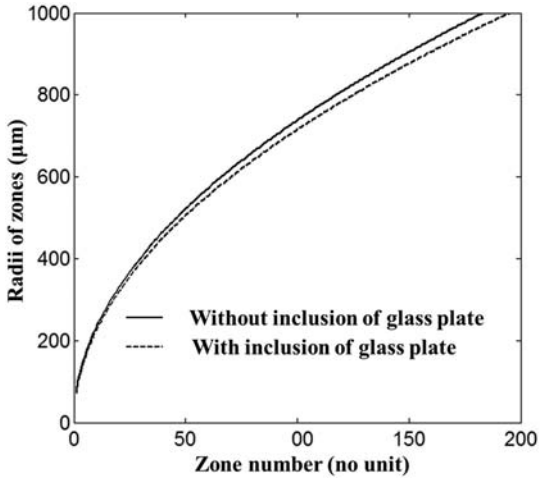

Figure 5.15 Plot of the radii of zones of a FZP designed without (solid line) and with (dashed line) inclusion of a glass plate for case 1 ($u = 5$ mm and $v = 30$ mm) (reprinted from Ref. 26).

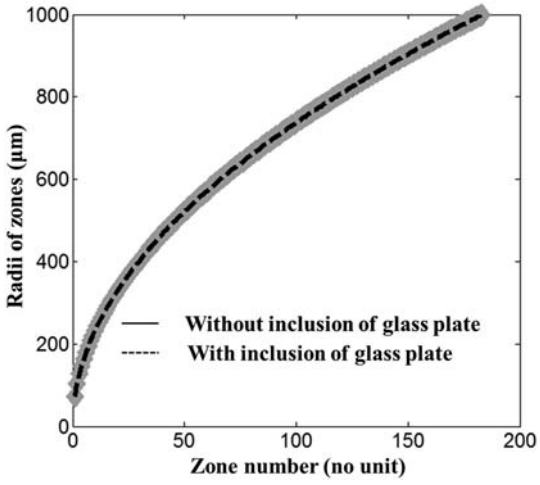

Figure 5.16 Plot of the radii of zones of a FZP designed without (gray line) and with (dashed line) inclusion of a glass plate for case 2 ($u = 30$ mm and $v = 5$ mm).

smaller widths of zones are required compared to the case when the glass plate is not present.

Figure 5.16 shows a good overlap between the plots of the radii of zones of the FZP designed with and without inclusion of the glass substrate, as the aberration introduced in this case is much smaller. The rays are traced from the FZP plane to the image plane. After aberration correction, the magnified image of the image plane shows no aberration, as expected. The ray tracing

Downloaded From: https://www.spiedigitallibrary.org/ebooks/ on 27 Feb 2022
Terms of Use: https://www.spiedigitallibrary.org/terms-of-use

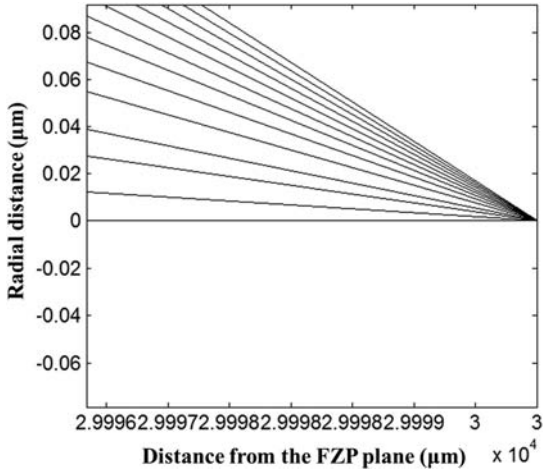

Figure 5.17 Ray tracing of the rays from the FZP plane with a glass plate after aberration correction for case 1 (reprinted from Ref. 26).

image with higher magnification (as seen in the horizontal axis) is shown in Figs. 5.17 and 5.18 for case 1 and case 2, respectively. The above results indicate that this aberration correction method has completely cancelled the aberration introduced by the glass substrate.

5.3.2 Aberration correction during fabrication

In an alternative method, aberration correction is carried out by deliberately introducing pre-calculated fabrication errors. FZPs can be fabricated using different lithography techniques such as photolithography,[18] electron beam lithography,[19,20] and ion beam lithography.[28] Different fabrication errors are

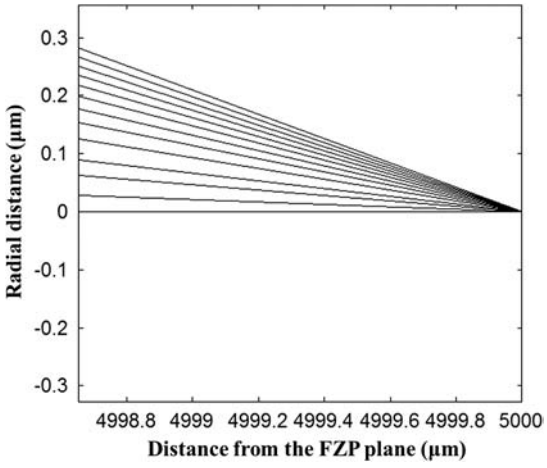

Figure 5.18 Ray tracing of the rays from the FZP plane with a glass plate after aberration correction for case 2.

Downloaded From: https://www.spiedigitallibrary.org/ebooks/ on 27 Feb 2022
Terms of Use: https://www.spiedigitallibrary.org/terms-of-use

associated with each of these techniques. One of the most common errors occurring during fabrication when using photolithography is the magnification error, which results from the gap between the mask plate and the substrate during exposure.[29]

From Eqs. (5.3), (5.4), and (5.5), the phase of the FZP can be given as

$$\Phi_{FZP} = \Phi_{out} - \Phi_{\text{in}} = k\sqrt{r^2 + v^2} + k\sqrt{r^2 + u^2} = \text{const} + 2\ m\pi, \qquad (5.19)$$

where $k = 2\pi/\lambda$. The constant can be estimated by substituting $m = r = 0$:

$$\Phi_{FZP} = k\sqrt{r^2 + v^2} + k\sqrt{r^2 + u^2} = k(u + v) + 2\ m\pi. \qquad (5.20)$$

In an ideal situation, i.e., in the absence of any errors in design, fabrication, and testing, the phases of the input and output waves are the same as those of Φ_{in} and Φ_{out}, respectively. However, in a practical system, this will not be the case. The aberrations or errors can be measured with respect to an output reference wave given by

$$\Phi_R(x,y) = k\sqrt{\rho^2 + v^2}. \qquad (5.21)$$

The phase aberration function is defined as the difference between the phase of the reference and the phase of the output waves, and is given by

$$\begin{aligned}\Phi_A &= \Phi_{out} - \Phi_R = \Phi_{FZP} + \Phi_{\text{in}} - \Phi_R \\ &= k\sqrt{(rM_r)^2 + v^2} + k\sqrt{(rM_r)^2 + u^2} - k\sqrt{r^2 + u^2} - k\sqrt{r^2 + v^2},\end{aligned} \qquad (5.22)$$

where, $M_r = R'/R$ is the radial magnification, R' is the radius of the fabricated device, and R is the expected radius of the device. This aberration function can be used for calculating the fabrication error. The phase aberration function for different values of radial magnification M_r (0.9 to 1.1 in steps of 0.05) is plotted in Fig. 5.19. The phases of the reference wave and the wave with aberration are plotted in Fig. 5.20.

From Figs. 5.7, 5.19, and 5.20, it can be seen that a wavefront with radial magnification error less than 1 has aberration opposite to that introduced by the glass substrate. It therefore ought to be possible to cancel the substrate aberration by introducing a specific magnification error during fabrication of the device. This can be achieved with the introduction of a pre-calculated gap between the substrate and the mask plate. The phase aberration function becomes

$$\Phi_A = k\sqrt{(rM_r)^2 + v^2} + k\sqrt{(rM_r)^2 + u^2} - k\sqrt{r^2 + u'^2} - k\sqrt{r^2 + v^2}. \qquad (5.23)$$

Equation (5.23) is minimized and the value of M_r is calculated as 0.969 for case 1. Ray tracing is performed again to verify the degree of aberration

Downloaded From: https://www.spiedigitallibrary.org/ebooks/ on 27 Feb 2022
Terms of Use: https://www.spiedigitallibrary.org/terms-of-use

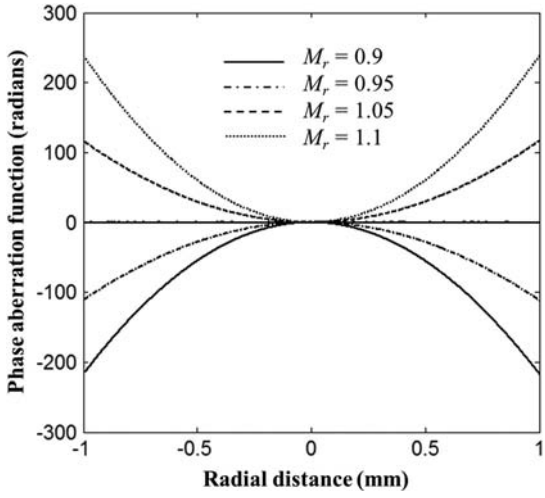

Figure 5.19 Phase aberration function plotted as a function of radial distance for radial magnifications $M_r = 0.9$ (solid line), $M_r = 0.95$ (dashed and dotted), $M_r = 1.05$ (dashed line), and $M_r = 1.1$ (dotted line) (reprinted from Ref. 26).

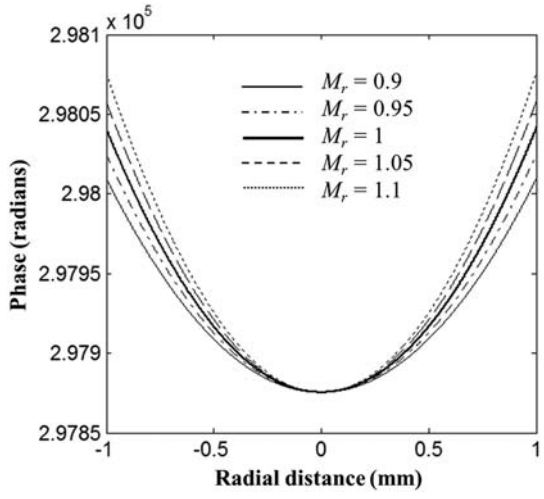

Figure 5.20 Phase of the wave plotted as a function of radial distance for radial magnifications $M_r = 0.9$ (solid line), $M_r = 0.95$ (dashed and dotted line), $M_r = 1$ (thick line), $M_r = 1.05$ (dashed line), and $M_r = 1.1$ (dotted line) (reprinted from Ref. 26).

correction, as shown in Fig. 5.21. It can be noted from this figure that this aberration correction scheme (i.e., introduction of magnification error during fabrication) prevents only the shift of the image plane and not the spatial spread, which is approximately 200 μm for the given experimental parameters. This scheme can be applied to case 2 as well, and a similar effect will be observed.

Downloaded From: https://www.spiedigitallibrary.org/ebooks/ on 27 Feb 2022
Terms of Use: https://www.spiedigitallibrary.org/terms-of-use

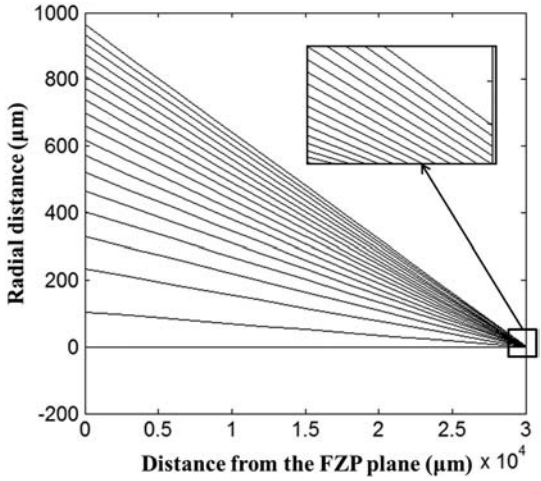

Figure 5.21 Ray tracing of rays emanating from the FZP plane to the image plane for case 1 (reprinted from Ref. 26).

5.3.3 Discussion

From the above observations, it is obvious that the aberration introduced by a glass substrate is more pronounced when the thickness of the glass plate is on the order of the front focal distance. This aberration is, of course, negligible in the infinite conjugate mode or when the front focal distance is much larger than the thickness of the substrate. While this correction may seem attractive, one should keep in mind that configurations with higher magnification will also have larger aberration. The optics configuration given in case 1 is more practical and at the same time has a high magnification of 6 (v/u). This results in an image plane shift of 14 mm. If the magnification of the system were reduced, say from 6 to 1 (i.e., $u = v$), the aberration would also reduce. If $u = v = 5$ mm, the image plane shift would be less than 500 μm, which has only 10% error; if $u = v = 30$ mm, the image plane shift would be only 350 μm, which is only 1% error. Hence, by suitable choice of the front focal distance and the magnification of the system, it is possible to make the aberration effect almost negligible.

5.4 Aberration Analysis in Fabrication and Experiments for FZPs

The aberration characterization described in Section 5.2 can also be used to characterize other aberrations that may occur during experiments. A few of the common errors that occur during experiments are considered for evaluation.

5.4.1 Error in object location along the z direction

The variation in the image location and size due to an error in the location of the object along the z direction is considered. Using Eq. (5.22), the shift in the

Downloaded From: https://www.spiedigitallibrary.org/ebooks/ on 27 Feb 2022
Terms of Use: https://www.spiedigitallibrary.org/terms-of-use

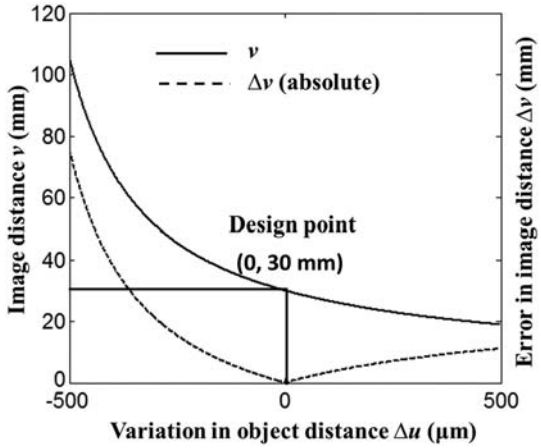

Figure 5.22 Plot of the location of the image plane (solid line) and error in image plane (dotted line) for variation in object distances.

location of the image plane is plotted for an error of ±500 μm in object distance, as shown in Fig. 5.22 for case 1. The FZP with aberration correction for the glass substrate is designed and the radii of zones are calculated. The error in the image distance is calculated by solving v for different values of the object distances u and for the radii of zones calculated for $u = 5$ mm. The MATLAB code for this aberration correction is given in Table 5.3.

Figure 5.22, shows that the optics configuration is highly sensitive to errors. For an error of –500 μm, the image location varies as much as 70 mm, while for an error of +500 μm, the image location shifts by only 10 mm. This asymmetry can be easily understood from the basic thin lens equation ($1/u + 1/v = 1/f$), which is a rough approximation (paraxial) of the design. Assuming that the translational stage has a resolution of 10 μm along all the three axes, the expected error in the location of image plane is <0.5 mm. The variation in magnification (v/u) of the system due to the change in image distance and an error in object distance is plotted as shown in Fig. 5.23. The $1/e^2$ diameter of the spot varies with the error in the magnification of the system and the diffraction-limited spot. The variation of the $1/e^2$ diameter of the spot for an error in the object position is plotted as shown in Fig. 5.24, assuming that the $1/e^2$ diameter at the waist is 5.5 μm. The spot size varies from 72 μm to 279 μm for an error of –500 μm, while it varies from 42 μm to 72 μm for an error of +500 μm. For an error of a 10-μm shift that can occur with the 3-axis stages, the error in the spot size is around 1 μm.

The above analysis was repeated for a case without a glass plate and aberration correction. It was found that the aberration-corrected system is more sensitive to errors compared to the case without a glass plate. As discussed earlier, the high sensitivity is due to the facts that (1) the object distance is closer to the thickness of glass plate and (2) the magnification of

Downloaded From: https://www.spiedigitallibrary.org/ebooks/ on 27 Feb 2022
Terms of Use: https://www.spiedigitallibrary.org/terms-of-use

Table 5.3 MATLAB code for analysis of aberration due to error in object location along the z direction.

```
%%program to analyze the aberration due to error in object
%location in z direction
% Input Parameters
    u1=5000; % Object distance in micrometers
    v=30000; % Image distance in micrometers
    l=0.632; % Wavelength in micrometers
    t=1050; % Thickness of glass substrate in micrometers
    na=1; % Refractive index of air
    ng=1.5; % Refractive index of glass
    n=1; % Zone number
    a=n*n*l*l+2*n*l*(u1+v)+2*u1*v;
    r=sqrt(((a*a)-4*u1*u1*v*v)/(4*(a+u1*u1+v*v))); %Radius of
    first zone before aberration correction
    theta=atan(r/u1);
    rr=r*((u1-t)/u1);
    r1=rr+t*tan(asin(na/ng*(sin(atan(r/u1)))));
    u2=u1*(r1/r);
    a1=n*n*l*l+2*n*l*(u2+v)+2*u2*v;
    rr=sqrt(((a1*a1)-4*u2*u2*v*v)/(4*(a1+u2*u2+v*v)));
    % Radius of first zone after aberration correction
%Error calculation
    s=1:1000;
    u4=s-501;
    u=5000+u4(s);
    u3=u(s).*(r1/r);
    b=(4*n*n*l*l+8*n*l.*u3(s)-4*rr*rr);
    c=(4*n^3*l^3+12*n*n*l*l.*u3(s)+8*n*l.*u3(s).*u3(s)-
    8*rr*rr*n*l-8*rr*rr.*u3(s));
    d=(n^4*l^4+4*n*n*l*l.*u3(s).*u3(s)+4*n^.3*l^3.*u3(s)-
    4*rr*rr.*u3(s).*u3(s)-4*rr*rr*n*n*l*l-8*rr*rr*n*l.*u3(s));
    v1=(-c(s)+sqrt(c(s).*c(s)-4.*b(s).*d(s))./(2.*b(s));
    ve=abs(v1(s)-v);
%Display results
    plot(u4,v1/1000)
    hold on
    plot(u4,ve/1000,'r')
```

the system is high. The same procedure may be repeated for case 2, and the effect of aberration with variations in image distance, magnification, and $1/e^2$ diameter of the beam may be studied.

In the above cases, only one variation was estimated: the variation in image location and size due to an error in the object position. It is however necessary to include the aberration introduced in the system, as the system was designed for one set of u and v values but was implemented using a different set of u and v values. This not only causes a shift but also introduces a blur that can be understood from the earlier descriptions. The ray tracing at the image plane for errors of –500 μm and 500 μm are shown in Figs. 5.25(a) and (b), respectively.

Downloaded From: https://www.spiedigitallibrary.org/ebooks/ on 27 Feb 2022
Terms of Use: https://www.spiedigitallibrary.org/terms-of-use

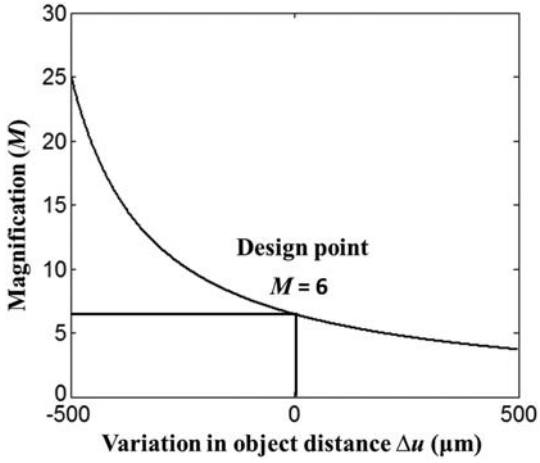

Figure 5.23 Plot of the magnification of the optics configuration for variation in object distances.

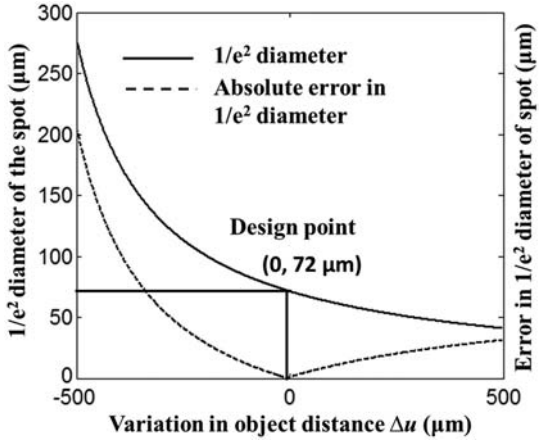

Figure 5.24 Plot of the location of the $1/e^2$ diameter (solid line) and error in the $1/e^2$ diameter (dotted line) for variation in object distances.

5.4.2 Error due to a shift in the location of zones

A FZP is designed using computer-aided design (CAD) software and later fabricated using a lithography system. Let us consider the case when the radii of zones are radially shifted inward or outward. We assume that the average shift in the location of zones introduced in the system during design and fabrication is around 100 nm. The simulation is carried out assuming that the zones are randomly shifted inward or outward by 100 nm while some zones are not shifted. Ray tracing was performed to understand the aberration in the image plane, as shown in Fig. 5.26. The ray tracing image is shown in Fig. 5.26. There is a shift of 2 μm on either side, corresponding to the shift in

Downloaded From: https://www.spiedigitallibrary.org/ebooks/ on 27 Feb 2022
Terms of Use: https://www.spiedigitallibrary.org/terms-of-use

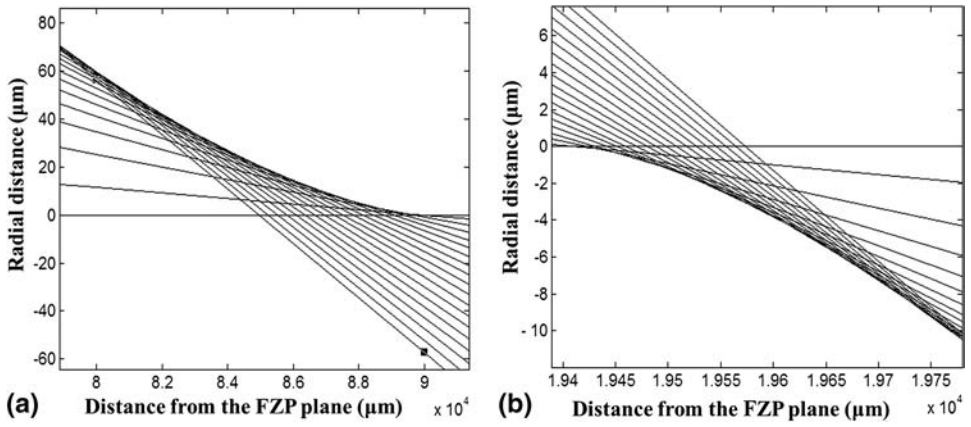

Figure 5.25 Ray tracing of rays emanating from the FZP plane when the object distance has an error of (a) –500 μm and (b) 500 μm.

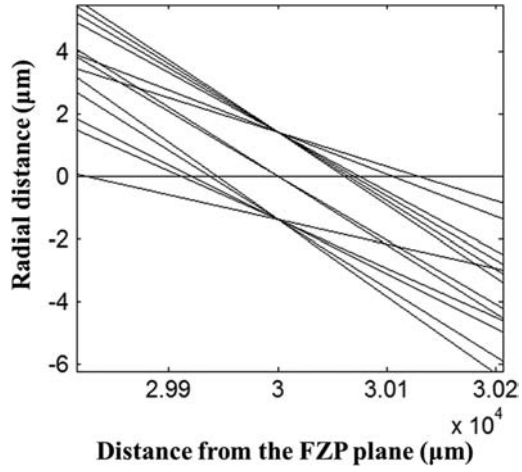

Figure 5.26 Ray tracing of rays emanating from the FZP plane when the zones are radially shifted by ±100 nm with random zone number.

location of zones by ±100 nm. This aberration will result in increase of spot size in the image plane, resulting in a blur.

5.4.3 Error due to a lateral shift in the object location

Ideally, during evaluation of the element, the element's center is aligned with the center of the source. In this section, the effect of misalignment of the source's center with the element's center in the image location is analyzed. There is definitely a spot blur at the image plane, but in this section, only the shift in location of the image in the image plane is considered. The object position is shifted as high as ±500 μm and the impact on the image plane is analyzed. The magnification of the system is 6.4 (v/u'). The image shift is given

Downloaded From: https://www.spiedigitallibrary.org/ebooks/ on 27 Feb 2022
Terms of Use: https://www.spiedigitallibrary.org/terms-of-use

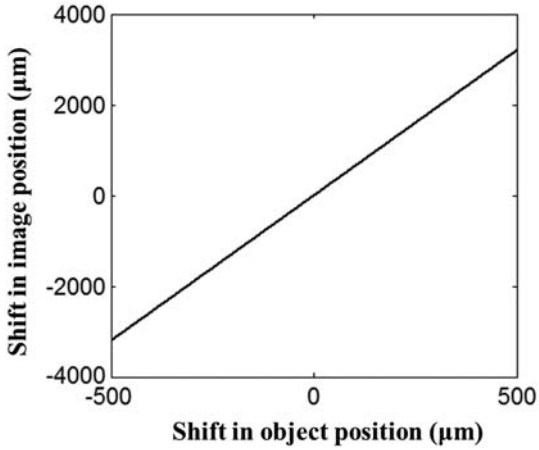

Figure 5.27 Plot of image shift from the optical axis in the image plane for a variation in the object shift from the optical axis in the object plane.

by the product of the object location shift and the magnification of the system, which gives an approximately linear relationship between the image and object location shift, as plotted in Fig. 5.27.

5.4.4 Error in resist thickness and duty ratio

In earlier sections, errors relating to the image size and image profile, and the transverse and longitudinal shift in the location of the image were analyzed. In particular, we looked at errors caused by the location of the object and a mismatch between design and fabrication. In this section, the variation in the efficiency values due to an error in the thickness of the resist is analyzed. The efficiency of a diffractive system is defined as the ratio of the optical power in the first diffraction order to the total optical power incident on the system. The diameter of the device is selected such that there is >98% throughput (neglecting Fresnel reflection losses). The efficiency of the system can be estimated for different values of phase height using the Fourier coefficients of the system, as was described in previous chapters. A plot of the normalized intensity in the 0^{th}, 1^{st}, and 2^{nd} diffraction orders as a function of the error in resist thickness is shown in Fig. 5.28.

Another error in fabrication that is highly sensitive to the development time and the electron beam dose is the duty ratio. The effect of the duty ratio error on the efficiency of the 1^{st} diffraction order is shown in Fig. 5.29. The duty ratio error is varied from 0% to 20%, and the efficiency in the 1^{st} diffraction order is calculated. It is found that for an error of 10%, the efficiency drops by 2.5%, while it drops by 10% for an error of 20% in the duty ratio. The simulation was carried out assuming no error in the resist thickness value. The MATLAB codes for design of DOEs with varying duty ratio are given in Chapter 2.

Downloaded From: https://www.spiedigitallibrary.org/ebooks/ on 27 Feb 2022
Terms of Use: https://www.spiedigitallibrary.org/terms-of-use

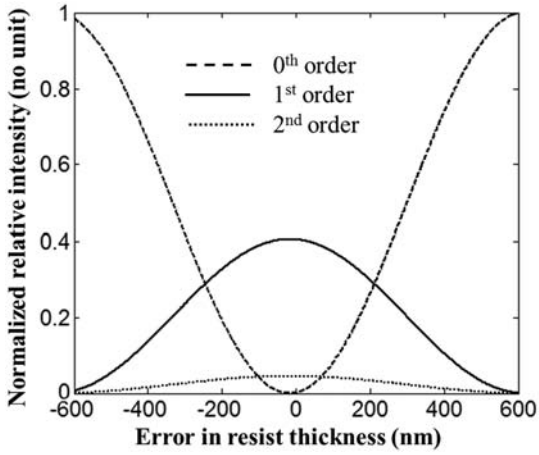

Figure 5.28 Plot of the normalized relative intensity of the 0th (dashed line), 1st (solid line), and 2nd (dotted line) diffraction orders as a function of error in resist thickness.

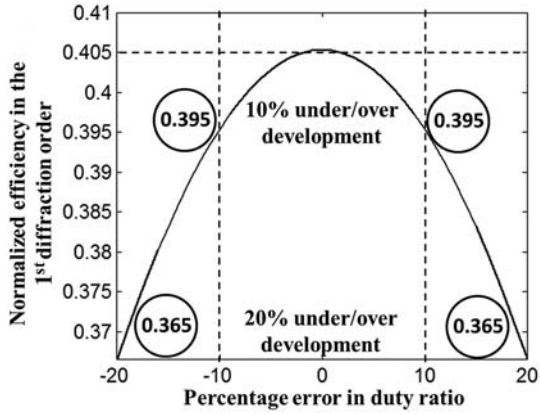

Figure 5.29 Plot of the normalized relative intensity of the 1st diffraction order for different percentages of error in the duty ratio of the resist.

5.5 Conclusions

In the above analysis, different types of errors and their influence on various parameters are studied independently. To characterize an optics configuration, it is necessary to understand the cumulative effect of all of the above errors.

For instance, the thickness of the resist and the element duty ratio control only the efficiency of light in various diffraction orders but do not have any influence on the shift of image plane or blur of spot. The location of zones and experimental errors do not affect the efficiency of the device but introduce aberrations such as image plane shift along the longitudinal or transverse directions and blur.

Downloaded From: https://www.spiedigitallibrary.org/ebooks/ on 27 Feb 2022
Terms of Use: https://www.spiedigitallibrary.org/terms-of-use

The above procedure has been used to demonstrate different types of errors in a simple FZP designed in finite conjugate mode. Most of the discussion on error analysis of FZPs, such as fabrication errors, applies to other DOEs as well. One of the parameters to be analyzed in the case of a simple DOE such as a grating or an axicon is the error in the period of the element. This simple analysis can be carried out using the grating equation and trigonometry. By applying the same method and modification of MATLAB codes, the aberration analysis can be easily extended to analyze a FZP in other configurations, such as the infinite conjugate mode, as well as other DOEs. By using the techniques described, it is possible to characterize and correct most of the anticipated errors during design, fabrication, and evaluation. Some of the aberrations such as the magnification error during fabrication can be used to our advantage to cancel other aberrations present in the system. There are other aberrations as well that are opposite to another and that can be engineered for perfect cancellation.

5.6 Exercises

E.5.1 Design a ring FZP in finite conjugate mode and perform the aberration correction for the glass substrate on which it is fabricated.

E.5.2 Design an FZP that includes aberration correction to compensate for the ring holder (made from a polymer) on which it is mounted. The polymer ring has a thickness of 2000 μm, refractive index of 1.5, and radii of $r_1 = 500$ μm and $r_1 = 700$ μm. The FZP has dimensions of $u = 30$ mm and $v = 5$ mm, and the glass substrate thickness is $t = 1$ mm. The schematic is shown below.

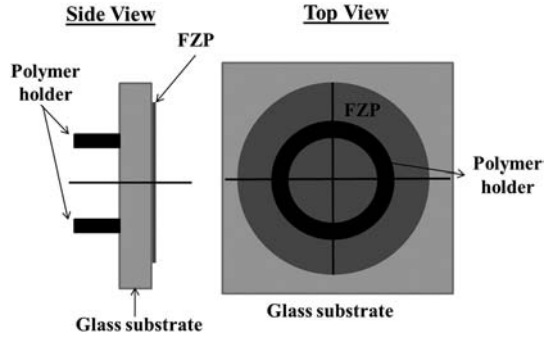

E.5.3 Design an FZP to be fabricated on a glass substrate, whose thickness varies from 1 mm to 2 mm over a radial distance of 1 mm. Compare the radii of zones with those of an FZP designed to be fabricated on a glass substrate with a constant thickness of 1 mm. Note: In this way, it is possible to include a refractive phase with a diffractive element.

Downloaded From: https://www.spiedigitallibrary.org/ebooks/ on 27 Feb 2022
Terms of Use: https://www.spiedigitallibrary.org/terms-of-use

References

1. J. W. Goodman, *Introduction to Fourier Optics*, Second Edition, McGraw-Hill Companies Inc., New York (1996).
2. F. A. Jenkins and H. E. White, *Fundamentals of Optics*, Fourth Edition, McGraw-Hill Companies Inc., New York (2001).
3. P. L. Knight and A. Miller, *The Ray and Wave Theory of Lenses*, Cambridge University Press, Cambridge (1995).
4. J. Upatnieks, A. Vander Lugt, and E. Leith, "Correction of lens aberrations by means of holograms," *Appl. Opt.* **5**, 589–593 (1966).
5. M. J. Kidger, *Fundamental Optical Design*, SPIE Press, Bellingham, Washington (2001) [doi: 10.1117/3.397107].
6. J. E. Ward, D. C. Auth, and F. P. Carlson, "Lens aberration correction by holography," *Appl. Opt.* **10**, 896–900 (1971).
7. N. López-Gil, H. C. Howland, B. Howland, N. Charman, and R. Applegate, "Generation of third-order spherical and coma aberrations by use of radially symmetrical fourth-order lenses," *J. Opt. Soc. Am. A* **15**, 2563–2571 (1998).
8. D. C. Leiner and R. Prescott, "Correction of chromatic aberrations in GRIN endoscopes," *Appl. Opt.* **22**, 383–386 (1983).
9. R. E. Hopkins, C. A. McCarthy, and R. Walters, "Automatic correction of third-order aberrations," *J. Opt. Soc. Am.* **45**, 363–363 (1955).
10. U. Dutta and L. Hazra, "Monochromatic primary aberrations of a diffractive lens on a finite substrate," *Appl. Opt.* **49**, 3613–3621 (2010).
11. U. Dutta and L. Hazra, "Primary chromatic aberrations of a diffractive lens on finite substrate," *Appl. Opt.* **51**, 494–497 (2012).
12. J. Sung, M. Pitchumani, and E. G. Johnson, "Aberration measurement of photolithographic lenses by use of hybrid diffractive photomasks," *Appl. Opt.* **42**, 1987–1995 (2003).
13. N. Bokor and N. Davidson, "Aberration-free imaging with an aplanatic curved diffractive element," *Appl. Opt.* **40**, 5825–5829 (2001).
14. T. Fujita, H. Nishihara, and J. Koyama, "Blazed gratings and Fresnel lenses fabricated by electron-beam lithography," *Opt. Lett.* **7**, 578–580 (1982).
15. K. Kodate, T. Kamiya, Y. Okada, and H. Takenaka, "Focusing characteristics of high efficiency Fresnel zone plate fabricated by deep ultraviolet lithography," *Jpn. J. Appl. Phys.* **25**, 223–227 (1986).
16. T. Shiono, M. Kitagawa, K. Setsune, and T. Mitsuyu, "Reflection micro-Fresnel lenses and their use in an integrated focus sensor," *Appl. Opt.* **28**, 3434–3442 (1989).
17. T. Shiono and K. Setsune, "Blazed reflection micro-Fresnel lenses fabricated by electron-beam direct writing and dry development," *Opt. Lett.* **15**, 84–86 (1990).

Downloaded From: https://www.spiedigitallibrary.org/ebooks/ on 27 Feb 2022
Terms of Use: https://www.spiedigitallibrary.org/terms-of-use

18. A. Vijayakumar and S. Bhattacharya, "Analysis of versatile phase zone plates," *Proc. SPIE* **8173**, 817316 (2010) [doi: 10.1117/12.897564].
19. A. Vijayakumar and S. Bhattacharya, "Design, fabrication, and evaluation of a multilevel spiral-phase Fresnel zone plate for optical trapping," *Appl. Opt.* **51**, 6038–6044 (2012).
20. A. Vijayakumar, M. Uemukai, and T. Suhara, "Phase-shifted Fresnel zone lenses for photomixing generation of coherent THz wave," *Jpn. J. Appl. Phys.* **51**, 070206 (2012).
21. H. Itoh, N. Matsumoto, and T. Inoue, "Spherical aberration correction suitable for a wavefront controller," *Opt. Express* **17**, 14367–14373 (2009).
22. D. Iwaniuk, P. Rastogi, and E. Hack, "Correcting spherical aberrations induced by an unknown medium through determination of its refractive index and thickness," *Opt. Express* **19**, 19407–19414 (2011).
23. M. J. Booth and T. Wilson, "Strategies for the compensation of specimen-induced spherical aberration in confocal microscopy of skin," *J. Microsc.* **200**(Pt 1), 68–74 (2000).
24. M. J. Booth, M. Schwertner, T. Wilson, M. Nakano, Y. Kawata, M. Nakabayashi, and S. Miyata, "Predictive aberration correction for multilayer optical data storage," *Appl. Phys. Lett.* **88**, 031109 (2006).
25. S. Ura, T. Suhara, and H. Nishihara, "Aberration characterizations of a focusing grating coupler in an integrated-optic disk pickup device," *Appl. Opt.* **26**, 4777–4782 (1987).
26. A. Vijayakumar and S. Bhattacharya, "Characterization and correction of spherical aberration due to glass substrate in the design and fabrication of Fresnel zone lenses," *Appl. Opt.* **52**, 5932–5940 (2013).
27. L. Hazra, N. Y. Han, and C. Delisle, "Effects of the thickness of the substrate on the performance and the design of planar kinoform lenses for axial stigmatism in finite-conjugate imaging," *Can. J. Phys.* **71**, 434–441 (1993).
28. M. John, "Focused ion beam technology and applications," *J. Vac. Sci. Technol. B* **5**, 469–495 (2009).
29. A. Vijayakumar, "Design, Fabrication and Evaluation of Diffractive Optical Elements for the Generation of Focused Ring Patterns," Doctoral Thesis, Indian Institute of Technology Madras, Chennai, India (2015) [doi: 10.13140/RG.2.2.25996.51847].

Downloaded From: https://www.spiedigitallibrary.org/ebooks/ on 27 Feb 2022
Terms of Use: https://www.spiedigitallibrary.org/terms-of-use

Chapter 6
Multifunctional Diffractive Optical Elements

Multifunctional DOEs are elements that can simultaneously perform various optical operations. The terms multifunctional and multiplexed diffractive optics come under the same category. Multiplexing refers primarily to spatial as well as wavelength multiplexing, where it is possible to encode several functions on the same element but extract one specific behavior at a time. In the case of phase multiplexing, however, rather than extracting one single behavior from the element independently, several functions can be combined and accessed simultaneously. Although, the above definition is used more commonly in computer-generated holograms (CGHs), we will use the same terminology to talk about diffractive optical elements.[1,2] Multifunctionality due to tenability—achievable, for example, when the DOE is created with a SLM or using micro-electromechanical systems (MEMSs)—was not taken into account in this chapter. However, all of the multifunctional static DOEs described in this chapter can also be created using a SLM.

There are various types of phase-multiplexed DOEs. One well-known multiplexing technique is to use multiple DOEs or ROEs with different functions.[3] Reports of beam shaping using multiple DOEs have been published.[4,5] Bandpass filters with two DOEs fabricated as two layers have also been reported.[6] In some cases, it is necessary to construct hybrid optical elements such as refractive–diffractive[7–9] or reflective–diffractive[10] combinations for different applications. While the above constructions are possible, there are many concerns that must be duly noted. In the case of multiple DOEs or ROEs, the optics configuration becomes bulky. The many optical components introduce problems during optical alignment and increase the overall weight of the system. In the case of hybrid DOEs, fabrication of the device is quite complex, as it involves fabricating high-resolution DOEs on curved surfaces.

Alternative techniques were developed to create multiplexed DOEs by combining the phase functions of two DOEs or a DOE and a ROE.[11–15]

Downloaded From: https://www.spiedigitallibrary.org/ebooks/ on 27 Feb 2022
Terms of Use: https://www.spiedigitallibrary.org/terms-of-use

In this case, the device is designed and fabricated as a single element, thereby, reducing the size and weight of the system and eliminating the problems associated with optical alignment. However, the efficiency of the multiplexed DOE is diminished when it is designed using certain techniques. The practice of combining two functions in a composite DOE leads to the development of some interesting properties, which will be discussed in detail in this chapter.

Two techniques, namely, the modulo-2π phase addition technique and the analog technique for designing multifunctional or composite DOEs are presented. These are used for design of amplitude-only DOEs,[12,13] phase-only DOEs,[11] and hybrid DOEs with both amplitude as well as phase variations.[15] Structures can be either binary or have blazed phase profiles.

6.1 Modulo-2π Phase Addition Technique

As the name suggests, the modulo-2π phase addition technique is a simple technique for combining two phase functions. The phase addition of two phase functions, Φ_1 and Φ_2, using modulo-2π phase addition technique is given by

$$\Phi = [\Phi_1 + \Phi_2]_{2\pi}. \tag{6.1}$$

Considering two binary phase profiles, phase addition can be achieved by the well-known X-OR (exclusive OR) binary operation. You may recall that this technique was introduced in Chapter 2 for construction of a checkerboard phase grating. The simplest multifunctional DOE is a checkerboard grating, which can simultaneously split light in both the x and y directions. Using the X-OR technique, any two binary DOEs can be combined. Before applying this technique to other DOEs, we present the procedure for combining DOEs using the modulo-2π phase addition method and the advantages of this method.

6.1.1 Comparison of a multifunctional binary DOE with two binary DOEs in tandem

In order to understand the advantages of the modulo-2π phase addition method, we compare the functioning of two DOEs in tandem with that of a multifunctional DOE. The basic differences between two DOEs and a single DOE can be easily realized. Advantages such as reduced space requirements and optical alignment are obvious. A deeper analysis, however, reveals additional advantages.

A 2D grating, denoted by Φ_{1D+1D}, was created by placing two 1D gratings Φ_{G1} and Φ_{G2} one after the other but orthogonal to each other. The period of both the gratings is assumed to be equal. The phase of the 2D grating is then given by

Downloaded From: https://www.spiedigitallibrary.org/ebooks/ on 27 Feb 2022
Terms of Use: https://www.spiedigitallibrary.org/terms-of-use

$$\Phi_{1D+1D} = \Phi_{G1} + \Phi_{G2}, \tag{6.2}$$

where the phase functions of the two gratings are given by

$$\Phi_{G1}(x,y) = \begin{cases} \Phi_1 & 0 \le x \le \frac{\Lambda}{2} \\ 0 & \frac{\Lambda}{2} \le x \le \Lambda \end{cases} \quad \Phi_{G1}(x) = \Phi_{G1}(x+\Lambda), \tag{6.3}$$

$$\Phi_{G2}(x,y) = \begin{cases} \Phi_2 & 0 \le y \le \frac{\Lambda}{2} \\ 0 & \frac{\Lambda}{2} \le y \le \Lambda \end{cases} \quad \Phi_{G2}(y) = \Phi_{G2}(y+\Lambda), \tag{6.4}$$

where Λ is the period of the grating.

In general, $\Phi_{1,2} = \pi + \delta_{1,2}$, where $\delta_{1,2}$ denotes the phase error in gratings Φ_{G1} and Φ_{G2}, respectively. For simplicity, let us assume that $\delta_1 \approx \delta_2 = \delta$. This is not an unreasonable assumption, as such phase errors occur due to resist thickness, which is calibrated and fairly uniform. In this case, it is assumed that the regions corresponding to a phase value of 0 have no resist remaining after exposure of the resist to e-beam or ultraviolet (UV) light and after development of the resist. The phase addition of the fundamental units of two 1D gratings with orthogonal periodicity given by Eq. (6.2) can be understood from Fig. 6.1. The phase profiles have four combinations, namely, C1, C2, C3, and C4. Phase addition shows that the resulting element has three distinct phase values in its fundamental building block. The four combinations are given in Table 6.1.

Let us consider the case with the modulo-2π phase addition method. The phase profile of a 2D grating generated by modulo-2π phase addition of two 1D gratings with orthogonal periodicity can be given by

$$\Phi_{2DG} = [\Phi_{G1} + \Phi_{G2}]_{2\pi}. \tag{6.5}$$

The phase profile of a 2D grating (checker board grating) has only two phase values, 0 and $\pi+\delta$. The fundamental building blocks of a 2D checkerboard

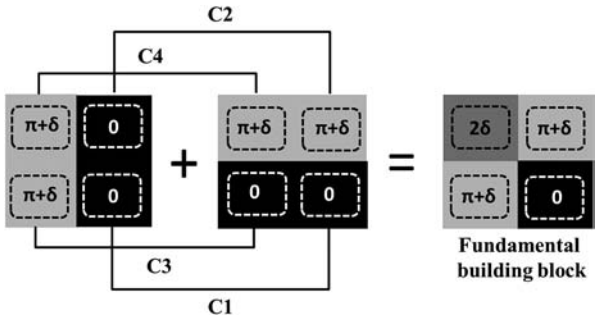

Figure 6.1 Phase addition of two orthogonal 1D gratings in tandem each with an error of δ in their phase heights (reprinted from Ref. 16).

Downloaded From: https://www.spiedigitallibrary.org/ebooks/ on 27 Feb 2022
Terms of Use: https://www.spiedigitallibrary.org/terms-of-use

Table 6.1 Phase values of the fundamental building blocks of two 1D gratings with orthogonal periodicity in tandem.

Combination	Φ_{G1}	Φ_{G1}	Φ_{2D}
C1	0	0	0
C2	0	$\pi+\delta$	$\pi+\delta$
C3	$\pi+\delta$	0	$\pi+\delta$
C4	$\pi+\delta$	$\pi+\delta$	2δ

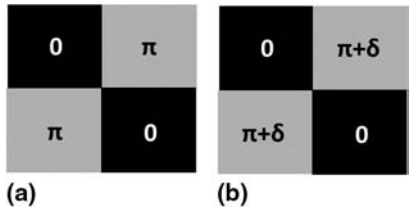

Figure 6.2 Phase profiles of the fundamental building blocks of a 2D grating (a) after design and (b) after fabrication (reprinted from Ref. 16).

grating after design and after fabrication are shown in Figs. 6.2(a) and (b), respectively.

Let us now compare the fundamental building blocks for the two cases in Figs. 6.1 and 6.2. In the first case, it can be observed that the design procedure of modulo-2π phase addition indirectly masks 25% of the area of the fundamental building block from any phase error.[16,17] In the case of a 2D grating, from the Fourier coefficients calculation shown in Chapter 2, we have seen that the maximum efficiency possible in the (±1, ±1) diffraction order is 16%. The relative intensity is the ratio of the intensity of light in a particular diffraction order to the intensity of the incident light, and in this case it can be given by ($I_{\pm1}/I_i$). The relative intensity of the (±1, ±1) diffraction order is plotted as a function of phase error in Fig. 6.3 for the above two cases.

A third case is considered that involves two 1D gratings with orthogonal periodicity in tandem, but it is assumed that the phase error is 0 in only one of the gratings. The other useful advantage of having a single DOE generated via the modulo-2π phase addition method over having two independent DOEs is now clearly visible. The variation in the relative intensity in the (±1, ±1) diffraction order is relatively slower for the multifunctional DOE compared to two independent DOEs. It is seen from Fig. 6.3 that the 2D grating generated by modulo-2π phase addition method behaves like two 1D gratings with phase error in only one of the gratings. This is a consequence of masking off regions by the design used in the modulo-2π phase addition method.

In the above analysis, the performance of two binary DOEs in tandem was compared to a single binary DOE generated by the modulo-2π phase addition of the phase profiles of the two binary DOEs. Although the

Downloaded From: https://www.spiedigitallibrary.org/ebooks/ on 27 Feb 2022
Terms of Use: https://www.spiedigitallibrary.org/terms-of-use

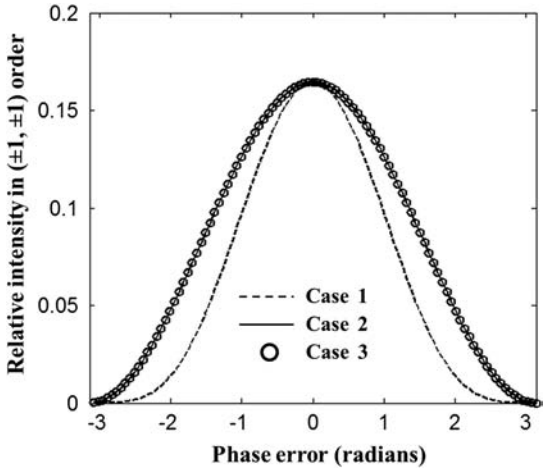

Figure 6.3 Plot of relative intensity in the (± 1, ± 1) diffraction order for different phase errors in the gratings for three cases: case 1 is two orthogonal binary gratings in tandem with phase error in both gratings; case 2 is a 2D checkerboard binary grating; and case 3 is two orthogonal binary gratings in tandem with phase error in one of the gratings (reprinted from Ref. 16).

comparison was made with binary DOEs, the modulo-2π technique can be utilized to combine the functions of two or more binary DOEs, one binary DOE with a blazed DOE, two blazed DOEs, as well as phase and amplitude DOEs. In the following sections, the techniques and MATLAB® codes for combining the aforementioned types of DOEs are discussed.

6.1.2 Design of multifunctional DOEs

In this section, we look at the design procedure for designing multifunctional DOEs by combining DOEs with different functions using modulo-2π phase addition method. To begin, let us consider the simplest case, similar to the one shown in Section 6.1.1 for combining two binary DOEs using the modulo-2π phase addition technique to generate a multifunctional binary DOE. The procedure, in fact, is similar to the design procedure given in Chapter 2 for designing a checkerboard grating. In this case, let us consider combining a circular grating with a 1D grating. The phase profile of circular grating (with period Λ_1) and a 1D grating with periodicity Λ_2 along the y direction are given by Eqs. (6.6) and (6.7), respectively:

$$\Phi_{CG}(r) = \begin{cases} \pi & 0 \le r \le \frac{\Lambda_1}{2} \\ 0 & \frac{\Lambda_1}{2} \le r \le \Lambda_1 \end{cases} \quad \Phi_{CG}(r) = \Phi_{CG}(r + \Lambda_1), \tag{6.6}$$

$$\Phi_{1D}(x,y) = \begin{cases} \pi & 0 \le y \le \frac{\Lambda_2}{2} \\ 0 & \frac{\Lambda_2}{2} \le y \le \Lambda_2 \end{cases} \quad \Phi_{G2}(y) = \Phi_{G2}(y + \Lambda_2). \tag{6.7}$$

Downloaded From: https://www.spiedigitallibrary.org/ebooks/ on 27 Feb 2022
Terms of Use: https://www.spiedigitallibrary.org/terms-of-use

The phase of the multifunctional DOE can be given by

$$\Phi_m = [\Phi_{CG} + \Phi_{1D}]_{2\pi}. \tag{6.8}$$

Let us consider the design of a multifunctional DOE containing the functions of a binary circular grating with period $\Lambda_1 = 50$ μm and a binary 1D grating with periodicity along the y direction with a period $\Lambda_2 = 25$ μm. The MATLAB code for designing this multifunctional DOE is given in Table 6.2.

The phase profile of the multifunctional DOE is shown in Fig. 6.4(a). The far-field diffraction pattern—calculated as discussed in earlier chapters using the `fft2` command—is shown in Fig. 6.4(b). The far-field diffraction pattern of a circular grating is a ring pattern due to circular symmetry. The 1D grating acts as a beamsplitter splitting light into different orders. When these two DOEs are combined, the resulting multifunctional DOE generates multiple ring patterns with intensity values corresponding to the intensity values of the diffraction spots of the 1D grating. The 1D grating directs 40% of the light into each of the two first diffraction orders, and the rest of the light is directed into the higher orders for $\Phi_{1D} = \pi$. Now, with the presence of the circular grating, the diffraction spots are rings with ~50% of the light in the 1st order. Hence, for the combined element, the final efficiency is the product of the individual efficiencies; i.e., 40% × ~50% of the light gets distributed along the

Table 6.2 MATLAB code for design of a multifunctional DOE from a circular grating and a 1D grating.

```
%Multifunctional DOE - CG and 1D grating
clear; %Clear all memory
% Defining Grating Parameters
  N=500; %Define Matrix sizes
  A1=zeros(N,N); %Define Matrices by assigning 1 to all pixels
  A2=zeros(N,N);
  P1=50;%Define the period of the binary axicon grating
  P2=25;%Define the period of the 1D grating
  FFr=0.5;%Define fill factor for radial periodicity
  FFy=0.5;%Define fill factor for periodicity along y direction
% Constructing the grating
  x=1:N;
  y=1:N;
  [X,Y]=meshgrid(x,y);
  r=sqrt((X-N/2).*(X-N/2)+(Y-N/2).*(Y-N/2));
  A1(rem(r,P1)<P1*FFr)=1;
  A2(rem(Y,P2)<P2*FFy)=1;
  A3=exp(1i*pi*xor(A1,A2));
  A3(r>150)=0;
%Observing the grating output in the far-field
  E=fftshift(fft2(A3));
  I=(abs(E)/(N*N)).*(abs(E)/(N*N));
```

Downloaded From: https://www.spiedigitallibrary.org/ebooks/ on 27 Feb 2022
Terms of Use: https://www.spiedigitallibrary.org/terms-of-use

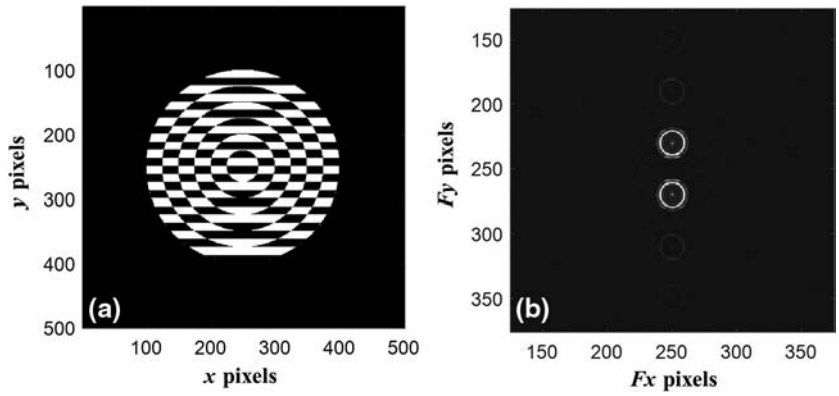

Figure 6.4 (a) Image of the phase profile of the multifunctional DOE designed by modulo-2π phase addition of a 1D grating (period = 25 μm) with a circular grating (period = 50 μm). (b) Far-field diffraction pattern of the multifunctional DOE designed by modulo-2π phase addition of a 1D grating with a circular grating.

circumference of the ring for $\Phi_{CG} = \pi$. In other words, the combined DOE has an effective efficiency of only ~20%.

The ring patterns having the same radii and with varying intensity values correspond to the different diffraction orders of the 1D grating. The larger ring patterns [seen as faint circles in Fig. 6.4(b)] surrounding the first ring patterns are the higher orders of the circular grating. Higher orders are not visible when using 'colormap (gray)' due to their poor intensity. However, it is possible to view even the lower-intensity profiles by choosing a different colormap.

In the above case, only two DOEs were combined. However, the same procedure can be extended to combine more DOEs. For instance, one could combine two orthogonal 1D gratings and a circular grating. This is same as combining a 2D grating (checkerboard) with a circular grating. The MATLAB code can be modified to first generate the binary phase profile of a 2D grating from two binary 1D gratings, followed by the generation of the phase profile of the binary multifunctional DOE from the phase profiles of the binary 2D grating and the circular grating. In this combination, the multifunctional DOE will generate four ring patterns along both the x and y directions, each with an intensity of 16% × ~50% of the input light and ring patterns with less intensity corresponding to the higher diffraction orders of the 2D grating. Hence, the effective efficiency in the (± 1, ± 1) order of the 2D grating and 1st order (+1 and –1 combined) of the circular grating is only ~8%. The circular grating has a period $\Lambda_1 = 50$ μm, and the binary 1D gratings have periodicity $\Lambda_{2x} = 25$ μm and $\Lambda_{2y} = 25$ μm in the x and y directions, respectively. An image of the phase profile of the 2D phase-modulated circular grating and its far-field diffraction pattern are shown in Figs. 6.5(a) and (b), respectively. The four ring patterns correspond to the

Downloaded From: https://www.spiedigitallibrary.org/ebooks/ on 27 Feb 2022
Terms of Use: https://www.spiedigitallibrary.org/terms-of-use

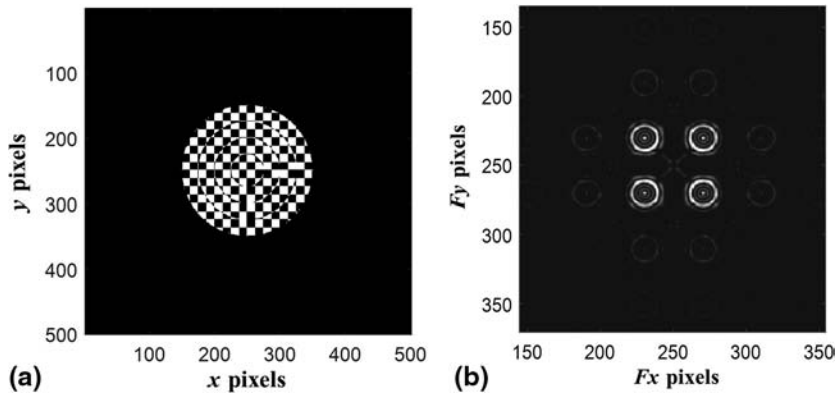

Figure 6.5 Image of the phase profile of the multifunctional DOE designed by modulo-2π phase addition of two orthogonal 1D gratings (period = 25 μm) and a circular grating (period = 50 μm). (b) Far-field diffraction pattern of the multifunctional DOE designed by modulo-2π phase addition of two orthogonal 1D gratings with a circular grating.

(±1, ±1) diffraction orders of the 2D grating and the +1 and –1 combined order of the circular grating.

The radius of the ring pattern and the spacing between the ring patterns can be determined in both of the above cases using the grating equation and trigonometry, as discussed in Chapter 2. The radius of the ring pattern is given by

$$r = z \tan\left[\sin^{-1}\left(\frac{\lambda}{\Lambda_1}\right)\right]. \tag{6.9}$$

Equation (6.9) can be used to determine the spacing between the spots by replacing Λ_1 with Λ_2. The radius of the ring pattern and the spacing between the ring patterns at a distance of 50 mm is found to be 632 μm and 2.5 mm, respectively.

The above procedure can also be extended to combine two binary DOEs such as an FZP and different gratings, which can be used to generate 2×2, 3×3 arrays of focused spots, etc., using the modulo-2π phase addition method. Array generation is required in applications that demand identical spots or patterns repeated along the x and y directions. One such application is micro-drilling using an axicon array.[18] A well-known element used for array generation is the Dammann grating.[19,20]

Using the above technique, it is also possible to tailor the intensity of different spots. Arrays of focused spots and ring patterns can also be easily generated by using an array of identical FZPs and circular gratings, respectively. However, there are many advantages to using a multifunctional DOE to generate the array compared to using an array of identical DOEs. First, in the case of DOEs containing an array of elements, different sections of the input beam are incident upon different elements, which may result

Downloaded From: https://www.spiedigitallibrary.org/ebooks/ on 27 Feb 2022
Terms of Use: https://www.spiedigitallibrary.org/terms-of-use

in discrepancy, as most light sources have a Gaussian intensity profile. Secondly, in the case of micro-lenses, the field of view is decreased, and the spot size increases. Lastly, it is difficult to fabricate such arrays with high precision in their relative positions due to the drift that is inherent in electron beam and focused ion beam systems. Hence, in many applications it is advantageous to use multifunctional DOEs instead of DOE arrays. However, multifunctional DOEs generate arrays whose direction of propagation is not parallel to one another but at some angle, which may introduce some asymmetry in the outermost spots.

From the above presentation and MATLAB code, we can see that it is easy to design a binary multifunctional DOE from the phase profiles of two or more binary DOEs. One of the main disadvantages is the decrease in efficiency with the increase in the number of elements. In case 1, where a 1D grating is combined with a circular grating, the effective efficiency is ~20%, which reduced to ~8% when another 1D grating is added. One method to solve the efficiency problem is to use blazed versions of the devices instead of binary ones.

Let us consider combining a binary DOE with a blazed DOE. The procedure is similar to the one given in the previous section except that the multifunctional DOE cannot be designed by a simple X-OR operation. The combination of the two DOEs still follows Eq. (6.1). Consider the addition of a blazed FZP and a binary 1D grating.[21] The phase profile of the blazed FZP is given by

$$\Phi_{FZP}(r) = \left[\frac{2\pi}{\lambda}\left(f - \sqrt{f^2 - r^2}\right)\right]_{2\pi}, \tag{6.10}$$

while the phase profile of a binary 1D grating is given by Eq. (6.3).

The phase of the multifunctional DOE can be generated by the modulo-2π phase addition of Eqs. (6.10) and (6.3), as given by Eq. (6.2) or Eq. (6.8). The FZP is designed with a focal length of $f = 10$ mm with $\lambda = 633$ nm, and the period of the 1D grating is $\Lambda_x = 200$ μm. The MATLAB code for designing a multifunctional DOE containing the functions of a blazed FZP and a binary 1D grating is shown in Table 6.3.

The phase profile of (1) a blazed FZP, (2) a binary 1D grating, (3) a multifunctional DOE after normal addition of phase profiles of a FZP and a binary 1D grating, and (4) a multifunctional DOE after modulo-2π addition of phase profiles of a FZP and a binary 1D grating are shown in Figs. 6.6(a)–(d), respectively.

In this case, the resulting multifunctional DOE is expected to have a higher efficiency compared to its binary version. The FZP has a blazed phase profile; hence, only one diffraction order has 100% theoretical efficiency, while the binary grating has an efficiency of 40% in its ± 1 diffraction order. Therefore, the effective efficiencies in the 1st diffraction order of the FZP and the ± 1 diffraction order of the 1D binary grating are 40% each.

Downloaded From: https://www.spiedigitallibrary.org/ebooks/ on 27 Feb 2022
Terms of Use: https://www.spiedigitallibrary.org/terms-of-use

Table 6.3 MATLAB code for design of a multifunctional DOE from a blazed FZP and a 1D grating.

```
%Multifunctional DOE - Blazed FZP and 1D grating
clear;%Clear all memory
%Define grating and FZP parameters
  N=500;%Define Matrix size
  f=10000;
  lambda=0.632;
  P=200;
  FFy=0.5;
  A1=zeros(N,N);%Define the matrices assigning ones to all pixels
  A2=zeros(N,N);
  A3=zeros(N,N);
%Grating and FZP construction
  x=1:N;
  y=1:N;
  [X,Y]=meshgrid(x,y);
  r=sqrt((X-N/2).*(X-N/2)+(Y-N/2).*(Y-N/2));
  A1=(f-sqrt(f*f+r.*r))*(2*pi)/(0.632);
  A2(rem(Y,P)<P*FFy)=pi;
  A=rem(A1+A2,2*pi);
  B1=exp(1i*A1);
  B2=exp(1i*A2);
  B3=exp(1i*A);
```

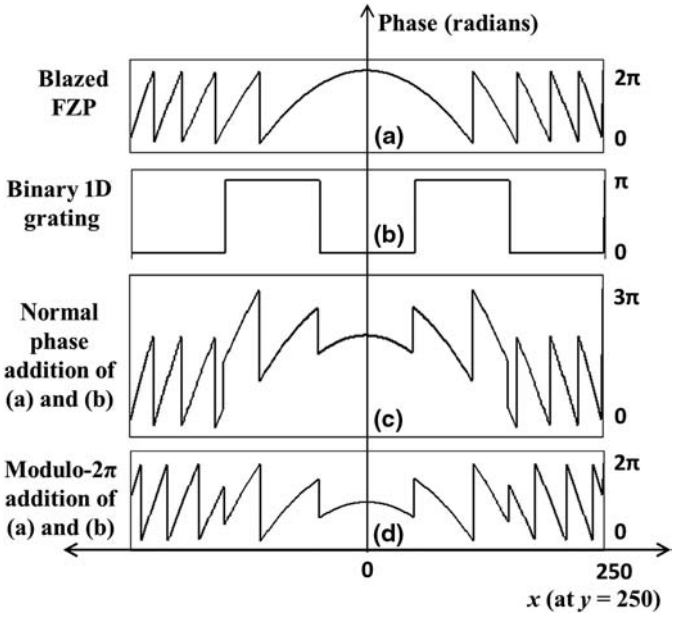

Figure 6.6 Plot of phase profiles of (a) a blazed FZP, (b) a binary 1D grating, (c) a multifunctional DOE after normal addition of phase profiles of FZP and 1D grating, and (d) binary 1D grating and multifunctional DOE after modulo-2π addition of phase profiles of FZP and binary 1D grating at $y = 250$ (adapted from Ref. 21).

Downloaded From: https://www.spiedigitallibrary.org/ebooks/ on 27 Feb 2022
Terms of Use: https://www.spiedigitallibrary.org/terms-of-use

Let us now repeat the procedure to combine a binary 2D checkerboard grating with a blazed circular grating.[22] The periods of the blazed circular grating and 2D checkerboard gratings are $\Lambda_1 = 50$ μm and $\Lambda_2 = 200$ μm, respectively. The MATLAB code is similar to the code shown in Table 6.3, except that the phase profile of the FZP must be replaced with that of a blazed circular grating, and the phase profile of 1D grating must be replaced with that of a checkerboard grating. An image of the phase profile of a multifunctional DOE containing the functions of a blazed circular grating with a checkerboard grating is shown in Fig. 6.7(a). The far-field diffraction pattern of the multifunctional DOE generates 4 ring patterns with 16% efficiency each, as shown in Fig. 6.7(b). The ring pattern does not have the multiple diffraction orders of the pattern in Fig. 6.5, as the axicon is blazed in this case. However, there are multiple ring patterns due to the 2D grating.

This procedure can be repeated to combine any blazed DOE with one or more binary DOEs. In this way, high-efficiency, multifunctional DOEs can be generated.

When combining two blazed DOEs, the procedure is similar to the design procedure given in the previous section. However, the output of the DOE is very different, as there is only one diffraction order for both of the DOEs; as a result, the multifunctional DOE also has only one diffraction order. Hence, it is possible to obtain a high efficiency close to 100%. The MATLAB code for combining a blazed circular grating with a blazed 1D grating with periods $\Lambda_1 = 25$ μm and $\Lambda_2 = 10$ μm, respectively, is shown in Table 6.4. Phase profiles of the blazed circular grating, the 1D blazed grating, and the multifunctional DOE are shown in Figs. 6.8(a)–(c), respectively. An image of the phase profile of the multifunctional DOE is shown in Fig. 6.9(a), and the far-field diffraction pattern is shown in Fig. 6.9(b).

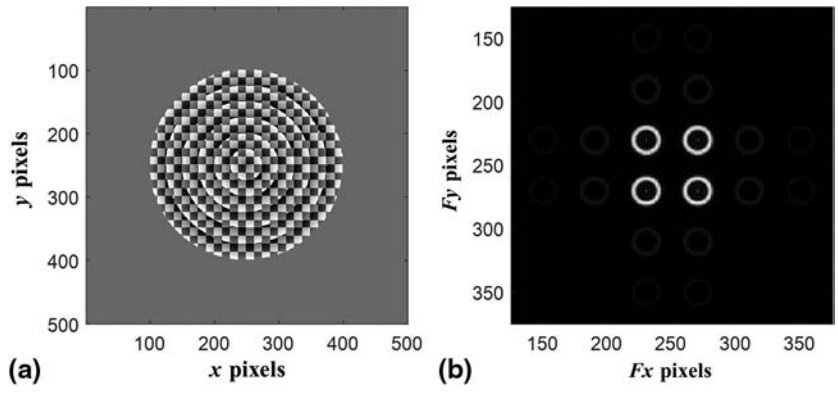

Figure 6.7 (a) Image of the phase profile of a multifunctional DOE generated by combining the phase functions of a blazed circular grating and a 2D binary checkerboard grating. (b) Far-field diffraction pattern of the same multifunctional DOE.

Downloaded From: https://www.spiedigitallibrary.org/ebooks/ on 27 Feb 2022
Terms of Use: https://www.spiedigitallibrary.org/terms-of-use

Table 6.4 MATLAB code for design of a multifunctional DOE from a blazed circular grating and a blazed 1D grating.

```
%Multifunctional DOE - Blazed circular grating and blazed 1D
%grating clear
% Clear all memory
%Define grating parameters
  N=500;%Define Matrix size
  Pr=25;
  Px=10;
%Blazed axicon and grating construction
  x=1:N;%Sampling
  y=1:N;
  [X,Y]=meshgrid(x,y);
  r=sqrt((X-N/2).*(X-N/2)+(Y-N/2).*(Y-N/2));
  P1=rem(r,Pr); %Construction of blazed axicon
  A1=(P1/Pr)*2*pi;
  P2=rem(X,Px);%Construction of blazed 1D grating
  A2=(P2/Px)*2*pi;
  A=rem(A1+A2,2*pi); %Modulo-2pi phase addition of the two phase
  %profiles
  B=exp(1i*A);
  B(r>150)=0;
```

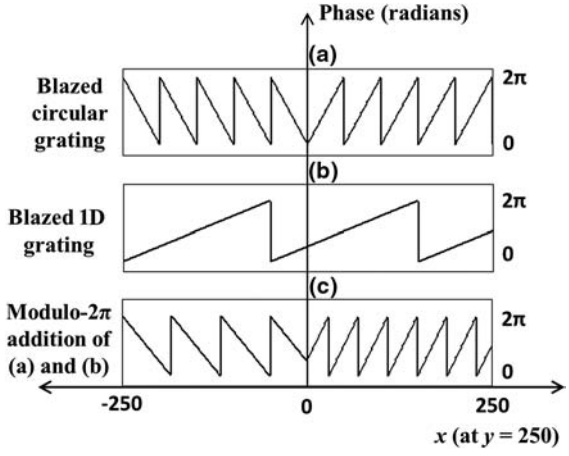

Figure 6.8 Phase profiles of (a) a blazed circular grating, (b) a blazed 1D grating, and (c) a multifunctional DOE.

The multifunctional DOE generates tilted Bessel-like beams in its near field and a shifted ring pattern in its far field.[23,24] If the multifunctional DOE is binarized, multiple ring patterns will be generated corresponding to the various diffraction orders of the circular and 1D gratings.

Finally, let us consider the design of multifunctional DOEs that contain the functions of a blazed and an amplitude DOE. Such elements have proven to be useful for some applications.[25,26] In this case, let us consider combining

Downloaded From: https://www.spiedigitallibrary.org/ebooks/ on 27 Feb 2022
Terms of Use: https://www.spiedigitallibrary.org/terms-of-use

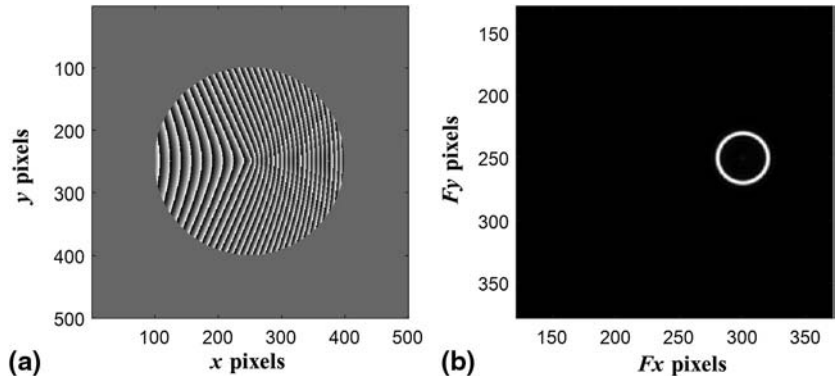

Figure 6.9 (a) Image of the phase profile of the multifunctional blazed DOE containing the functions of a blazed circular grating and a blazed 1D grating. (b) Far-field diffraction pattern of the same multifunctional blazed DOE.

the functions of an amplitude FZP with a blazed spiral phase plate. The MATLAB code for generation of the phase profile of this multifunctional DOE is shown in Table 6.5. The image of the phase profile of the multifunctional DOE is shown in Fig. 6.10.

Table 6.5 MATLAB code for design of a multifunctional DOE from a blazed spiral phase plate and an amplitude FZP.

```
%Multifunctional DOE - Blazed circular grating and blazed 1D
%grating clear;
%Clear all memory
%Define grating parameters
  N=500; %Define Matrix size
  M=32; %Define number of zones
  A1=zeros(N,N); %Define Matrices by assigning 0 or 1 to all
  %elements
  r1=zeros(M,M);
  r=zeros(N,N);
  f=3000; %Define focal length and wavelength (in micrometers)
  lambda=0.633;
  L=1;%Define topological charge
% Construction of the spiral FZP
for n=1:M; %Calculate the widths of the zones
  r1(n)=sqrt(n*f*lambda);
end
for n=1:2:M; %Scan element by element using two for loops
  for p=1:N;
    for q=1:N;
      r(p,q)=sqrt((p-N/2)*(p-N/2)+(q-N/2)*(q-N/2));
        if r(p,q) > r1(n) && r(p,q) < r1(n+1);
          A1(p,q)=exp(1i*L*(atan2((q-N/2),(p-N/2))));
        end
    end
  end
end
```

Downloaded From: https://www.spiedigitallibrary.org/ebooks/ on 27 Feb 2022
Terms of Use: https://www.spiedigitallibrary.org/terms-of-use

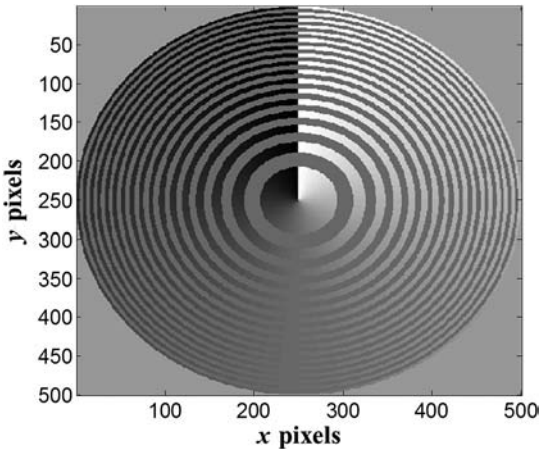

Figure 6.10 Image of the phase profile of a multifunctional DOE containing the functions of an amplitude FZP and a blazed spiral phase plate.

6.1.3 The composite effect of multifunctional DOEs

In the previous section, the design of different types of multifunctional DOEs was discussed in detail. The number of orders and, therefore, the maximum efficiency, was different in each case, depending on the profiles of the input functions. In Section 6.6.1, the advantages of multifunctional DOEs in terms of space, efficiency, resistance to errors, etc., are discussed. It is interesting to look at the other effects that arise due to combining two DOEs using the modulo-2π phase addition method. For example, we know that, individually, each DOE is highly sensitive to changes in wavelength. What happens to the combined element? To answer this, we will look at the combination of a FZP with a 1D grating and study the combined DOE and each individual DOE separately.

When light is incident on a multifunctional DOE, the DOE focuses light at a distance that is the focal length of the FZP and simultaneously splits light into spots corresponding to the different diffraction orders, namely, ± 1, ± 3, etc., of the grating. From the grating diffraction equation and trigonometry, the spacing between the 0^{th} diffraction order and the $\pm 1^{\text{st}}$ diffraction order is given by

$$d(\lambda) = \frac{\lambda f(\lambda)}{\sqrt{\Lambda^2 - \lambda^2}}. \tag{6.11}$$

The variation in the focal length f of the FZP with variation in wavelength is given by

$$f(\lambda) = \frac{r_n^2 - n^2\lambda^2}{2n\lambda}. \tag{6.12}$$

Assuming that $\Lambda \gg \lambda$, the spacing between the spots is directly proportional to the variation in wavelength per Eq. (6.11). This means that

Downloaded From: https://www.spiedigitallibrary.org/ebooks/ on 27 Feb 2022
Terms of Use: https://www.spiedigitallibrary.org/terms-of-use

at a particular plane, when the wavelength varies, the spacing between the diffraction spots varies linearly with wavelength. According to Eq. (6.12), assuming that $r_n^2 \gg n^2\lambda^2$, the focal length is inversely proportional to the variation in wavelength. These equations, therefore, tell us that d and f change in opposite ways with respect to the wavelength. Now let us combine Eqs. (6.11) and (6.12) by substituting Eq. (6.12) in Eq. (6.11), giving rise to

$$d(\lambda) = \left(\frac{\lambda}{\sqrt{\Lambda^2 - \lambda^2}}\right)\left(\frac{r_n^2 - n^2\lambda^2}{2n\lambda}\right). \tag{6.13}$$

After applying the assumptions that $\Lambda \gg \lambda$ and $r_n^2 \gg n^2\lambda^2$, Eq. (6.13) reduces to

$$d(\lambda) = \left(\frac{r_n^2}{2n\Lambda}\right). \tag{6.14}$$

Equation (6.14) does not depend on the wavelength. In other words, the spacing between the spots is independent of the wavelength. How does this independence come about? When the wavelength of light increases, the spacing between the diffraction spots increases at the plane that is a focal length distance away. On the other hand, when the wavelength of light increases, the focal length of the multifunctional DOE decreases. This results in the diffraction spots being focused at a plane that is closer to the DOE plane when compared to the situation before the wavelength change. Hence, these two effects cancel each other out, rendering a wavelength-independent spot spacing. There is an alternate way to think about this effect. In the case of a diffraction grating, when wavelength increases, the spacing between the spots increases, and vice versa, at a particular plane of interest. However, when the diffraction grating is used together with a FZP, the location of the plane of interest is controlled by the FZP and varies to compensate for the change in the spot spacing. This effect, when regarded from the application point of view, proves quite useful. If the 1D grating is replaced by a binary axicon in the multifunctional DOE, a focused ring pattern will be generated at the focal plane of FZP. The ring pattern with a static ring diameter can be moved in space just by varying the wavelength of light. Although the ring diameter stays constant, the focal plane position changes; therefore, such combined elements can be said to be quasi-achromatic.

The above effect is valid only when the features of the grating and the FZP are much larger than the wavelength of light used, or in other words, when both of the DOEs are scalar (refer to Chapter 1). It is also useful to note that the above effect is true for only the 1st diffraction order.

What happens for the higher diffraction orders? Modifying Eq. (6.11) to represent the 2nd and 3rd orders yields Eqs. (6.15) and (6.16), respectively:

Downloaded From: https://www.spiedigitallibrary.org/ebooks/ on 27 Feb 2022
Terms of Use: https://www.spiedigitallibrary.org/terms-of-use

$$d(\lambda) = \frac{2\lambda f(\lambda)}{\sqrt{\Lambda^2 - 4\lambda^2}}, \tag{6.15}$$

$$d(\lambda) = \frac{3\lambda f(\lambda)}{\sqrt{\Lambda^2 - 9\lambda^2}}, \tag{6.16}$$

When the diffraction order increases, the denominator becomes more dependent on the wavelength of the light. As a result, the wavelength dependence cannot be neglected as before. However, for gratings with very large periods, the abovementioned quasi-achromatic behaviour can be found. Another way to understand this is that the higher order corresponds to higher diffraction angles that arise only from narrower periods. Hence, in a way, a higher diffraction order of a grating with a larger period is equivalent to the 1st diffraction order of a grating with a smaller period.

Let us consider a FZP designed with a focal length of $f = 30$ mm and a 1D grating with a period of $\Lambda = 50$ μm. Using Eq. (6.12), the variation in focal length is plotted as a function of wavelength, as shown in Fig. 6.11. A plot of the spacing between the spots for the same wavelength range for the 1D grating alone and the multifunctional DOE is shown in Fig. 6.12. This plot shows that in the case of the multifunctional DOE, the variation in the spacing between the diffraction spots increases only by a few nanometers, while the variation is closer to 0.5 mm for the 1D grating.

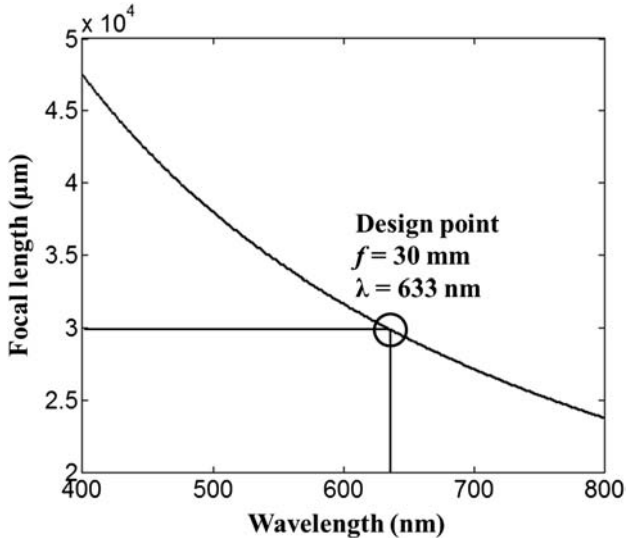

Figure 6.11 Plot of the focal length of the FZP with variation in the wavelength of light (Reprinted from Ref. 29).

Downloaded From: https://www.spiedigitallibrary.org/ebooks/ on 27 Feb 2022
Terms of Use: https://www.spiedigitallibrary.org/terms-of-use

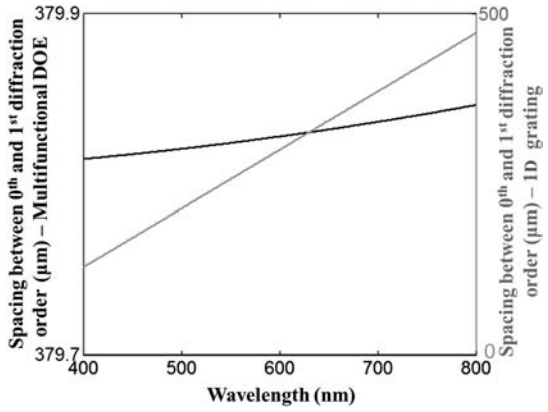

Figure 6.12 Plot of the spacing between the 0^{th} and 1^{st} diffraction order for the multifunctional DOE (black line) and the 1D binary grating (gray line) with variation in wavelength of light (reprinted from Ref. 29).

6.1.4 Conclusion

In Section 6.1, different types of multifunctional DOEs generated by the modulo-2π phase addition are presented, and different diffractive features of the combined DOEs are analyzed. The efficiency of binary multifunctional DOEs is found to be less sensitive to phase errors. In the last section, the wavelength-independent property arising due to combining two DOEs is discussed. These interesting features can be used to our advantage in the design and fabrication of DOEs for different applications. One important point should not be overlooked when dealing with multifunctional DOEs: In the generation of the phase profile of the multifunctional DOE, modulo-2π phase addition is carried out on the phase profiles of the two or more independent DOEs. This can give rise to subwavelength features, as seen in Figs. 6.4, 6.6, and 6.9. Such features are quite difficult to fabricate, and diffraction by such features cannot be explained by scalar diffraction formulation.

6.2 Analog Method

The analog method is similar to the technique described in Chapter 5 for aberration correction in the design of a FZP. This section presents a way to use the technique to design DOEs with multiple functions. This procedure is equivalent to that presented in Section 6.1.4, where two blazed DOEs are combined using the modulo-2π phase addition method. The principle can be understood in the following way: In a diffractive element with circular symmetry, the locations of the zones of the element control its behavior. Combining functions can be thought of as changing the locations of the zones in a particular way. In the aberration correction procedure, after inclusion of the glass substrate, the efficiency of the FZP did not decrease. Hence, by using this technique, it is possible to design binary multifunctional DOEs with higher efficiencies.

Downloaded From: https://www.spiedigitallibrary.org/ebooks/ on 27 Feb 2022
Terms of Use: https://www.spiedigitallibrary.org/terms-of-use

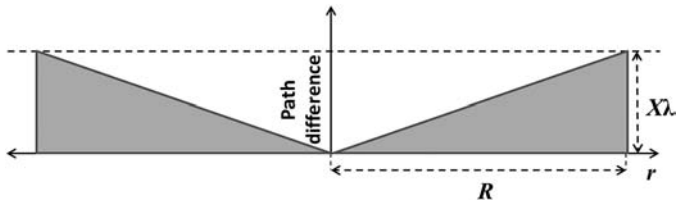

Figure 6.13 Path difference profile of a negative axicon (reprinted from Ref. 16).

To understand this technique, let us consider combining a refractive negative axicon with a FZP. The path difference equation of a FZP in infinite conjugate mode can be given by

$$\sqrt{f^2 + r^2} - f = n\lambda. \tag{6.17}$$

When another function is added to this—for example, that of the negative axicon X shown in Fig. 6.13—the equation will change to include the additional phase provided by the axicon.

By combining the path difference profile of the negative axicon X with a FZP, Eq. (6.17) can be modified as

$$\sqrt{f^2 + r^2} - f = n\lambda + \frac{X\lambda r}{R}. \tag{6.18}$$

The maximum path difference introduced by the negative axicon is $X\lambda = (n_g - 1)t$, where n_g is the refractive index of the negative axicon, and t is the maximum thickness at $r = R$.

The radii of the zones calculated using Eq. (6.18) is given as

$$r_{nDOE} = \frac{-B \pm \sqrt{B^2 - 4AC}}{2A}, \tag{6.19}$$

where

$$A = \left(\frac{\lambda^2 X^2 - R^2}{R^2}\right), B = \frac{2\lambda X}{R}(f + n\lambda), \text{ and } C = (2n\lambda f + n^2\lambda^2).$$

Let us consider a case where $f = 5$ mm and $X = 5$. The modulo-2π phase profile of the multifunctional DOE is plotted in Fig. 6.14. The radius of zones of the multifunctional DOE and the FZP are plotted as a function of zone number in Fig. 6.15. From this figure it can be seen that the addition of the phase profile of the negative axicon shifts the location of the zones of the FZP. Equation (6.18) shows that the shift in the location of zones increases with the path difference introduced by the negative axicon.

In the case of the modulo-2π phase addition method, subwavelength features were introduced into the DOE; however, in the analog method, it is

Downloaded From: https://www.spiedigitallibrary.org/ebooks/ on 27 Feb 2022
Terms of Use: https://www.spiedigitallibrary.org/terms-of-use

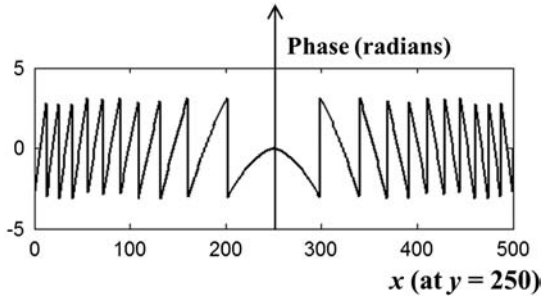

Figure 6.14 Phase profile of the multifunctional DOE containing the functions of a negative axicon and a FZP.

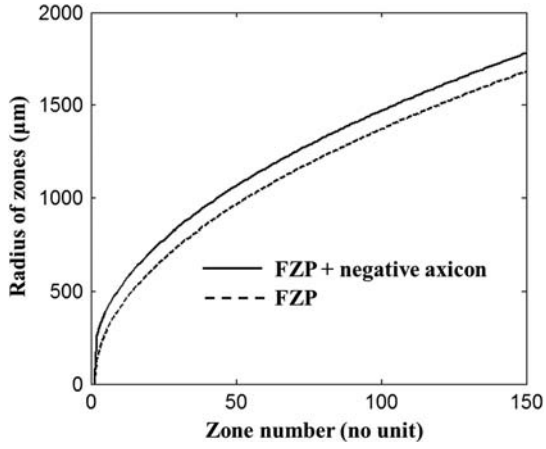

Figure 6.15 Plot of the radius of zones of the multifunctional DOE with an FZP and a negative axicon (solid line) and the FZP alone (dashed line) (reprinted from Ref. 16).

noted that the presence of the DOE increases the zone width within the diameter of the device. A closer look will reveal that this facility of larger zone width at the outermost region has been created at the expense of the *f*-number of the DOE. Therefore, after addition of the phase, if the device is fabricated with the previous radius R, then the *f*-number of the device is less than that of the FZP alone. Secondly, the efficiency of the DOE is preserved as in the case of the aberration correction technique. The effective efficiency of the binary multifunctional DOE is 40% (32% if it is through the modulo-2π phase addition technique). When light is incident on the multifunctional DOE, a focused ring pattern is formed at the focal plane of the FZP function. The width of the ring pattern is given by $1.65\times$ the diffraction-limited spot size.[27,28]

The same procedure can be used to combine any refractive phase with any DOE to generate a multifunctional DOE.

Downloaded From: https://www.spiedigitallibrary.org/ebooks/ on 27 Feb 2022
Terms of Use: https://www.spiedigitallibrary.org/terms-of-use

Table 6.6 Comparison of the characteristics of multifunctional DOEs created by three different techniques: (1) a circular grating and a FZP in tandem, (2) a circular grating and a FZP combined by the modulo-2π phase addition method, and (3) a circular grating and a FZP combined by the analog method.

Multifunctionality achieved by	Maximum Efficiency (%)	Fabrication Ease	Focal Depth	Ring width size[25]
Two Independent Binary Elements	32	Easy	Focal depth of FZP	$1.65w$
Modulo-2π phase addition	32	Difficult	Less due to fine features	$1.65w$
Analog Addition	40	Easier	Larger than FZP	$>1.65w$

6.3 Conclusions

In this chapter, the art of designing a multifunctional DOE by combining one or more DOE functions is presented in detail. Two schemes, namely, the modulo-2π phase addition method and the analog method, are presented to combine two or more DOEs. The two main disadvantages associated with the modulo-2π phase addition method are the poor efficiency and the fine features that are generated during design. The fine features decrease the focal depth of the device, and if they are subwavelength, they introduce polarization effects as well. The analog method seems to have higher efficiency and results in relatively easier fabrication. This is because the feature sizes increase within the radius of the element after inclusion of the refractive phase, although at the expense of the *f*-number of the DOE. This increases the focal depth of the device with an increase in the ring width. The width of the ring pattern is 1.65× the diffraction-limited spot size.[27,28]

Table 6.6 provides a comparison of the characteristics of multifunctional DOE created by three different techniques: (1) a circular grating (or axicon) and a FZP in tandem, (2) a circular grating and a FZP combined by the modulo-2π phase addition method, and (3) a circular grating and an FZP combined by the analog method.

6.4 Exercises

E.6.1 Design a multifunctional DOE to generate a focused ring pattern with a diameter of 1 mm at a distance of 30 mm from the DOE using both the modulo-2π phase addition method[29] and the analog method. Extract some useful parameters. Assume that the fabrication system is capable of fabricating DOEs with a maximum size of 2 mm × 2 mm.

E.6.2 Design a multifunctional DOE to make two signals with wavelengths of $\lambda_1 = 600$ nm and $\lambda_2 = 604$ nm (with Gaussian profiles) that are propagating at an angle of $\theta = +5$ deg and $\theta = -5$ deg with respect to the optical axis, to be focused as Bessel intensity profiles with the central maximum half-width of

Downloaded From: https://www.spiedigitallibrary.org/ebooks/ on 27 Feb 2022
Terms of Use: https://www.spiedigitallibrary.org/terms-of-use

20 μm, and propagating along the same direction from the DOE plane as shown in the optical configuration given in the figure below.

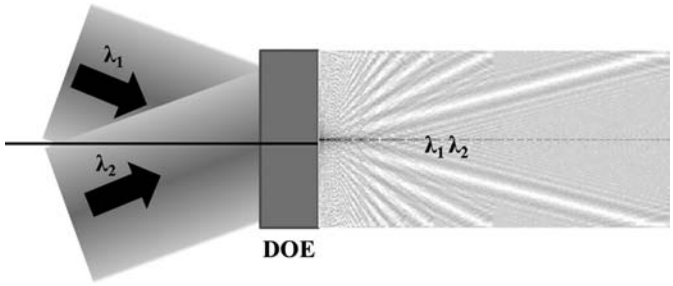

E.6.3 Design a helical axicon containing the functions of a spiral phase plate with charge $L = 10$ and an amplitude binary axicon with a period $\Lambda = 10$ μm using the modulo-2π phase addition method. Calculate the far-field diffraction pattern with an aperture having a 100-μm diameter.

E.6.4 Design a binary multifunctional DOE to generate a 2×2 array of ring patterns with a diameter of 200 μm and a 758-μm spacing between the centers of the $\pm 1^{st}$ diffraction order ring patterns. Choose the DOE and the integration method to obtain a wavelength-independent ring diameter and spot spacing when a shift in the focal plane is permitted.[30,31]

References

1. J. W. Goodman, *Introduction to Fourier Optics*, Second Edition, McGraw-Hill Companies Inc., New York (1996).
2. B. C. Kress and P. Meyrueis, *Applied Digital Optics*, John Wiley & Sons, Chichester, UK (2009).
3. C. Zhang, N. R. Quick, and A. Kar, "Diffractive optical elements for pitchfork beam shaping," *Opt. Eng.* **48**, 078001 (2009) [doi: 10.1117/1.3183919].
4. M. Honkanen and J. Turunen, "Tandem systems for efficient generation of uniform-axial-intensity Bessel fields," *Opt. Commun.* **154**, 368–375 (1998).
5. J. M. Herrera-Fernandez, L. M. Sanchez-Brea, and E. Bernabeu, "Near-field shaping with two binary diffractive optical elements in tandem," *Opt. Commun.* **297**, 182–189 (2012).
6. S. Tibuleac and R. Magnusson, "Narrow-linewidth bandpass filters with diffractive thin-film layers," *Opt. Lett.* **26**, 584–586 (2001).
7. T. Stone and N. George, "Hybrid diffractive-refractive lenses and achromats," *Appl. Opt.* **27**, 2960–2971 (1988).
8. N. Davidson, A. A. Friesem, and E. Hasman, "Analytic design of hybrid diffractive–refractive achromats," *Appl. Opt.* **32**, 4770–4774 (1993).

Downloaded From: https://www.spiedigitallibrary.org/ebooks/ on 27 Feb 2022
Terms of Use: https://www.spiedigitallibrary.org/terms-of-use

9. A. P. Wood, "Design of infrared hybrid refractive–diffractive lenses," *Appl. Opt.* **31**, 2253–2258 (1992).
10. K.-H. Brenner and F. Sauer, "Diffractive–reflective optical interconnects," *Appl. Opt.* **27**, 4251–4254 (1988).
11. S. N. Khonina, V. V. Kotlyar, V. A. Soifer, M. V. Shinkaryev, and G. V. Uspleniev, "Trochoson," *Opt. Commun.* **91**, 158–162 (1992).
12. C. Paterson and R. Smith, "Higher-order Bessel waves produced by axicon-type computer-generated holograms," *Opt. Commun.* **124**, 121–130 (1996).
13. N. R. Heckenberg, R. McDuff, C. P. Smith, and A. G. White, "Generation of optical phase singularities by computer-generated holograms," *Opt. Lett.* **17**, 221–223 (1992).
14. A. Vasara, J. Turunen, and A. T. Friberg, "Realization of general nondiffracting beams with computer-generated holograms," *J. Opt. Soc. Am. A* **6**, 1748–1754 (1989).
15. B. Zhang and D. Zhao, "Focusing properties of Fresnel zone lens with spiral phase," *Opt. Express* **18**, 12818–12823 (2010).
16. A. Vijayakumar and S. Bhattacharya, "Design of multifunctional diffractive optical elements," *Opt. Eng.* **54**, 024104 (2015) [doi: 10.1117/1.OE.54.2.024104].
17. A. Vijayakumar, P. Parthasarathi, S. S. Iyengar, R. Selvan, S. Ananthamurthy, S. Bhattacharya, and S. Bhattacharya, "Conical Fresnel zone lens for optical trapping," *Proc. SPIE* **9654**, 965426 (2015) [doi: 10.1117/12.2180850].
18. R. Grunwald, U. Griebner, F. Tschirschwitz, E. T. J. Nibbering, T. Elsaesser, V. Kebbel, H.-J. Hartmann, and W. Jüptner, "Generation of femtosecond Bessel beams with microaxicon arrays," *Opt. Lett.* **25**, 981–983 (2000).
19. H. Dammann and K. Görtler, "High-efficiency in-line multiple imaging by means of multiple phase holograms," *Opt. Commun.* **3**, 312–315 (1971).
20. U. Krackhardt and N. Streibl, "Design of Dammann gratings for array generation," *Opt. Commun.* **74**(1–2), 31–36 (1989).
21. A. Vijayakumar, M. Uemukai, and T. Suhara, "Phase-shifted Fresnel zone lenses for photomixing generation of coherent THz wave," *Jpn. J. Appl. Phys.* **51**, 070206 (2012).
22. A. Vijayakumar and S. Bhattacharya, "Phase-shifted Fresnel axicon," *Opt. Lett.* **37**, 1980–1982 (2012).
23. R. Dharmavarapu, A. Vijayakumar, and S. Bhattacharya, "Design and fabrication of holographic optical elements for the generation of tilted and accelerating airy beams," *Asian J. Physics* **24**(1), 1363–1372.
24. S. H. Moosavi, C. Gohn-Kreuz, and A. Rohrbach, "Feedback phase correction of Bessel beams in confocal line light-sheet microscopy: a simulation study," *Appl. Opt.* **52**, 5835–5842 (2013).

Downloaded From: https://www.spiedigitallibrary.org/ebooks/ on 27 Feb 2022
Terms of Use: https://www.spiedigitallibrary.org/terms-of-use

25. B. Zhang and D. Zhao, "Focusing properties of Fresnel zone plates with spiral phase," *Opt. Express* **18**, 12818–12823 (2010).
26. A. Vijayakumar and S. Bhattacharya, "Design, fabrication, and evaluation of a multilevel spiral-phase Fresnel zone plate for optical trapping," *Appl. Opt.* **51**, 6038–6044 (2012).
27. P.-A. Bélanger and M. Rioux, "Ring pattern of a lens–axicon doublet illuminated by a Gaussian beam," *Appl. Opt.* **17**, 1080–1088 (1978).
28. A. Vijayakumar, "Design, Fabrication, and Evaluation of Diffractive Optical Elements for the Generation of Focused Ring Patterns," Doctoral Thesis, Indian Institute of Technology Madras, Chennai, India (2015) [doi: 10.13140/RG.2.2.25996.51847].
29. A. Vijayakumar and S. Bhattacharya, "Quasi-achromatic Fresnel zone lens with ring focus," *Appl. Opt.* **53**, 1970–1974 (2014).
30. A. Vijayakumar and S. Bhattacharya, "Design, fabrication, and evaluation of diffractive optical elements for generation of focused ring patterns," *Proc. SPIE* **9449**, 944902 (2015) [doi: 10.1117/12.2077407].
31. J. J. Zambuto, R. E. Gerber, J. K. Erwin, and M. Mansuripur, "Ring-lens focusing and push-pull tracking scheme for optical disk systems," *Appl. Opt.* **33**, 7987–7994 (1994).

Downloaded From: https://www.spiedigitallibrary.org/ebooks/ on 27 Feb 2022
Terms of Use: https://www.spiedigitallibrary.org/terms-of-use

Chapter 7
Computer-Generated Holographic Optical Elements

In earlier chapters, designs of simple binary, multilevel, and blazed DOEs using basic diffraction equations were presented. The proposed techniques were suitable for design of DOEs only for simple applications such as array generation, focusing, etc. On the other hand, DOEs generating arbitrary intensity profiles at the Fourier plane can be designed using the IFTA. In this chapter, an alternative method for beam shaping is presented using computer-generated holographic (CGH) optical elements. The design of simple to complex beam-shaping HOEs (holographic optical elements) is presented.

7.1 Fundamentals of CGHs

The name CGH arises from the holographic technique used to design these elements. CGHs are nothing but processed interferograms obtained by the superposition of two beams.[1–3] In general, for the recording and reconstruction of HOEs, an object needs to be physically present.[4–7] However, in the case of CGHs, the interference experiment is simulated on a computer by superposing two wavefields. The resulting interferogram is processed and used for beam-shaping applications.

Holography was invented in 1948 by Dennis Gabor.[1] It involves two steps: recording and reconstruction. In the first step, the light diffracted from an object is made to interfere with a reference wave, which in most cases is a plane wave. The interference pattern is recorded on a photosensitive film. In the second step, the developed photosensitive film (hologram), is illuminated by the reference wave to generate the object wave. In this way, it is possible to record and reconstruct 3D information of the object, unlike photography. This technique can also be used to generate waves with interesting and useful amplitude and phase profiles.[5] The technical difficulties in recording a hologram are similar to those of arranging any interferometer setup with additional spatial filtering and intensity-controlling components such as

Downloaded From: https://www.spiedigitallibrary.org/ebooks/ on 27 Feb 2022
Terms of Use: https://www.spiedigitallibrary.org/terms-of-use

neutral density filters (NDFs). CGHs can overcome the difficulties faced when physically recording a hologram.[8–11]

The basic principle of the generation of any HOE involves the superposition of two optical waves $A_1\exp(j\Phi_1)$ and $A_2\exp(j\Phi_2)$, and the resulting interference pattern modulated as $2A_1A_2\cos(\Phi_1 - \Phi_2)$ is a HOE.[1,8,9] In the case of CGHs, this interference is simulated, and the resulting fringe pattern is processed and fabricated using lithography techniques or is printed out on transparent sheets. The basic optics configuration for recording and reconstructing a HOE is shown in Figs. 7.1 and 7.2, respectively.

The intensity of the interference pattern created by the superposition of the object wave $A_1\exp(i\Phi_1)$ and the reference wave $A_2\exp(i\Phi_2)$ is given by

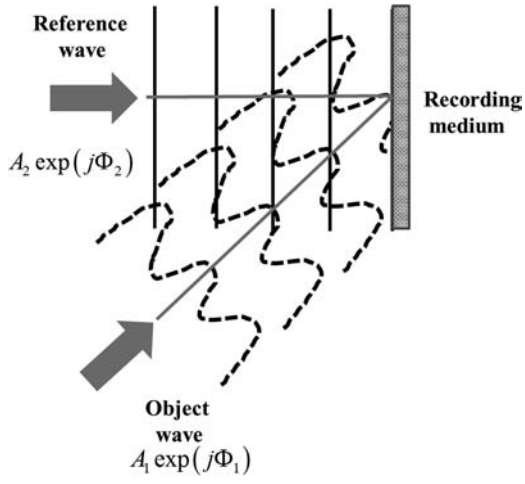

Figure 7.1 Optics configuration for recording the interference pattern (hologram) formed by the superposition of an object wave with a reference wave.

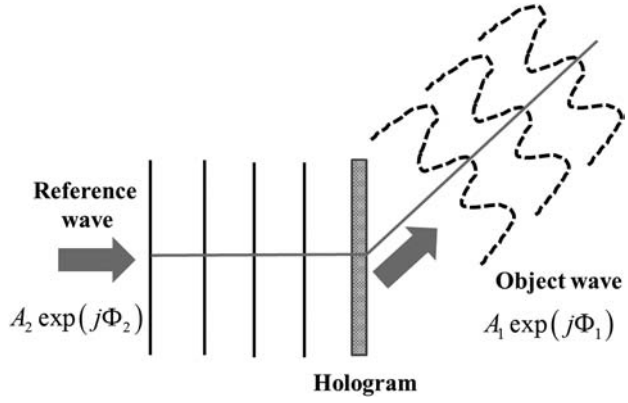

Figure 7.2 Optics configuration for reconstruction of the object wave by illuminating the hologram with the reference wave.

Downloaded From: https://www.spiedigitallibrary.org/ebooks/ on 27 Feb 2022
Terms of Use: https://www.spiedigitallibrary.org/terms-of-use

$$I(x,y) = |A_1(x,y)|^2 + |A_2(x,y)|^2 + 2|A_1(x,y)||A_2(x,y)|\cos[\Phi_1(x,y) - \Phi_2(x,y)]. \tag{7.1}$$

The interference pattern is incident on a photosensitive recording medium, and, upon development, the amplitude transmittance profile of the hologram will match the intensity profile of the interference pattern. When illuminated with the reference wave $A_2\exp(i\Phi_2)$, the hologram generates the object wave $A_1\exp(i\Phi_1)$, and vice versa. During reconstruction, the object wave (real) and its complex conjugate (virtual) are generated.

In the case of CGHs, the interference pattern generated by the computer is converted into an equivalent phase profile and can be transformed into a binary, multilevel, or grayscale profile that can be fabricated using lithography techniques.

7.2 Design of Simple CGHs with MATLAB

The design of CGHs for simple cases such as 1D gratings to complex cases such as forked gratings is presented. Unlike the design of DOEs discussed in previous chapters, the design of CGHs is relatively simpler involving only three steps, irrespective of the element's complexity. The design algorithm of a CGH is shown in Fig. 7.3.

There are, of course, other steps, such as binarization (or quadruplication, etc.) and the verification step, where the diffraction pattern of the CGH is simulated. The critical step is designing the amplitude and phase profile of object and reference waves.

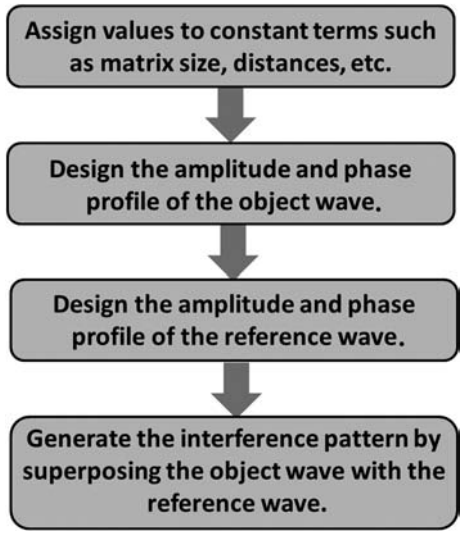

Figure 7.3 Algorithm for the design of a CGH.

Downloaded From: https://www.spiedigitallibrary.org/ebooks/ on 27 Feb 2022
Terms of Use: https://www.spiedigitallibrary.org/terms-of-use

7.2.1 Design of 1D gratings

When two plane waves with uniform amplitude profiles—one propagating along the direction of the optical axis and the other at an angle—are superposed, the resulting interference fringes are a set of parallel lines,[12] similar to the pattern of a 1D grating. These waves can be considered to be the reference and object waves of the hologram, and a DOE can be designed with a phase profile that matches their interference profile. When the resulting hologram is illuminated with one of the plane waves, the other is generated. The reference and object waves are assumed to have a constant amplitude profile, and their equations at the interference plane are given by Eqs. (7.2) and (7.3), respectively:

$$\Psi_1(x,y) = \exp[2\pi j], \tag{7.2}$$

$$\Psi_2(x,y) = \exp\left[j\left(\frac{x}{\lambda}\right)\tan(\theta)\times 2\pi\right]. \tag{7.3}$$

As both waves are considered at a specific plane, the z dependence need not appear in the equation. The plane wave propagates at an angle of θ with the z direction, so the tilted-plane wavefront makes an angle of θ with the x direction. Hence, the phase of the wave varies linearly along the x direction. In the discussion presented in Chapter 2 on the refractive equivalents of DOEs, it was shown that the refractive prism is equivalent to a diffractive grating. A similar connection may be found in CGHs as well. To generate a 1D grating, the phase profile variation along the x direction is the phase of a refractive prism. The optics configuration is shown in Fig. 7.4, and the MATLAB code is given in Table 7.1.

It can be noted from Eq. (7.3) that for larger values of θ, it may be difficult to view the fringe patterns, as the width of the fringe pattern can be less than the smallest currently available pixel size of approximately 1 μm. Hence, in order to expand the fringe pattern, the pixel size is decreased by several factors. From Eq. (1.7) we find that the period of the grating corresponding to

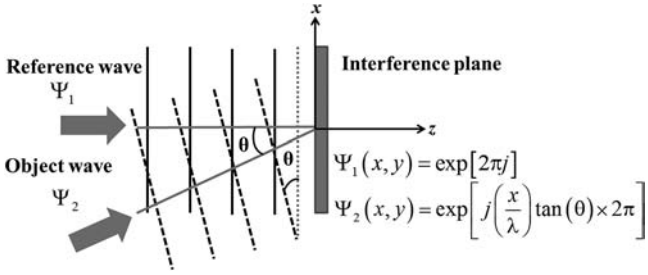

Figure 7.4 Optics configuration for superposition of two plane waves propagating in different directions.

Downloaded From: https://www.spiedigitallibrary.org/ebooks/ on 27 Feb 2022
Terms of Use: https://www.spiedigitallibrary.org/terms-of-use

Table 7.1 MATLAB code for the design of a 1D grating using the computer-generated holographic method.

```
%%1D grating
%Define parameters
N=500;%%Define size of the matrix
   Angle=1;%Define angle of the second plane wave
   V=0.5;%%Visibility controller
   lambda=0.632*1e-6;%Define wavelength
%Create sampled space
   del=1*1e-6;%sampling
   x=-N/2:N/2-1;
   y=-N/2:N/2-1;
   [X,Y]=meshgrid(x*del,y*del);
%Simulate interference
   A=V*exp(1i*(Y/lambda)*tand(Angle)*2*pi);
   B=V*exp(1i*2*pi);
   D=A+B;%Interference of the object and reference wave
   I=abs(D).*abs(D);
%%Construct grating
   I1=im2bw(I);%Binarize the matrix
   Grating=exp(1i*pi*I1);%Generate the phase grating
```

a diffraction angle $\theta = 1$ deg for the 1st diffraction order is $\Lambda = 36.2$ μm. The period of the sinusoidal grating obtained from the MATLAB program is 36 pixels, which matches the calculated value.

The period of the grating is 3.6 μm if the angle between the two plane waves is 10 deg. However, it is not possible to view 3.6 μm accurately with a mesh of pixel size 1 μm. Hence, the sampling period must be decreased 10×, resulting in a magnification of the fringe pattern. The nonbinarized hologram (fringe pattern) generated due to the interference between two plane waves, with an angle of 10 deg between them, and a cross section of its intensity profile are shown in Figs. 7.5(a) and (b), respectively. The period of the grating generated by MATLAB is 36 pixels. This has to be multiplied by the sampling period, 0.1 μm in this case, to obtain 3.6 μm. The orientation of the grating can be modified by changing the object waves' propagation direction.

7.2.2 Design of FZPs

A FZP is used for focusing light to a point. Hence, a hologram can be generated by superposing a spherical wavefront with a plane wavefront, similar to the method used in experiments involving Newton's rings.[12] The reference and object waves are assumed to have a constant amplitude profile, and their equations at the interference plane are given by Eqs. (7.4) and (7.5), respectively:

$$\Psi_1(x,y) = \exp[j2\pi], \tag{7.4}$$

Downloaded From: https://www.spiedigitallibrary.org/ebooks/ on 27 Feb 2022
Terms of Use: https://www.spiedigitallibrary.org/terms-of-use

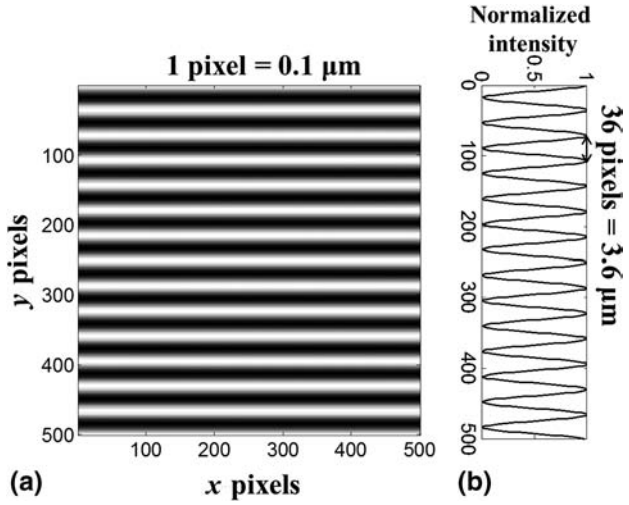

Figure 7.5 (a) Image and (b) intensity profile of the 1D sinusoidal grating.

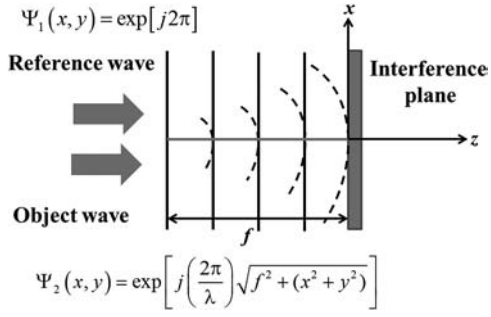

Figure 7.6 Optics configuration for superposition of a plane wave with a spherical wave.

$$\Psi_2(x,y) = \exp\left[j\left(\frac{2\pi}{\lambda}\right)\sqrt{f^2 + (x^2 + y^2)}\right]. \tag{7.5}$$

The optics configuration is shown in Fig. 7.6, and the MATLAB code is given in Table 7.2.

The binarized hologram (fringe pattern) generated due to the interference between a plane wave and a spherical wave, and a plot of its binary phase profile are shown in Figs. 7.7(a) and (b), respectively. The radius of the first zone is measured to be 154 μm, which matches the value calculated using the formula given in Eq. (2.14). The same procedure can be used to design an FZP for off-axis focusing light.

7.2.3 Design of diffractive axicons

A binary diffractive axicon can be designed by superposing a conical wavefront with a plane wavefront. Once again, the reference and object waves

Downloaded From: https://www.spiedigitallibrary.org/ebooks/ on 27 Feb 2022
Terms of Use: https://www.spiedigitallibrary.org/terms-of-use

Table 7.2 MATLAB code for design of a FZP using the computer-generated holographic method.

```
%%Fresnel zone plate
%Define parameters
   N=500;%%Define size of the matrix
   Angle=1;%Define angle of the second plane wave
   V=0.5;%%Visibility controller
   lambda=0.632*1e-6;%Define wavelength
%Create sampled space
   del=1*1e-6;%sampling
   x=-N/2:N/2-1;
   y=-N/2:N/2-1;
   [X,Y]=meshgrid(x*del,y*del);
   f=0.01; %Focal length of 1 cm
%Simulate interference
   A=V*exp(1i*((2*pi)/(lambda))*sqrt(X.^2+Y.^2+f*f));
   B=V*exp(1i*2*pi);
   D=A+B;%Interference of the object and reference wave
   I=abs(D).*abs(D);
   figure (2)
   colormap gray
   imagesc(IN)
%%Construct FZP
   I1=im2bw(I);%Binarize the matrix
   Grating=exp(1i*pi*I1);%Generate the FZP
```

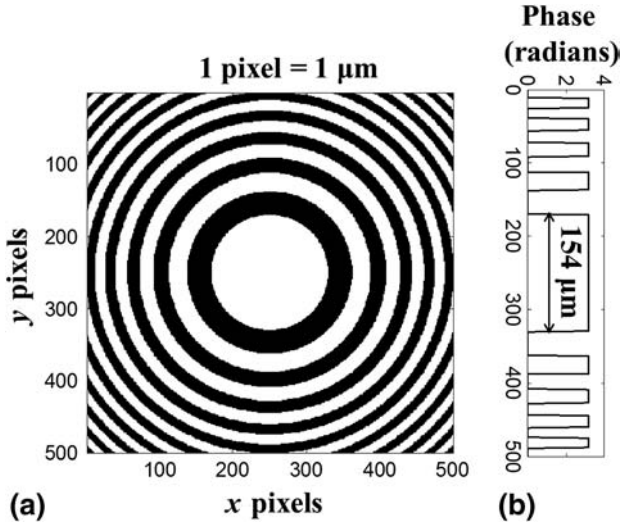

Figure 7.7 (a) Binarized fringe pattern and (b) plot of the phase profile of the FZP.

are assumed to have a constant amplitude profile. The conical wave is generated when a plane wave is incident normally on a refractive axicon. In this case, a negative refractive axicon is considered. This conical wavefront has linear variation of phase along the radial direction, resulting in an equally

Downloaded From: https://www.spiedigitallibrary.org/ebooks/ on 27 Feb 2022
Terms of Use: https://www.spiedigitallibrary.org/terms-of-use

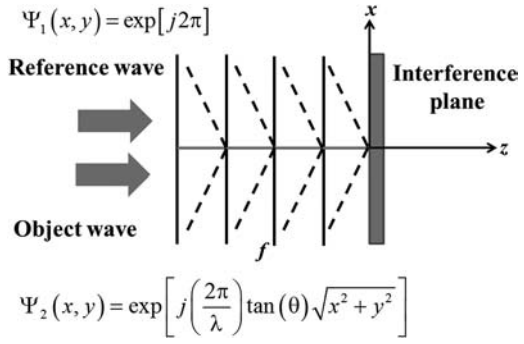

Figure 7.8 Optics configuration for superposition of a plane wave with a conical wave.

Table 7.3 MATLAB code for design of a diffractive axicon using the computer-generated holographic method.

```
%Diffractive axicon
%Simulate interference
A=V* exp(1i*(sqrt(X.^2+Y.^2)/lambda)*tand(Angle)*2*pi);
B=V*exp(1i*2*pi);
```

spaced fringe pattern in this direction. The reference wave is identical to that given in Eq. (7.4), and the equation for the conical wave at the interference plane is given by

$$\Psi_2(x,y) = \exp\left[j\left(\frac{2\pi}{\lambda}\right)\tan(\theta)\sqrt{x^2+y^2}\right]. \tag{7.6}$$

The optics configuration for superposition of a conical wave with a plane wave is shown in Fig. 7.8. The MATLAB code is similar to that given in Table 7.1 for a 1D grating, except that the object wave must be generated with radial instead of linear (x or y) dependence. The code for design of the object wave is shown in Table 7.3. In this case, it is necessary to increase the sampling period to view the fringe pattern with larger diffraction angles, similar to the procedure shown in the case of a 1D grating.

The image of the generated sinusoidal axicon is shown in Fig. 7.9. The period of the measured grating is 36 μm, which matches the calculation result for a diffraction angle of 1 deg.

The procedure presented here can be used to design any CGH, irrespective of its phase profile, and the design section of the MATLAB code can be modified to generate the fringe pattern.

7.3 Design of Multifunctional CGHs with MATLAB

The design and analysis of multifunctional DOEs are presented in Chapter 5. This section will show that multifunctional DOEs can be

Downloaded From: https://www.spiedigitallibrary.org/ebooks/ on 27 Feb 2022
Terms of Use: https://www.spiedigitallibrary.org/terms-of-use

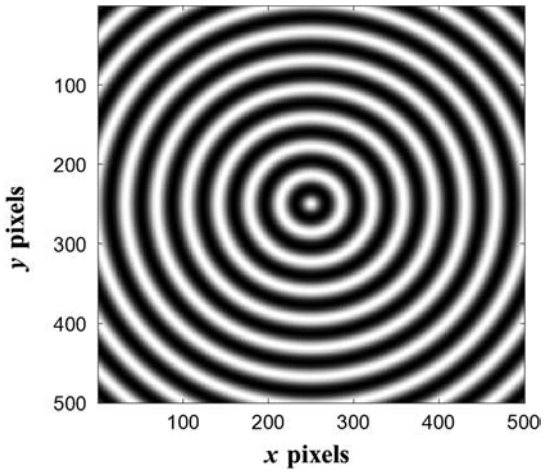

Figure 7.9 Image of the sinusoidal axicon generated by the superposition of a plane wave with a conical wave of having a diffraction angle of 1 deg (reprinted from Ref. 33).

designed more easily using a holographic method. In the case of CGHs, multifunctional elements can be realized by generating the interference pattern between two object waves and reconstructing them using a plane wave with uniform intensity.[1,3] Figure 7.10 demonstrates this idea for a hologram constructed by the interference of two tilted plane waves. Reconstruction by an untilted plane wave generates a wave at an angle that equals the sum of the angles of the two original tilted waves. From the basic interference equation [Eq. (7.1)], let us consider the term of interest, i.e., $2A_1A_2\cos(\Phi_1 - \Phi_2)$, where Φ_1 and Φ_1 are the phase functions of the two tilted plane waves. During reconstruction, if an untilted plane wave ($\Phi = 0$) is used, it generates a tilted plane wave whose phase profile is given by $(\Phi_1 + \Phi_2)$. Using this method, CGHs can be used to generate interesting integrated wavefronts. This idea of linearity can be used in numerous ways in the design of CGHs.

The integrated field information can be extracted by reconstruction using a constant phase and uniform intensity. A simple scenario has been illustrated to explain the extraction of multifunctionality from a CGH. However, the idea can be applied to different cases with varied geometries of recording and reconstruction.

7.3.1 Design of 1D gratings

Two plane waves at angles ± 1 deg with respect to the propagation direction are considered. The two plane waves at the interference plane are given by

Downloaded From: https://www.spiedigitallibrary.org/ebooks/ on 27 Feb 2022
Terms of Use: https://www.spiedigitallibrary.org/terms-of-use

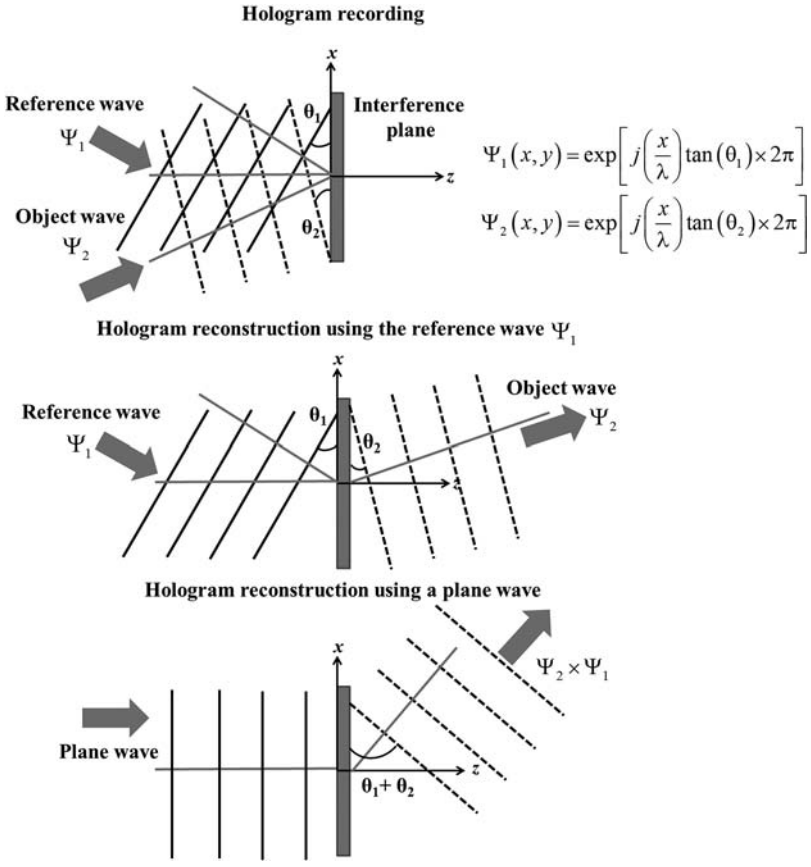

Figure 7.10 Hologram recording and reconstruction using a reference wave and a plane wave.

$$\Psi_1(x,y) = \exp\left[j\left(\frac{2\pi}{\lambda}\right)\tan(\theta)x\right], \tag{7.7}$$

$$\Psi_2(x,y) = \exp\left[j\left(\frac{2\pi}{\lambda}\right)\tan(-\theta)x\right]. \tag{7.8}$$

The MATLAB code given in Table 7.1 can be modified by replacing the equation of the reference wave with that given in Eq. (7.8). The resulting fringe pattern has a period of 18 μm, which will be the same when a plane wave tilted 2 deg is superposed with a plane wave with no tilt.

7.3.2 Design of off-axis axicons

An off-axis axicon is used for the generating off-axis Bessel beams in the near field and a tilted ring pattern in the far field.[13,14] Upon binarization, the CGH generates two ring patterns at $\pm\theta$ in its far field. Using the same linearity

Downloaded From: https://www.spiedigitallibrary.org/ebooks/ on 27 Feb 2022
Terms of Use: https://www.spiedigitallibrary.org/terms-of-use

property, a CGH off-axis axicon can be designed by superimposing a conical wave with a tilted plane wave. When the CGH is illuminated with an untilted plane wave, it generates a tilted conical wave. The conical wave and tilted plane wave can be described by Eqs. (7.6) and (7.3), respectively, at the interference plane.

The MATLAB code is similar to that described earlier. The axicon is designed for a diffraction angle of 1 deg. The tilt angles of the plane wave are selected as 1 deg and 2 deg. Images of the binary off-axis axicons designed for these tilt angles are shown in Figs. 7.11(a) and (b), respectively, and their respective far-field diffraction patterns are shown in Figs. 7.11(c) and (d). The distance between the two ring patterns indicates the diffraction angle; hence, the distance is larger for a tilt angle of 2 deg compared to the distance with a tilt angle of 1 deg.

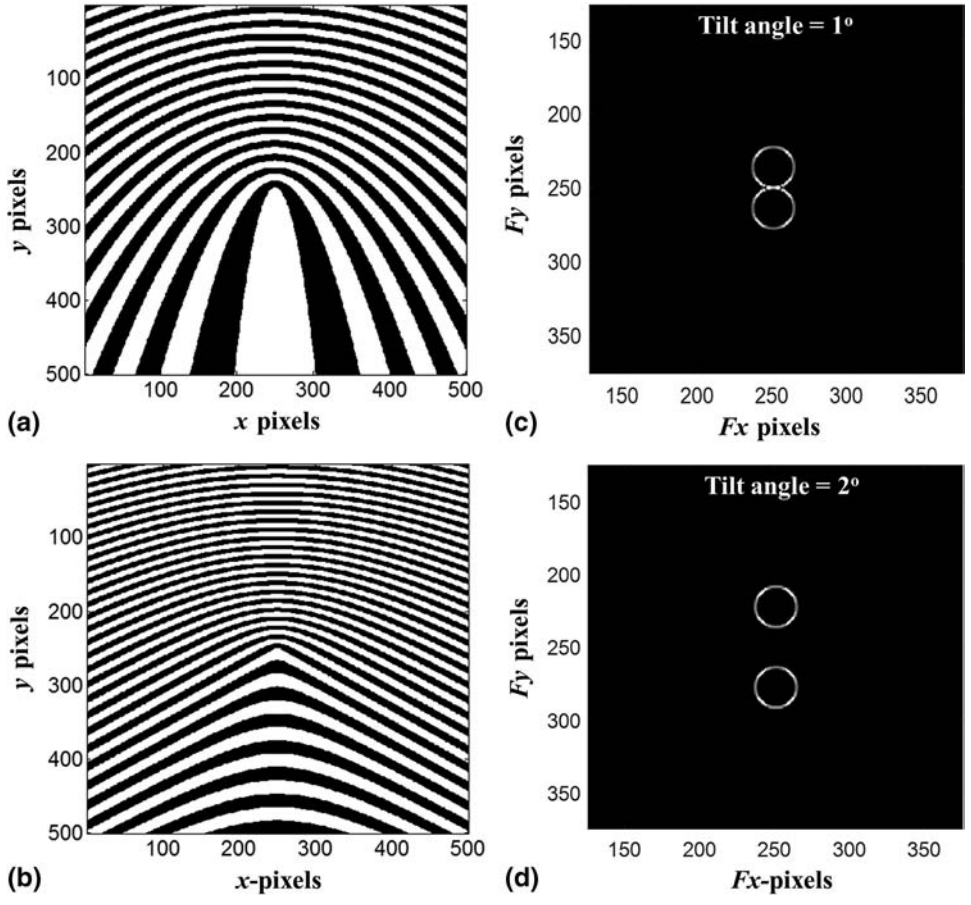

Figure 7.11 Images of the off-axis binary axicons with tilt angles of (a) 1 deg and (b) 2 deg, and (c), (d), their respective far-field diffraction patterns (reprinted from Ref. 33).

Downloaded From: https://www.spiedigitallibrary.org/ebooks/ on 27 Feb 2022
Terms of Use: https://www.spiedigitallibrary.org/terms-of-use

The same procedure can be used to generate the phase profile of off-axis axicons with different orientations. The same procedure can also be used for generation of tilted beams with other types of CGHs such as an off-axis FZP. The twin images occur because the phase profile is binary (or sinusoidal) and can be reduced to one image by modifying the profile to a blazed one.

7.3.3 Design of forked gratings

A spiral phase plate is used for generation of donut beams with helical wavefronts as discussed in Chapter 3.[15–17] However, manufacturing a spiral phase plate is a challenging task; hence, in many cases, a CGH such as a forked grating is used instead.[18] Forked gratings are designed by the interference of a helical wave with that of a tilted plane wave, given by Eq. (7.7). A helical wave with uniform amplitude can be described at the interference plane by

$$\Psi_1(x,y) = \exp[jL\theta], \tag{7.9}$$

where L is the topological charge, which is defined as the number of 2π phase changes along the azimuthal direction within a distance of λ. The MATLAB code for generation of the phase profile of a binary forked grating is similar to the codes given in Tables 7.1 and 7.2. The design of helical and reference waves is given in Table 7.4. The images of the binary forked gratings for $L = 1$ and $L = 3$ are shown in Figs. 7.12(a) and (b), respectively. The charge number is reflected in the number of lines in the fork, and the tilt angle is reflected in the period of the grating. Binary forked gratings generate donut beams of different diffraction orders in the far field. The zoomed-in far-field diffraction patterns of forked gratings with topological charges $L = 1$ and $L = 3$ are shown in Figs. 7.12(c) and (d), respectively. The higher orders are clearly visible, while the 0^{th} diffraction order is completely cancelled. The size of the donut beam increases with the charge number, as expected.

7.3.4 Design of binary helical axicons

Helical axicons are used for the generation of higher-order Bessel beams (HOBBs).[19–21] A helical axicon can be generated by the interference between a helical wave and a conical wave. Helical axicons can be designed as either amplitude or phase HOEs, both yielding interesting results. When a

Table 7.4 MATLAB code for the design of a binary forked grating using the computer generated-holographic method.

```
%Forked grating
L=1;
A=V*exp(1i*L*(atan2(Y,X)));
B=V*exp(1i*(2*pi/lambda)*tand(Angle)*Y);
```

Downloaded From: https://www.spiedigitallibrary.org/ebooks/ on 27 Feb 2022
Terms of Use: https://www.spiedigitallibrary.org/terms-of-use

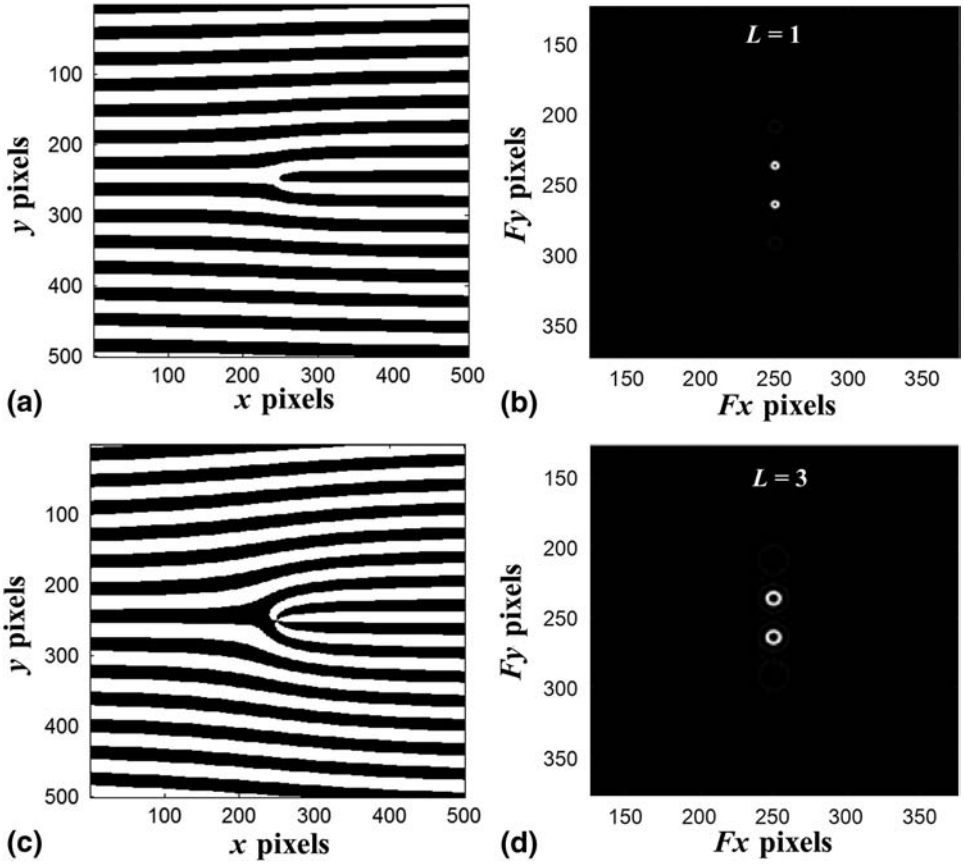

Figure 7.12 Images of the binary forked gratings with tilt angle $\theta = 1$ deg and topological charge (a) $L = 1$ and (b) $L = 3$, and (c), (d) their respective far-field diffraction patterns.

Laguerre–Gaussian beam generated by a spiral phase plate is incident on an axicon, a HOBB can be generated.[19,20] Hence, by generating a composite element that has the functions of both the spiral phase plate and axicon, a HOBB can be generated in just one pass. In the case of a phase CGH, the odd and even zones are out of phase by π, generating a flower-shaped intensity profile in its far field.[22,23] As with the spiraling wavefront in the case of HOBBs, the flower-shaped intensity profile rotates along the optical axis with propagation distance. The helical wave and conical wave are given in Eqs. (7.9) and (7.6), respectively. The MATLAB code is similar to the codes for the above cases. The phase profile of a helical axicon (tilt angle $\theta = 1$ deg) with topological charges $L = 3$ and $L = 5$ are shown in Figs. 7.13(a) and (b), respectively. The corresponding far-field diffraction patterns are shown in Figs. 7.13(c) and (d), from which it can be noted that the number of petals corresponds to twice the topological charge L, as explained in literature.[24,25]

Downloaded From: https://www.spiedigitallibrary.org/ebooks/ on 27 Feb 2022
Terms of Use: https://www.spiedigitallibrary.org/terms-of-use

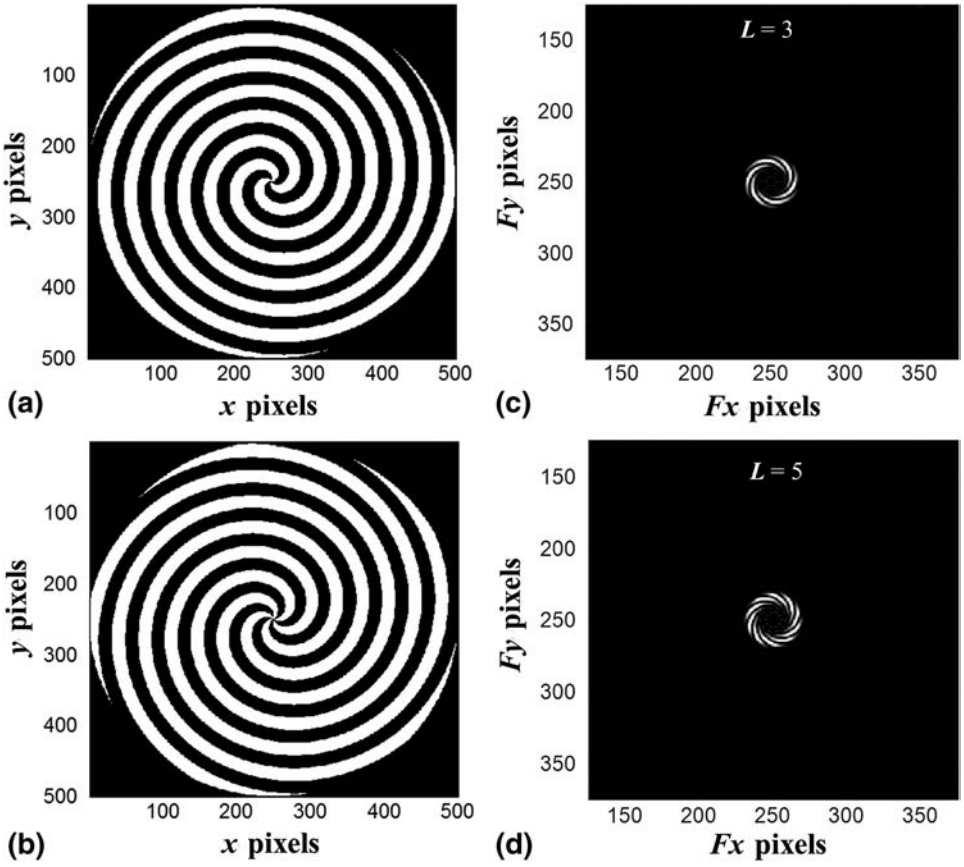

Figure 7.13 Images of the phase profile of the helical axicon with topological charges (a) $L = 3$ and (b) $L = 5$, and (c), (d) their respective far-field diffraction patterns.

7.3.5 Design of off-axis axilenses

As the name suggests, an axilens is an optical element whose behavior lies between a FZP and an axicon, as discussed in Chapter 3.[26,27] An axilens is useful as it has a tailored focal depth with high lateral resolution. This is unlike both the FZP, which has a point focus with a short focal depth, and an axicon, which has a large focal depth. An off-axis axilens is designed by superposition of a wave generated by an axilens with that of a tilted plane wave. The equation of a wave generated by an axilens with a focal length of f_0, focal depth of Δf, and radius of R is given by

$$\Psi_2(x,y) = \exp\left[j\left(\frac{2\pi}{\lambda}\right)\left(f(x,y) - \sqrt{f(x,y)^2 - (x^2+y^2)}\right)\right], \tag{7.10}$$

where

Downloaded From: https://www.spiedigitallibrary.org/ebooks/ on 27 Feb 2022
Terms of Use: https://www.spiedigitallibrary.org/terms-of-use

$$f(x,y) = f_0 + \left(\frac{\Delta f}{R}\right)\sqrt{x^2 + y^2}. \tag{7.11}$$

The equation of a tilted plane wave is given in Eq. (7.7). The MATLAB code for design of the axilens is given in Table 7.5. The element is designed with $f_0 = 10$ mm and $\Delta f = 3$ mm, and the tilt angle $\theta = 1$ deg.

The binary phase profile of the generated CGH is shown in Fig. 7.14(a), and its diffraction pattern is shown in Fig. 7.14(b). The diffraction pattern shows twin

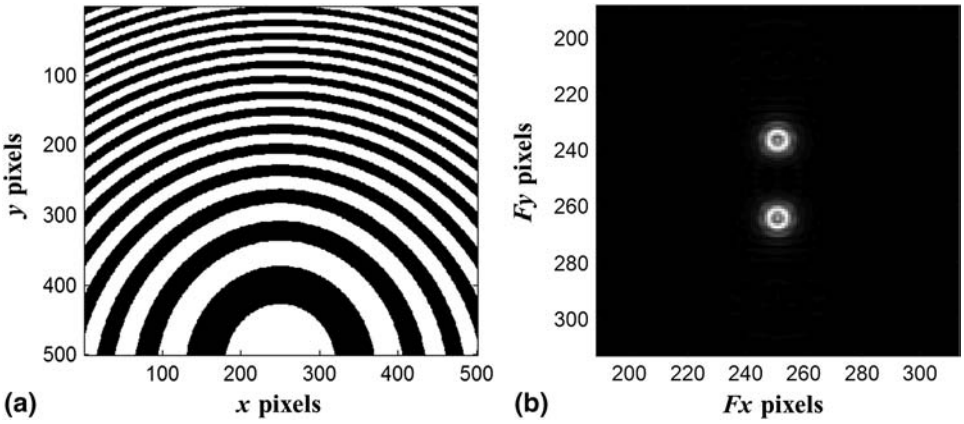

Figure 7.14 (a) Phase profile of an off-axis binary axilens and (b) the far-field diffraction pattern of the axilens.

Table 7.5 MATLAB code for design of an off-axis axilens using the holographic method.

```
%Off axis axilens
%Define parameters
   N=500;%%Define size of the matrix
   Angle=1;%Define angle of the second plane wave
   V=0.5;%%Visibility controller
   lambda=0.632*1e-6;%Define wavelength
   L=3;
   f0=0.01;
   delf=0.003;
%Create sampled space
   del=1*1e-6;%sampling
   x=-N/2:N/2-1;
   y=-N/2:N/2-1;
   [X,Y]=meshgrid(x*del,y*del);
   f=f0+delf*sqrt(X.^2+Y.^2);
%Simulate interference
   A=V*exp(1i*((2*pi)/lambda)*(f-sqrt(f.*f-(X.^2+Y.^2))));
   B=V*exp(1i*(2*pi/lambda)*tand(Angle)*Y);
   D=A+B;%Interference of the object and reference wave
   IN=abs(D).*abs(D);
```

(*Continued*)

Downloaded From: https://www.spiedigitallibrary.org/ebooks/ on 27 Feb 2022
Terms of Use: https://www.spiedigitallibrary.org/terms-of-use

Table 7.5. Continued

```
   figure (2)
   colormap gray
   imagesc(IN)
%%Construct FZP
   IN1=im2bw(IN);%Binarize the matrix
   Grating=exp(1i*pi*IN1);%Generate the Axicon
```

beams, as the phase profile of the CGH is either binary or sinusoidal. Otherwise, the diffraction pattern is similar to that of an off-axis axicon, as expected.

7.3.6 Accelerating beams

Recently, beams that can propagate along curved paths (hence, known as accelerating beams) have attracted attention due to their interesting properties and prospective applications.[28–31] The geometrical optics technique for design of CGHs that generate accelerating Airy beams is presented in this section.[32,33] An axicon is a conical prism that generates a 0^{th} order Bessel-like beam.[34,35] When an additional optical element is attached to the front surface of the axicon, the path direction can be precisely controlled by the thickness or refractive index profile of the beam path steering element (BPSE). The optics configuration for focusing light propagating along the z direction using a refractive axicon is shown in Fig. 7.15. The base angle and refractive index of the axicon are denoted as α_1 and n_g, respectively. The divergence angle β_1 is estimated using trigonometry as

$$\beta_1 = (n_g - 1)\alpha_1. \tag{7.12}$$

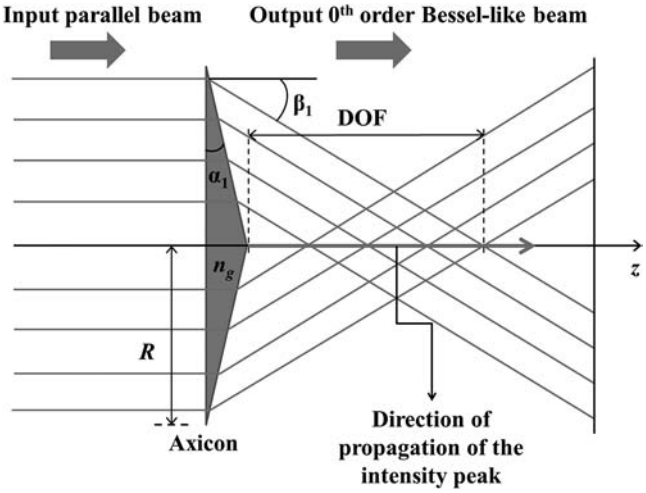

Figure 7.15 Optics configuration for focusing light using a refractive axicon (reprinted from Ref. 33).

Downloaded From: https://www.spiedigitallibrary.org/ebooks/ on 27 Feb 2022
Terms of Use: https://www.spiedigitallibrary.org/terms-of-use

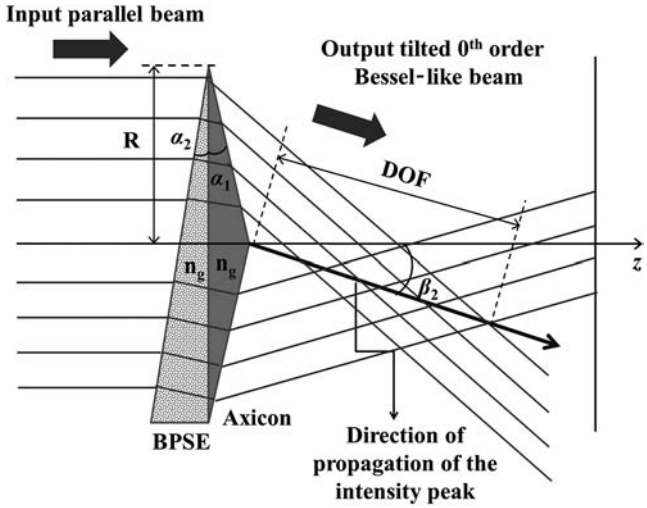

Figure 7.16 Optics configuration for generation of a tilted Bessel-like beam using a refractive axicon and a thin prism (BPSE) in tandem (reprinted from Ref. 33).

The depth of focus is given as

$$\mathrm{DOF} = R\tan\beta. \tag{7.13}$$

If the BPSE is a thin prism with an angle α_2 and refractive index n_g as shown in Fig. 7.16, then the input light is converted into a tilted 0^{th} order Bessel-like beam.

The path of the beam is precisely controlled by the properties (α_1, n_g, etc.) of the thin prism. The thickness profile of a thin prism is given as

$$t_1(x,y) = a_1 x + b_1 y, \tag{7.14}$$

where, a_1 and b_1 are the coefficients of the thickness profile of the thin prism.

The direction of propagation of the 0^{th} order Bessel-like beam is then given as

$$\beta_2 = (n_g - 1)\alpha_2. \tag{7.15}$$

This case is similar to that presented in Section 7.3.2 on off-axis axicons, where the CGH was designed by the interference of a conical wave with a tilted-plane-wave CGH.

It is interesting to see what happens when the BPSE is a curved element, as shown in Fig. 7.17. The thickness profile of the BPSE is given as

$$t_2(x,y) = f_1(x) + f_2(y). \tag{7.16}$$

A CGH for generation of accelerating Airy beams can be designed by generating the interference between a conical wave and a curved wave with a profile similar to that of the BPSE shown in Fig. 7.17. For demonstration,

Downloaded From: https://www.spiedigitallibrary.org/ebooks/ on 27 Feb 2022
Terms of Use: https://www.spiedigitallibrary.org/terms-of-use

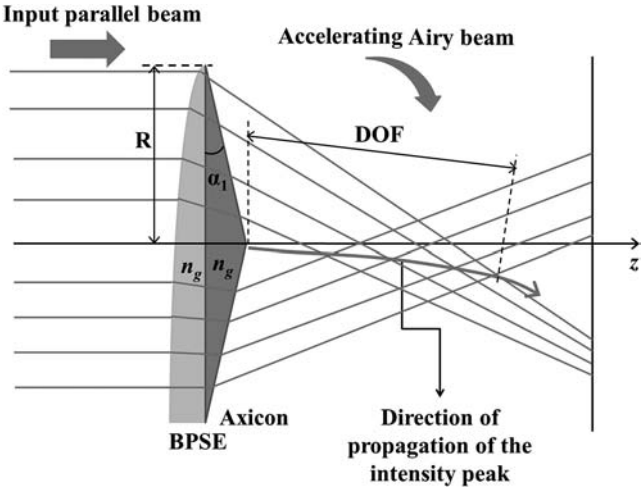

Figure 7.17 Optics configuration for generation of an accelerating Airy beam using a refractive axicon and a thin prism (BPSE) in tandem (reprinted from Ref. 33).

the angle of the axicon is selected as 0.1 deg, and the thickness profile of the BPSE is selected as

$$t_2(x,y) = 10x^{0.5} + 10y^{0.5}. \tag{7.17}$$

The MATLAB code is similar to that given in Tables 7.1 and 7.2. The design section of the MATLAB code is shown in Table 7.6. The phase profile of the CGH is shown in Fig. 7.18(a), and the far-field diffraction pattern is shown in Fig. 7.18(b).

The two first diffraction orders result due to the binary or sinusoidal phase profile of the CGH. The above procedure can be repeated to generate accelerating Airy beams with interesting path profiles. As with any diffractive element, the beam very close to the element is not easily accessible and hence is not useful for many applications. Additionally, the intensity at each plane is less because the light intensity is spread over the entire focal depth. These issues can be resolved by replacing the axicon with an axilens.

Table 7.6 MATLAB code for design of a CGH for generating accelerating beams.

```
%Accelerating beams
%Define parameters
   N=500;%%Define size of the matrix
   Angle=0.1;%Define angle of the second plane wave
   V=0.5;%%Visibility controller
   lambda=0.632*1e-6;%Define wavelength
%Create sampled space
   del=1*1e-6;%sampling
   x=-N/2:N/2-1;
   y=-N/2:N/2-1;
```

(*Continued*)

Downloaded From: https://www.spiedigitallibrary.org/ebooks/ on 27 Feb 2022
Terms of Use: https://www.spiedigitallibrary.org/terms-of-use

Table 7.6. Continued

```
   [X,Y]=meshgrid(x*del,y*del);
   r=sqrt(X.^2+Y.^2);
   A=V*exp(1i*(r/lambda)*tand(Angle)*2*pi);
   B=V*exp(1i*(10*sqrt(Y/del+N/2)+10*sqrt(X/del+N/2)));
   D=A+B;%Interference of the object and reference wave
%%Intensity profile
   I=abs(D).*abs(D);
   I1=im2bw(I);
   AB=exp(1i*pi*I1);
   % AB(r>100*del)=0;
   E=fftshift(fft2(AB));
   I2=(abs(E).*abs(E));
   colormap(gray);%%Display result
   imagesc(I2);
```

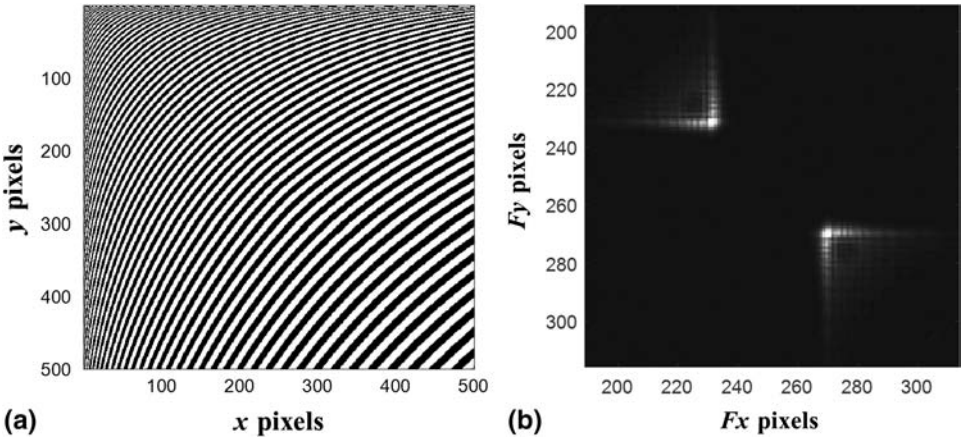

Figure 7.18 (a) Image of the binary phase profile of the CGH generated by the interference of a conical wave and a BPSE and (b) its far-field diffraction pattern (reprinted from Ref. 33).

7.4 Multiple-Beam Interference CGH

Multiple-beam interference has many advantages, including its extremely narrow interference maxima compared to that of two-beam interference.[36] Fabrication of large-area devices using electron beam lithography, focused ion beam lithography, and photolithography is difficult. In such cases, laser-based multiple-beam or multiple-exposure interferometry is a viable solution as long as the pattern is periodic.[37] The technique described here is not for fabrication but to verify the pattern generated by the different optical beams. In general, for generation of an interference pattern with periodicity along one direction, two optical waves are required. To generate a pattern with periodicity along two directions, three optical waves are required, and so on. Interference of four tilted plane waves is carried out to obtain periodicity along two directions in this case. The four tilted waves are expressed by

Downloaded From: https://www.spiedigitallibrary.org/ebooks/ on 27 Feb 2022
Terms of Use: https://www.spiedigitallibrary.org/terms-of-use

$$\Psi_1(x,y) = \exp\left[i\left(\frac{x}{\lambda}\right)\tan(\theta)\times 2\pi\right], \tag{7.18}$$

$$\Psi_2(x,y) = \exp\left[i\left(\frac{x}{\lambda}\right)\tan(-\theta)\times 2\pi\right], \tag{7.19}$$

$$\Psi_3(x,y) = \exp\left[i\left(\frac{y}{\lambda}\right)\tan(\theta)\times 2\pi\right], \tag{7.20}$$

$$\Psi_4(x,y) = \exp\left[i\left(\frac{y}{\lambda}\right)\tan(-\theta)\times 2\pi\right]. \tag{7.21}$$

For normalizing the matrices, a visibility factor of 0.25 is selected for each optical wave. The MATLAB code for generation of an interference pattern with 2D periodicity by the superposition of the above four optical wavefronts is given in Table 7.7. The image of the interference pattern is shown in Fig. 7.19(a). The procedure can be repeated by replacing the tilted-plane wavefronts by other wavefronts with interesting profiles.[38–41] The change in the interference pattern when the orientation of two of the tilted plane waves is varied is shown in Fig. 7.19(b). These interference patterns can have subwavelength features and, hence, are useful as antireflection coatings and in photonic crystal waveguide fabrication.[42]

Table 7.7 MATLAB code for generation of multiple-beam interference patterns.

```
%%Multiple beam interference
%Define parameters
   N=500;%%Define size of the matrix
   Angle=1;%Define angle of the second plane wave
   V=0.25;%%Visibility controller
   lambda=0.632*1e-6;%Define wavelength
%Sampling
   del=1*1e-6;%sampling
   x=-N/2:N/2-1;
   y=-N/2:N/2-1;
   [X,Y]=meshgrid(x*del,y*del);
%Simulate interference
   A=V*exp(1i*(Y/lambda)*tand(Angle)*2*pi);
   B=V*exp(1i*(X/lambda)*tand(-Angle)*2*pi);
   C=V*exp(1i*(X/lambda)*tand(Angle)*2*pi);
   D=V*exp(1i*(Y/lambda)*tand(-Angle)*2*pi);
   I=A+B+C+D;%Interference of the object and reference wave
%%Intensity profile
   IN=abs(I).*abs(I);
```

Downloaded From: https://www.spiedigitallibrary.org/ebooks/ on 27 Feb 2022
Terms of Use: https://www.spiedigitallibrary.org/terms-of-use

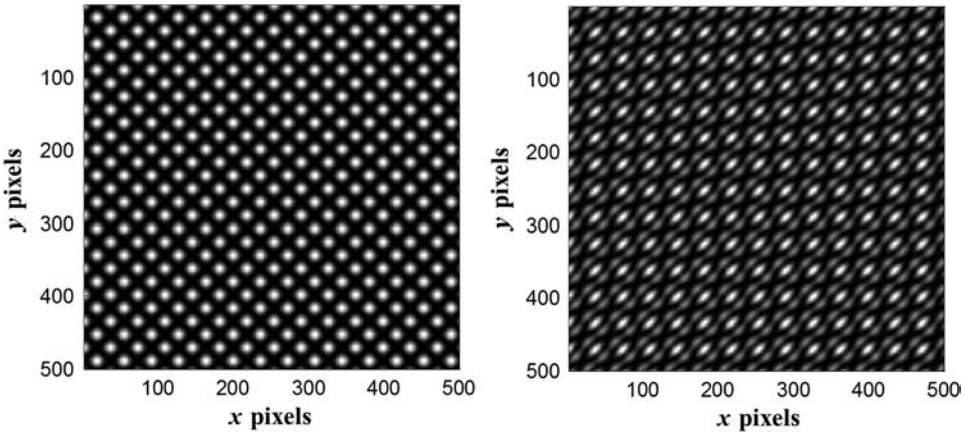

Figure 7.19 (a) Interference pattern obtained by the superposition of four tilted plane waves described by Eqs. (7.18)–(7.21). (b) Interference pattern obtained by the superposition of four tilted plane waves with different orientations.

7.5 Computer-Generated Amplitude Fourier Holograms

In earlier sections, the design of CGHs for different beam-shaping applications was discussed. This section presents the design of a computer-generated Fourier amplitude hologram to generate any arbitrary intensity pattern. Let the object be a planar amplitude mask (ξ, η) plane called the object plane. Let (x, y) be the hologram plane, which is at a distance f from the object plane, where f is the focal plane of the lens. The amplitude transmittance functions for the object and the reference waves are $T_o(\xi, \eta)$ and $T_r(\xi, \eta)$ respectively. By applying the linearity theorem of Fourier transforms, the two transmission functions can be added first, and the sum of their wave fields at the image plane can be calculated as

$$U(x,y) = \frac{e^{jkf}\, e^{j\frac{k}{2f}(x^2+y^2)}}{j\lambda f} \int_{-\infty}^{+\infty}\int_{-\infty}^{+\infty} \left[T_o(\xi,\eta) + T_r(\xi,\eta)\right] \exp\left[-j\frac{2\pi}{\lambda f}(x\xi + y\eta)\right] d\xi d\eta. \tag{7.22}$$

The reference beam is considered to be a plane wave with uniform intensity in the hologram plane. The setup for recording and reconstruction of a Fourier hologram includes a convex lens such that the hologram/image plane is at the focal plane of the lens, as shown in Fig. 7.20. A point source is chosen as the reference, which, upon Fourier transformation, yields uniform illumination in the image plane.

The intensity distribution in the hologram plane is given by

$$I = UU^*. \tag{7.23}$$

Downloaded From: https://www.spiedigitallibrary.org/ebooks/ on 27 Feb 2022
Terms of Use: https://www.spiedigitallibrary.org/terms-of-use

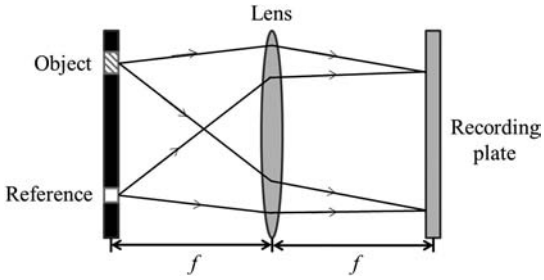

Figure 7.20 Hologram recording setup (reprinted from Ref. 43).

The transmission function $T(x, y)$ of the hologram is proportional to the intensity distribution. The reconstruction is performed by evaluating the function $T(x, y)$ using the Fraunhofer diffraction formula:

$$U(x,y) = \frac{e^{jkf}\, e^{j\frac{k}{2f}(x^2+y^2)}}{j\lambda f} \int_{-\infty}^{+\infty}\int_{-\infty}^{+\infty} \left[T(\xi,\eta)\right] \exp\left[-j\frac{2\pi}{\lambda f}(x\xi + y\eta)\right] d\xi d\eta \qquad (7.24)$$

The result of the integration yields four terms. The first term corresponds to the Fourier transform of a constant. The second term is the autocorrelation function of the object wave with itself. The third and fourth terms are of interest and correspond to the interference between the object and reference waves from the point source.[1] The steps for simulating the recording and reconstruction of a Fourier hologram are presented in Fig. 7.21.

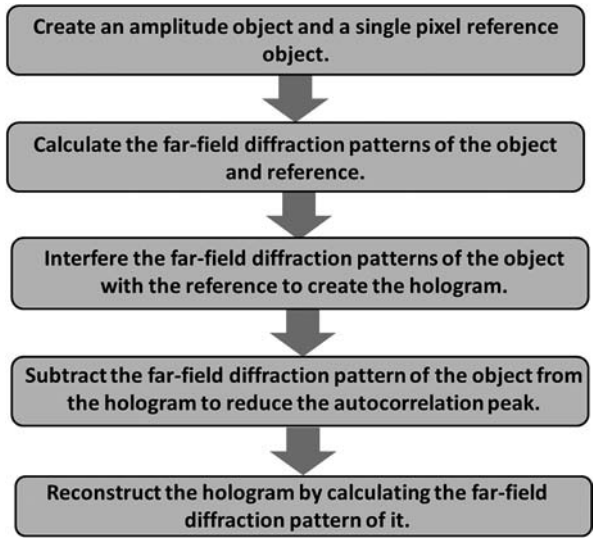

Figure 7.21 Flow chart for simulating the recording and reconstruction of a Fourier hologram.

Downloaded From: https://www.spiedigitallibrary.org/ebooks/ on 27 Feb 2022
Terms of Use: https://www.spiedigitallibrary.org/terms-of-use

Table 7.8 MATLAB code for the design of computer-generated Fourier holograms.

```
%Fourier Hologram
% Load the object and create the object and reference matrices
   N=500;%Define the size of the matrix
   A=imread('F:\IITM.jpg','jpg');%Loading the image
   A=double(A);
   A=A(1:N,1:N);
   A=imresize(A,[N,N]);
   B=zeros(N,N);%Dirac delta function
   B(250,250)=100;
%Calculate the far field diffraction patterns of the object and
%reference
   A1=fftshift(fft2(A));%Calculate the diffraction pattern for
   the object
   I1=abs(A1).*abs(A1);
   B1=fftshift(fft2(B));%Calculate the diffraction pattern for
   the reference
   I2=abs(B1).*abs(B1);
%Create the hologram by interfering the far field diffracted
%fields of object and reference
   D1=A1+B1;
   I3=abs(D1).*abs(D1);
%Filtering
   I4=(I3-I1);%Filtering of autocorrelation term
%Hologram reconstruction
   D2=fftshift(fft2(I4));
   I5=abs(D2).*abs(D2);
```

The reconstructed image shows two images of the object, one of which is inverted, as expected. The image of the object can be easily created in Microsoft PowerPoint or Paint. The MATLAB code for design of Fourier holograms and their reconstruction is given in Table 7.8. The image of the object is shown in Fig. 7.22(a). The image of the hologram is shown in Fig. 7.22(b). The reconstructed images without and with filtering are shown in Figs. 7.23(a) and (b), respectively.

The hologram can be used for the study of low- and high-pass filtering computational experiments. In the hologram, the high spatial frequencies of the object are at the outer parts due to high diffraction angles, and the low spatial frequencies of the object are at the center. Hence, by zero padding either the outer or inner regions of the hologram before reconstruction, the areas of different frequency content can be identified. The center part of the hologram (100 pixels $\times$ 100 pixels) is zero padded in the first case, and the outer parts with length of 100 pixels are zero padded in the second case. The results of reconstruction in each case are shown in Figs. 7.24(a) and (b).

For the high-pass-filtered case, it can be seen that only the edges of the letters are visible, indicating that light is diffracted at higher angles at the edges and at lower angles in the center. In the case of low-pass filtering, the

Downloaded From: https://www.spiedigitallibrary.org/ebooks/ on 27 Feb 2022
Terms of Use: https://www.spiedigitallibrary.org/terms-of-use

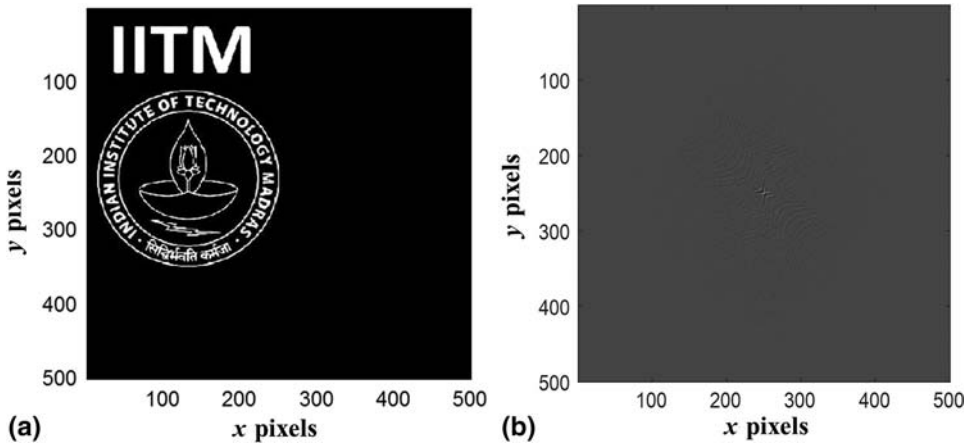

Figure 7.22 (a) Image of the object used for the generation of the computer-generated Fourier hologram and (b) image of the Fourier hologram obtained by the interference of the object and reference waves.

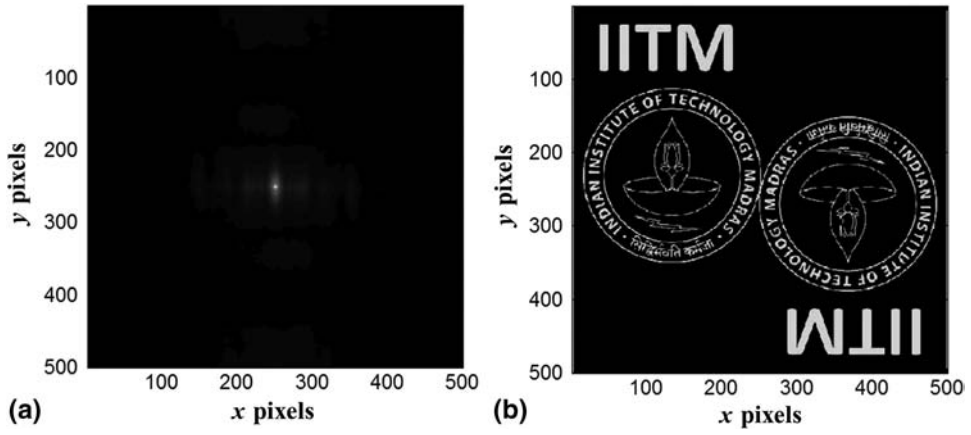

Figure 7.23 Reconstruction of the hologram (a) without filtering and (b) with filtering of the autocorrelation factor.

reconstructed image is slightly blurred, as the higher-frequency components responsible for sharpness in the image are filtered out. The experiment can be repeated by zero padding different regions of the hologram before reconstruction. These experiments highlight a significant difference between photography and holography. In photography, removal of a portion means loss of information. However, in holography, all of the information can be reconstructed with only a part of the hologram. Optical reconstruction of the same can be carried out by binarizing the hologram, printing the hologram on transparent sheets, and illuminating the sheets with the light from a laser source in an optics configuration similar to that in Fig. 7.20.[43,44]

Downloaded From: https://www.spiedigitallibrary.org/ebooks/ on 27 Feb 2022
Terms of Use: https://www.spiedigitallibrary.org/terms-of-use

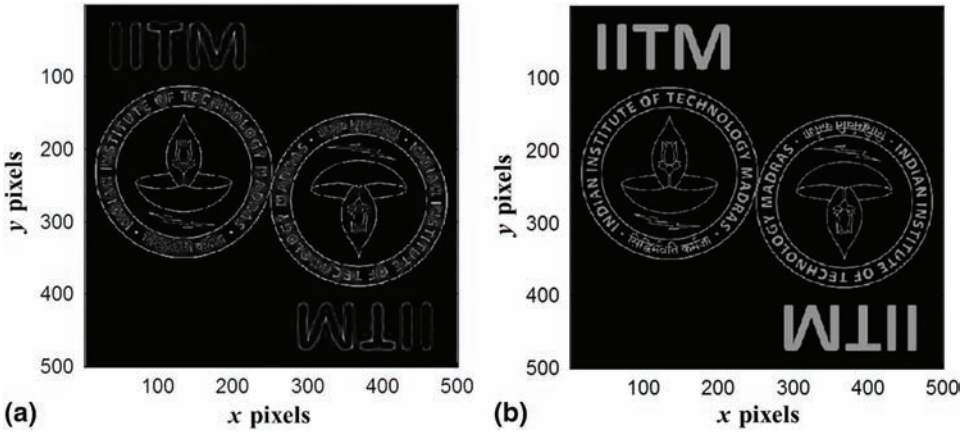

Figure 7.24 Reconstructed images from the hologram after (a) high-pass and (b) low-pass filtering.

7.6 Computer-Generated Amplitude Fresnel Holograms

Fresnel holograms can be considered to be the superposition of multiple FZPs. Hence, unlike Fourier holograms, Fresnel holograms do not require a lens for reconstruction. They can be designed in a manner similar to that presented in Chapter 3. The object plane is described using (ξ, η) coordinates, while the hologram plane, which is at a distance z from the object plane, has (x, y) coordinates. The amplitude transmittance functions for the object and the reference waves are $T_o(\xi, \eta)$ and $T_r(\xi, \eta)$, respectively. The diffracted light from the object plane can be described by the Fresnel diffraction integral:

$$U(x,y) = \frac{e^{jkz} e^{j\frac{k}{2z}(x^2+y^2)}}{j\lambda z} \int_{-\infty}^{+\infty}\int_{-\infty}^{+\infty} T_o(\xi,\eta) \exp\left[-j\frac{k}{2z}(x^2+y^2)\right] \times \exp\left[-j\frac{2\pi}{\lambda z}(x\xi + y\eta)\right] d\xi d\eta. \tag{7.25}$$

Even though this equation is analytical, the calculation of the field is achieved by a discrete or a fast Fourier transform. The diffraction field can be written as

$$U(x,y) = \frac{1}{N}\sum_{x=1}^{N}\sum_{y=1}^{N} T_o(\xi,\eta) \exp\left[-j\frac{k}{2z}(x^2+y^2)\right] \exp\left[-j\frac{2\pi}{N}(x\xi + y\eta)\right]. \tag{7.26}$$

Downloaded From: https://www.spiedigitallibrary.org/ebooks/ on 27 Feb 2022
Terms of Use: https://www.spiedigitallibrary.org/terms-of-use

Comparing Eqs. (7.25) and (7.26) results in an interesting relationship:

$$N = \lambda z. \tag{7.27}$$

Equation 7.28 shows that the distance z can be controlled by varying the matrix size N. This also solves the problem of scaling, as Eqs. (7.25) and (7.26) are equal. From Eq. (7.25), it can be understood that the Fresnel diffraction calculation involves three steps. The object matrix must be multiplied by the parabolic phase factor in the first step, followed by the Fourier transform operation, and once again multiplication by the parabolic phase factor. The reference wave is a plane wave; hence, a matrix with constant values can be used to represent it. The hologram can be generated by adding the two matrices and performing the filtering operations discussed in Section 7.3. The computer reconstruction has to be done in the same sequence to obtain the reconstructed image. The MATLAB code for the design of a Fresnel hologram is given in Table 7.9. The image of the object is shown in Fig. 7.25.

Table 7.9 MATLAB code for the design of computer-generated Fresnel holograms.

```
%Fresnel Hologram
%Load object and create the object and reference matrices
   N=500;% Define the matrix size
   B=ones(N,N);%Reference wave
   A=imread('C:\Vijayakumar\mesh.jpg','jpg');%Loading the
   %image
   A=double(A);%Convert symbolic object to numeric object
   A=A(1:N,1:N);
   A=A/max(max(A));%Normalizing the matrix
%Sampling
   del=1;%
   x=-N/2:N/2-1;
   y=-N/2:N/2-1;
   [X,Y]=meshgrid(x*del,y*del);
%Calculate the Fresnel diffraction pattern of the object
   A1=A.*exp(-1i*(pi/N)*(X.^2+Y.^2));
   A2=fftshift(fft2(fftshift(A1)));
   A3=A2.*exp(1i*(pi/N)*(X.^2+Y.^2));
%Create interference between the object and reference waves
   H1=B+A3;%Interference pattern
%Filtering
   I1=abs(A3).*abs(A3);
   I2=abs(H1).*abs(H1);
   H2=I2-I1;%Filtering
   H2=H2/max(max(H2));%Normalizing the hologram
%Reconstruct the hologram
   H3=H2.*exp(-1i*(pi/N)*(X.^2+Y.^2));
   H4=fftshift(fft2(fftshift(H3)));
   H5=H4.*exp(1i*(pi/N)*(X.^2+Y.^2));
   H6=(abs(H5).*abs(H5));
   H7=rot90(H6,2);
   colormap(gray)%Display reconstructed image
   imagesc(H7)
```

Downloaded From: https://www.spiedigitallibrary.org/ebooks/ on 27 Feb 2022
Terms of Use: https://www.spiedigitallibrary.org/terms-of-use

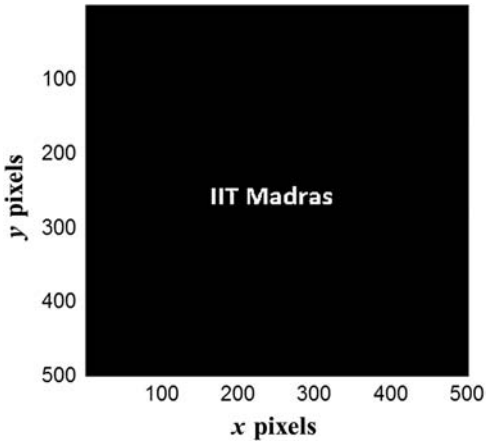

Figure 7.25 Image of the object used for generation of the Fresnel hologram.

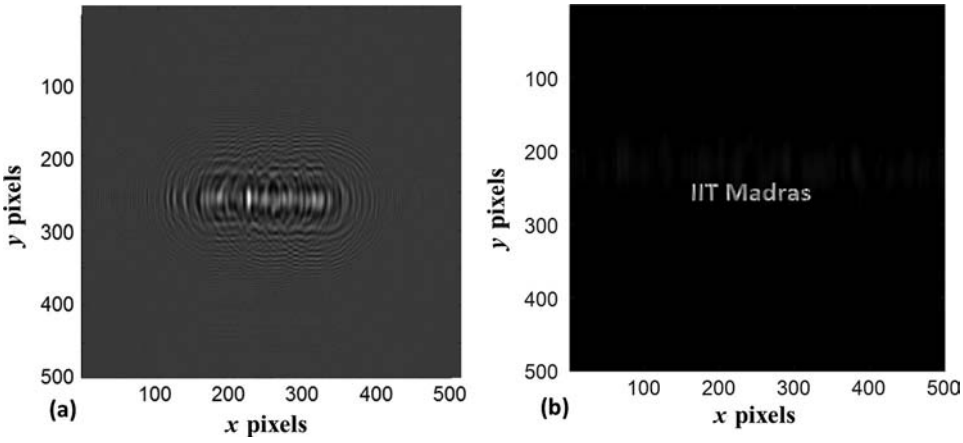

Figure 7.26 (a) Image of the hologram and (b) reconstructed image of the object.

The image of the hologram and the reconstructed image are shown in Figs. 7.26(a) and (b), respectively. Using the same method, it is also possible to design holograms for objects with depth information. Objects at different distances can be realized by constructing them in matrices with different numbers of pixels.[45] During reconstruction, different objects will be reconstructed at different distances.

7.7 Conclusions

The design of DOEs using the computer-generated holographic method is discussed in detail. CGHs ranging from simple 1D gratings to recently developed elements that generate accelerating Airy beams are covered. The procedures discussed in this chapter can be used for designing CGHs to be

Downloaded From: https://www.spiedigitallibrary.org/ebooks/ on 27 Feb 2022
Terms of Use: https://www.spiedigitallibrary.org/terms-of-use

used in a computational optics lab, to understand interferometers without any physical optical setup, and for research or industry applications. A variety of interesting experiments are possible using the given MATLAB codes. The elements designs use only binary phase profiles. However, it is possible to redesign the elements as multilevel or grayscale patterns in MATLAB. Designs were presented with matrix sizes of only 500 pixels. Larger matrices must be employed to achieve higher resolution. Computer-generated Fresnel and Fourier holograms can be designed with minimal facilities. Amplitude versions can be printed on transparent sheets for optical reconstruction at low cost.

7.8 Exercises

E.7.1 Design a CGH that focusus a diverging wavefront with a wavelength of 633 nm emanating from a point source a distance 10 mm away from the CGH plane to a point a distance 20 mm from the FZP plane.

E.7.2 Design an off-axis FZP with a focal length of 25 mm and a tilt angle of 3 deg for a wavelength of 633 nm.

E.7.3 Using the holographic method, design a modified axicon with two angles α_1 and α_2 such that α_1 is twice that of α_2 as shown in the figure below.

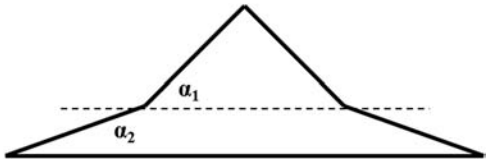

E.7.4 Design a CGH that can generate a focused ring pattern with a radius of 100 μm at a distance of 5 mm when illuminated by a uniform plane wave.

E.7.5 Design a CGH that can generate a helical wave front with topological charge $L = 5$ and focus it at a distance of 5 mm from the CGH plane.

References

1. J. W. Goodman, *Introduction to Fourier Optics*, Second Edition, McGraw-Hill Companies Inc., New York (1996).
2. B. C. Kress and P. Meyrueis, *Applied Digital Optics*, John Wiley & Sons, Chichester, UK (2009).
3. P. Hariharan, *Optical Holography: Principles, Techniques and Applications*, Second Edition, Cambridge University Press, Cambridge, UK (1996).

Downloaded From: https://www.spiedigitallibrary.org/ebooks/ on 27 Feb 2022
Terms of Use: https://www.spiedigitallibrary.org/terms-of-use

4. D. H. Close, "Holographic optical elements," *Opt. Eng.* **14**(5), 145402 (1975) [doi: 10.1117/12/7971806].
5. K. A. Winick and J. R. Fienup, "Optimum holographic elements recorded with nonspherical wave fronts," *J. Opt. Soc. Am.* **73**, 208–217 (1983).
6. J. N. Cederquist and J. R. Fienup, "Analytic design of optimum holographic optical elements," *J. Opt. Soc. Am. A* **4**, 699–705 (1987).
7. E. Hasman and A. A. Friesem, "Analytic optimization for holographic optical elements," *J. Opt. Soc. Am. A* **6**, 62–72 (1989).
8. D. C. Chu, J. R. Fienup, and J. W. Goodman, "Multi-emulsion, on-axis, computer generated hologram," *Appl. Opt.* **12**, 1386–1388 (1973).
9. M. R. Feldman and C. C. Guest, "Computer generated holographic optical elements for optical interconnection of very large scale integrated circuits," *Appl. Opt.* **26**, 4377–4384 (1987).
10. A. J. MacGovern and J. C. Wyant, "Computer-generated holograms for testing optical elements," *Appl. Opt.* **10**, 619–624 (1971).
11. G. Tricoles, "Computer generated holograms: an historical review," *Appl. Opt.* **26**, 4351–4360 (1987).
12. E. Hecht, *Optics*, Fourth Edition, Addison Wesley, San Francisco (2002).
13. S. I. Hwang, D. H. Song, and D. K. Ko, "Tailoring light structures using an off-axis double axicon holographic pattern," *Opt. Commun.* **283**, 4208–4213 (2010).
14. A. Vasara, J. Turunen, and A. T. Friberg, "Realization of general nondiffracting beams with computer-generated holograms," *J. Opt. Soc. Am. A* **6**, 1748–1754 (1989).
15. R. L. Phillips and L. C. Andrews, "Spot size and divergence for Laguerre Gaussian beams of any order," *Appl. Opt.* **22**, 643–644 (1983).
16. T. Watanabe, M. Fujii, Y. Watanabe, N. Toyama, and Y. Iketaki, "Generation of a doughnut-shaped beam using a spiral phase plate," *Rev. Sci. Instrum.* **75**, 5131–5135 (2004).
17. M. W. Beijersbergen, R. P. C. Coerwinkel, M. Kristensen, and J. P. Woerdman, "Helical-wavefront laser beams produced with a spiral phase plate," *Opt. Commun.* **112**, 321–327 (1994).
18. G. F. Brand, "Phase singularities in beams," *Am. J. Phys.* **67**, 55–60 (1999).
19. J. Arlt and K. Dholakia, "Generation of high-order Bessel beams by use of an axicon," *Opt. Commun.* **117**, 297–301 (2000).
20. V. Jarutis, R. Paskauskas, and A. Stabinis, "Focusing of Laguerre–Gaussian beams by axicon," *Opt. Commun.* **184**, 105–112 (2000).
21. S. N. Khonina, V. V. Kotlyar, V. A. Soifer, M. V. Shinkaryev, and G. V. Uspleniev, "Trochoson," *Opt. Commun.* **91**, 158–162 (1992).
22. A. Vijayakumar and S. Bhattacharya, "Multifunctional diffractive optical elements for the generation of higher order Bessel-like-beams," *Proc. SPIE* **9370**, 937034 (2015) [doi: 10.1117/12.2079081].

Downloaded From: https://www.spiedigitallibrary.org/ebooks/ on 27 Feb 2022
Terms of Use: https://www.spiedigitallibrary.org/terms-of-use

23. A. Vijayakumar, "Design, Fabrication, and Evaluation of Diffractive Optical Elements for the Generation of Focused Ring Patterns," Doctoral Thesis, Indian Institute of Technology Madras, Chennai, India (2015) [doi: 10.13140/RG.2.2.25996.51847].
24. A. Dudley and A. Forbes, "From stationary annular rings to rotating Bessel beams," *J. Opt. Soc. Am. A* **29**, 567–573 (2012).
25. N. Londoño, E. Rueda, J. A. Gómez, and A. Lencina, "Generation of optical vortices by using binary vortex producing lenses," *Appl. Opt.* **54**, 796–801 (2015).
26. N. Davidson, A. A. Friesem, and E. Hasman, "Holographic axilens: high resolution and long focal depth," *Opt. Lett.* **16**, 523–525 (1991).
27. J. Sochacki, Z. Jaroszewicz, A. Kołodziejczyk, and S. Bará, "Phase retardation of the uniform-intensity axilens," *Opt. Lett.* **17**, 7–9 (1992).
28. G. A. Siviloglou, J. Broky, A. Dogariu, and D. N. Christodoulides, "Observation of accelerating Airy beams," *Phys. Rev. Lett.* **99**, 213901 (2007).
29. M. A. Bandres, "Accelerating beams," *Opt. Lett.* **34**, 3791–3793 (2009).
30. G. A. Siviloglou and D. N. Christodoulides, "Accelerating finite energy Airy beams," *Opt. Lett.* **32**, 979–981 (2007).
31. G. A. Siviloglou, J. Broky, A. Dogariu, and D. N. Christodoulides, "Ballistic dynamics of Airy beams," *Opt. Lett.* **33**, 207–209 (2008).
32. S. Vo, K. Fuerschbach, K. P. Thompson, M. A. Alonso, and J. P. Rolland, "Airy beams: a geometric optics perspective," *J. Opt. Soc. Am. A* **27**, 2574–2582 (2010).
33. R. Dharmavarapu, A. Vijayakumar, and S. Bhattacharya, "Design and fabrication of holographic optical elements for the generation of tilted and accelerating Airy Beams," *Asian J. Phys.* **24**, 1363–1371 (2015).
34. J. H. McLeod, "The axicon: a new type of optical element," *J. Opt. Soc. Am.* **44**, 592–592 (1954).
35. J. H. McLeod, "Axicons and their uses," *J. Opt. Soc. Am.* **50**, 166–166 (1960).
36. O. Marchenko, S. Kazantsev, and L. Windholz, *Demonstrational Optics, Part 2: Coherent and Statistical Optics*, Springer, New York (2007).
37. S. H. Zaidi and S. R. J. Brueck, "Multiple-exposure interferometric lithography," *J. Vac. Sci. Technol. B* **11**, 658–666, (1993).
38. M. Kumar and J. Joseph, "Embedding a nondiffracting defect site in helical lattice wave-field by optical phase engineering," *Appl. Opt.* **52**, 5653–5658 (2013).
39. M. Kumar and J. Joseph, "Digitally reconfigurable complex two-dimensional dual-lattice structure by optical phase engineering," *Appl. Opt.* **53**, 1333–1338 (2014).
40. M. Campbell, D. N. Sharp, M. T. Harrison, R. G. Denning, and A. J. Turberfield, "Fabrication of photonic crystals for the visible spectrum by holographic lithography," *Nature (London)* **404**, 53–56 (2000).

Downloaded From: https://www.spiedigitallibrary.org/ebooks/ on 27 Feb 2022
Terms of Use: https://www.spiedigitallibrary.org/terms-of-use

41. L. Pang, W. Nakagawa, and Y. Fainman, "Fabrication of two-dimensional photonic crystals with controlled defects by use of multiple exposures and direct write," *Appl. Opt.* **42**, 5450–5456 (2003).
42. G. M. Burrow and T. K. Gaylord, "Multi-beam interference advances and applications: nano-electronics, photonic crystals, metamaterials, subwavelength structures, optical trapping, and biomedical structures," *Micromachines* **2**, 221–257 (2011).
43. A. Vijayakumar, B. J. Jackin, and P. K. Palanisamy, "Computer generated Fourier holograms for undergraduate optics laboratory," *Phys. Education* **28**, 1–10 (2012).
44. S. Trester, "Computer simulated holography and computer generated holograms," *Am. J. Phys.* **64**, 474–478 (1996).
45. S. Trester, "Computer-simulated Fresnel holography," *Eur. J. Phys.* **21**, 317–331 (2000).

Downloaded From: https://www.spiedigitallibrary.org/ebooks/ on 27 Feb 2022
Terms of Use: https://www.spiedigitallibrary.org/terms-of-use

Chapter 8
Fabrication of Diffractive Optical Elements

In earlier chapters, the design and analysis of simple and multifunctional DOEs using different techniques are presented. In this chapter, pre-fabrication techniques such as designing the lithography files, etc., and fabrication techniques with basic fabrication recipes are presented. The fabrication of micro-optical elements using photolithography has been studied for almost a century, while electron beam lithography (EBL) and focused ion beam (FIB) lithography are relatively new. Hence, for photolithography, only fabrication recipes are provided with a brief explanation of the fundamentals.

The chapter is divided into four sections. In Section 8.1, the different methods for designing lithography files are presented. The procedure for fabrication of DOEs using photolithography, EBL, and FIB systems are presented in Sections 8.2, 8.3, and 8.4, respectively.

8.1 Design of Lithography Files

Once the DOE is designed using the techniques described in the previous chapters, the next step is to convert the DOE design data into the file format that will be understood by the fabrication tool to be used. There are different types of lithography file formats, such as Graphic Data System (GDSII™), Drawing Exchange Format (DXF™), STereoLithography (STL), Caltech Intermediate Format (CIF), etc., for fabrication of DOEs using the various lithography systems.[1] In most photolithography, EBL, and FIB lithography systems, it is possible to create the DOE lithography files within the CAD software provided with the system. This can be done using built-in basic structures such as lines, boxes, and circles provided by the software. This manual drawing method is easier if the DOE is a simple periodic structure such as a grating. However, if the design is not linear, even something as simple as a FZP becomes difficult to achieve. In a FZP, for example, the circular zones have to be drawn one by one with different widths. If the FZP has a large

Downloaded From: https://www.spiedigitallibrary.org/ebooks/ on 27 Feb 2022
Terms of Use: https://www.spiedigitallibrary.org/terms-of-use

number of zones, say, around 1000, then the procedure becomes tiresome and time consuming, and the chances of making an error during design are high. In some cases, such as multifunctional DOEs, it is not possible to create the DOE's design with the basic structures available in the software.

In advanced lithography systems such as the RAITH150^{TWO}, Quanta™ 400F (FEI), or the Quanta 3D FEG (FEI), to name a few, the CAD software is fairly sophisticated. For example, it is possible to generate matrix copies in the RAITH150^{TWO}, which makes the design of periodic structures possible with a single command. Additional Boolean operations such as OR, AND, etc., also exist and are useful for designing multifunctional DOEs. In the case of the Quanta 3D FEG, there is provision to load a bitmap file of a DOE generated using another source, and this file can be scaled in the software before fabrication. In older versions of some lithography systems, the DOE design can be broken down and can be fabricated in sections. For instance, a grating can be fabricated line-by-line. This technique is quite useful, as the DOE patterning is possible with limited computational space and at the same time with high resolution. The same technique can be extended to multifunctional DOEs as well, by breaking them into a set of line data.

A major difference between a DOE design file created as an image file and one created using CAD software is that in the former the circular objects are piece-wise continuous, while in the latter they are polygons. As a result, the file sizes are larger when they are created as image files. It is not straightforward to create lithography files within MATLAB®. Hence, the image files created using MATLAB are converted into lithography files using software such as LinkCAD™. However, in software such as Python™, it is possible to directly create output files in a lithography format such as GDSII.

8.1.1 Lithography file generation with LinkCAD

The MATLAB codes given in the earlier chapters for the design of binary DOEs can be used to design DOEs for lithography as well. The MATLAB codes given earlier had a matrix size of 500 pixels $\times$ 500 pixels, and the dimensions of the physical quantities are given in micrometers. Using such a file would mean that the size of the DOE is also 500 μm $\times$ 500 μm with a pixel size of 1 μm. Theoretically, this pixel size is sufficient, as this is a super-wavelength DOE. However, when a circular DOE is designed, because it is piece-wise continuous, it has many sharp edges that result in diffraction patterns with errors. The images of rings with a width of 10 μm created using matrices with pixel sizes of 1 μm and 0.01 μm are shown in Figs. 8.1(a) and (b), respectively.

The rough-edge effect is not present if the DOE is a simple 1D or 2D grating with periods Λ that are integral multiples n of the pixel size Δ ($\Lambda = n\Delta$). However, this is not always the case. Hence, it is necessary to design DOEs with a higher resolution to eliminate or reduce this effect.

Downloaded From: https://www.spiedigitallibrary.org/ebooks/ on 27 Feb 2022
Terms of Use: https://www.spiedigitallibrary.org/terms-of-use

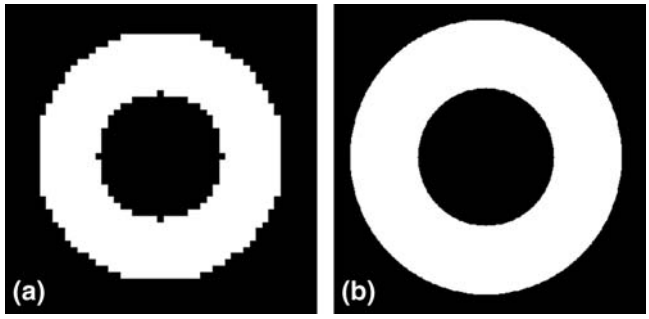

Figure 8.1 Images of rings with a width of 10 μm with (a) pixel size of 1 μm and (b) pixel size of 0.01 μm.

The same equations that were used for simulation can be employed again for designing the DOEs but with an increased spatial resolution for the lithography processes. The resolution of a design is given by the ratio of the physical lengths of the pattern to the number of pixels in the length design. For instance, if the length of a design file is 1000 pixels, and the physical dimension is 10 μm, then the resolution of the design is 10 nm. In our designs, most of the elements[2,3] were generated with a matrix size of 20,000 × 20,000 corresponding to a device size of 2 mm × 2 mm and, hence, a resolution of 100 nm. In some lithography systems such as the Quanta 3D FEG, the bitmap file can be directly used for fabrication. The physical dimension of each pixel of a bitmap file can be defined within the system. However, in most lithography systems, including mask writers for photolithography, the input design file must be in specific CAD formats such as DXF, GDSII, etc., as discussed earlier.

For complex structures such as HOEs or IFTA-based DOEs, which cannot be designed with CAD software, the following procedure can be used. The DOE is designed as a bitmap file and converted to either DXF or GDSII formats using LinkCAD software. The time of execution of the MATLAB codes with a computer with a 3.4-GHz processor and a RAM of 16 GB varied from few minutes to a couple of hours, depending on the different operations involved. The choice of the scheme for designing DOEs depends on the geometric composition of the structure and the required resolution.

For most of the examples in this book, the designs were generated using MATLAB and converted to GDSII or DXF formats using LinkCAD. This method of generating the design in a format accepted by the lithography system may not be required when using advanced software that can be purchased separately with systems like the RAITH150^{TWO}. This software accepts many file formats and allows one to create designs with high resolution. However, such software is quite expensive. Therefore, alternative procedures are needed. One such procedure for converting a matrix representing a DOE to a GDSII file using LinkCAD is shown in Fig. 8.2.

Downloaded From: https://www.spiedigitallibrary.org/ebooks/ on 27 Feb 2022
Terms of Use: https://www.spiedigitallibrary.org/terms-of-use

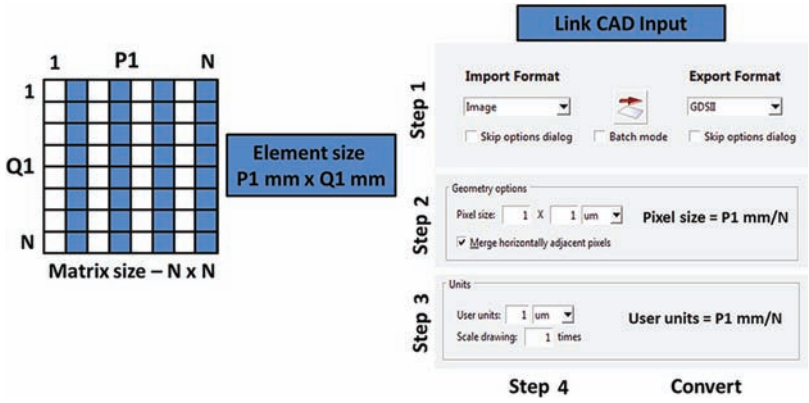

Figure 8.2 Schematic of the procedure for converting a matrix or image generated in MATLAB into a GDSII file using LinkCAD.

The pixel size of the element is the ratio of the element's length in millimeters to the size of the matrix. The pixel size is the same as the user units in this case.

Using LinkCAD is easy. The import format can be selected as 'Image', and the export format can be selected as 'GDSII'. There are a wide variety of export formats such as DXF, CIF, etc. Next, the pixel size is selected. If the matrix size is 20,000 × 20,000 for a device of size 2 mm × 2 mm, then the pixel size is 100 nm. The scaling factor can be selected, which in this case is 1. Then the file can be loaded and converted. There are numerous other facilities within the software that are useful for conversion. The converted file can be viewed either in LinkCAD or with any other CAD software before patterning. The output from LinkCAD can be directly used with any lithography system. This is a far less expensive method of creating lithography files than using the in-built special software available with some e-beam systems.

8.1.2 Special lithography files

As discussed in Section 8.1, in some lithography systems, it is possible to create the DOE design in the form of lines. In other words, the entire DOE is broken down into data that includes the starting and the ending point of each line. This is advantageous for the design of periodic rectilinear structures, as the file size can be considerably reduced. Let us consider the design of a 1D grating with 20,000 points in each line. In the vector method, the 20,000 points that make up a line can be replaced in the design file by just two points (x_1, y_1) and (x_2, y_2) that are the starting and the ending point of the line. The data points can be stored in a text file, and the size will be three to four orders of magnitude smaller than the corresponding bitmap file.

However, two important points need to be considered. For a HOE or DOE generated using the IFTA, there are few or no lines connecting points. This means that the data size generated using this method will equal the data

Downloaded From: https://www.spiedigitallibrary.org/ebooks/ on 27 Feb 2022
Terms of Use: https://www.spiedigitallibrary.org/terms-of-use

Table 8.1 MATLAB code for generating lithography data of a grating as lines.

```
%Generating line data for lithography
N=2000; % Size of the matrix
A=zeros(N,N); % Define matrices
B=zeros(N,N);
P=100; % Define period of the grating
p1=0; % Initialize line number
for q=1:N;
   if rem(q,P)<=P/2;
      p1=p1+1;
      X1(p1)=1;
      Y1(p1)=q;
      X2(p1)=N;
      Y2(p1)=q;
   end
end
fid = fopen('F:\1D grating.txt','wt');%Open a text file
for s=1:p1;
     fprintf(fid,'Draw Line %d,%d',X1(s),Y1(s));
     fprintf(fid,'\n');
     fprintf(fid,'    %d,%d',X2(s),Y2(s));
     fprintf(fid,'\n');
end
fclose(fid);%Close the text file
```

size generated as image file. Secondly, some analysis is needed before converting an image into a text file containing line data. For instance, if the image data of a 1D grating is converted into line data along the direction orthogonal to the direction of periodicity, then the file size will be smaller than if converting along the direction of periodicity. The MATLAB code for converting a 1D grating into line data and saving it as a text file is given in Table 8.1. The starting point and ending point of the line are calculated, assuming that the physical dimension of the DOE is 200 μm and the pixel size or spot size is 100 nm.

The size of the text file is only 40 kB, while the file size when generated as a bitmap file is 3.8 MB. Hence, it is advantageous to create a lithography file as a set of lines. This is the format used in most CAD software. As discussed earlier, this technique is not suitable for DOEs generated using the IFTA. It is also not suitable for patterning circular elements such as a circular grating or a FZP. Hence, in those cases, the data for points on the circle (polygon) must be generated and fabricated circle-by-circle or zone-by-zone, depending on the memory size of the lithography system. The MATLAB code for generation of the polygon point data of a circular grating is given in Table 8.2. The radial pixel size or the spot size is assumed to be 100 nm.

The image of a circular grating with three periods that was drawn with polygonal path scanning is shown in Fig. 8.3(a). A magnified image of the central part of Fig. 8.3(a) is shown in Fig. 8.3(b), where the polygon approximation is clearly visible.

Downloaded From: https://www.spiedigitallibrary.org/ebooks/ on 27 Feb 2022
Terms of Use: https://www.spiedigitallibrary.org/terms-of-use

Table 8.2 MATLAB code for generating lithography data of a circular grating as polygon-approximated circles.

```
%Generating polygon data for lithography
N=2000; % Size of the DOE
A=zeros(N,N); % Define matrices
B=zeros(N,N);
theta1=zeros(M);
P=100; % Define period of the grating
M=1000; % Define the number of points in the circle
p1=0; % Initialize the iteration variable
for r=1:300; % Generate point data of every circle
   for theta=1:M;
      if rem(r,P)<P/2;
      theta1(theta)=((2*pi)/M)*theta;
      p1=p1+1;
      X1(p1)=(r-1)*cos(theta1(theta));
      Y1(p1)=(r-1)*sin(theta1(theta));
      end
   end
end
fid = fopen('F:\circular grating.txt','wt');%Open text file
for s=1:p1;
fprintf(fid,'Draw Line %d,%d',X1(s),Y1(s));
fprintf(fid,'\n');
end
fclose(fid);%Close text file
```

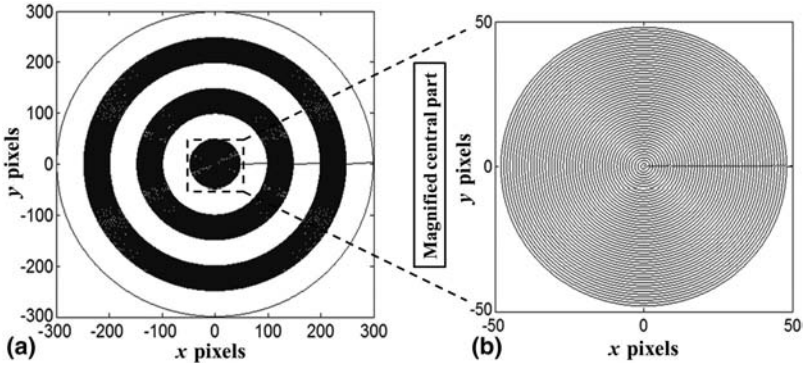

Figure 8.3 (a) Plot of the points of the polygons approximated on the circles with 1000 vertices for a circular grating. (b) Magnified central portion of the image in part (a).

In this case, the DOE has been designed with 1000 points for each circle. However, the number of points needs to be optimized based on the element radius and the memory limit of the system. The central parts of polygonal-approximated circular gratings with 10 and 25 vertices are shown in Figs. 8.4(a) and (b), respectively.

The MATLAB code given in Table 8.1 for 1D gratings follows raster scanning. The MATLAB code given in Table 8.2 for circular gratings follows

Downloaded From: https://www.spiedigitallibrary.org/ebooks/ on 27 Feb 2022
Terms of Use: https://www.spiedigitallibrary.org/terms-of-use

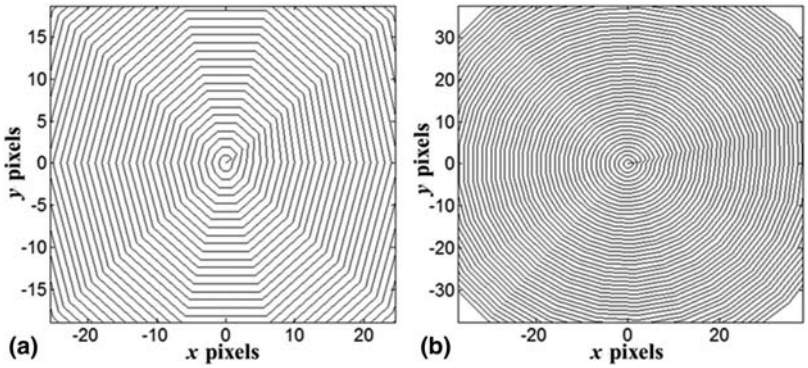

Figure 8.4 Plot of the polygonal path scanning of circular gratings with (a) 10 vertices and (b) 25 vertices.

outward circular scanning. By modifying the MATLAB code given in Table 8.1, the scanning type can be modified to time-effective serpentine scanning. Similarly, the code given in Table 8.2 can be modified to perform inward circular scanning. Additionally, any DOE (single or multifunctional) can be converted to a set of lines or circles by advanced MATLAB coding.

In advanced lithography systems such as RAITH150^{TWO}, during fabrication it is possible to choose the type of scanning from a list that includes: raster, serpentine, circular inward, circular outward, and combinations of these scanning types. For instance, in the fabrication of a grating, serpentine scanning takes about half the time compared to the time needed for raster scanning. Every type of scanning has its own advantages and disadvantages, depending on the lithography technique being used.

8.2 Photolithography

A brief description of the fabrication of devices using photolithography[4,5] with basic fabrication recipes is presented in this section. A mask writer such as Heidelberg Instruments DWL66 is used to prepare the mask pattern on a glass plate with a chromium layer and a resist layer. The laser head can be selected based on the minimum feature of the design, which is created using MATLAB and then converted into a GDSII file using LinkCAD. The GDSII file is converted into a binary file within the system for patterning.[6,7] The pattern is transferred to the resist layer of the mask plate by laser exposure. The mask plate is developed using potassium hydroxide solution, during which, the regions of the resist layer exposed to laser are removed. The mask plate is then immersed in chrome etchant solution to remove the chromium layer in the regions where the resist is removed. The chrome etchant is prepared by combining a solution made from ammonium ceric nitrate and acetic acid in de-ionized (DI) water. The mask plate is then rinsed in acetone (80 °C) to remove the unexposed and undeveloped resist layer.

Downloaded From: https://www.spiedigitallibrary.org/ebooks/ on 27 Feb 2022
Terms of Use: https://www.spiedigitallibrary.org/terms-of-use

The mask plate can now be used for fabrication of a device on a resist-coated glass plate. The size and shape of the glass substrate can be customized, but in most cases the substrates used are ready-made large circular wafers. The wafer can be diced into smaller sizes as required. In our case, we used borosilicate glass wafers with a refractive index of 1.5 and with a diameter and thickness of 3 inches and 500 μm, respectively. The glass wafer is diced using diamond cutters or a dicing machine (Ultratec's ULTRASLICE). The diced glass wafer is cleaned in an ultrasonic bath in isopropyl alcohol (IPA) and acetone for 2 min each to remove any chemical contaminants and dust particles, followed by a rinse in DI water. It is then dried with nitrogen gas. S1813 (Microchem) photoresist is used for fabrication of the device. The resist is spin-coated on the glass substrate with a thickness of 1.5 μm. It is prebaked, followed by an exposure in the UV lithography system ($\lambda = 365$ nm). The resist is developed with sodium hydroxide developer and post-baked. The baking conditions are optimized to harden the S1813 resist for etching processes.

The pattern in the resist layer can be transferred to the glass substrate by wet[8] or dry etching.[9] Wet etching can be done using hydrofluoric acid (HF) with the etch rates controlled by the concentration of the acid. The plasma etching is carried out using Ar and SF_6 gases. The etch rate in this case can be precisely controlled by controlling the temperature, pressure, and power of the system. If the period of the DOE is uniform throughout the pattern, then constant etch depth can be obtained. However, this is not the scenario for many DOEs. Let us consider a DOE such as a FZP, where the period of the structure decreases radially outward with the minimum features occurring at the outermost edges of the device. In this case, the etch rate will be higher for larger openings than that for smaller ones. There is a strong etch depth dependence with feature size. For demonstration purposes, a FZP with a negative axicon phase is considered.

The DOE is designed for a wavelength of $\lambda = 1064$ nm to generate a ring pattern with a radius of $r_0 = 25$ μm. The DOE is designed with a diameter of 8 mm. The inner maximum zone width and outermost minimum zone width of the DOE are 67 μm and 4 μm, respectively. The optical microscope images of the central and outermost parts of the DOE in chromium mask are shown in Figs. 8.5(a) and (b), respectively. In this case, due to a slight overdevelopment of resist in the mask plate, an error of $\approx$7% was found in the width of the zones. The piece-wise continuous approximation of circles is visible in the outermost zones in Fig. 8.5(b). The thickness of the chromium pattern is measured using a confocal microscope (Olympus) as shown in Fig. 8.6. This is the first evaluation step. The image of the DOE on the resist is shown in Fig. 8.7(a). The profile of the DOE after wet etching with 10% HF with an etch rate of 12.2 nm/min is shown in Fig. 8.7(b). The profile of the DOE after plasma etching is shown in Fig. 8.7(c). In wet etching the control of the thickness is not very accurate and besides it gives isotropic etching.

Downloaded From: https://www.spiedigitallibrary.org/ebooks/ on 27 Feb 2022
Terms of Use: https://www.spiedigitallibrary.org/terms-of-use

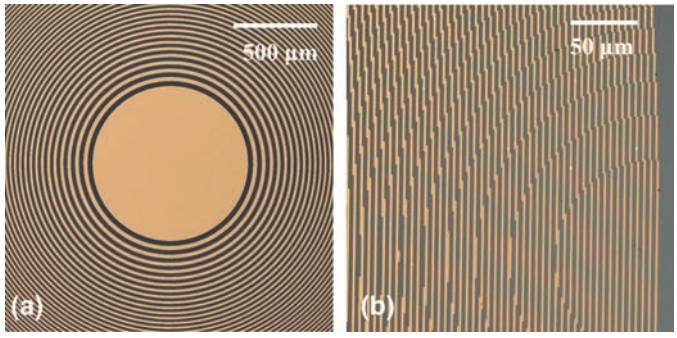

Figure 8.5 Optical microscope images of the (a) central part and (b) outermost part of the DOE on a chromium layer.

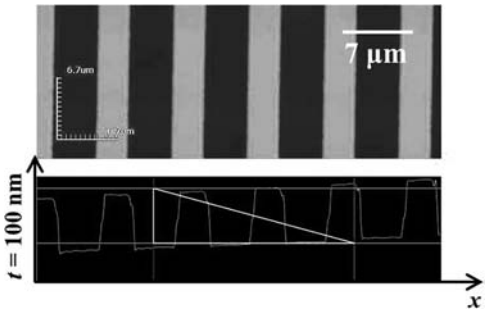

Figure 8.6 Profile of the pattern measured using the Olympus confocal microscope system.

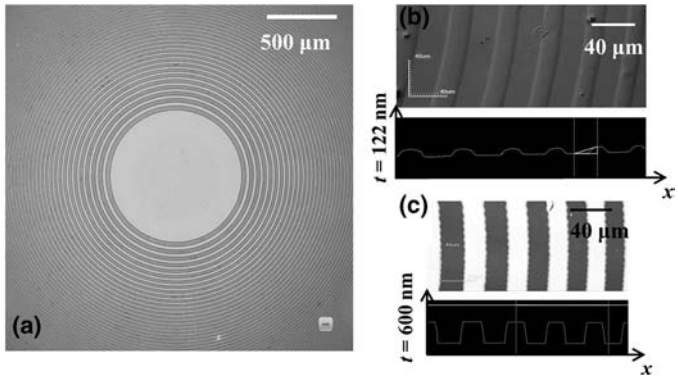

Figure 8.7 (a) Optical microscope image of the DOE in the resist (S1813) layer, (b) profile of the DOE fabricated using wet etching with 10% hydrofluoric acid, and (c) profile of the DOE fabricated using plasma etching with Ar and SF_6 (reprinted from Ref. 7).

In the case of wet as well as dry etching, S1813 was used as the mask. The experiment was repeated to etch a larger depth of 1064 nm. The etch depth was 1034 nm at the central part and 930 nm for the outermost part of the

Downloaded From: https://www.spiedigitallibrary.org/ebooks/ on 27 Feb 2022
Terms of Use: https://www.spiedigitallibrary.org/terms-of-use

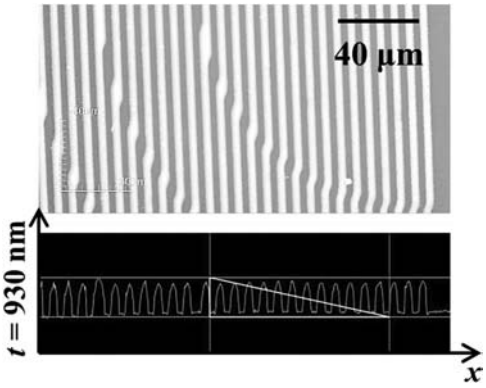

Figure 8.8 Profile of the outermost part of the DOE after plasma etching with a recipe for etching 1064 nm (reprinted from Ref. 7).

device, with corresponding maximum errors of 3% and 12.5%, respectively. The verticality was not very high, as seen in Fig. 8.8. By varying the plasma etching parameters, different results can be obtained. In many cases of plasma etching, instead of a resist mask, a metal mask is used, particularly if larger etch depth are required.[10] This would involve two additional steps, namely, metallization after development of resist and removal of resist by ultrasonification of the substrate in acetone. The complete process flow is given in Table 8.3.

Table 8.3 Process flow for fabrication using photolithography.

Step No.	Process	Description
1	Lithography File Generation	The DOE pattern is generated in MATLAB as an image file and is converted to GDSII format using LinkCAD software.
2	Mask Preparation	(a) The GDSII file is loaded, and the pattern is fabricated using the Heidelberg Mask Writer. (b) The resist layer of the mask plate is developed in KOH solution for 40 s. (c) The chrome layer is etched using chrome etchant (10 g of $H_8N_8CeO_{18}$ in 36 ml of DI water +4 ml of CH_3COOH in 45 ml of DI water) for 60–90 s.
3	Substrate Cleaning	The borosilicate glass wafer is diced and cleaned in acetone, IPA and DI water for 2 min each in ultrasonic bath and dried in nitrogen gas.
4	Spin Coating	The resist is spin coated with an rpm of 5000 and an acceleration of 600 rpm/s for 45 s to obtain a thickness of 1.5 μm.
5	Exposure	The resist is prebaked at 80 °C for 17 min, followed by an exposure in the UV lithography system ($\lambda = 365$ nm) for 12 s. The post-exposure bake is carried out at 90 °C for 10 min.
6	Development	The resist is developed with NaOH developer for 40 s and post-baked at 120 °C for more than 45 min.
7	Etching	The plasma etching is carried out using Ar and SF_6 gases with a pressure of 20 mT, a forward power of 200 W, and an inductively coupled plasma (ICP) power of 50 W, resulting in an etch rate of 60 nm/s.
8	Cleaning	The substrate is rinsed in acetone at 80 °C for 30 min to remove the S1813 resist.

Downloaded From: https://www.spiedigitallibrary.org/ebooks/ on 27 Feb 2022
Terms of Use: https://www.spiedigitallibrary.org/terms-of-use

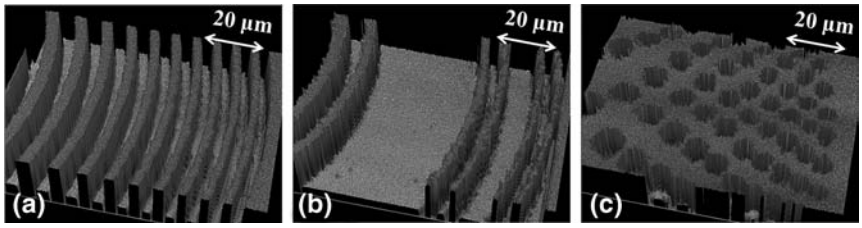

Figure 8.9 Surface profile images of sections of (a) a FZP, (b) a fractal zone plate, and (c) a photon sieve after development and UV exposure (reprinted from Ref. 6).

This discussion has been limited to binary DOEs. Many publications are available that address fabrication of multilevel DOEs using photolithography with multiple masks using alignment markers and consecutive exposures.[1,11–13]

After fabrication on resist and etching, the element must be characterized using an optical microscope and a surface profiler for feature measurements along the x, y, and z directions. The surface profile images obtained from an interferometry-based profiler (such as one from Veeco Instruments) of sections of a FZP, a fractal zone plate, and a photon sieve soon after development and UV exposure are shown in Figs. 8.9(a)–(c), respectively.[6,14,15] The final investigation is performed through optical means by passing light through the DOE and observing its diffraction pattern at the plane of interest using a 2D detector such as a CCD.

Employing an interferometer-based surface profiler for characterization of fabricated DOEs requires a certain level of expertise in optical alignment to obtain the fringe pattern. Additionally, it is not possible to view features smaller than the wavelength of light. In the recent advanced profilers such as Olympus confocal microscopes, most of the features are automated, enabling high precision and at the same time allowing a layman to analyze fabricated devices. Apart from these profilers, there are mechanical contact stylus profilers that can measure the profile of the fabricated DOEs by moving a pin head over the surface of the DOE. (Pin heads with 0.1-μm diameter are available.) However, this method of measurement can damage the DOE pattern, and give only one line of data at a time. Hence, it is advantageous to use optical surface profilers that can obtain the 3D information of the pattern in a short duration.

8.3 Electron Beam Lithography

In the case of EBL,[16–22] exposure is carried out using an electron beam instead of light, and a polymer layer that is sensitive to electrons is used for the fabrication of DOEs. With EBL it is possible to fabricate features as low as tens of nanometers. EBL does not require any mask, but the entire pattern cannot be transferred at once. This imposes a limit on the total size of the

Downloaded From: https://www.spiedigitallibrary.org/ebooks/ on 27 Feb 2022
Terms of Use: https://www.spiedigitallibrary.org/terms-of-use

pattern, as it is time consuming to fabricate DOEs with large areas. In the case of EBL, DOEs are fabricated by deflection of the electron beam using electric and magnetic fields. The spot size of the electron beam is controlled by the different apertures in the lithography system. Aberrations such as astigmatism, etc., that are present in optical systems also exist in EBL systems. However, most of the recently developed EBL systems have built-in tools to minimize such aberrations. The results presented are from DOEs fabricated with a RAITH150^{TWO} EBL system. Most other EBL systems will have similar procedures and operations.

8.3.1 Substrate selection

Transparent substrates such as glass plates with high transmittivity are required for fabrication of DOEs. For DOE fabrication using EBL, the substrate must possess some conductivity! Why? The electrons emitted by the electron gun are focused by the electric and magnetic field lenses onto the substrate. The electrons break the polymer chains of the resist wherever they are incident on the resist layer if they have sufficient energy. These electrons generate secondary electrons that must be grounded. If they are not grounded, there is an accumulation of charge on the surface of the substrate, creating a negative potential that deflects the incoming electrons. Hence, when a dielectric substrate such as glass is used, there will be an accumulation of electrons, and the incoming electrons cannot be used to pattern or image the substrate.

The most common way of overcoming the charging problem is to coat a thin metallic layer of gold or silver directly on the substrate or the resist.[19] In the latter case, after patterning, the metallic layer is etched in a chemical solution, followed by development in the resist development solution. Although the charging problem is now solved, the etching of the gold layer prior to development of the resist affects the uniformity of the resist layer. This is a problem especially if the element is to be used in the resist itself and is not going to be further transferred to the glass substrate. In order to avoid this problem, glass substrates with an indium tin oxide (ITO) layer are used for fabrication. The ITO layer offers high electrical conductivity and at the same time transmittivity of around 85% (at $\lambda = 633$ nm). By using ITO-coated substrates, the fabrication process can be made simpler, as metallization and etching are no longer necessary (if pre-coated substrates are used).

8.3.2 Resist selection and thickness optimization

As with photolithography, EBL can also be carried out using positive as well as negative photoresist. In this book, the discussion is limited to only positive photoresists. A positive resist, poly methyl methacrylate (PMMA), with anisole concentrations of A4 and A8, corresponding to 4% and 8% anisole, were used. DOEs for low-power applications need not be transferred to a

Downloaded From: https://www.spiedigitallibrary.org/ebooks/ on 27 Feb 2022
Terms of Use: https://www.spiedigitallibrary.org/terms-of-use

harder substrate and can be used in the resist layer itself. As discussed in earlier chapters, the phase (relating to the height of the DOE features) is crucial when obtaining maximum efficiency in the 1st diffraction order. The phase corresponds to a particular optical path length. For example, the thickness of a resist layer that is equivalent to a phase value of π is given by $\lambda/2(n_r - 1)$, where n_r is the refractive index of the resist. The refractive index of the resist layer can be calculated from Cauchy's coefficients, which are provided in the resist data sheet or obtained by ellipsometry measurements.

The anisole concentration of the resist must be selected such that the spin-coating speed for obtaining the necessary resist thickness is higher than 1000 rpm. This is necessary to obtain good uniformity of the resist layer. For a large sample, a spin speed >5000 rpm requires higher pressure in the chuck to hold the sample. High speeds may result in the sample been thrown from the chuck. Given these constraints, PMMA A8 was selected, as the spin-coating speed decreases to the desired range for $\lambda = 633$ nm and for binary DOEs. For PMMA A8, the refractive index is such that the resist thickness value is approximately the wavelength of the source used. Hence, for a wavelength of 633 nm, the resist height required is also 633 nm. PMMA A4 can be used in a two-step spin-coating process. However, in this case, a resist layer with one-half the thickness value is coated and baked, and the process is repeated to obtain the full thickness value. There is no measurable difference between the output intensity profiles achieved using A4 twice and A8 once, but the latter is preferred due to the reduced number of steps required.

In order to repeatedly obtain the desired resist height, a calibration chart for spin speed versus resist thickness (and acceleration) needs to be generated for each resist to be used. One such graph for PMMA A8 is shown in Fig. 8.10. The system was set at a fixed acceleration of 300 rpm/s and a coating duration of 45 s. The thickness of the resist was measured using a confocal microscope.

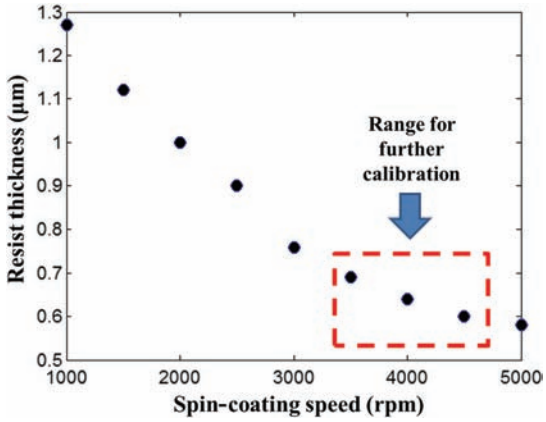

Figure 8.10 Plot of resist thickness measured using a confocal microscope versus coating speed. Acceleration was fixed at 300 rpm/s and spin coating time at 45 s.

Downloaded From: https://www.spiedigitallibrary.org/ebooks/ on 27 Feb 2022
Terms of Use: https://www.spiedigitallibrary.org/terms-of-use

Figure 8.10 is an initial crude estimate of the resist thickness versus spin speed. However, since phase is very sensitive to errors in height, a finer calibration curve is required. The range chosen for the more accurate calibration is shown in the dashed box. The experiment is repeated, varying the spin speed in steps of 100 rpm from 3500 rpm to 4500 rpm with constant acceleration, resist quantity, resist temperature, and baking temperature. The spin speed that generates a resist thickness of 633 nm was found to be 4300 rpm. The resist thickness measurement values were found to have an error of ± 10 nm.

During electron beam patterning, some of the ITO layer needs to be exposed to enable grounding and avoid charging effects. Therefore, after baking, a section of the resist at the edge of the substrate was removed using acetone. However, this method was found to affect other parts of the substrate as well, causing some parts of the patterned region to peel off during development. In order to avoid this problem, a region of the top of the sample was masked using adhesive tape prior to spin coating the resist. The bottom of the sample was also completely masked using tape to avoid any resist getting coated on the back of the substrate due to suction because of the pressure in the chuck. Both pieces of tape were removed immediately after spin coating and prior to baking.

8.3.3 Electron beam lithography optimization

The DOEs described in this book were fabricated using the RAITH150^{TWO} system. Figure 8.11 is a schematic showing the loading of the glass sample with the metal contact.[23] Other EBL systems will have similar processes. The metal clip of the sample holder was brought into contact with the exposed ITO layer of the substrate. Connecting the metal clip to the resist layer, as is done for semiconductor samples, led to charging, and the resulting image was grainy. The EBL system was then operated at lower acceleration voltages (10 kV) to further reduce the charging problem.

The main parameters that determine the result of patterning in EBL fabrication are focus adjustment, stigmation adjustment, aperture alignment,

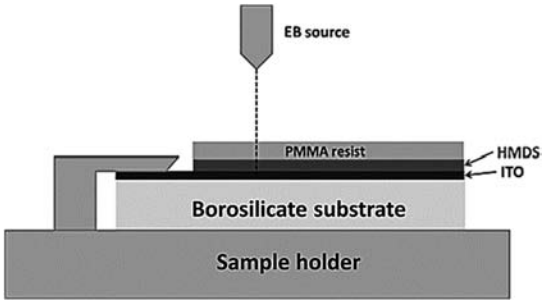

Figure 8.11 Schematic of the ITO sample mounted in the RAITH150^{TWO} system (HMDS is hexamethyldisilizane, an adhesion promoter) (adapted from Ref. 23).

Downloaded From: https://www.spiedigitallibrary.org/ebooks/ on 27 Feb 2022
Terms of Use: https://www.spiedigitallibrary.org/terms-of-use

write-field alignment, working distance, etc. Most of the DOEs discussed in this book were fabricated with an acceleration voltage of 10 kV, 30-μm aperture, and a working distance of 10 mm. Focus and stigmation correction were achieved by burning a contamination spot on the substrate. An alternative and relatively easier method—recommended for beginners—is to use polystyrene beads to adjust the focus and stigmation of the system.

For ITO glass substrates, the focus is initially corrected systematically in steps from lower magnification to higher magnification until the view region size is around 1 μm × 1 μm. Once the best focus is set, stigmation is corrected along the x and y directions until the ITO layer is visible, as shown in the scanning electron microscope (SEM) image in Fig. 8.12. This image indicates that the focus and stigmation are well corrected. If either the focus or the stigmation is not corrected, the structure of the ITO layer will not be visible. A second test to check the focus and stigmation setting involves burning a contamination spot on the substrate. The image of the contamination pillar must be circular for a perfectly focused and stigmation-corrected beam. The SEM images of the cases with and without perfect stigmation correction are shown in Figs. 8.13(a) and (b), respectively.

The contamination spots cannot be burnt for other electron beam settings of larger apertures (60 μm or 120 μm) of the electron beam system. In such cases, the second test can be carried out using polystyrene beads; the working distance must be set to these focus and stigmation correction settings.

The data buses used in RAITH150^{TWO} are 16-bit buses. Hence, 2^{16} (= 65,536) pixels of data can be transferred at a time. This sets a limit on the pixel size of the write field. For example, if a write field of size 2 mm × 2 mm is selected, the pixel size is given by (2000 μm / 65,536) = 30 nm. If the selected write field (with size $M \times M$) is larger than the design size ($N \times N$), the resolution of the system is wasted. If the write field is smaller than the design

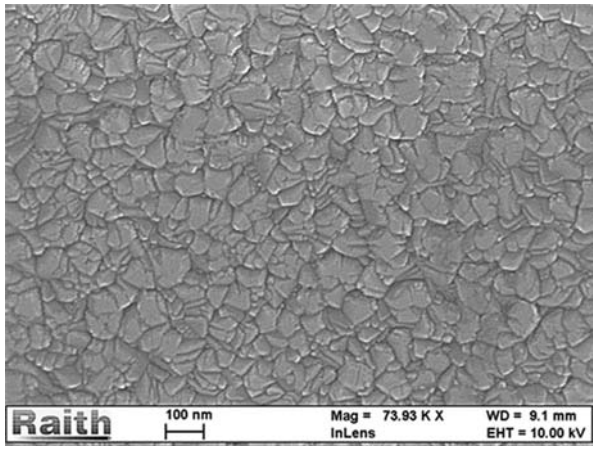

Figure 8.12 SEM image of the ITO layer after focus and stigmation correction.

Downloaded From: https://www.spiedigitallibrary.org/ebooks/ on 27 Feb 2022
Terms of Use: https://www.spiedigitallibrary.org/terms-of-use

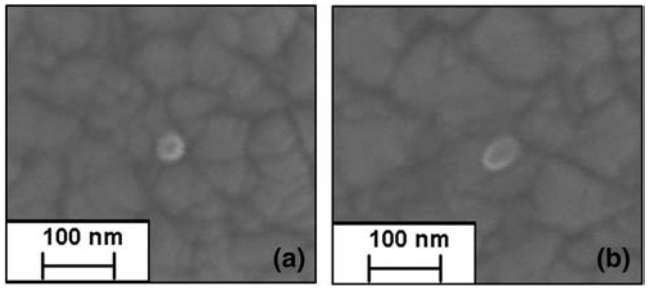

Figure 8.13 SEM images of the contamination spot burnt on the ITO layer with: (a) perfect focus and stigmation correction, and (b) perfect focus without stigmation correction.

size, the resolution is higher, but stitching with adjacent fields is required, resulting in stitching error. If the write field equals the design size, the maximum resolution of the system can be utilized without any stitching. These three cases are shown in Figs. 8.14(a), (b), and (c), respectively. A FZP designed with front and back focal distances of 5 mm and 30 mm, respectively, and $\lambda = 633$ nm is considered for analysis.

In the first case [Fig. 8.14(a)], it is clear that the resolution of the system is wasted by choosing a larger write field. The possible resolution of patterning in this case is N/65536, which is higher than the available resolution of M/65,536. Therefore, this case should not be used to write any structures. In the second case [Fig. 8.14(b)], the resolution is higher, as the write field is much smaller than the design size. However, stitching is required, and the stitching error was found to increase with the size of the write field. An alternative method of increasing the resolution is to design different sections of the element and then integrate during fabrication. However, this procedure may not be successful due to the drift error present in the stage, as will be further discussed in the following sections. Hence, the best scenario for fabrication of DOEs is to exactly match the write field to the design size. Whichever method is chosen, exposure and development times need to be

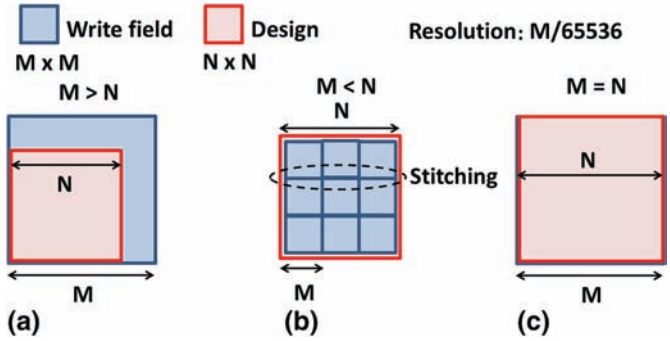

Figure 8.14 Write field with size $M \times M$ and design size $N \times N$ configuration for three cases: (a) $M > N$, (b) $M < N$, and (c) $M = N$.

Downloaded From: https://www.spiedigitallibrary.org/ebooks/ on 27 Feb 2022
Terms of Use: https://www.spiedigitallibrary.org/terms-of-use

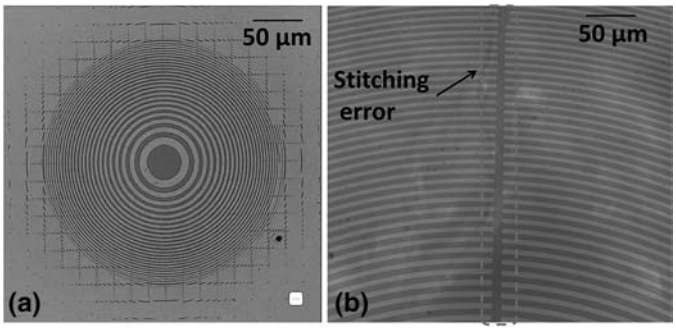

Figure 8.15 Optical microscope images of the DOEs fabricated using electron beam direct writing with (a) write field = 20 μm and design size = 2 mm, and (b) write field = 4 mm and design size = 8 mm.

optimized, as certain settings make the pattern more sensitive to these parameters. For example, the outer parts of the device were overdeveloped and removed during development for a write field of 20 μm. Elements of 2-mm diameter written with write fields of 20 μm and 4 mm are shown in Figs. 8.15(a) and (b), respectively.

Write-field alignment was carried out to calibrate the deflection of the electron beam with the stage deflection. The error in write-field alignment can be read in RAITH150^{TWO} and was found to be less than 10 nm. The next parameter that must be optimized is the electron beam dose ($\mu C/cm^2$). Clearing dose is defined as the dose value for which the resist layer in the exposed regions is completely removed after a particular duration of development. The dose value was determined as 55 $\mu C/cm^2$ for a development time of 50 s in methyl isobutyl ketone (MIBK):IPA in a ratio of 1:3 followed by a 20-s rinse in IPA. When the development time was increased beyond 1 min and rinse time in IPA was >40 s, it was found that even unexposed parts of the resist were affected, resulting in a decrease in the resist height and an increase in surface roughness. Figure 8.16 is an image of a section of a FZP fabricated with RAITH150^{TWO} and overdeveloped.

The adhesion between the PMMA and ITO layer was found to be poor; hence, the adhesion promoter HMDS was used prior to coating the PMMA resist on the substrate. An alternative method was attempted (to avoid using HMDS) by varying the baking temperatures before and after spin coating, but the adhesion did not improve very much. The optical microscope images of the DOE fabricated with no HMDS prime layer and with and without modified baking temperatures are shown in Figs. 8.17(a) and (b), respectively.

From Fig. 8.17 it can be seen that the adhesion between the resist and the substrate is poor, causing the resist to peel off during development. The duty ratio of the central zones clearly indicates the correct values of electron beam dose and development duration. Examples of the nonuniform dose profile over the area of the pattern due to varying electron beam current and focus at

Downloaded From: https://www.spiedigitallibrary.org/ebooks/ on 27 Feb 2022
Terms of Use: https://www.spiedigitallibrary.org/terms-of-use

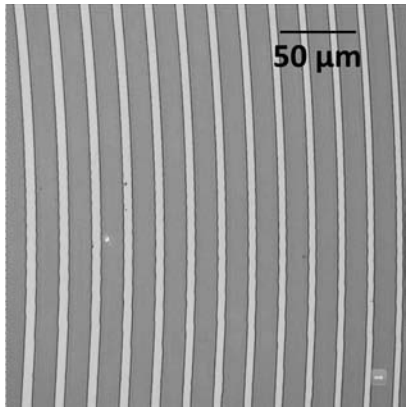

Figure 8.16 Optical microscope image of a DOE fabricated using electron beam direct writing and overdeveloped.

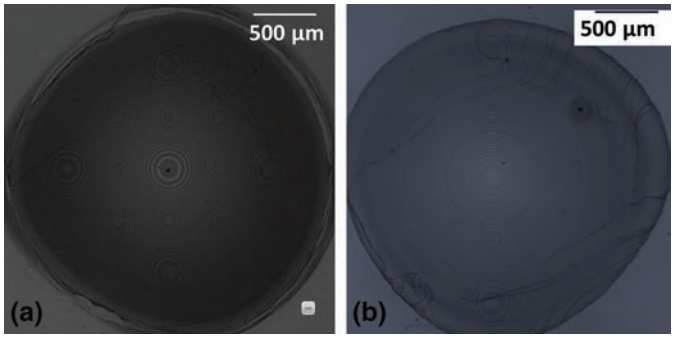

Figure 8.17 Optical microscope images of the DOEs fabricated using electron beam direct writing with no HMDS layer: (a) with modified baking temperatures and (b) without modified baking temperatures.

the outermost part of the device are shown in Fig. 8.18. This problem was solved by improving the manual focus and stigmation correction procedure. Optical microscope images of the outermost part of the device and the full device fabricated with optimized conditions are shown in Figs. 8.19(a) and (b), respectively.

Naturally, when optimizing the fabrication procedure using EBL, users will need to follow a version of this procedure that helps optimize fabrication based on the system and resist that they are using. An example of a repeatable, high-resolution fabrication technique developed after optimization of EBL (RAITH150^{TWO}) is given in Table 8.4. The outermost zones of a 2-mm device are found to have a slight zig-zag of around 50 nm due to high beam deflection [Fig. 8.19(a)] that cannot not be solved. In the RAITH150^{TWO} system, the smaller displacements of the stage are controlled by piezoelectric devices. When glass substrates were used, it was noted that some charge accumulation in that device resulted in a slight drift that was corrected by

Downloaded From: https://www.spiedigitallibrary.org/ebooks/ on 27 Feb 2022
Terms of Use: https://www.spiedigitallibrary.org/terms-of-use

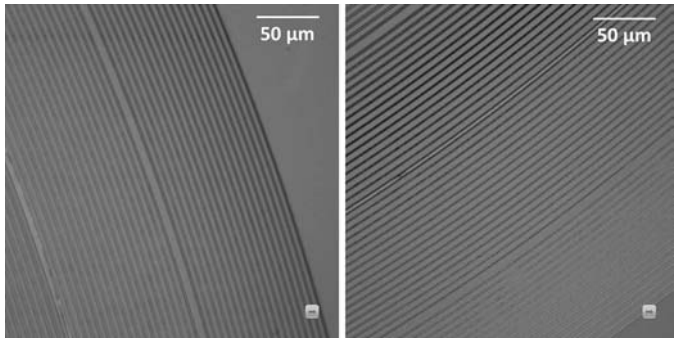

Figure 8.18 Optical microscope images of the DOEs fabricated using electron beam direct writing when the dose value was decreased at the outermost part of the devices.

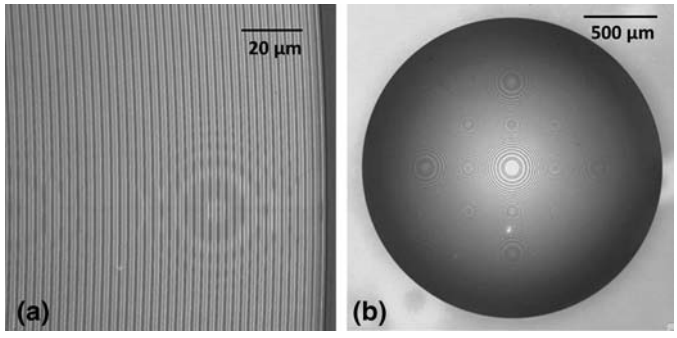

Figure 8.19 Optical microscope images of the (a) outermost part of the DOE and (b) the full device fabricated using electron beam direct writing with optimized fabrication parameters (reprinted from Ref. 2).

turning off the joystick controller during patterning. There were other minor technical problems due to the varying life of the chemicals, varying temperature and humidity conditions, etc., that varied the fabrication results. In most cases, the glass sample was not reused, as the quality of the resist layer deteriorated with each re-use. The process flow for fabrication of DOEs using EBL (RAITH150^{TWO}) is given in Table 8.4.

There are different modes for patterning. For small patterns, the stage must be kept fixed and the beam is deflected using electric and magnetic fields (high resolution). For large patterns, the beam is kept fixed and the stage is moved (low resolution) in what is called the fixed-beam moving stage (FBMS) mode. In the DOEs presented in this book, the patterns were written with a single write field without stitching and without FBMS. The acceleration voltage, which controls the sharpness of the electron beam spot, the aperture, which controls the electron beam spot size, and the working distance (the distance between the column and the substrate), which controls the magnification of the system, are set to the optimized values. The dose values are optimized to calculate the clearing dose for every resist thickness for

Downloaded From: https://www.spiedigitallibrary.org/ebooks/ on 27 Feb 2022
Terms of Use: https://www.spiedigitallibrary.org/terms-of-use

Table 8.4 Process flow for fabrication using EBL.

Step No.	Process	Description
1	Lithography File Generation	The DOE pattern is generated in MATLAB as an image file and converted to GDSII format using LinkCAD software.
2	Substrate Cleaning	The ITO-coated borosilicate glass wafer is cleaned in acetone, IPA, and DI water for 2 min each in an ultrasonic bath and dried in N_2 gas.
3	Baking	The wafer is baked at 80 °C for 30 min to remove the residual IPA and acetone.
4	Spin Coating	Adhesive tape is used to mask the edges of the ITO-coated glass substrate prior to spin coating. The tape is attached at the bottom of the substrate as well to avoid any resist getting coated on the back side of the substrate. First, HMDS is coated with an rpm of 2000 and a spin duration of less than 30 s. PMMA is immediately applied on the substrate and spun with the calculated rpm (4300 rpm for A8 resist) for 45 s. The masked region will be connected to the metal clip during fabrication in electron beam system.
5	Baking	The sample is baked at 180 °C for 3 min or 120 °C for 5 min.
6	Initial Adjustments	The initial adjustments, such as setting the aperture and focus, stigmation correction, write-field alignment, etc., are carried out. For patterning 2 mm × 2 mm patterns, an aperture of 30 μm and acceleration voltage of 10 kV are used. For patterning larger patterns with low resolution (>500 nm features), 60 μm or 120 μm aperture is used.
7	Dose Settings	Electron beam current is measured by moving the electron beam to the Faraday cup. The dwell time of the electron beam at each pixel can be calculated by entering the clearing dose.
8	Development	Patterns are developed using MIBK:IPA (1:3) at 24 °C for a duration of 30 s (600-nm thick resist), then are rinsed with IPA for 10 s to remove the developer residues, followed by rinsing in deionized water. The developed patterns are dried in N_2 gas.

binary patterns. For gradient patterns, the resist thickness is optimized for different values of electron beam dose. Further fabrication of DOEs using RAITH150^{TWO} reveals that it is possible to fabricate elements with diameters $\leq$ 6.66 mm × 6.66 mm without stitching and with a minimum feature of $\geq$50 nm. The patterning time was reasonable, with 30–40 min for pattern sizes of 2 mm × 2 mm for a 120-μm aperture and 10-kV acceleration voltage.

8.3.4 Fabrication of multilevel structures

Fabrication of multilevel structures using an electron beam system has been reported.[24–26] One method to carry out this type of fabrication is to use a grayscale resist such as PMMA 35K, which has a linear dose-to-resist-thickness profile. In this section, we present techniques to fabricate multilevel structures with a binary electron beam resist. The design of multilevel structures and the calculation of resist thickness have already been presented in detail in previous chapters.

Four-level and eight-level circular gratings with a period of 250 μm were fabricated using electron beam direct writing in the RAITH150^{TWO} system using the fabrication parameters given in Table 8.4. The spin-coating conditions and baking temperatures were optimized to obtain a resist

Downloaded From: https://www.spiedigitallibrary.org/ebooks/ on 27 Feb 2022
Terms of Use: https://www.spiedigitallibrary.org/terms-of-use

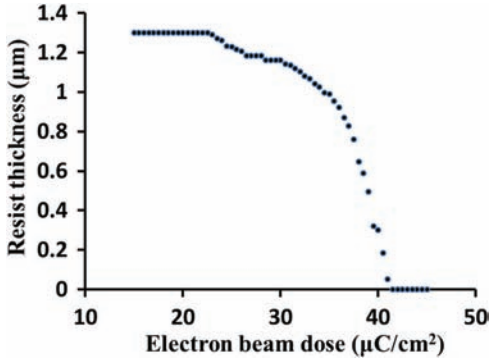

Figure 8.20 Plot of resist thickness after developing for different values of electron beam dose.

thickness as close as possible to the calculated value of 1266 nm. The electron beam resist selected for use is a binary resist with a very sharp resist-thickness-versus-dose profile. The profile is also very sensitive to temperature variations during processing. To improve the accuracy of the height, the resist-thickness-versus-dose characterization must be carried out immediately before device fabrication. Dose optimization is carried out by varying the dose from 10 $\mu C/cm^2$ to 50 $\mu C/cm^2$ in steps of 0.5 $\mu C/cm^2$. In each case, the development time is kept at 5 min. With such a high developing time, the dose requirement is less, and the patterning time is considerably reduced. The resist-thickness-versus-dose profile is plotted in Fig. 8.20.

The dose values corresponding to the different resist thickness values for a four-level and an eight-level structure are noted from the graph. The device is fabricated using two schemes. In the first scheme, the design is generated using MATLAB, a much faster technique than the second scheme, where the design is directly made using RAITH design software. In the first scheme, the design is split into different layers with different dose values as a stack. During fabrication, these layers are combined by assigning the same location. For the four-level and eight-level circular gratings, the stack consists of four and eight images, respectively. The images are generated for each dose value, as shown in Fig. 8.21 for a four-level grating. During fabrication these images are

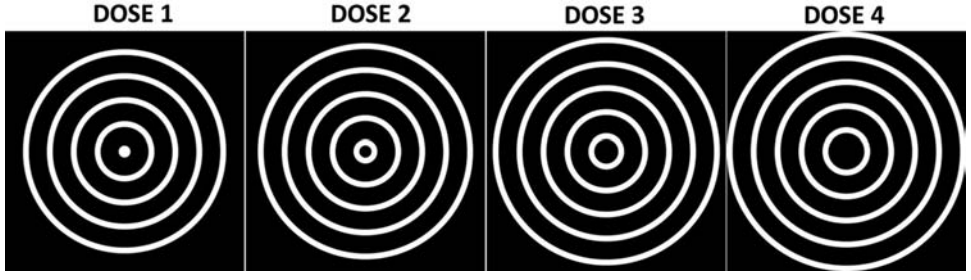

Figure 8.21 Images of sections of four-level axicons with different dose values.

Downloaded From: https://www.spiedigitallibrary.org/ebooks/ on 27 Feb 2022
Terms of Use: https://www.spiedigitallibrary.org/terms-of-use

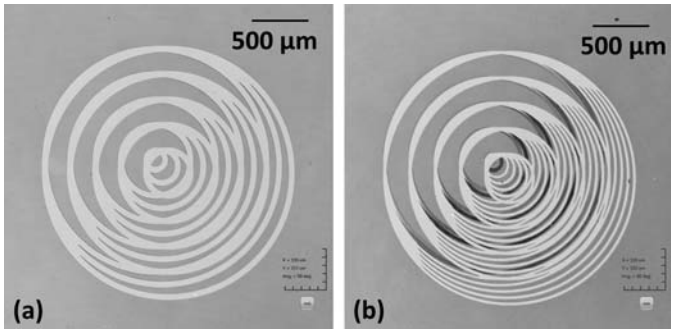

Figure 8.22 Optical microscope images of the fabricated (a) four-level and (b) eight-level axicons using the stack method.

stacked at the same location. A similar procedure is carried out for the fabrication of the eight-level grating.

Optical microscope images of the four- and eight-level circular gratings fabricated by the stack method are shown in Figs. 8.22(a) and (b), respectively. Due to a stage error of few microns, the stack's center shifted by a fixed amount in the same direction for every layer of the stack. This stage error is prevalent in many electron beam systems. Many lithography systems possess an in-built correction for this error. In FEI systems, which we will discuss in the final section, it can be noted that the drift correction can be completely nullified.

In the second method, the design is created in RAITH design software. Each ring is designed individually with a different dose factor. The design was initially carried out with no spacing between the two levels, resulting in proximity errors,[27] as shown in Fig. 8.23.

These proximity errors are minimized by giving spaces with a dose value of 0 between each level. The optimized value of the manual proximity correction space is 100 nm between every level. Optical microscope images of the four- and eight-level circular gratings are shown in Figs. 8.24(a) and (b), respectively. Resist profiles of the four- and eight-level axicons measured using a confocal microscope are shown in Figs. 8.25(a) and (b), respectively.

The profiles clearly show that the proximity errors were reduced. The roughness measurement using a profiler show a roughness variation from

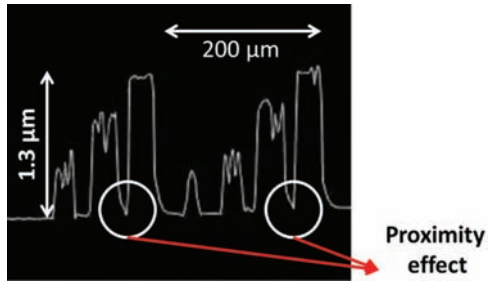

Figure 8.23 Resist thickness profile variation over the period of the circular grating.

Downloaded From: https://www.spiedigitallibrary.org/ebooks/ on 27 Feb 2022
Terms of Use: https://www.spiedigitallibrary.org/terms-of-use

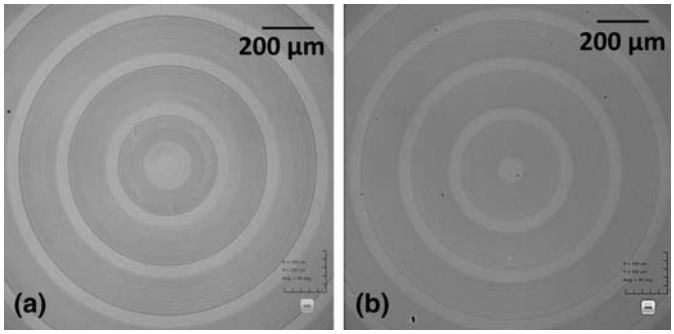

Figure 8.24 Optical microscope images of the fabricated (a) four-level and (b) eight-level circular gratings designed using RAITH design software.

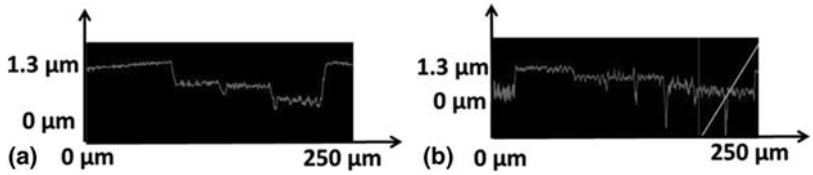

Figure 8.25 Resist profiles of (a) an eight-level and (b) a four-level circular grating measured using a confocal microscope.

23 nm to 47 nm across the resist profile. The roughness value is higher for the levels fabricated with higher electron beam dose. An average resist height error of $<11\%$ was obtained. The four-level and eight-level axicons were evaluated using a diode laser with a wavelength of 633 nm. The light from the laser source was collimated using a 10X objective. The Bessel beams generated by the four-level and eight-level axicons and their corresponding intensity profiles are shown in Figs. 8.26 and 8.27, respectively.

The calculated value of the $1/e^2$ diameter was 150 µm, while the experimental value was found to be 162 µm. The average transmittivity of the ITO layer is 85% for $\lambda = 633$ nm. The efficiencies of the four-level and eight-level circular grating were found to be 41% and 75%, respectively.

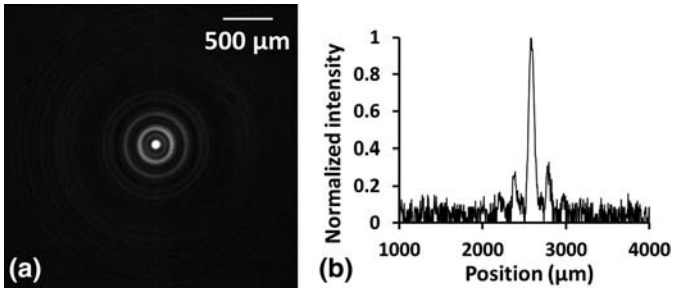

Figure 8.26 (a) Image of the Bessel beam and its (b) intensity profile generated by a four-level circular grating.

Downloaded From: https://www.spiedigitallibrary.org/ebooks/ on 27 Feb 2022
Terms of Use: https://www.spiedigitallibrary.org/terms-of-use

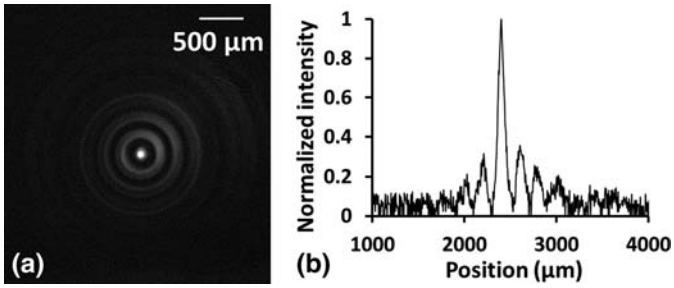

Figure 8.27 (a) Image of the Bessel beam and its (b) intensity profile generated by an eight-level circular grating.

The decrease in efficiency was partly due to the transmittivity of the ITO layer and partly due to the resist height errors.

Multilevel axicons with four and eight levels were designed and fabricated using electron beam direct writing. The fabrication was carried out using a binary electron beam resist with a very steep resist-thickness-versus-dose profile. The evaluation results show the generation of Bessel beams within the focal depth of the devices. The efficiency of the eight-level structure was close to the theoretical efficiency, although this was not the case for the four-level structure. The repeatability in fabrication was improved, as the fabrication was carried out immediately after dose calculation. Some other possible reasons for the decrease in repeatability might be the life of the developer solution, variation in electron beam current, manual errors in fabrication processes with identical conditions, etc. Also, color changes in the resist were noted; these changes corresponded to different thicknesses of the resist, which might be an additional reason for the decrease in efficiency.

8.3.5 Fabrication and testing results

This section presents the optical microscope images and optical testing results for some of the binary DOEs whose design and analysis was presented in previous chapters. The testing setup involves a fiber-coupled diode laser, a collimator, a DOE, and a CCD. We use a CCD (Thorlabs) with 1024×768 pixels corresponding to a size of 4.76 mm $\times$ 3.57 mm with a pixel size of 4.64 μm. All of these components are mounted on two- and three-axis stages with a mechanical stage resolution of 10 μm for fine adjustments. A schematic of the optical testing configuration is shown in Fig. 8.28.

An optical microscope image of the FZP designed in finite conjugate mode with $u = 5$ mm, $v = 30$ mm, and $t = 1$ mm after aberration correction using the scheme discussed in Section 5.3.1 is shown in Fig. 8.29.[2]

The FZPs fabricated with and without aberration correction are evaluated at the image plane $v = 30$ mm. The intensity profiles at the image plane are plotted for the FZPs without any aberration correction, with aberration

Downloaded From: https://www.spiedigitallibrary.org/ebooks/ on 27 Feb 2022
Terms of Use: https://www.spiedigitallibrary.org/terms-of-use

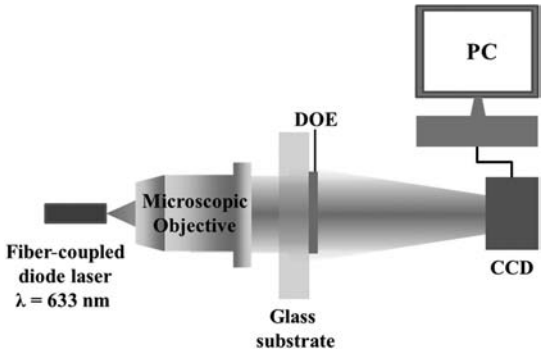

Figure 8.28 Schematic of the optical testing set up for evaluation of DOEs.

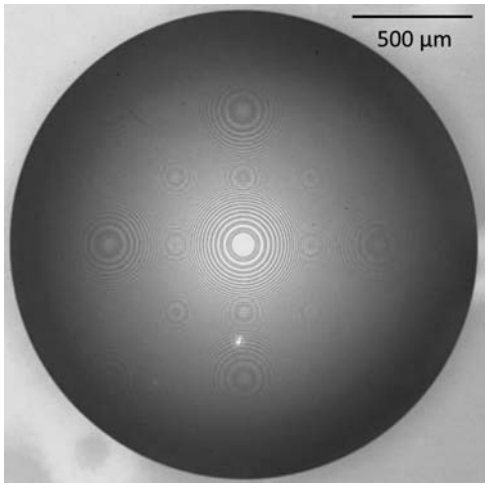

Figure 8.29 Optical microscope image of the FZP designed in finite conjugate mode after aberration correction (reprinted from Ref. 2).

correction scheme 1 (Section 5.3.1), and with aberration correction scheme 2 (Section 5.3.2), as shown in Fig. 8.30.

An optical microscope image of the multifunctional DOE containing the functions of a binary FZP ($f = 30$ mm) and a binary circular grating ($\Lambda = 50$ μm) designed using the modulo-2π phase addition method (Exercise E.6.1) and fabricated using RAITH 150^{TWO} is shown in Fig. 8.31(a). The element was evaluated using light from $\lambda_1 = 633$ nm and $\lambda_2 = 532$ nm, and it was found to generate ring patterns with equal diameters but at two focal lengths $f_1 = 30$ mm and $f_2 = 36$ mm for the two wavelengths, respectively.[3] The ring patterns recorded by the CCD are shown in Figs. 8.31(b) and (c), respectively.

An optical microscope image of the multifunctional DOE with a ring FZP[28] ($f = 30$ mm, $r_0 = 100$ μm) and 1D and 2D binary gratings ($\Lambda = 50$ μm) (Exercise E.6.4) generated by the modulo-2π phase addition method is shown in Figs. 8.32(a) and (b), respectively. The diffraction patterns recorded at a

Downloaded From: https://www.spiedigitallibrary.org/ebooks/ on 27 Feb 2022
Terms of Use: https://www.spiedigitallibrary.org/terms-of-use

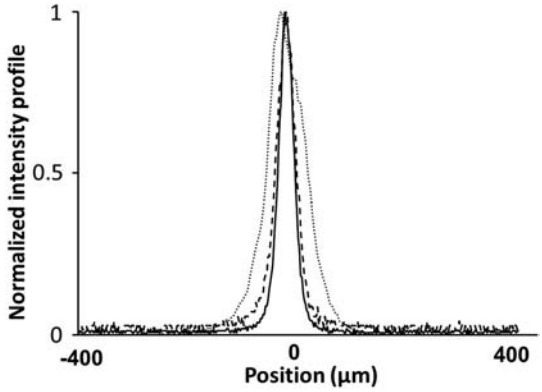

Figure 8.30 Normalized intensity profile at the image plane for the FZP without aberration correction (dotted line), with aberration correction using scheme 1 (solid line), and with aberration correction using scheme 2 (dashed line) (reprinted from Ref. 2).

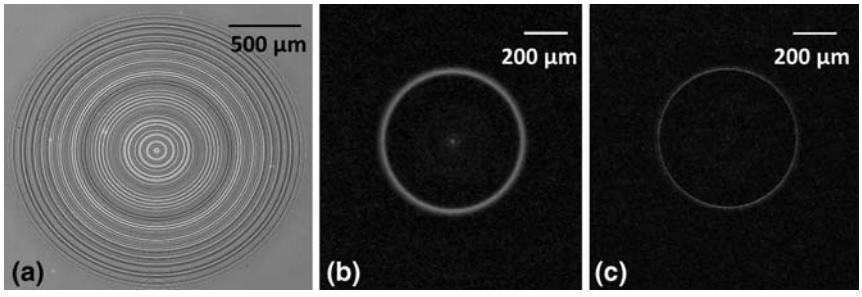

Figure 8.31 (a) Optical microscopic image of the multifunctional DOE containing the functions of a binary FZP and a binary circular grating, and images of the ring pattern generated by the DOE for the wavelengths (b) 635 nm and (c) 532 nm (reprinted from Ref. 2).

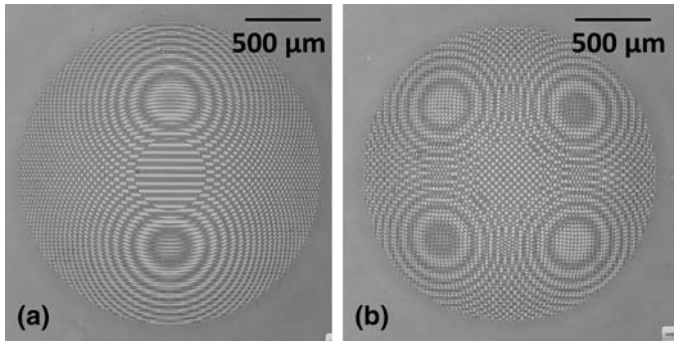

Figure 8.32 Optical microscope images of the multifunctional DOE containing the functions of a ring FZP ($f = 30$ mm, $r_0 = 100$ μm) with (a) a 1D grating and (b) a 2D checkerboard grating ($\Lambda = 50$ μm).

Downloaded From: https://www.spiedigitallibrary.org/ebooks/ on 27 Feb 2022
Terms of Use: https://www.spiedigitallibrary.org/terms-of-use

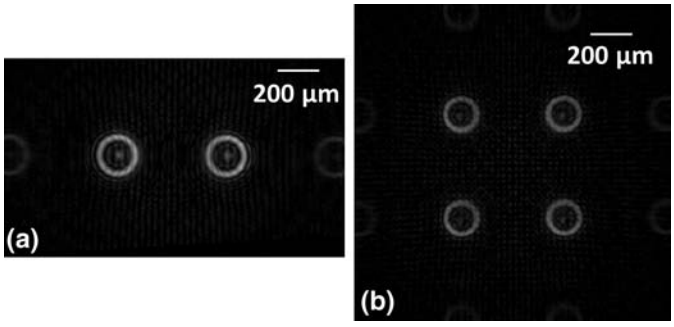

Figure 8.33 Images of the diffraction patterns of the ring pattern arrays generated by the DOEs shown in (a) Fig. 8.32(a) and (b) Fig. 8.32(b).

distance of 30 mm from the DOEs in Figs. 8.32(a) and (b) are shown in Figs. 8.33(a) and (b), respectively.

Optical microscope images of the multifunctional DOE designed by combining a binary circular grating and a binary 1D grating and 2D grating (Section 6.1.2) are shown in Figs. 8.34(a) and (b), respectively. The far-field diffraction patterns of Figs. 8.34(a) and (b) measured at a distance of 200 mm are shown in Figs. 8.35(a) and (b), respectively.

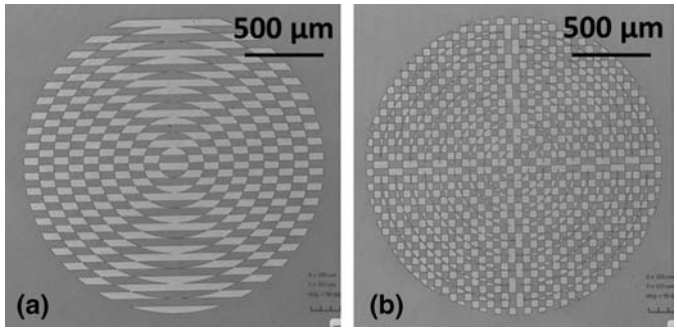

Figure 8.34 Optical microscope images of the multifunctional DOE containing the functions of a circular grating ($\Lambda = 200$ μm) and a (a) 1D grating and (b) 2D checkerboard grating ($\Lambda = 100$ μm).

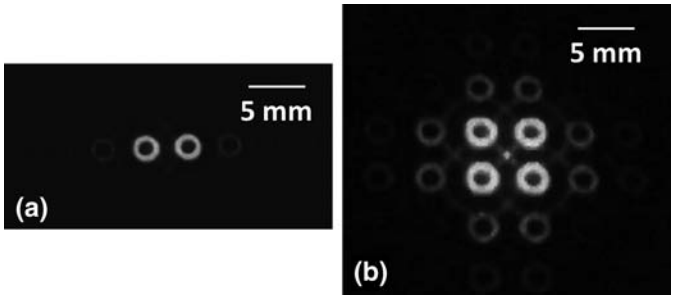

Figure 8.35 Image of the 1st and 3rd order diffraction patterns of the ring pattern arrays generated from the DOEs shown in (a) Fig. 8.34(a) and (b) Fig. 8.34(b) recorded in a CCD.

Downloaded From: https://www.spiedigitallibrary.org/ebooks/ on 27 Feb 2022
Terms of Use: https://www.spiedigitallibrary.org/terms-of-use

Optical microscope images of the fabrication results for the circular grating array that generates 3×3 Bessel intensity profiles discussed in Section 6.1.2 and an image of the Bessel intensity profile array are shown in Figs. 8.36(a) and (b), respectively.

Optical microscope images of the sections of the binary multifunctional DOE generated by combining the FZP ($f = 30$ mm) containing the phase of a negative axicon[29] ($X = 1.32$ and 2.64) (Exercise E.6.1) for generation of ring patterns with radius $r_0 = 25$ μm and 50 μm are shown in Figs. 8.37(a) and (c), respectively. The ring patterns recorded at a distance of 30 mm from the DOE plane are shown in Figs. 8.37(b) and (d), respectively.

An optical microscope image of the central part of a binary HOE (Section 7.3.6) used for generating an accelerating Airy beam[30] with a path profile of $t_2(x, y) = 10(x)^{0.5} + 10(y)^{0.5}$ is shown in Fig. 8.38(a), and its far-field diffraction patterns are shown in Figs. 8.38(b) and (c).

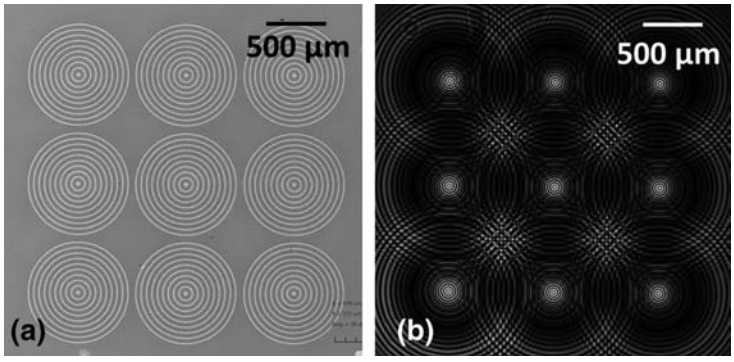

Figure 8.36 (a) Optical microscope image of the 3×3 circular grating array and (b) the Bessel intensity interference pattern recorded using a CCD.

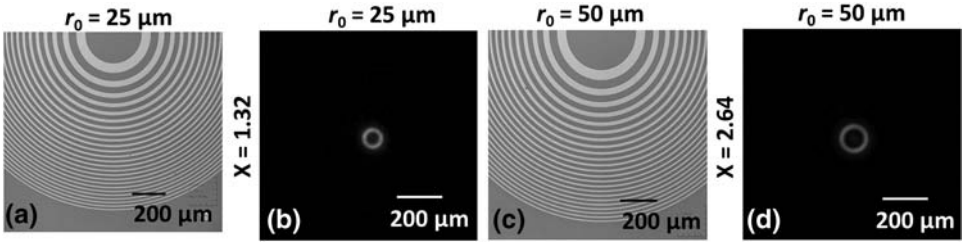

Figure 8.37 Optical microscope images of the binary multifunctional DOE generated by combining the FZP ($f = 30$ mm) containing the phase of a negative axicon with (a) $X = 1.32$ and (c) $X = 2.64$. (b) Image of the ring patterns generated by the same DOE radius values of $r_0 = 25$ μm and (d) $r_0 = 25$ μm recorded by a CCD (reprinted from Ref. 29).

Downloaded From: https://www.spiedigitallibrary.org/ebooks/ on 27 Feb 2022
Terms of Use: https://www.spiedigitallibrary.org/terms-of-use

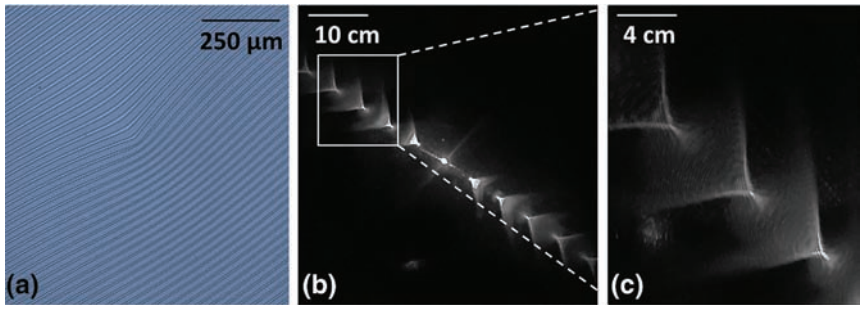

Figure 8.38 (a) Optical microscope image of a HOE used for the generation of an accelerating Airy beam with a path profile of $t_2(x, y) = 10(x)^{0.5} + 10(y)^{0.5}$. (b) Far-field diffraction pattern of the HOE generated by the superposition of a curved plane wavefront and a conical wavefront with $t_2(x, y) = 10(x)^{0.5} + 10(y)^{0.5}$. (c) A magnified version of the far-field diffraction pattern in (b) (reprinted from Ref. 30).

8.4 Focused Ion Beam Lithography

This section presents the fabrication of DOEs using FIB lithography.[31–33] Unlike photolithography and EBL, FIB does not require a resist and can be used to directly mill a pattern on a substrate. Hence, fabrication of elements using FIB involves almost no pre-processing steps except for cleaning the substrates.

8.4.1 FIB milling on substrates

Fabrication of DOEs on substrates was carried out using the Quanta 3D FEG system with a gallium source. The Quanta 3D FEG is a dual-beam system consisting of a FIB system for milling and a SEM for real-time monitoring of the milling. In this FIB system, a binary or grayscale (24 bit) bitmap file of the DOE can be directly loaded and can be scaled to any physical dimension within the system. CAD files are also accepted in this system. However, unlike many other lithography systems, the files do not have to be in this particular format. Hence, the bitmap files were generated in MATLAB as presented in previous chapters, and used directly. The substrate requirements for FIB are similar to those of the electron beam system. Therefore, ITO-coated glass substrates were used for fabrication. Cleaning of the substrates is similar to the process given in Table 8.4. The mounting of the sample is slightly different from that of an EBL system. In the Quanta 3D FEG, the holders are aluminum stubs with a circular shape. The mounting of the ITO glass substrates on the holders is shown in Fig. 8.39(a). A conducting tape (such as double-sided adhesive carbon tape) provides an electrical connection between the aluminum stub and the ITO layer of the substrate. A photograph of the fabrication chamber in a Quanta 3D FEG is shown in Fig. 8.39(b).

The entire basis of diffractive optics involves the phase changes encountered by an incident beam at the DOE. Therefore, depth optimization[34] is crucial in

Downloaded From: https://www.spiedigitallibrary.org/ebooks/ on 27 Feb 2022
Terms of Use: https://www.spiedigitallibrary.org/terms-of-use

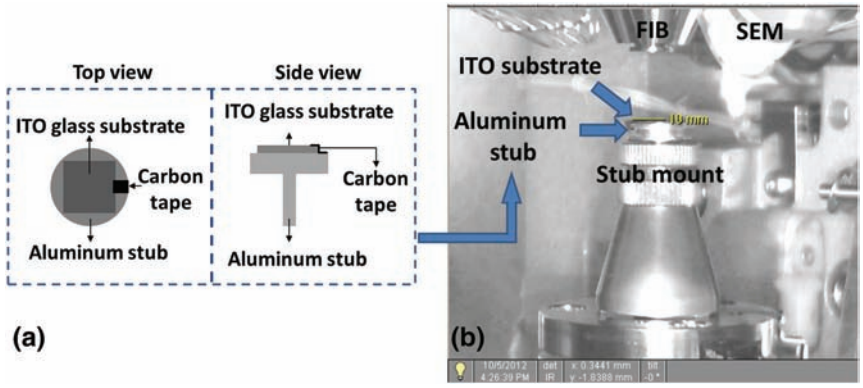

Figure 8.39 (a) Schematic of ITO-coated samples mounted in a Quanta 3D FEG system and (b) photograph of the fabrication chamber of a Quanta 3D FEG.

order to obtain the correct functionality. The FIB system consists of different application files containing material parameters corresponding to substrates such as silicon, gold, etc. However, there is no built-in application file for glass or for the ITO-coated substrates. Hence, the system is optimized by varying the current, while maintaining the parameters acceleration voltage, volume per dose, and dwell time at 30kV, 0.02 μm^3/nC, and 1 μs, respectively. The software of the FIB converts the 24-bit bitmap files into dwell time and beam position information. White pixels correspond to the user-defined dwell time, while black pixels correspond to a minimum dwell time of 100 ns. The current is varied between 0.1 and 1 nA, with 1 nA providing good results.

These numbers can be taken as a guide as to where to begin the optimization of the milling process. However, in general, optimization of milling take into account the material being milled and the structure sizes. For example, re-deposition will be a major problem, especially with finer features.[35] Most researchers will carry out an extensive optimization[36–38] before fabricating the final structures. In this system, multilevel structures are possible using the stack method (Fig. 8.21), which failed with the electron beam system. The stack method was employed for fabrication of multilevel spiral phase plates (SSPs).[39] An electron beam image of the fabricated FZP is shown in Fig. 8.40.

The design files of the stack for fabrication of a four-level SPP and the electron beam image of the fabricated device are shown in Figs. 8.41(a) and (b), respectively. The design files of a blazed 1D grating and a SPP along with their respective electron beam images are shown in Fig. 8.42. The parameters for the blazed structures are 30 kV, 3 nA, set depth of 3 μm, and volume per dose of 0.15 μm^3/nC. For the four-level SPP, the values are 30 kV, 0.3 nA, set depth varying in each wedge pattern, and 0.15 μm^3/nC. Both elements were fabricated using the Si application file.

FIB milling has many advantages over EBL and photolithography in terms of the number of processing steps involved. However, FIB milling has

Downloaded From: https://www.spiedigitallibrary.org/ebooks/ on 27 Feb 2022
Terms of Use: https://www.spiedigitallibrary.org/terms-of-use

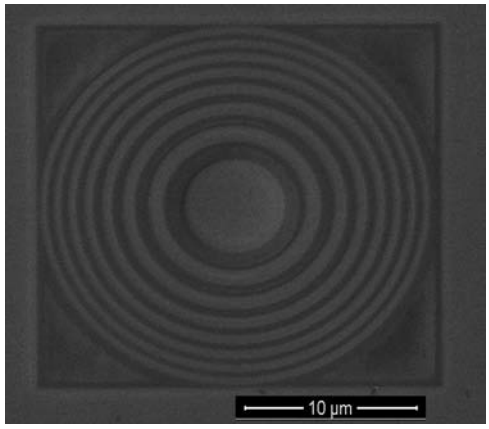

Figure 8.40 Electron beam image of the FZP fabricated using Quanta 3D FEG.

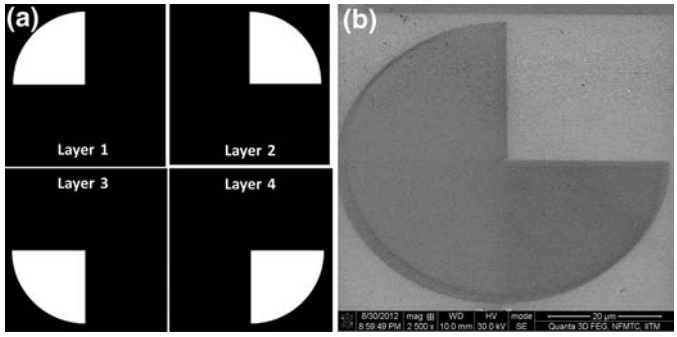

Figure 8.41 (a) Images of the stack files for fabrication of four-level SPP and (b) electron beam image of the fabricated four-level SPP.

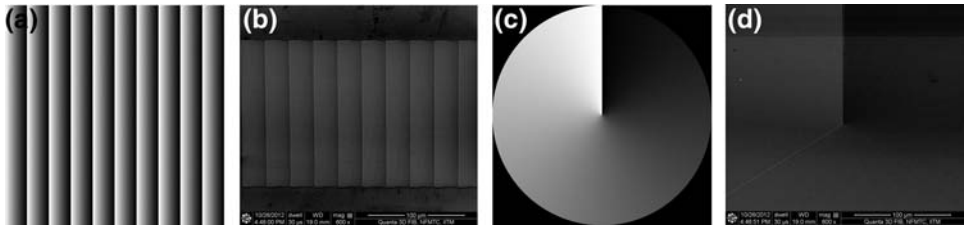

Figure 8.42 (a) Image of the blazed grating, (b) electron beam image of the fabricated blazed grating, (c) Image of the gradient SPP, and (d) electron beam image of the fabricated gradient SPP.

other technical difficulties. One serious problem is re-deposition, wherein the milled material gets re-deposited in another area of the substrate. Secondly, after milling a particular depth, charging may occur, which introduces deflection of the ion beam and leads to fabrication errors.

Downloaded From: https://www.spiedigitallibrary.org/ebooks/ on 27 Feb 2022
Terms of Use: https://www.spiedigitallibrary.org/terms-of-use

8.4.2 FIB milling on a fiber tip

FIB systems are the simplest way of directly creating a DOE on a fiber tip. The advantage of doing so means that light leaves the fiber in the desired shape without the need for further elements or alignment. In addition, the special beam can reach otherwise inaccessible areas. Fabrication of DOEs on a fiber tip was carried out using a Nova Nanolab™ 600 from FEI. FIB milling on a fiber tip is relatively a complex procedure when compared to fabrication on ITO glass substrates. For this reason, only a few research groups have reported on the fabrication of DOEs on fiber tip.[30–43] However, the impact of fabrication of DOEs on the tip of optical fiber is reflected in the unique applications that are possible only using them.[44–49] In this section, step-by-step procedures for fiber processing and FIB milling are presented, along with results of the fabrication.

8.4.2.1 Fiber processing

Single-mode fibers (SMF 28e® from Corning®) of approximately 20–25 cm in length are cleaned with IPA before cleaving with a Fujikura fiber cleaver (Cleaver MAX CL-01A company: ILSINTECH). The fiber tip is inspected using the camera in the fiber splicing machine (Fitel S175 V2000). Images of the fiber tip along the x and y directions before and after cleaving are shown in Figs. 8.43(a) and (b), respectively.

The cleaved fibers are again cleaned in IPA and dried using N_2 gas. The fibers are then loaded using a specially designed mount in a sputter-coating (metallization) unit for coating a thin metallic layer of gold (around 100 nm). One of the problems associated with fibers is the contamination that occurs during their handling. Since the core is about 8 μm in diameter, even small dust particles can completely cover it, making the sample unusable. Therefore, to reduce the amount of handling, a specially designed mount is made that fits in the sputtering unit as well as in the FIB system. With this mount, the fibers after metallization can be loaded immediately into the FIB system. The mount is designed such that four fibers can be loaded simultaneously and milled without any extra handling. A photograph of the mount is shown in Fig. 8.44(a). The electron beam image of a fiber (loaded in the FIB system) is shown in

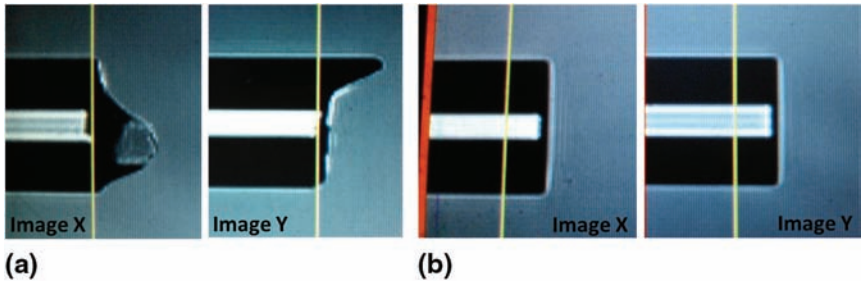

Figure 8.43 Images of the fiber tip along the x and y directions (a) after stripping the buffer layer and (b) after cleaving.

Downloaded From: https://www.spiedigitallibrary.org/ebooks/ on 27 Feb 2022
Terms of Use: https://www.spiedigitallibrary.org/terms-of-use

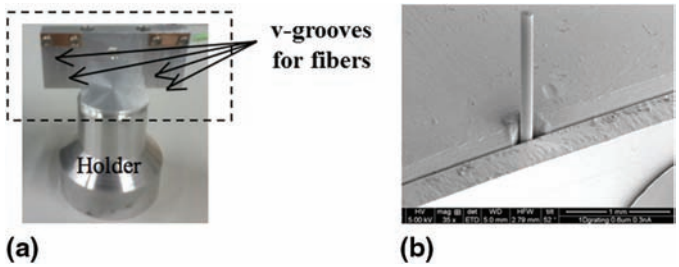

Figure 8.44 (a) Holder with v-grooves to hold four fibers. The top part (shown in the dashed rectangle) fits into the FIB system. When coating the fibers, the top part along with the holder, sit in the coating chamber of the sputtering unit. (b) Close-up SEM photograph of one fiber in the FIB system (reprinted from Ref. 45).

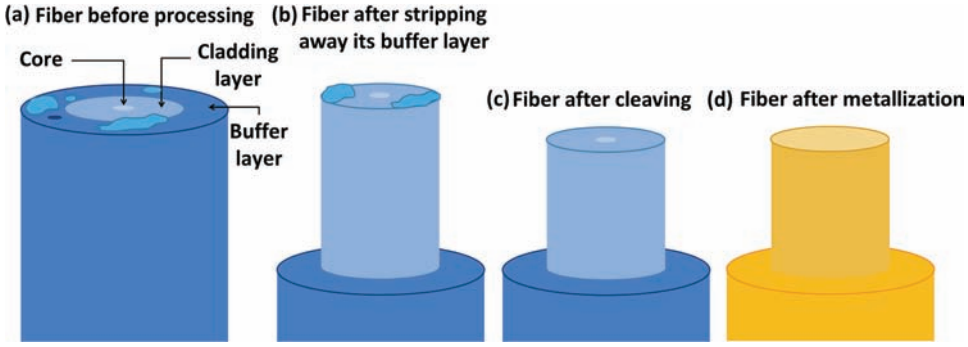

Figure 8.45 Images of the fiber (a) before processing, (b) after stripping away its buffer layer, (c) after cleaving, and (d) after metallization. (Figures not drawn to scale.)

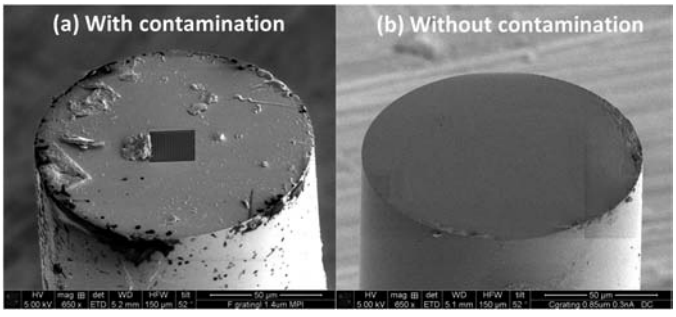

Figure 8.46 Electron beam images of the fiber tip (a) with and (b) without contamination.

Fig. 8.44(b). The processing steps before FIB milling are shown in Fig. 8.45. Electron beam images of the fiber tip with and without contamination are shown in Figs. 8.46(a) and (b), respectively.

A unique problem faced when milling fiber relates to the placement of the structure with respect to the core of the fiber. The structure must be milled over the core. However, due to the thin metal coating, the core may not be visible. If the patterns of the structure vary only in one direction or two orthogonal

Downloaded From: https://www.spiedigitallibrary.org/ebooks/ on 27 Feb 2022
Terms of Use: https://www.spiedigitallibrary.org/terms-of-use

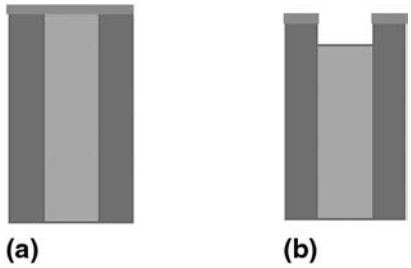

Figure 8.47 Cross section of a length of fiber (a) before and (b) after etching and metallization. The central lighter color represents the core.

directions, one can overcome the problem of locating the center in the following way. Initially, the center of the fiber can be geometrically located and a structure larger than the core can be written. However, for structures with circular symmetry, it is important for the center of the structure to match the center of the core, which is difficult to achieve when the core is not visible. One way to solve this problem is to etch the fiber tip before metallization.[44] The slightly higher etch rate of the core compared to that of the cladding creates a step that is visible even after metallization. The center of the step can then be geometrically located. Cross sections of the core and cladding are shown in Fig. 8.47.

Alternatively, the gold layer around the core region can be removed by milling a circle of 20 μm with an ion beam current of 3 nA for 4 min. This initial patterning exposes the core, which helps to accurately position the pattern. Depth optimization is achieved as before. The parameters acceleration voltage, volume per dose, and dwell time are kept constant at 30 kV, 0.15 μm^3/nC, and 1 μs, respectively. The current is varied between 0.1 and 0.3 nA, with 0.3 nA providing good results. The set depth is varied for these parameters from 0.5 to 1.5 μm. To test the depth obtained in each case, an extra line of platinum is deposited using the gas injector needle available with the system. An extra portion of the milled structure is removed by further milling in order to measure the cross section (and thereby obtain the actual depth milled). A SEM image of the structure from which the cross section can be measured is shown in Fig. 8.48.

For the actual fabrication of the structures on the fiber tips, 300 pA of beam current and 30-kV acceleration voltage with a maximum dwell time of 1 μs, 10-nm steps, and an antiparallel beam movement are utilized. Since the substrate is a dielectric, accumulation of charge is possible, especially if the core is exposed by milling out a circle. This, in turn, can cause a drift of the ion beam during the milling process. The effects are clear in Fig. 8.49(a), which shows a 1D grating milled with no drift correction applied. With each layer milled, the beam position changes slightly, and the final grating appears to be smeared out. In contrast, the grating is written without this error when drift correction is applied, as seen in Fig. 8.49(b).

Drift correction is carried out by first milling a pattern that will act as an alignment marker. Typically, a cross with good contrast is milled as shown in

Downloaded From: https://www.spiedigitallibrary.org/ebooks/ on 27 Feb 2022
Terms of Use: https://www.spiedigitallibrary.org/terms-of-use

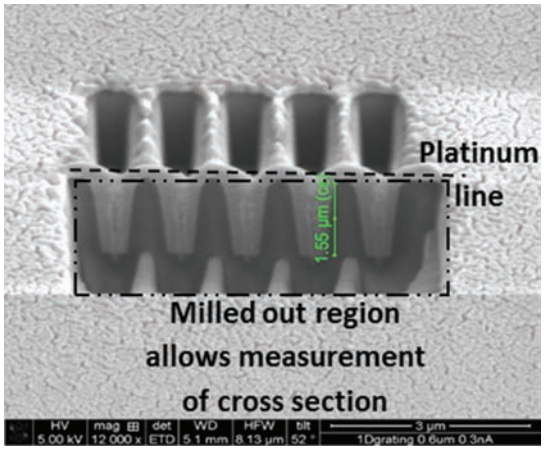

Figure 8.48 SEM image showing the depth milled for a structure consisting of four parallel lines (reprinted from Ref. 45).

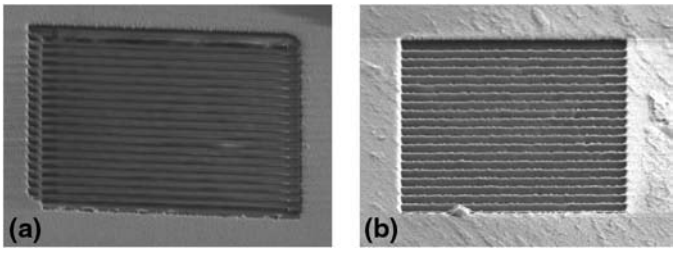

Figure 8.49 Image of a 1D grating milled (a) with beam drift and (b) with drift correction.

Fig. 8.50. In order to achieve the better contrast, a region of platinum is deposited and the cross milled into that area. A binary axicon (of diameter 10 μm with a period of 1 μm and fill factor of 50%) written on the core of a fiber is shown in Fig. 8.51. Drift correction is applied, and the obtained pattern is clear.

Recent research by Juodkazis et al. shows that illumination of the substrate with UV light can help to discharge ions from the surface, indicating

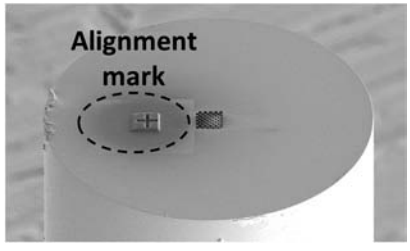

Figure 8.50 Image of a fiber with an alignment mark (to the left of the core) that subsequently will have a diffractive structure written on it. The alignment mark is shown enclosed within the dashed ellipse.

Downloaded From: https://www.spiedigitallibrary.org/ebooks/ on 27 Feb 2022
Terms of Use: https://www.spiedigitallibrary.org/terms-of-use

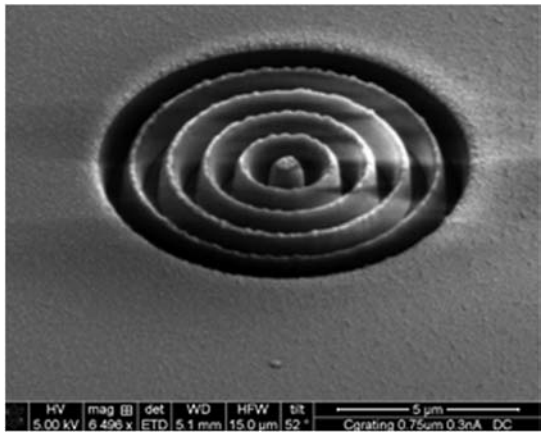

Figure 8.51 Image of a binary axicon written over the core of a single-mode fiber (Reprinted from Ref. 45).

that FIB milling can be done even without a metal coating.[50] This would be extremely useful when working with fibers.

8.5 Conclusions

This chapter studies the fabrication of DOEs using photolithography, EBL, and FIB lithography. Of particular importance is the transition from the diffraction equations to a design (CAD file) that can be understood by the writing tool. The simplest methods for generating the CAD files required for fabrication are discussed in detail. The basic recipes for fabrication of DOEs with all three types of lithography tools are also presented. As there is already a lot of literature on photolithography, the focus of this chapter was more on fabrication using electron beam and focused ion beam lithography systems.

Fabrication of DOEs using FIB is a relatively new area compared to photolithography and EBL. However, the advantages of fabrication of DOEs using FIB are enormous. In particular, FIB makes it almost easy to fabricate elements on a fiber tip, which has immense potential in the newly evolving fields of nanophotonics, plasmonics, and biomedicine. The different problems associated with the fabrication of DOEs using FIB are addressed, and step-by-step procedures for such are presented.

References

1. B. C. Kress and P. Meyrueis, *Applied Digital Optics*, John Wiley & Sons, Chichester, UK (2009).
2. A. Vijayakumar and S. Bhattacharya, "Characterization and correction of spherical aberration due to glass substrate in the design and fabrication of Fresnel zone lenses," *Appl. Opt.* **52**, 5932–5940 (2013).

Downloaded From: https://www.spiedigitallibrary.org/ebooks/ on 27 Feb 2022
Terms of Use: https://www.spiedigitallibrary.org/terms-of-use

3. A. Vijayakumar and S. Bhattacharya, "Quasi-achromatic Fresnel zone lens with ring focus," *Appl. Opt.* **53**, 1970–1974 (2014).
4. P. Walker and W. H. Tarn, *Handbook of Metal Etchants*, CRC Press, Boca Raton, Florida (1991).
5. W. B. Glendinning and J. N. Helbert, *Handbook of VLSI Microlithography: Principles, Technology and Applications*, Noyes Publications, Saddle River, New Jersey (1991).
6. A. Vijayakumar and S. Bhattacharya, "Analysis of versatile phase zone plates," *Proc. SPIE* **8173**, 817316 (2011) [doi: 10.1117/12.897564].
7. A. Vijayakumar, P. Parthasarathi, S. S. Iyengar, R. Selvan, S. Ananthamurthy, S. Bhattacharya, and S. Bhattacharya, "Conical Fresnel zone lens for optical trapping," *Proc. SPIE* **9654**, 965426 (2015) [doi: 10.1117/12.2180850].
8. G. A. C. M. Spierings, "Wet chemical etching of silicate glasses in hydrofluoric acid based solutions," *J. Mater. Sci.* **28**, 6261–6273 (1993).
9. S. Ronggui and G. C. Righini, "Characterization of reactive ion etching of glass and its applications in integrated optics," *J. Vac. Sci. Technol. A* **9**, 2709–2712 (1991).
10. S. Franssila, *Introduction to Microfabrication*," Second Edition, John Wiley & Sons, Singapore (2010).
11. W. Däschner, P. Long, R. Stein, C. Wu, and S. H. Lee, "Cost-effective mass fabrication of multilevel diffractive optical elements by use of a single optical exposure with a gray-scale mask on high-energy beam-sensitive glass," *Appl. Opt.* **36**, 4675–4680 (1997).
12. W. Yu, K. Takahara, T. Konishi, T. Yotsuya, and Y. Ichioka, "Fabrication of multilevel phase computer-generated hologram elements based on effective medium theory," *Appl. Opt.* **39**, 3531–3536 (2000).
13. M. LeCompte, X. Gao, and D. W. Prather, "Photoresist characterization and linearization procedure for the gray-scale fabrication of diffractive optical elements," *Appl. Opt.* **40**, 5921–5927 (2001).
14. G. Saavedra, W. D. Furlan, and J. A. Monsoriu, "Fractal zone plates," *Opt. Lett.* **28**, 971–973 (2003).
15. L. Kipp, M. Skibowski, R. L. Johnson, R. Berndt, R. Adelung, S. Harm, and R. Seemann, "Sharper images by focusing soft X-rays with photon sieves," *Nature* **414**, 184–188 (2001).
16. A. N. Broers, E. G. Lean, and M. Hatzakis, "1.75-GHz acoustic-surface-wave transducer fabricated by an electron beam," *Appl. Phys. Lett.* **15**, 98–110 (1969).
17. A. N. Broers, A. C. F. Hoole, and J. M. Ryan, "Electron beam lithography—Resolution limits," *Microelectron. Eng.* **32**, 131–142 (1996).
18. R. F. W. Pease, "Electron beam lithography," *Contemp. Phys.* **22**, 265–290 (1981).

Downloaded From: https://www.spiedigitallibrary.org/ebooks/ on 27 Feb 2022
Terms of Use: https://www.spiedigitallibrary.org/terms-of-use

19. T. Fujita, H. Nishihara, and J. Koyama, "Fabrication of micro lenses using electron-beam lithography," *Opt. Lett.* **6**, 613–615 (1981).
20. C. Vieu, F. Carcenac, A. Pépin, Y. Chen, M. Mejias, A. Lebib, L. Manin-Ferlazzo, L. Couraud, and H. Launois, "Electron beam lithography: resolution limits and applications," *Appl. Surf. Sci.* **164**, 111–117 (2000).
21. W. Chen and H. Ahmed, "Fabrication of 5–7 nm wide etched lines in silicon using 100 keV electron-beam lithography and polymethylmethacrylate resist," *Appl. Phys. Lett.* **62**, 1499–1501 (1993).
22. T. Shiono, K. Setsune, O. Yamazaki, and K. Wasa, "Rectangular-apertured micro-Fresnel lens arrays fabricated by electron-beam lithography," *Appl. Opt.* **26**, 587–591 (1987).
23. A. Vijayakumar and S. Bhattacharya, "Multifunctional diffractive optic elements for the generation of higher-order Bessel-like beams," *Proc. SPIE* **9370**, 937034 (2015) [doi: 10.1117/12.2079081].
24. E. Di Fabrizio, F. Romanato, M. Gentili, S. Cabrini, B. Kaulich, J. Susini, and R. Barrett, "High-efficiency multilevel zone plates for keV X-rays," *Nature* **401**, 895–898 (2001).
25. E.-B. Kley, "Continuous profile writing by electron and optical lithography," *Microelectron. Eng.* **34**, 261–298 (1997).
26. M. Ekberg, B. Nilsson, M. Larsson, and S. Hård, "Multilevel phase holograms manufactured by electron-beam lithography," *Opt. Lett.* **15**, 568–569 (1990).
27. T. H. P. Chang, "Proximity effect in electron-beam lithography," *J. Vac. Sci. Technol.* **12**, 1271–1275 (1975).
28. A. Vijayakumar and S. Bhattacharya, "Design, fabrication, and evaluation of diffractive optical elements for generation of focused ring patterns," *Proc. SPIE* **9449**, 944902 (2015) [doi: 10.1117/12.2077407].
29. A. Vijayakumar and S. Bhattacharya, "Design of multifunctional diffractive optical elements," *Opt. Eng.* **54**, 024104 (2015) [doi: 10.1117/1.OE.54.2.024104].
30. R. Dharmavarapu, A. Vijayakumar, and S. Bhattacharya, "Design and fabrication of holographic optical elements for the generation of tilted and accelerating Airy beams," *Asian J. Phys.* **24**(10), 1363–1372 (2105).
31. A. A. Tseng, "Recent developments in micromilling using focused ion beam technology," *J. Micromech. Microeng.* **14**, R15–R34 (2004).
32. Y. Fu and N. K. A. Bryan, "Diffractive optical elements with continuous relief fabricated by focused ion beam for monomode fiber coupling," *Opt. Express* **7**, 141–147 (2000).
33. S. Reyntjens and R. Puers, "A review of focused ion beam applications in microsystem technology," *J. Micromech. Microeng.* **11**, 287–300 (2001).
34. N. P. Hung, Y. Q. Fu, and M. Y. Ali, "Focused ion beam machining of silicon," *J. Mat. Proc. Tech.* **127**, 256–260 (2002)

Downloaded From: https://www.spiedigitallibrary.org/ebooks/ on 27 Feb 2022
Terms of Use: https://www.spiedigitallibrary.org/terms-of-use

35. L. Frey, C. Lehrer, and H. Ryssell, "Nanoscale effects in focused ion beam processing," *Appl. Phys. A* **76**, 1017–1023 (2003).
36. W. C. L. Hopman, "Focused ion beam scan routine, dwell time and dose optimizations for submicrometre period planar photonic crystal components and stamps in silicon," *Nanotech.* **18**, 195305 (2007).
37. V. L. Ferrara, P. M. Aneesh, P. Delli. Veneri, L. V. Mercaldo, I. Usatii, T. Polichetti, A. Ricciardi, G. Quero, and A. Cusano, "Focused ion beam strategy for nanostructure milling in doped silicon oxide layer for light trapping applications," *Vacuum* **99**, 135–142 (2014).
38. S. N. Bhavsar, S. Aravindan, and P. V. Rao, "Investigating material removal rate and surface roughness using multi-objective optimization for focused ion beam (FIB) micro-milling of cemented carbide," *Prec. Engg.* **40**, 131–138 (2015).
39. P. Vayalamkuzhi, A. Vijayakumar, and S. Bhattacharya, "Fabrication of multilevel spiral phase plates by focused ion beam milling," *Proc. SPIE* **8769**, 87691S (2013) [doi: 10.1117/12.2021061].
40. P. M. Nellen and R. Bronnimann, "Milling micro-structures using focused ion beams and its application to photonic components," *Meas. Sci. Technol.* **17**, 943–948 (2006).
41. V. Callegari, D. Iwaniuk, R. Bronnimann, E. Schmid, and U. Sennhauser, "Optimized fabrication of curved surfaces by a FIB for direct focusing with glass fibers," *J. Micromech. Microeng.* **19**, 107003 (2009).
42. H. Yoda, H. Ikedo, T. Ketsuka, A. Irie, K. Shiraishi, and C. S. Tsai, "A high-performance micro-GRIN-chip spot-size converter formed with focused ion beam," *IEEE Photon. Technol. Lett.* **18**, 1554–1556 (2006).
43. A. Micco, A. Ricciardi, M. Pisco, V. La Ferrara, and A. Cusano, "Optical fiber tip templating using direct focused ion beam milling," *Sci. Reports* **5**, 15935 (2015).
44. S. Cabrini, C. Liberale, D. Cojoc, A. Carpentiero, M. Prasciolu, S. Mora, V. Degiorgio, F. D. Angelis, and E. D. Fabrizio, "Axicon lens on optical fiber forming optical tweezers, made by focused ion beam milling," *Micro. Engg.* **83**, 804–807 (2006).
45. A. Vijayakumar, U. Eigenthaler, K. Keskinbora, G. M. Sridharan, P. Vayalamkuzhi, M. Hirscher, J. P. Spatz, and S. Bhattacharya, "Optimizing the fabrication of diffractive optical elements using a focused ion beam system," *Proc. SPIE* **9130**, 91300X (2014) [doi: 10.1117/12.2051925].
46. R. M. Gelfand, S. Wheaton, and R. Gordon, "Cleaved fiber optic double nanohole optical tweezers for trapping nanoparticles," *Opt. Lett.* **39**, 6415–6417 (2014).
47. J. Han, M. Sparkes, and W. O'Neill, "Controlling the optical fiber output beam profile by focused ion beam machining of a phase hologram on fiber tip," *Appl. Opt.* **54**, 890–894 (2015).

Downloaded From: https://www.spiedigitallibrary.org/ebooks/ on 27 Feb 2022
Terms of Use: https://www.spiedigitallibrary.org/terms-of-use

48. R. S. Rodrigues Ribeiro, O. Soppera, J. Viegas, A. Guerreiro, and P. A. S. Jorge, "The efficiency of fiber optical tweezers for cell manipulation using distinct fabrication methods," *Proc. SPIE* **9379**, 93790N (2015) [doi: 10.1117/12.2079798].
49. P. Vayalamkuzhi, S. Bhattacharya, U. Eigenthaler, K. Keskinbora, C. T. Samlan, M. Hirscher, J. P. Spatz, and N. K. Viswanatham, "Direct patterning of vortex generators on fiber tip using a focused ion beam," *Opt. Lett.* **41**(10), 2133–2136 (2016)
50. G. Gervinskas, G. Seniutinas, and S. Juodkazis, "Control of surface charge for high-fidelity nanostructuring of materials," *Laser Photon. Rev.* **7**, 1049–1053 (2013).

Acknowledgment

We thank Dr. Pramitha Vayalamkuzhi, Department of Electrical Engineering, IIT Madras, Chennai, India for her special contributions to and review of this chapter.

Downloaded From: https://www.spiedigitallibrary.org/ebooks/ on 27 Feb 2022
Terms of Use: https://www.spiedigitallibrary.org/terms-of-use

Appendix
MATLAB® Functions

Table A.1 MATLAB function to generate normalized output for amplitude structures.

```
function Norm_outputA(x, N)
% This function generates the output intensity pattern with
%intensity normalized for amplitude DOEs
% function arguments (required when calling the function) are
% DOE amplitude (x) and matrix size (N)
E=fftshift(fft2(A)); %fftshift is used to re-order the terms in
%their natural order
IN=(abs(E)/(N*N)).*(abs(E)/(N*N)); % Calculating intensity
figure (1)
colormap(gray); %colormap(gray) is used to display grayscale
%image
imagesc(A);% imagesc is used to display a high constrast image
figure (2)
colormap(gray);
imagesc(IN);
```

Table A.2 MATLAB function to generate output for amplitude structures.

```
function outputA(x)
% This function generates the output intensity pattern for
%amplitude structures
% DOE amplitude is the only function argument
E=fftshift(fft2(x));
  I=abs(E).*abs(E);
  figure(1)
  colormap(gray)
  imagesc(x)
  figure(2)
  colormap(gray)
  imagesc(I)
end
```


Downloaded From: https://www.spiedigitallibrary.org/ebooks/ on 27 Feb 2022
Terms of Use: https://www.spiedigitallibrary.org/terms-of-use

Table A.3 MATLAB function to generate normalized output for phase structures.

```
function Norm_outputP(x, N)
% This function generates the output intensity pattern with
%intensity normalized for phase DOEs
% function arguments (required when calling the function) are
% DOE amplitude (x) and matrix size (N)
E=fftshift(fft2(x)); %fftshift is used to re-order the terms in
%their natural order
IN=(abs(E)/(N*N)).*(abs(E)/(N*N)); % Calculating intensity
figure (1)
colormap(gray); %colormap(gray) is used to display grayscale
%image
imagesc(angle(x));% imagesc is used to display a high constrast
%image
figure (2)
colormap(gray);
imagesc(IN);
```

Table A.4 MATLAB function to generate output for phase structures.

```
function outputP(x)
% This function generates the output intensity pattern for phase
%structures
% DOE amplitude is the only function argument
E=fftshift(fft2(x));
  I=abs(E).*abs(E);
  figure(1)
  colormap(gray)
  imagesc(angle(x))
  figure(2)
  colormap(gray)
  imagesc(I)
End
```

Downloaded From: https://www.spiedigitallibrary.org/ebooks/ on 27 Feb 2022
Terms of Use: https://www.spiedigitallibrary.org/terms-of-use

SPIE.

A. Vijayakumar and Shanti Bhattacharya,

Design and Fabrication of Diffractive Optic Elements with MATLAB®

SPIE Press, Bellingham, Washington (2017).

Click here to download supplementary material.

In case the above button does not work, the supplemental files for this eBook are also available for download by copying and pasting the following link to a browser:

http:/spie.org/Samples/Pressbook_Supplemental/TT109_sup.zip

Downloaded From: https://www.spiedigitallibrary.org/ebooks/ on 27 Feb 2022
Terms of Use: https://www.spiedigitallibrary.org/terms-of-use

Solutions to the Exercises

Chapter 2 Solutions

E.2.1 Equate Eqs. (2.4) and (2.5).

$$I_{\pm 1} = 0.5 I_0,$$

$$\frac{4}{\pi^2}\sin^2\left(\frac{\Phi}{2}\right) = 0.5\cos^2\left(\frac{\Phi}{2}\right),$$

$$\Phi = 1.67\,\text{rad}.$$

Displayed values in figure window 2 are 0.22 and 0.45 for the ± 1 and 0^{th} diffraction orders, respectively.

E.2.2 Equate Eqs. (2.9) and (2.10).

$$\left[\frac{2}{\pi}\sin\left(\frac{\Phi}{2}\right)\right]^2\left[\frac{2}{\pi}\sin\left(\frac{\Phi}{2}\right)\right]^2 = \left[\frac{2}{\pi}\sin\left(\frac{\Phi}{2}\right)\right]^2\left[\frac{2}{3\pi}\sin\left(\frac{\Phi}{2}\right)\right]^2,$$

$$\Phi = 2.01.$$

Verification of the result cannot be carried out by substitution of the phase value alone, in the MATLAB® code for checkerboard phase grating. In this case, the XOR operation will not work. Instead, it is necessary to add the angle matrices corresponding to two orthogonal 1D gratings with phase values of 2.01 and 0. The resulting grating has 3 phase values: 0, 2.01, and 4.02. The displayed value in figure window 2 is 8.3% for all 3×3 diffraction spots. Figure window 2 is shown in Fig. E.2.2.

Downloaded From: https://www.spiedigitallibrary.org/ebooks/ on 27 Feb 2022
Terms of Use: https://www.spiedigitallibrary.org/terms-of-use

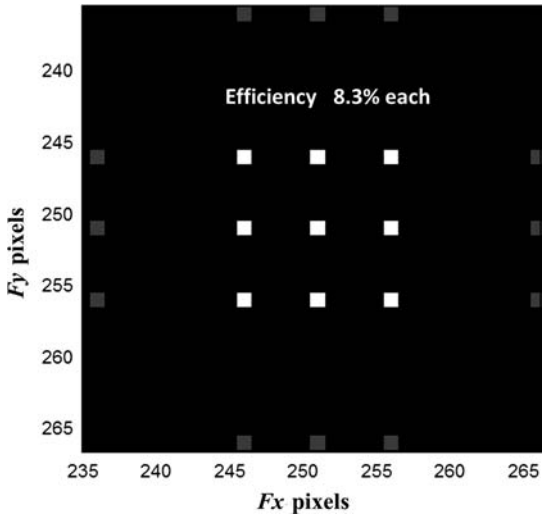

Figure E.2.2 Image of the diffraction spots seen by zooming in on figure window 2.

E.2.3 The simplest method is to draw a triangle of size 100×100 pixels and generate the full matrix with the '`repmat`' command.

E.2.4 Define two focal length values $fx = 3000$ μm and $fy = 6000$ μm for the grating lines along the x and y directions, respectively, in MATLAB code. The MATLAB code for generation of a 2D FZP is shown in Table E.2.4. The image of the 2D grating seen in figure window 1 is shown in Fig. E.2.4.

Table E.2.4 MATLAB code for design of a 2D binary FZP.

```
%%2-d FZP%%
clear; %Clear all memory
    N=500; %Define Matrix sizes
    M=50;%Define the number of grating lines
    A1=zeros(N,N);%Define Matrices by assigning zeros to all
%pixels
    A2=zeros(N,N);
    x=zeros(M,M);
    y=zeros(M,M);
    fx=3000; %Define focal lengths (in micrometers)
    fy=6000;
    lambda=0.633; %Define wavelength (in micrometers)
for n=1:M; %Calculate the width of the grating lines
  x(n)=sqrt(n*fx*lambda);
  y(n)=sqrt(n*fx*lambda);
end
for n=1:2:M;
  for p=1:N;
    for q=1:N;
      if abs(q-N/2) > x(n) && abs(q-N/2) < x(n+1);
      A1(p,q)=1;
      end
```

(*Continued*)

Downloaded From: https://www.spiedigitallibrary.org/ebooks/ on 27 Feb 2022
Terms of Use: https://www.spiedigitallibrary.org/terms-of-use

Table E.2.4. Continued

```
      if abs(p-N/2) > y(n) && abs(p-N/2) < y(n+1);
      A2(p,q)=1;
      end
    end
  end
end
A3=exp(1i*pi*xor(A1,A2));
```

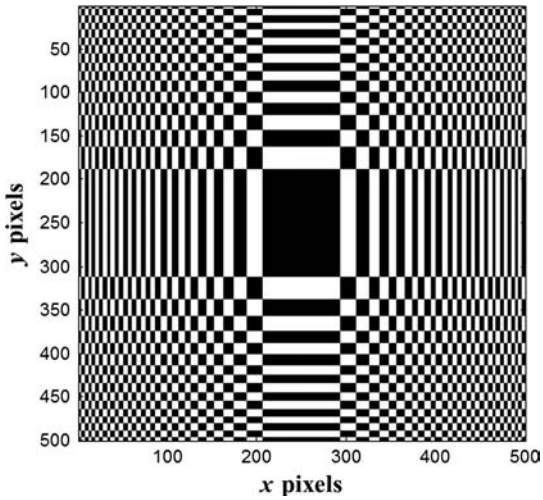

Figure E.2.4 Image of the 2D FZP seen in figure window 1.

E.2.5 The elliptical FZP behaves similar to a FZP.[41,42] In the case of an elliptical FZP, the focal lengths are different along the x and y directions, resulting in elliptical spots at the two focal planes. In many semiconductor lasers [distributed Bragg reflector (DBR), distributed feedback (DFB)], the beam waist is elliptical, resulting in an elliptical spot when focused. By using an elliptical FZP of suitable focal length ratio along the x and y directions, the elliptical wavefront can be compensated and converted into a spherical wavefront. The MATLAB code given for design of a FZP is modified with the equation of the ellipse with two radius values along the x and y directions. The MATLAB code for design of an elliptical FZP is shown in Table E.2.5. The image of the elliptical FZP is shown in the Fig. E.2.5.

Downloaded From: https://www.spiedigitallibrary.org/ebooks/ on 27 Feb 2022
Terms of Use: https://www.spiedigitallibrary.org/terms-of-use

Table E.2.5 MATLAB code for design of an elliptical FZP.

```
%%Elliptical FZP%%
clear; %Clear all memory
    N=500; %Define Matrix sizes
    M=25;%Define the number of grating lines
    A=ones(N,N);%Define Matrices by assigning zeros to all pixels
    rx=zeros(M,M);
    r=zeros(N,N);
    fx=3000; %Define focal lengths (in micrometers)
    fy=4500;
    lambda=0.633; %Define wavelength (in micrometers)
for n=1:M; %Calculate the width of the grating lines
  rx(n)=sqrt((n-1)*fx*lambda);
end
for n=1:2:M;%Construct elliptical FZP
  for p=1:N;
    for q=1:N;
      r(p,q)=sqrt(((p-N/2)*(p-N/2))*(fx/fy)+((q-N/2)*(q-N/
      2)));
      if r(p,q) > rx(n) && r(p,q) < rx(n+1);
      A(p,q)=exp(1i*pi);
      end
    end
  end
end
```

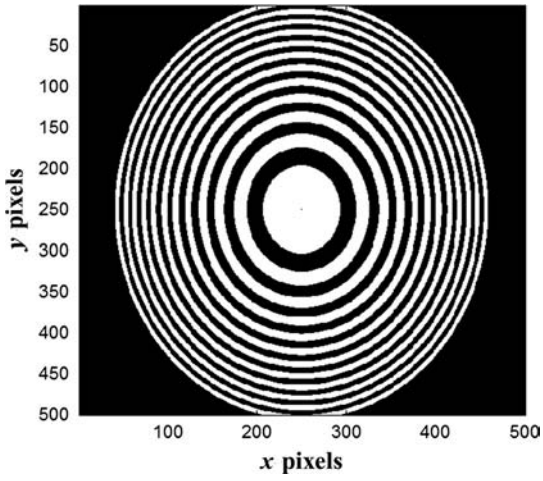

Figure E.2.5 Image of the elliptical FZP generated with focal length values $f_x = 3000$ μm and $f_y = 4500$ μm.

E.2.6 An axicon array is used for the generation of an array of Bessel-like beams in the near field and a ring pattern array in the far field. Such elements are useful for micro-drilling applications.[43,44] The MATLAB code for design of a micro-axicon array is similar to the array generation code given in Tables 2.7

Downloaded From: https://www.spiedigitallibrary.org/ebooks/ on 27 Feb 2022
Terms of Use: https://www.spiedigitallibrary.org/terms-of-use

and 2.8. A single axicon is designed and is subsequently replicated to form the complete device. The MATLAB code is given in Table E.2.6. The image of the axicon array generated using MATLAB is shown in Fig. E.2.6.

Table E.2.6 MATLAB code for design of an axicon array.

```
%Axicon array
    clear; %Clear all memory
    N1=100; %Define matrix sizes
    N2=500;
    ratio=N2/N1;
    A1=zeros(N1,N1); %Define a Matrix by assigning 0 to all
%elements
    r=zeros(N1,N1);
    P=10; %Define the period of the axicon
for p=1:N1; %Generate the fundamental building block - single
%axicon
  for q=1:N1;
      r(p,q)=sqrt((p-N1/2)*(p-N1/2)+(q-N1/2)*(q-N1/2));
      if r(p,q)<N1/2;
        if rem(r(p,q),P)<P/2;
          A1(p,q)=1;
        end
      end
  end
end
A2=repmat(A1,ratio); %Generate the full grating
```

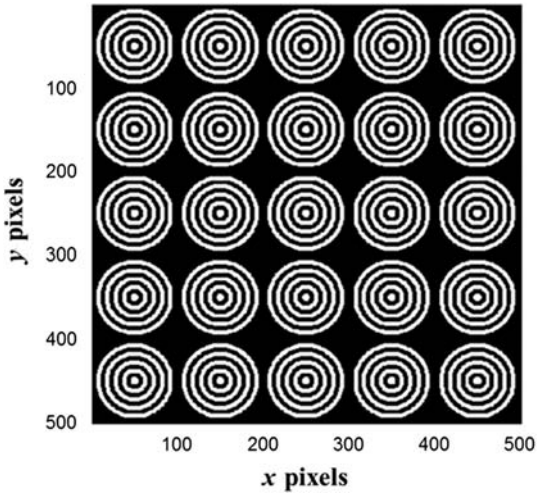

Figure E.2.6 Image of the axicon array generated with a period of $\Lambda = 100$ μm.

Downloaded From: https://www.spiedigitallibrary.org/ebooks/ on 27 Feb 2022
Terms of Use: https://www.spiedigitallibrary.org/terms-of-use

Chapter 3 Solutions

E.3.1 Calculate the phase values in steps of π/8 and the corresponding resist thickness values. The values are shown in Fig. E.3.1a.

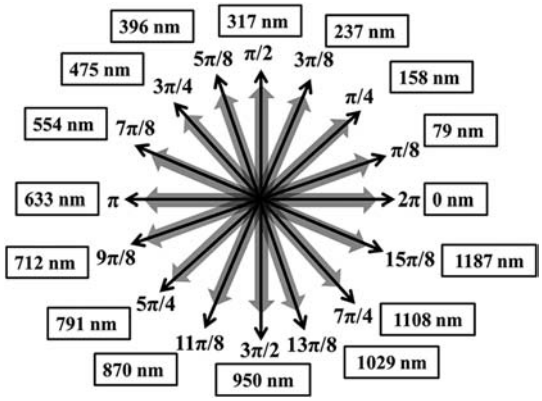

Figure E.3.1a Phase values and resist thickness values of a 16-level 1D phase grating.

The MATLAB code shown in Table 3.2 can be modified by changing the number of phase levels and the phase increment as given in Table E.3.1. The phase profile of the 16-level 1D phase grating is shown in Fig. E.3.1b. The displayed efficiency value is 0.987, which matches with the value (0.987) calculated using Eq. 3.1. The image of the phase profile looks similar to that of a blazed grating.

Table E.3.1 MATLAB code for design of a 16-level 1D phase grating.

```
%%16-level 1D grating
g=16;%Define the number of phase levels
delphase=pi/8;%Define the phase step size
```

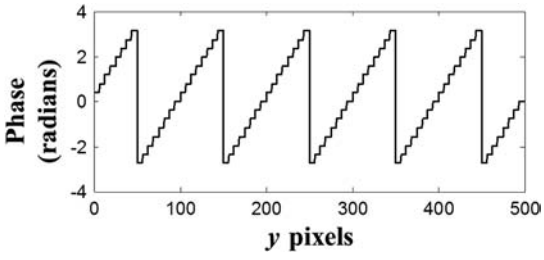

Figure E.3.1b Plot of the phase profile of a 16-level 1D phase grating.

Downloaded From: https://www.spiedigitallibrary.org/ebooks/ on 27 Feb 2022
Terms of Use: https://www.spiedigitallibrary.org/terms-of-use

E.3.2 The phase profile of a negative FZP is given by

$$\Phi_{\mathrm{FZP}}(r) = \left[\frac{2\pi}{\lambda}\left(f + \sqrt{f^2 + r^2}\right)\right]_{2\pi}. \tag{E.3.2}$$

The MATLAB code for design of a four-level negative FZP is given in Table E.3.2.

Table E.3.2 MATLAB code for design of a four-level negative FZP.

```
%%4-level 1D FZP
clear;%Clear all memory
%Define the FZP parameters
     N=500;%Define Matrix size
     f=10000;%Define the focal length in μm
     lambda=0.632;%Define the wavelength in μm
     C=ones(N,N);
     g=4;
%Constructing the negative FZP
     x=1:N;
     y=1:N;
     [X,Y]=meshgrid(x,y);
     r=sqrt((X-N/2).*(X-N/2)+(Y-N/2).*(Y-N/2));
     A=(f+sqrt(f*f+r.*r))*(2*pi)/(0.632);
     B=rem(A,2*pi);
     B1=exp(1i*B);
     B(r>N/2)=0;
for p=1:N;%Construct the 4-level FZP
  for q=1:N;
    for n=1:g;
      if B(p,q)> (n-1)*pi/2 && B(p,q) <= n*pi/2;
        C(p,q)=exp(1i*n*pi/2);
      end
    end
  end
end
```

The image of the phase profile of a negative blazed FZP and a four-level FZP are shown in Fig. E.3.2.

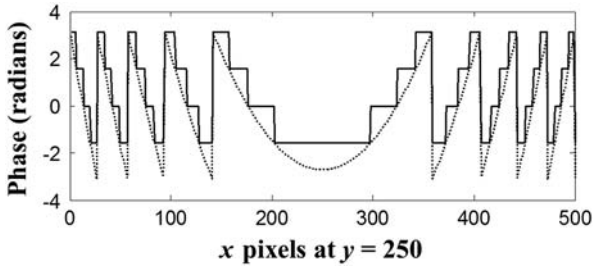

Figure E.3.2 Phase profile of (a) a blazed negative FZP (dotted line) and (b) its four-level approximation (solid line).

Downloaded From: https://www.spiedigitallibrary.org/ebooks/ on 27 Feb 2022
Terms of Use: https://www.spiedigitallibrary.org/terms-of-use

E.3.3 A binary SPP with topological charge $L = 5$ can be constructed by designing a SPP with charge $L = 5$ followed by the binarization step. The MATLAB code for design of a binary SPP is shown in Table E.3.3.

Table E.3.3 MATLAB code for design of a binary SPP with $L = 5$.

```
%%Binary SPP with L=5
clear;
%Defining the SPP parameters
     N=500;%Define the matrix size
     L=5;%Define the topological charge number
%Constructing the SPP
     x=1:N;
     y=1:N;
     [X,Y]=meshgrid(x,y);
     theta=atan2((X-N/2),(Y-N/2));
     r=sqrt((X-N/2).*(X-N/2)+(Y-N/2).*(Y-N/2));
     A1=L*(theta+pi);
     A2=rem(A1,2*pi);
for p=1:N;%Construct the SPP using atan2 function and binarize
  for q=1:N;
    if rem(A2(p,q),2*pi)<=pi;
      A3(p,q)=exp(1i*pi);
    else
      A3(p,q)=exp(1i*0);
    end
  end
end
A3(r>30)=0;
%Observation of far field pattern
E=fftshift(fft2(A3));%Calculate the Fourier transform and
%rearrange terms
I=abs(E).*abs(E);
```

The phase profile of the binary SPP with charge $L = 5$ before applying radius constraint and its far-field diffraction pattern are shown in Figs. E.3.3 (a) and (b), respectively.

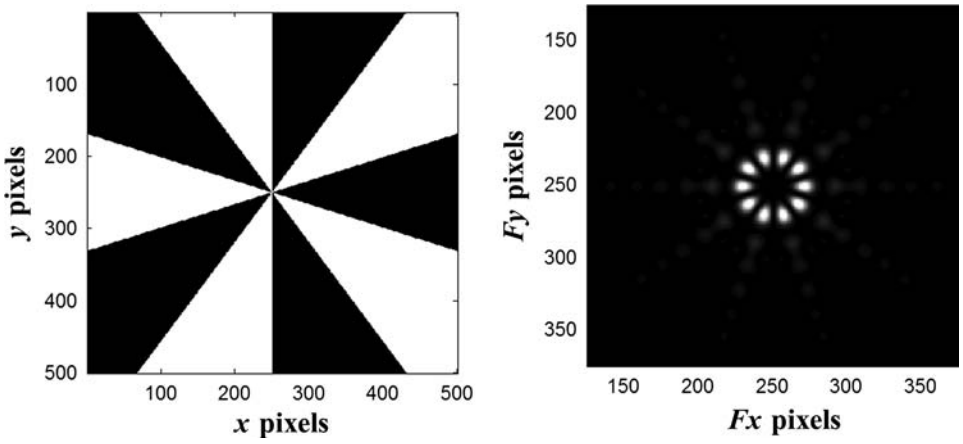

Figure E.3.3 (a) Phase profile of a binary SPP with topological charge of $L = 5$ and (b) its far-field diffraction pattern.

Downloaded From: https://www.spiedigitallibrary.org/ebooks/ on 27 Feb 2022
Terms of Use: https://www.spiedigitallibrary.org/terms-of-use

E.3.4 To design the three-level DOE, the same logo was considered with ten iterations. The MATLAB code is same as that given in Table 3.9 except that the grayscale phase profile of the DOE has to be converted into a three-level phase profile. The MATLAB code for design of a three-level DOE is shown in Table E.3.4.

Table E.3.4 MATLAB code for design of a three-level DOE using the IFTA.

```
DOE1=zeros(N,N);
g=3;%Define the number of phase levels
delphase=2*pi/3;%Define the phase increment
for p=1:N;%Convert the greyscale phase profile into a 3-level
%phase profile
  for q=1:N;
    for n=1:g;
    if DOE(p,q)>-pi+(n-1)*delphase && DOE(p,q)<=-pi+(n)*
    delphase;
      DOE1(p,q)=(n-1)*delphase;
    end
    end
  end
end
%Verification of result
     DOE2=exp(1i*DOE1);
     I=abs(fft2(DOE2)); %Calculate the Fourier transform
     colormap(gray)
     Imagesc(I)
```

The image of the logo generated by the three-level DOE is shown in Fig. E.3.4. It can be noted that the twin image is removed. Three-level DOEs have an efficiency close to 70%. By designing three-level DOEs, the twin image problem can be solved with reasonably high efficiency. Besides, it is relatively easier to fabricate a three-level DOE compared to a grayscale DOE.

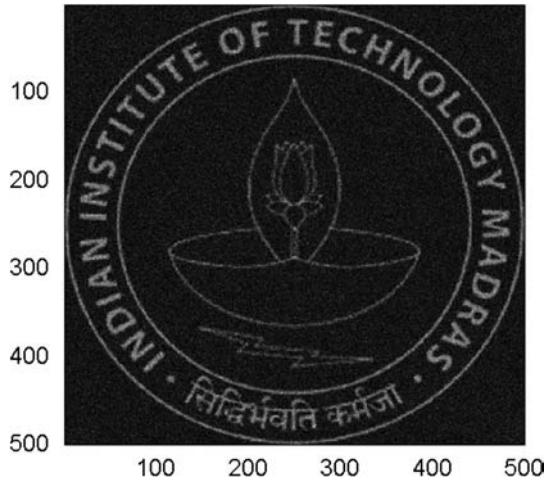

Figure E.3.4 Image of the logo generated from the three-level DOE.

Downloaded From: https://www.spiedigitallibrary.org/ebooks/ on 27 Feb 2022
Terms of Use: https://www.spiedigitallibrary.org/terms-of-use

E.3.5 The design of a ring lens is similar to that described in Chapter 2. The optics configuration for focusing light on a ring using a ring lens is shown in Fig. E.3.5a.

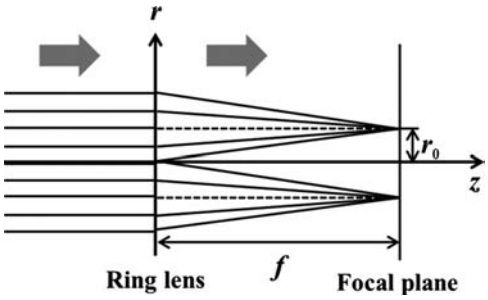

Figure E.3.5a Optics configuration for focusing a plane wave on a ring.

The phase equation of a ring lens is given by

$$\Phi_{\text{Ring lens}}(r) = \left[\frac{2\pi}{\lambda}\left(f - \sqrt{f^2 + (r - r_0)^2}\right)\right]_{2\pi}. \tag{E.3.5}$$

The MATLAB code is similar to that of a gradient FZP with the replacement of the phase equation, as shown in Table E.3.5. The image of the ring lens and the plot of its phase profile are shown in Figs. E.3.5b and Fig. E.3.5c, respectively.

Table E.3.5 MATLAB code for design of a grayscale ring lens.

```
%%Greyscale ring lens
     clear;%Clear all memory
     %Define lens parameters
     N=500;%Define Matrix size
     f=2000;%Define the focal length in um
     r0=100;%Define radius of ring in um
     lambda=0.632;%Define the wavelength in um
%Constructing the lens
     x=1:N;
     y=1:N;
     [X,Y]=meshgrid(x,y);
     r=sqrt((X-N/2).*(X-N/2)+(Y-N/2).*(Y-N/2));
     A=(f-sqrt(f*f+(r-r0).*(r-r0)))*(2*pi)/(0.632);
     B=rem(A,2*pi);
     B1=exp(1i*B);
```

Downloaded From: https://www.spiedigitallibrary.org/ebooks/ on 27 Feb 2022
Terms of Use: https://www.spiedigitallibrary.org/terms-of-use

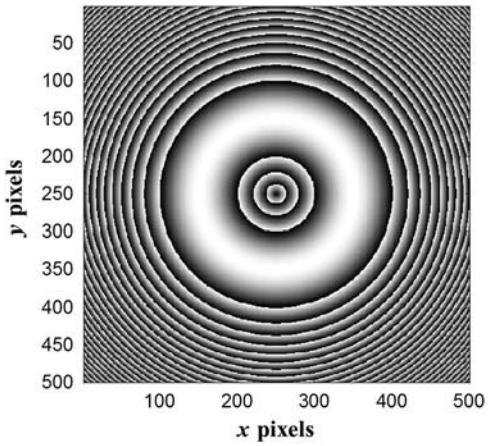

Figure E.3.5b Image of the phase profile of the gradient ring lens.

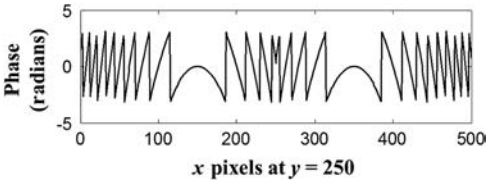

Figure E.3.5c Plot of the phase profile of the gradient ring lens at $y = 250$ pixels.

Chapter 4 Solutions

E.4.1 The MATLAB code is similar to that shown in Table 4.2 while the DOE design script has to be replaced with that in Table E.4.1.

The diffraction pattern at $z = 50$ m is shown in Fig. E.4.1. It can be noted that the other higher-order ring patterns vanished, with only a high-efficiency first-order ring pattern remaining.

Downloaded From: https://www.spiedigitallibrary.org/ebooks/ on 27 Feb 2022
Terms of Use: https://www.spiedigitallibrary.org/terms-of-use

Table E.4.1 MATLAB code for design and analysis of blazed axicon using the Fresnel diffraction formula.

```
%Fresnel diffraction of blazed axicon%
     clear; %Clear all memory
% Defining the parameters
     N=500;% Define the matrix size
     lambda=0.633*10^-6;%Define wavelength in meters
     z=50;%Propagation distance = 50 m
     P=10^-4;%Period of axicon = 0.1 mm
     wsamp=10*lambda;%sampling period or width
%Sampling the space
x=1:N;
y=1:N;
[X,Y]=meshgrid(x,y);%Sampling
Rsamp=sqrt((X-N/2).^2+(Y-N/2).^2).*wsamp;%Define sampled
%radius
%Constructing the DOE
     A=ones(N,N);%Define matrix by assigning ones to all pixels
     A=exp(1i*(rem(Rsamp,P))*(2*pi)/P);
     A(Rsamp>N/2*wsamp)=0;
% Calculating the Fresnel diffraction
     PPF=exp(1i*pi/(lambda*z).*Rsamp.*Rsamp); %Calculate the
     %parabolic phase factor
     A1=A.*PPF; %Multiply the circular aperture function with
     %the parabolic phase factor
E=abs(fftshift(fft2(fftshift(A1)))); %Calculate Fourier
%transform
```

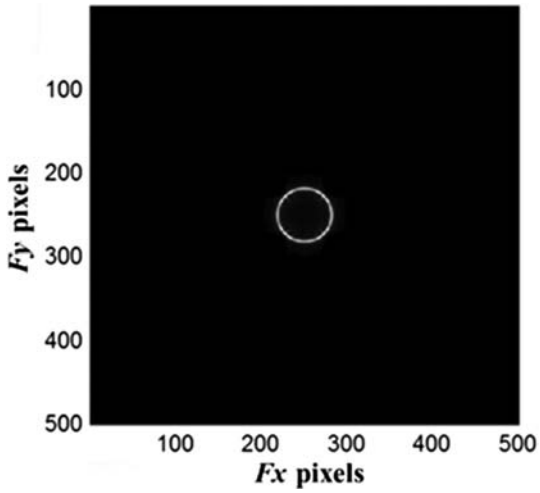

Figure E.4.1 Fresnel diffraction pattern of a blazed axicon at a distance of $z = 50$ m.

Downloaded From: https://www.spiedigitallibrary.org/ebooks/ on 27 Feb 2022
Terms of Use: https://www.spiedigitallibrary.org/terms-of-use

E.4.2 The MATLAB code for designing the phase element is given in Table E.4.2. The images of the diffracted fields at $z = 5$ mm, 10 mm, 20 mm, and 50 mm are shown in Fig. E.4.2a, and the plots of the cross section in the same figure are shown in Fig. E.4.2b. There is a shift in the location of the maximum intensity. The shift in the peaks shows a nonlinear response that matches the phase profile of the DOE.

Table E.4.2 MATLAB code for design and analysis of a DOE using the Fresnel diffraction formula.

```
%Fresnel diffraction of DOE%
%clear; %Clear all memory
% Defining the parameters
     N=500;% Define the matrix size
     lambda=0.633*10^-6;%Define wavelength in meters
     z=10*1e-3;%Propagation distance
     del=1*1e-6;%sampling period or width
%Sampling the space
     x=-N/2:N/2-1;
     y=-N/2:N/2-1;
     [X,Y]=meshgrid(x*del,y*del);%Sampling
     R=sqrt(X.^2+Y.^2);%Define sampled radius
%Constructing the DOE
     A=exp(1i*(X+250*1e-6).^3*2*pi*5*10^11);
% Calculating the Fresnel diffraction
     PPF=exp(1i*pi/(lambda*z)*R.*R); %Calculate the parabolic
     %phase factor
     A1=A.*PPF; %Multiply the circular aperture function with
     %the parabolic phase factor
     E=abs(fftshift(fft2(fftshift(A1)))); %Calculate Fourier
     %transform
     E=E/max(max(E));
     figure (1)
     imagesc(E);
     figure (2)
%plot(E(N/2,:)/(max(max(E(N/2,:)))))
```

Downloaded From: https://www.spiedigitallibrary.org/ebooks/ on 27 Feb 2022
Terms of Use: https://www.spiedigitallibrary.org/terms-of-use

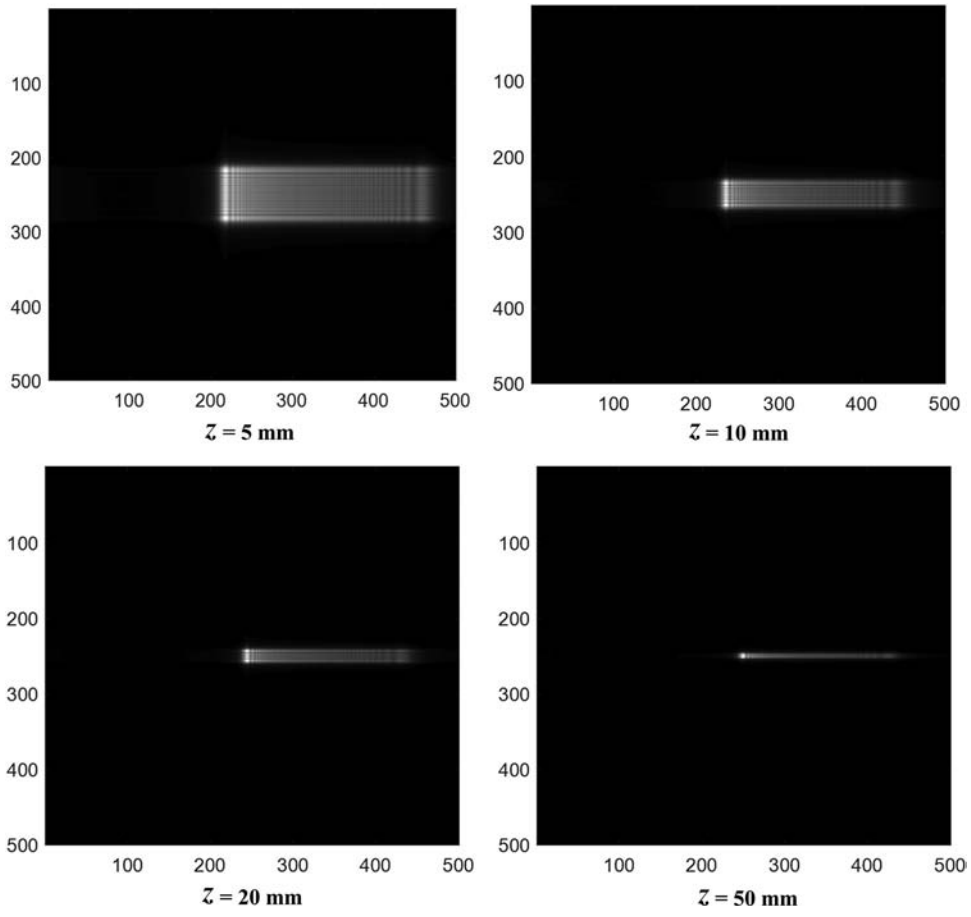

Figure E.4.2a Images of the intensity profile at $z = 5$ mm, 10 mm, 20 mm, and 50 mm.

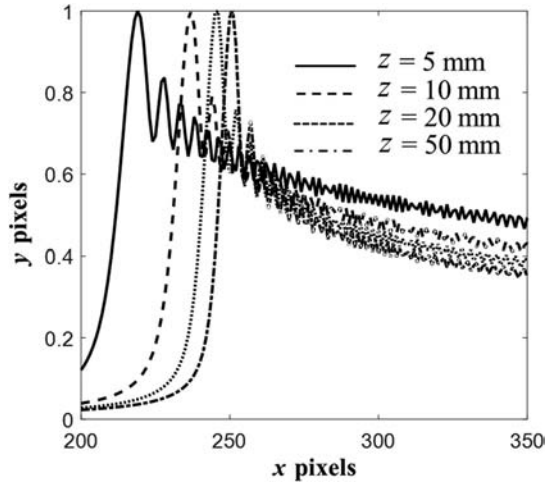

Figure E.4.2b Plots of the intensity profile at $z = 5$ mm (solid line), 10 mm (dashed line), 20 mm (dotted line), and 50 mm (dashed and dotted line).

Downloaded From: https://www.spiedigitallibrary.org/ebooks/ on 27 Feb 2022
Terms of Use: https://www.spiedigitallibrary.org/terms-of-use

E.4.3 When a linear phase is used, there is no shift of the maximum intensity with respect to the propagation distance due to the scaling factor that compensates for the shift that appears in a lab experiment.

Chapter 5 Solutions

E.5.1 The optical path length equation for focusing a diverging wave on a ring of radius r_0 is given by

$$\sqrt{u^2 + r_n^2} + \sqrt{v^2 + (r_n - r_0)^2} - \sqrt{u^2 + r_0^2} - v = n\lambda, \tag{E.5.1}$$

where, u and v are the object and image distances, respectively. Assuming that $r_0 << (r, u \text{ and } v)$, Eq. (E.5.1) can be expressed as

$$\sqrt{u^2 + r_n^2} + \sqrt{v^2 + (r_n - r_0)^2} - u\left[1 + \frac{r_0^2}{2u^2}\right] - v = n\lambda. \tag{E.5.2}$$

For $(r_0{}^2/2u^2) << 1$, using binomial expansion,

$$u\sqrt{1 + \frac{r_0^2}{u^2}} \cong u\left[1 + \frac{r_0^2}{2u^2}\right]. \tag{E.5.3}$$

Solving Eq. (E.5.3) for r_n yields

$$r_n = \frac{-b \pm \sqrt{b^2 - 4ac}}{2a}, \tag{E.5.4}$$

where

$$a = u^2 + v^2 + n^2\lambda^2 + 2uv + 2n\lambda(u + v) + \frac{{r_0}^4}{4u^2} + \frac{{r_0}^2}{u}(v + n\lambda),$$

$$b = -r_0\left[n^2\lambda^2 + \frac{{r_0}^4}{4u^2} + 2uv + 2n\lambda(u + v) + \frac{{r_0}^2}{u}(v + n\lambda) + 2u^2\right],$$

$$c = -\frac{1}{4}\left[n^2\lambda^2 + \frac{{r_0}^4}{4u^2} + 2uv + 2n\lambda(u + v) + \frac{{r_0}^2}{u}(v + n\lambda)\right]^2 + u^2(v^2 + {r_0}^2).$$

The technique discussed in Section 5.2 is used to find the location of the virtual sources u' generated by the glass substrate:

$$r_n' = \frac{-b' \pm \sqrt{b'^2 - 4a'c'}}{2a'}, \tag{E.5.5}$$

Downloaded From: https://www.spiedigitallibrary.org/ebooks/ on 27 Feb 2022
Terms of Use: https://www.spiedigitallibrary.org/terms-of-use

where

$$a' = u'^2 + v^2 + n^2\lambda^2 + 2u'v + 2n\lambda(u' + v) + \frac{{r_0}^4}{4u'^2} + \frac{{r_0}^2}{u'}(v + n\lambda),$$

$$b' = -r_0\left[n^2\lambda^2 + \frac{{r_0}^4}{4u'^2} + 2u'v + 2n\lambda(u' + v) + \frac{{r_0}^2}{u'}(v + n\lambda) + 2u'^2\right],$$

$$c' = -\frac{1}{4}\left[n^2\lambda^2 + \frac{{r_0}^4}{4u'^2} + 2u'v + 2n\lambda(u' + v) + \frac{{r_0}^2}{u'}(v + n\lambda)\right]^2 + u'^2(v^2 + {r_0}^2).$$

E.5.2 The radius of a FZP can be calculated with the inclusion of the glass substrate and the additional polymer holder using Eq. (5.18). The thickness function is not constant as in the earlier case, but is binary with two values, namely, 1 mm and 3 mm, respectively at different radial sections. The plot of the radii of zones as a function of zone number for case 1, $t = 1$ mm (constant) and case 2, $t = 3$ mm ($0.5\text{ mm} < r < 0.7$ mm), and $t = 1$ mm elsewhere is shown in Fig. E.5.2. The radii values are different in the region ($0.5\text{ mm} < r <$ 0.7 mm), as expected.

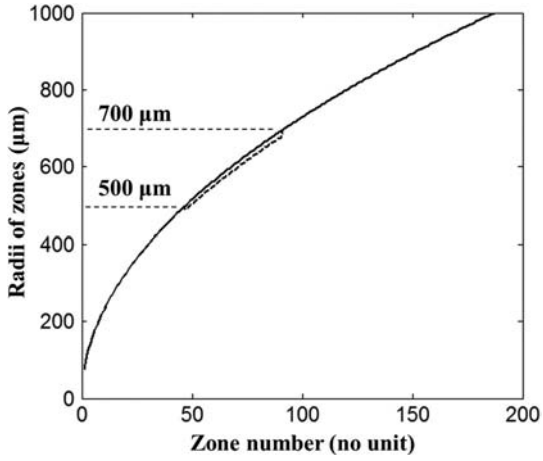

Figure E.5.2 Plot of the radii of zones for case 1: $t = 1$ mm (solid line) and case 2: $t = 3$ mm ($0.5\text{ mm} < r < 0.7$ mm), and $t = 1$ mm elsewhere (dotted line).

E.5.3 The radius of a FZP can be calculated with the inclusion of the glass substrate whose thickness varies with respect to the radial coordinate. The radii values are plotted as a function of zone number for two cases—case 1: $t = 1$ mm and case 2: $t = 1 + r$, as shown in Fig. E.5.3.

Downloaded From: https://www.spiedigitallibrary.org/ebooks/ on 27 Feb 2022
Terms of Use: https://www.spiedigitallibrary.org/terms-of-use

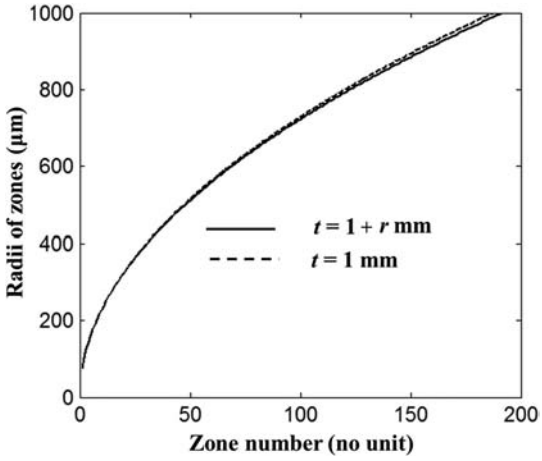

Figure E.5.3 Plot of the radii of zones for case 1: $t = 1$ mm (dotted line) and case 2: $t = 1 + r$ (solid line).

Chapter 6 Solutions

E.6.1 The two DOEs of choice are a FZP and a circular grating or axicon to generate a focused ring pattern with a diameter of 1 mm at a distance of 30 mm. A circular grating generates a ring pattern in its far field and when it is used together with a FZP, and it generates a focused ring pattern at the focal plane of the FZP. Hence, the focal length of $f = 30$ mm and the period of the circular grating can be estimated from the diameter of the ring pattern, which is 1 mm.

Case 1: Modulo-2π Phase Addition Method
The period of the grating necessary to generate a ring pattern with a diameter of 1 mm at a distance of 30 mm is given by Eq. (6.11):

$$\sin\theta = \frac{\lambda}{\Lambda} = \frac{\frac{d}{2}}{\sqrt{\frac{d^2}{4} + f^2}}. \tag{E.6.1a}$$

After simplification,

$$\Lambda = \frac{\lambda\sqrt{d^2 + 4f^2}}{d} = 38\,\mu\text{m}. \tag{E.6.1b}$$

The MATLAB code for generation of the binary phase profile of a FZP and a circular grating using the modulo-2π phase addition method for generation of the multifunctional DOE are given in Table E.6.1.

Downloaded From: https://www.spiedigitallibrary.org/ebooks/ on 27 Feb 2022
Terms of Use: https://www.spiedigitallibrary.org/terms-of-use

Table E.6.1 MATLAB code for design of a multifunctional DOE from a binary circular grating and a binary FZP using the modulo-2π phase addition method.

```
%Multifunctional DOE - Circular grating and FZP - Modulo-2π phase
%addition method
clear; %Clear all memory
%Define grating parameters
     N=1000;%Define matrix size
     M=10;%Define number of half period zones of FZP
     f=30000; %Define focal length of FZP
     lambda=0.633;%Define wavelength
     A1=zeros(N,N); %Define a Matrix by assigning 0 to all
     %elements
     A2=zeros(N,N);
     r=zeros(N,N);
     r1=zeros(M);
     Pr=38; %Define the period of the grating
     FFr=0.5; %Define fill factors for x and y periodicity
%Construct the binary FZP and binary circular grating
for n=1:M;
  r1(n)=sqrt(n*f*lambda);
end
for n=1:2:M;
for p=1:N;
  for q=1:N;
    r(p,q)=sqrt((p-N/2)*(p-N/2)+(q-N/2)*(q-N/2));
    if r(p,q)<N/2;
      if rem(r(p,q),Pr)<Pr*FFr;
        A1(p,q)=1;
      end
      if r(p,q) > r1(n) && r(p,q) < r1(n+1);
        A2(p,q)=1;
      end
    end
  end
end
end
A3=exp(1i*pi*xor(A1,A2)); %XOR operation between A1 and A2
```

Downloaded From: https://www.spiedigitallibrary.org/ebooks/ on 27 Feb 2022
Terms of Use: https://www.spiedigitallibrary.org/terms-of-use

The image of the multifunctional DOE is shown in Fig. E.6.1a.

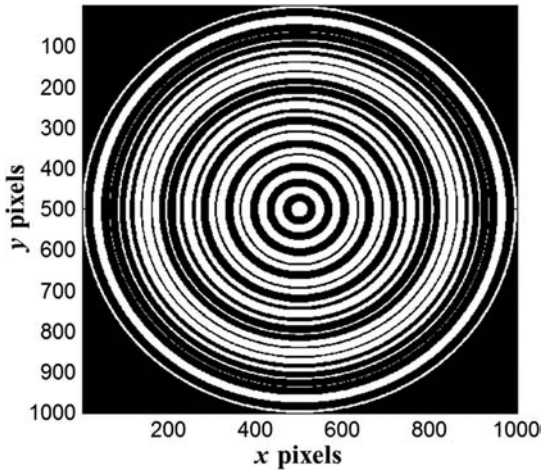

Figure E.6.1a Image of the phase profile of the multifunctional DOE containing the functions of a circular grating with a period of 38 μm and a FZP with a focal length of $f = 30$ mm.

Case 2: Analog Method

The base angle of the negative axicon necessary to generate a ring pattern with a diameter of 1 mm at a distance of 30 mm can be calculated as follows. The divergence angle required is given by

$$\beta = \sin^{-1}(n_g \sin\alpha) - \alpha = \frac{d/2}{f} = 0.0167 \text{ rad.} \qquad \text{(E.6.1c)}$$

Assuming that $n_g = 1.5$, the base angle of the axicon is given by 0.0335 rad. Hence, from the relationship between the thickness and X, we find that $X =$ 26.5. The radii of zones of the multifunctional DOE can be estimated using Eq. (6.19).

The MATLAB code for designing the multifunctional DOE using the analog method is similar to the code given in Table E.6.1. However, the equation of radii of zones must be replaced by Eq. (6.19). The plot of radii of zones as a function of zone number is shown in Fig. E.6.1b. It can be noted that the radius of the first zone is > 1 mm. Hence, it is not possible to design the element using the analog method for the above design values.

Downloaded From: https://www.spiedigitallibrary.org/ebooks/ on 27 Feb 2022
Terms of Use: https://www.spiedigitallibrary.org/terms-of-use

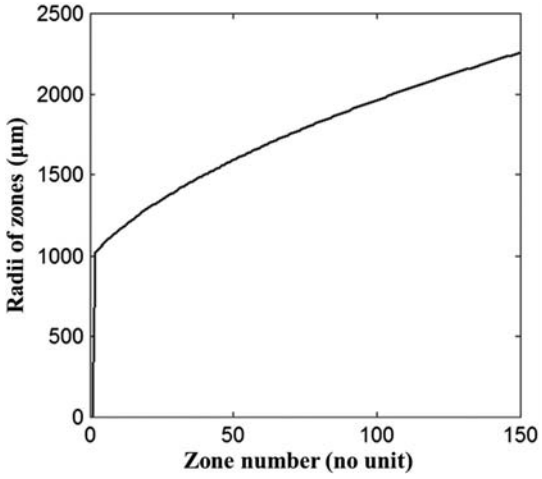

Figure E.6.1b Plot of the radii of zones of the multifunctional DOE as a function of the zone number.

E.6.2 There are many interesting optics configurations for superposing two signals with slightly different wavelengths. A simple configuration is as follows. The multifunctional DOE needs to have an axicon and a grating. The axicon converts the Gaussian intensity profile into a Bessel intensity profile, while the grating can be used for beam combining. The period of the grating must be selected to obtain a diffraction angle of 5 deg (0.0872 rad). As the wavelengths are close to one another, a grating with same period can be used for the average wavelength $\lambda_{avg} = 602$ nm. The period of the grating is estimated as $\Lambda_1 = 7$ μm. The distance between the central maximum and the first minimum is given by

$$r_0 = \frac{1.22\lambda}{\pi \sin\beta}. \tag{E.6.2}$$

Hence, the period of the axicon is $\Lambda_1 = 51$ μm. The element can be designed using the MATLAB code given in Table E.6.2.

Downloaded From: https://www.spiedigitallibrary.org/ebooks/ on 27 Feb 2022
Terms of Use: https://www.spiedigitallibrary.org/terms-of-use

Table E.6.2 MATLAB code for design of multifunctional DOE from a blazed axicon and a 1D grating.

```
%%Multifunctional DOE- Blazed axicon and binary grating
clear;%Clear all memory
%Define grating parameters
     N=500;%Define Matrix size
     Pr=51;
     Px=7;
     FFx=0.5;
     A2=zeros(N,N);%Define the matrices assigning ones to all
     %pixels
%Construction of blazed axicon and binary grating
     x=1:N;
     y=1:N;
     [X,Y]=meshgrid(x,y);
     r=sqrt((X-N/2).*(X-N/2)+(Y-N/2).*(Y-N/2));
     P1=rem(r,Pr);
     A1=(P1/Pr)*2*pi;
     A2(rem(X,Px)<Px*FFx)=pi;
     A=exp(1i*rem(A1+A2,2*pi));
```

The grating needs to be binarized such that the $+1^{st}$ diffraction order of one of the beams will superpose the -1^{st} diffraction order of the other beam, as shown in Fig. E.6.2a. The magnified central region of the DOE is shown in Fig. 6.2b.

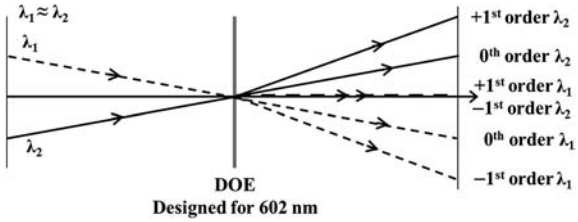

Figure E.6.2a Optics configuration for superposing light beams with slightly different wavelengths propagating at +5 deg and –5 deg.

Downloaded From: https://www.spiedigitallibrary.org/ebooks/ on 27 Feb 2022
Terms of Use: https://www.spiedigitallibrary.org/terms-of-use

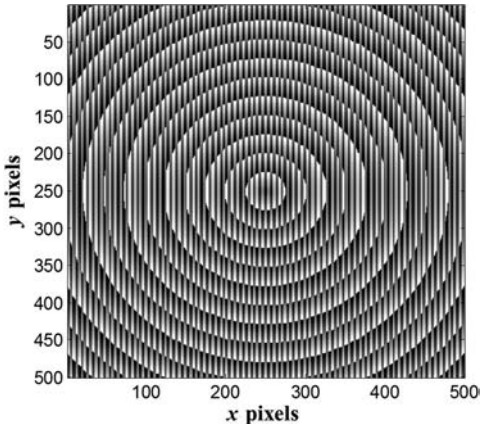

Figure E.6.2b Image of the phase profile of a multifunctional DOE containing the functions of a blazed axicon and a binary grating used for converting a Gaussian intensity profile into a Bessel intensity profile and for beam combining.

E.6.3 The phase profiles of a blazed spiral phase plate with charge $L = 10$ and a binary amplitude axicon with period $\Lambda = 10$ μm are added. The MATLAB code is similar to that given in Table 6.5, and the FZP phase profile must be replaced by the phase profile of a binary axicon or a circular grating. The image of the multifunctional DOE and its far-field diffraction pattern are shown in Fig. E.6.3(a) and (b), respectively.

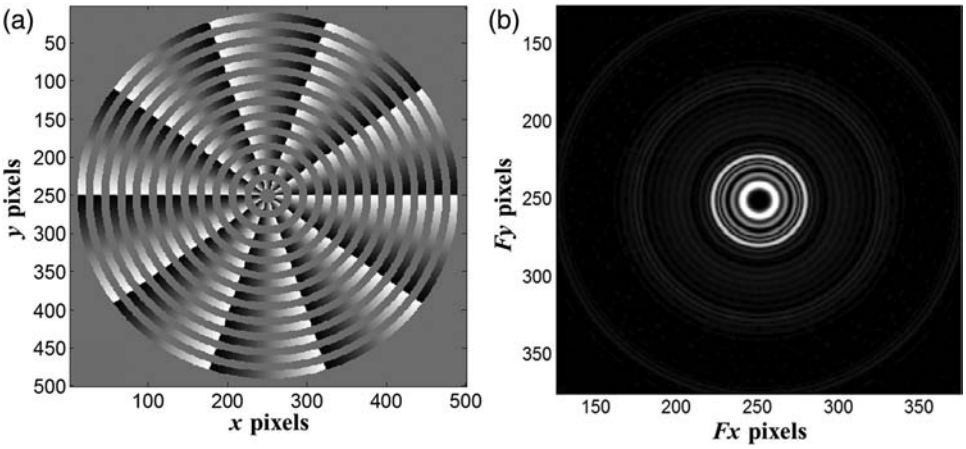

Figure E.6.3 (a) Image of the phase profile of a helical axicon and (b) the far-field diffraction pattern of a helical axicon.

Downloaded From: https://www.spiedigitallibrary.org/ebooks/ on 27 Feb 2022
Terms of Use: https://www.spiedigitallibrary.org/terms-of-use

E.6.4 Two DOEs, namely, a ring lens[29,30] and a checkerboard grating, are selected for generation of 2×2 ring patterns. The period of the grating calculated using trigonometry and the diffraction equation for generation of ring patterns with a spacing of 758 μm is 50 μm. The binary phase profile of the ring FZP can be generated using the path length equation, given by[27]

$$\sqrt{(r_n - r_0)^2 + f^2} - f = n\lambda. \tag{E.6.4a}$$

The equation of the zones of the ring FZP is given by

$$r_n = r_0 \pm \sqrt{n^2\lambda^2 + 2nf\lambda}. \tag{E.6.4b}$$

The MATLAB code is similar to Table 6.2, where the phase profiles of the binary axicon and 1D grating must be replaced by those of the ring FZP and the 2D checkerboard grating. The image of the DOE is shown in Fig. E.6.4. It can be observed that the diameter of the ring pattern is independent of wavelength, as the element is a ring lens. The distance between the rings is also independent of wavelength, as the variation in the focal length of the ring lens due to wavelength variation compensates for the variation in distance between the ring patterns due to wavelength variation.

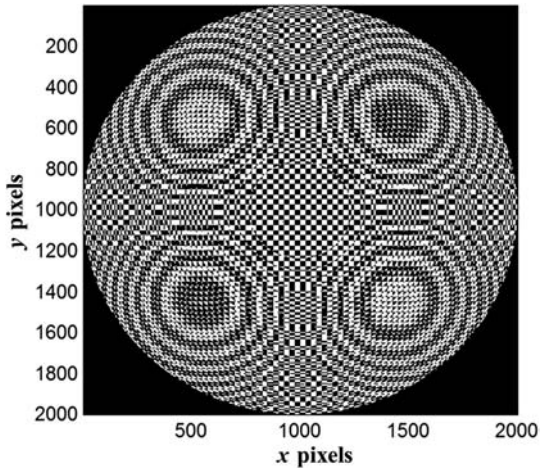

Figure E.6.4 Image of a multifunctional DOE containing the functions of a binary ring FZP and a binary checkerboard grating.

Chapter 7 Solutions

E.7.1 The CGH that focuses a diverging wavefront into a point is nothing but a FZP designed in finite conjugate mode. The object and image distances are 10 mm and 20 mm, respectively. This CGH can be designed by superposition

Downloaded From: https://www.spiedigitallibrary.org/ebooks/ on 27 Feb 2022
Terms of Use: https://www.spiedigitallibrary.org/terms-of-use

of the two wavefronts described by Eqs. (E.7.1.a) and (E.7.1.b). The design part of the MATLAB code is given in Table E.7.1. The image of the FZP generated using the above MATLAB code is given in Fig. E.7.1.

Table E.7.1 MATLAB code for design of a FZP in finite conjugate mode.

```
%FZP finite conjugate mode
     u=0.01;%Define object distance
     v=0.02;%Define image distance
     A=V*exp(1i*((2*pi)/lambda)*(u-sqrt(u*u-sqrt(X.^2+Y.
     ^2))));
     B=V*exp(1i*((2*pi)/lambda)*(-v+sqrt(v*v-(X.^2+Y.^2);
     D=A+B;%Interference
```

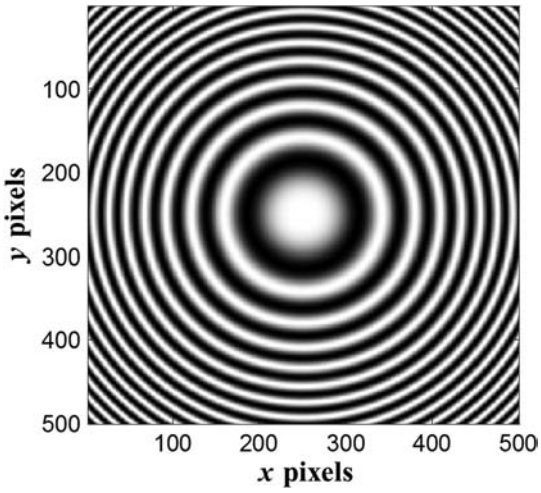

Figure E.7.1 Image of the sinusoidal phase profile of a CGH that can focus a diverging wavefront at a distance of 10 mm from a FZP plane to a point a distance of 20 mm from the FZP plane.

$$\Psi_1(x,y) = \exp\left[j\left(\frac{2\pi}{\lambda}\right)\left(u - \sqrt{u^2 - (x^2+y^2)}\right)\right], \tag{E.7.1.a}$$

$$\Psi_2(x,y) = \exp\left\{j\left(\frac{2\pi}{\lambda}\right)\left[\sqrt{v^2 - (x^2+y^2)} - v\right]\right\}. \tag{E.7.1.b}$$

E.7.2 An off-axis FZP-type CGH can be designed by superposing a spherical wavefront with a tilted-plane wavefront. The MATLAB code is similar to that

Downloaded From: https://www.spiedigitallibrary.org/ebooks/ on 27 Feb 2022
Terms of Use: https://www.spiedigitallibrary.org/terms-of-use

of Table 7.5; the wavefront profile of the axilens must be replaced by the wavefront profile of a FZP. The image of the off-axis FZP with a tilt angle of 3 deg and focal length of 25 mm is shown in Fig. E.7.2.

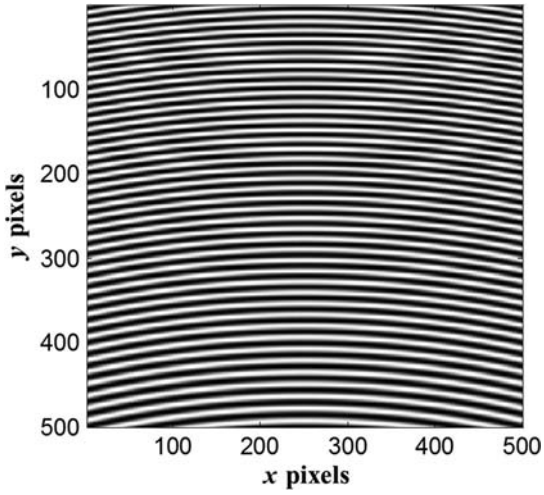

Figure E.7.2 Image of the sinusoidal phase profile of a CGH that can focus a plane wavefront a distance of 25 mm from the FZP plane with an angle of 3 deg.

E.7.3 An axicon is designed with $\alpha_1 = 2$ deg and $\alpha_1 = 1$ deg. The MATLAB code is similar to that of Table 7.3 with slight modifications, as shown in Table E.7.3. The image of the resulting CGH is shown in Fig. E.7.3.

Table E.7.3 MATLAB code for the design of an axicon with two base angles.

```
%Axicon with two base angles
     N=500;
     Angle=1;
     V=0.5;
     lambda=0.632;
for p=1:N;%%Design of a conical wave with two angles and a plane
%reference wave
  for q=1:N;
    r(p,q)=sqrt((p-N/2)*(p-N/2)+(q-N/2)*(q-N/2));
    if r(p,q)<125;
    A(p,q)=V*exp(1i*(r(p,q)/lambda)*tand(Angle*2)*2*pi);
    else
    A(p,q)=V*exp(1i*(((125/lambda)*tand(Angle*2)*2*pi)+
    (((r(p,q)- 125)/lambda)*tand(Angle)*2*pi)));
    end
    B(p,q)=V*exp(1i*0);
  end
end
D=A+B;%Interference
```

Downloaded From: https://www.spiedigitallibrary.org/ebooks/ on 27 Feb 2022
Terms of Use: https://www.spiedigitallibrary.org/terms-of-use

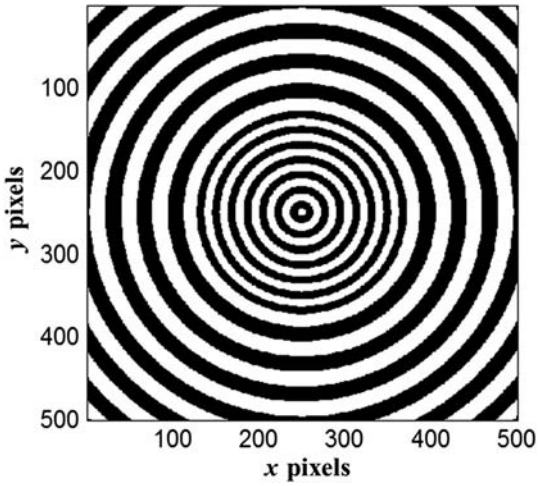

Figure E.7.3 Image of a binarized CGH generated by superposing a plane wave with a wave generated by an axicon with two base angles.

E.7.4 An optical element that generates a ring pattern in its far field is an axicon. If this axicon is used together with a FZP, then it generates a focused ring pattern at the focal plane of the FZP. The divergence angle of the axicon necessary to generate a ring pattern of radius 100 μm at the focal plane at a distance of 5 mm is given by

$$\beta = \tan^{-1}\left(\frac{r}{f}\right) = \tan^{-1}\left(\frac{100}{5000}\right) \cong 1.15 \text{ deg}.$$

The CGH can be designed by superposing a spherical wavefront emanating from a distance of 5 mm with a conical wave. The MATLAB code for design of the CGH is given in Table E.7.4.

Table E.7.4 MATLAB code for design of a CGH for generation of a focused ring pattern.

```
%CGH with ring focus
      N=500;
      Angle=1.15;%Define divergence angle
      V=0.5;%%Visibility controller
      lambda=0.632*1e-6;%Define wavelength
      f=0.005;%Define wavelength
      del=1*1e-6;%
      x=-N/2:N/2-1;
      y=-N/2:N/2-1;
      [X,Y]=meshgrid(x*del,y*del);
      R=sqrt(X.^2+Y.^2);
      A=V*exp(1i*((2*pi)/lambda)*(f-sqrt(f*f-R.*R)));
      B=V*exp(1i*(R/lambda)*tand(Angle)*2*pi);
      D=A+B;%Interference of the object and reference wave
```

Downloaded From: https://www.spiedigitallibrary.org/ebooks/ on 27 Feb 2022
Terms of Use: https://www.spiedigitallibrary.org/terms-of-use

The image of the interference pattern is similar to that of the profile of a ring lens capable of generating a focused ring pattern at the focal plane, as shown in Fig. E.7.4. The radius of the ring measured from Fig. E.7.4 shows 100 μm, which matches the calculated value.

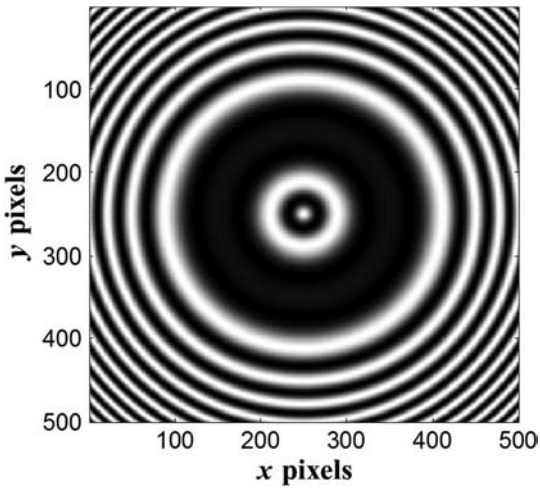

Figure E.7.4 Image of a sinusoidal CGH that can focus light on a ring with a radius of 100 μm at a distance of 5 mm.

E.7.5 The CGH can be designed by superposition of a helical wavefront with charge $L = 5$ with a spherical wave emanating from a point a distance of 5 mm from the CGH plane. The MATLAB code for design of the CGH is given in Table E.7.5. The image of the CGH is shown in Fig. E.7.5.

Table E.7.5 MATLAB code for design of a CGH for generation of a helical wavefront with $L = 5$ and focused at a distance of 5 mm.

```
%CGH for generation and focusing of a helical wavefront
      N=500;
      L=5;
      V=0.5;%%Visibility controller
      lambda=0.632*1e-6;%Define wavelength
      f=0.005;%Define wavelength
      del=1*1e-6;%
      x=-N/2:N/2-1;
      y=-N/2:N/2-1;
      [X,Y]=meshgrid(x*del,y*del);
      R=sqrt(X.^2+Y.^2);
      B=V*exp(1i*((2*pi)/lambda)*(f-sqrt(f*f-R.*R)));
      A=V*exp(1i*L*(atan2(X,Y)));
      D=A+B;%Interference of the object and reference wave
```

Downloaded From: https://www.spiedigitallibrary.org/ebooks/ on 27 Feb 2022
Terms of Use: https://www.spiedigitallibrary.org/terms-of-use

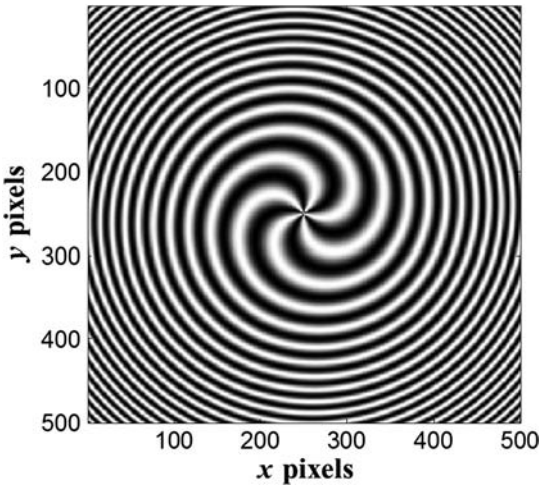

Figure E.7.5 Image of a sinusoidal CGH that can focus a helical wavefront with $L = 5$ at a distance of 5 mm.

Downloaded From: https://www.spiedigitallibrary.org/ebooks/ on 27 Feb 2022
Terms of Use: https://www.spiedigitallibrary.org/terms-of-use

Index

Downloaded From: https://www.spiedigitallibrary.org/ebooks/ on 27 Feb 2022
Terms of Use: https://www.spiedigitallibrary.org/terms-of-use

Downloaded From: https://www.spiedigitallibrary.org/ebooks/ on 27 Feb 2022
Terms of Use: https://www.spiedigitallibrary.org/terms-of-use

Downloaded From: https://www.spiedigitallibrary.org/ebooks/ on 27 Feb 2022
Terms of Use: https://www.spiedigitallibrary.org/terms-of-use

Downloaded From: https://www.spiedigitallibrary.org/ebooks/ on 27 Feb 2022
Terms of Use: https://www.spiedigitallibrary.org/terms-of-use

Downloaded From: https://www.spiedigitallibrary.org/ebooks/ on 27 Feb 2022
Terms of Use: https://www.spiedigitallibrary.org/terms-of-use

Anand Vijayakumar completed his Ph.D. under the guidance of Prof. Shanti Bhattacharya at the Indian Institute of Technology Madras, Chennai, India in 2015. Prior to this, he obtained an M.Tech. degree in Laser Technology from the College of Engineering, Anna University, Chennai, India. He also has M.S and B.S. degrees in Physics from the American College, Madurai. He is currently a postdoctoral research fellow at the Ben-Gurion University of the Negev, Beersheva, Israel. He holds this position as a recipient of the Planning and Budgeting Committee outstanding postdoctoral fellowship of the Israel government (2015). He is a recipient of several academic prizes, namely, the Einstein prize (2004), the Manual Thangaraj prize (2004), and the Richard Riez prize (2007) for proficiency in physics from The American College, Madurai, India. In addition, he was awarded the Monbukagakusho fellowship by the Japanese government (2010), an Institute of Mathematical Sciences' summer research fellowship (2006), and a Jawaharlal Nehru Center for Advanced Scientific Research summer research fellowship (2003). His current research interests include diffractive optics, microfabrication, and digital holography.

Shanti Bhattacharya obtained her Ph.D. in Physics from the Indian Institute of Technology, Madras in 1997. Her doctoral work was in the area of optical array illuminators. After completing her Ph.D., she worked at the Technical University of Darmstadt, Germany, first as an Alexander von Humboldt Fellow and then as a Guest Scientist. Her research work there included development of an optical pick-up for CD/DVD systems and the design of DOEs for beam shaping of high-power laser beams. She subsequently joined the MEMS division of Analog Devices, Cambridge, USA, where she worked on the design of an optical MEMS switch. She is currently an Associate Professor and has been with the Department of Electrical Engineering, IIT Madras since 2005. Her current research interests are diffractive optics, optical MEMS, and the development of measurement and imaging techniques using fiber interferometry.

Downloaded From: https://www.spiedigitallibrary.org/ebooks/ on 27 Feb 2022
Terms of Use: https://www.spiedigitallibrary.org/terms-of-use